



WESTFÄLISCHE WILHELMS-UNIVERSITÄT
MÜNSTER

PHD THESIS

Non-perturbative investigations of
light bound states of $\mathcal{N} = 1$
supersymmetric Yang-Mills theory

Henning Gerber

supervised by
Prof. Dr. Gernot MÜNSTER

28th May 2019

Theoretische Physik

Non-perturbative investigations of
light bound states of $\mathcal{N} = 1$
supersymmetric Yang-Mills theory

Inaugural-Dissertation
zur Erlangung des Doktorgrades
der Naturwissenschaften im Fachbereich Physik
der Mathematisch-Naturwissenschaftlichen Fakultät
der Westfälischen Wilhelms-Universität Münster

vorgelegt von
Henning Gerber
aus Bielefeld
- 2019 -

Dekan:

Prof. Dr. Gerhard Wilde

Erster Gutachter:

Prof. Dr. Gernot Münster

Zweiter Gutachter:

Apl. Prof. Dr. Jochen Heitger

Tag der mündlichen Prüfung(en):

.....

Tag der Promotion:

.....

This version of the thesis differs slightly from the official document submitted to the faculty. Typos are corrected while results and conclusions are unchanged.

Abstract

In this thesis the light bound states of $\mathcal{N} = 1$ supersymmetric Yang-Mills theory (SYM) with the gauge groups $SU(2)$ and $SU(3)$ are studied in the framework of lattice quantum field theory. SYM is the supersymmetric extension of Yang-Mills theory and it describes the interactions between gluons and their superpartners, the gluinos. Similarly to QCD, SYM is confining at low temperatures. Its lightest bound states form a mass degenerate (chiral) multiplet consisting of three states. Two of these, a scalar and a pseudoscalar state, are mixed states of glueballs and mesons. The third state is a spin- $1/2$ bound state of gluons and gluinos. Using the variational method in combination with APE and Jacobi smearing we have been able to determine the masses of the ground and first excited states of the chiral multiplet. For this purpose, the techniques to analyze the light states have been systematically optimized leading to a significantly increased precision of the results compared to previous investigations concerning the ground states of SYM with the gauge group $SU(2)$. Supersymmetry is broken by the lattice discretization and thus we have extrapolated the results to the chiral and continuum limit where the symmetry is restored. Indeed, we find the expected mass degeneracies of the ground and first excited states of the chiral supermultiplet. The supersymmetry restoration in the chiral and continuum limit is further supported by the supersymmetric Ward identities, which we have analyzed numerically, and which are fulfilled in this limit. Furthermore, we have quantitatively analyzed the mixing of glueball and meson components of the scalar and pseudoscalar states and we have studied the effect of soft supersymmetry breaking by a non-vanishing gluino mass.

Notational Conventions

Throughout this thesis the natural unit system

$$1 = c = \hbar = k_B \quad (0.1)$$

is used and hence all dimensionful quantities are expressed in powers of eV. Furthermore, Einstein summation convention is used, i.e. indices appearing twice in a term shall be summed over. We denote the Dirac (spinor) components of an object by upper Greek indices and the gauge (color) components by upper Latin indices. On the discretized lattice, the space-time dependency of fields and operators can also be written in index notation such as

$$\bar{\lambda}_x^{\alpha a} \lambda_x^{\alpha a} \quad (0.2)$$

which implies a summation over the Dirac and gauge indices α and a , respectively, as well as a sum over all lattice sites x . Using a multi-index notation, where capital Latin letters denote the collection of gauge and Dirac and lattice-site indices, Eq. 0.2 can be written as

$$\bar{\lambda}_M \lambda_M. \quad (0.3)$$

To avoid the implicit summation, the space-time dependency of the fields can be written in parentheses. For example, the expression

$$\bar{\lambda}^{\alpha a}(x) \lambda^{\alpha a}(x) \quad (0.4)$$

implies a summation over the Dirac and gauge indices, but not over the lattice sites. To differentiate between Euclidean and Minkowskian space, the temporal component of the four vector x is labeled by x^0 in Minkowskian space-time and by x^4 in Euclidean space-time. Three dimensional spatial vectors are denoted as \vec{x} and its components are labeled by Latin indices, e.g. x^i , to distinguish them from four dimensional space-time vectors x whose components are denoted by Greek indices x^μ . Thus,

$$\bar{\lambda}_{\vec{x}}^{\alpha a}(x^4) \lambda_{\vec{x}}^{\beta b}(x^4) \quad (0.5)$$

implies only a spatial sum over all lattice sites at a fixed value x^4 of the temporal component.

The trace over gauge and spin indices is denoted by Tr , whereas Tr_c denotes the trace over the gauge (color) indices only.

Contents

1. Introduction	11
2. Supersymmetric Yang-Mills Theory	17
2.1. Yang-Mills Theory	17
2.2. Supersymmetry	18
2.3. $\mathcal{N} = 1$ Supersymmetric Yang-Mills theory (SYM)	19
2.3.1. Symmetry breaking	21
2.3.2. Low energy spectrum	22
3. Lattice Formulation of SYM	25
3.1. Discretizing the action	26
3.2. Breaking of SUSY on the lattice and its restoration	29
3.3. Improving the lattice action	31
3.4. Calculation of observables in SYM on the lattice	33
4. Towards the supersymmetric limit: Scale setting and the adjoint pion	37
4.1. Tuning the renormalized gluino mass	37
4.2. Scale setting	38
4.2.1. Mass dependent and mass independent scale setting	39
5. Generation of gauge configurations	41
5.1. Polynomial and rational approximation	42
5.2. Running the algorithm	43
5.2.1. Tuning the parameters	44
5.3. Thermalization	45
5.4. Potential barriers and topological freezing	46
5.5. Monitoring the sign of the Pfaffian	47
5.6. Finite size effects	48
6. Summary of the gauge ensembles	50
6.1. SU(2)-SYM	50
6.2. SU(3)-SYM	50
7. Measuring bound state masses	54
7.1. Extracting bound state masses from the correlation function	54
7.2. Fitting the correlator	57
7.3. The variational method	60

7.4.	Determining uncertainties, Jackknife method	62
7.5.	Eliminating autocorrelations, Binning	63
8.	Constructing variational bases and measuring correlation functions	65
8.1.	Local interpolating operators	65
8.2.	Evaluating the correlators and the $a\text{-}\pi$	67
8.3.	Smearing techniques	69
8.3.1.	APE smearing	69
8.3.2.	Jacobi smearing	70
8.4.	Calculation of the propagators	72
8.4.1.	Connected piece	73
8.5.	Disconnected piece and SET	74
8.5.1.	Gluino-glue	75
8.6.	Speeding up the inverter	76
8.6.1.	Truncated Eigenmode approximation	76
8.6.2.	Even Odd preconditioning	78
9.	Optimizing the variational bases	80
9.1.	Smearing parameters	80
9.1.1.	APE smearing	81
9.1.2.	Jacobi smearing	82
9.2.	Number of stochastic estimators	90
9.3.	Optimizing the variational operator bases	91
9.3.1.	Single Smearing Levels	92
9.3.2.	Combining several smearing Levels	94
9.3.3.	Mixed operator bases	98
10.	Glueball and meson mixing in the two lowest chiral supermultiplets	102
11.	Further details of the variational analysis	106
11.1.	Solving the GEVP and the truncation method	106
11.2.	t_0	107
11.3.	Offset Handling / Derivative Trick	109
11.4.	Ordering and fixed vector method	113
11.5.	Normalization and Symmetrization	115
12.	Summary of the measurements	117
13.	Extrapolations	118
13.1.	Two-step and combined extrapolations	118
13.1.1.	Combined extrapolation	119
13.1.2.	Two-step extrapolation	121

13.1.3. Theoretical comparison of the two approaches	122
13.2. Optimizing the two-step extrapolation	123
13.3. Optimizing the combined extrapolation	127
13.4. Summary of the extrapolations	131
14. Results of the mass spectra and the mixing in the scalar channel	133
14.1. Light bound state masses of SU(2)-SYM	133
14.2. Light bound state masses of SU(3)-SYM	137
14.3. Soft supersymmetry breaking	139
14.4. Mixing coefficients in the scalar channel	141
14.5. Summary and discussion of the extrapolated mass spectra	143
15. SUSY Ward Identities	145
16. Conclusions and Outlook	148
A. Appendix	150
A.1. Data layout and vectorization	150
A.2. Jacobi smearing the fermion fields and the propagator	152
A.3. Hermiticity of the correlation matrix $C(t)$	153
A.4. SET bias	153
A.5. Independence of the results of the scale setting observables	156
A.6. Summary tables of the ensembles and measured data	158
A.7. Plots	162
A.7.1. Spectra	162
A.7.2. Mixing coefficients	164
Bibliography	166

1. Introduction

The search for the fundamental laws of nature belongs to the oldest and greatest challenges of humanity. Throughout history scientists have achieved tremendous progress to answering this puzzle by learning from ever more elaborate experiments and extensive theoretical studies. This hunt for the elementary building blocks of nature and their interactions has culminated in two theories: *General Relativity* (GR) and the *Standard Model of Particle Physics* (SM). GR is the theory of gravitation between macroscopic objects and the SM is the theory of the known elementary particles and their electroweak and strong interactions. These two theories accurately predict the physics from the smallest up to the highest scales accessible in present-day experiments. Particularly impressive examples are the discovery of gravitational waves almost 100 years after they have been predicted by Albert Einstein on the basis of GR [1, 2], and the agreement of measured and predicted values of the electron’s anomalous magnetic moment to more than 10 significant figures [3].

Despite their great success, GR and the SM cannot be the final theory of everything. In fact, GR and the SM are actually not even compatible with one another since GR is a classical theory, while the SM is a quantum field theory (QFT). All attempts to quantize GR in the framework of QFT have failed because the resulting theory is not renormalizable perturbatively. A non-trivial UV-fixed point of the renormalization group flow could lead to consistent non-perturbative renormalizability. However, such a fixed point has not been found, yet. Therefore, many physicists believe that a fundamental theory of the laws of nature, which includes quantum gravity, cannot be a QFT of particle fields. Such a QFT could then be viewed as an effective theory that can be derived from the fundamental theory. *String Theory* and *Loop Quantum Gravity* are possible candidates for such an underlying fundamental theory. However, these theories are still under development and it has not been possible, yet, to recover the known physics from these theories.

Gravity is by far the weakest of all known interactions (at the subatomic scale it is a factor 10^{-37} weaker than the weak interaction). The effects of quantum gravity are therefore expected to become important only for very large gravitational fields, such as in the presence of black holes or at very large energy scales, such as the Planck scale. In this thesis we therefore leave aside the problem of quantum gravity and work in the framework of QFT which provides the currently most accurate, complete and consistent description of elementary particles and their interactions.

1. Introduction

Apart from the the conflict with GR at the fundamental level, there are further theoretical and observational indications that the SM is not complete. Some of the most prominent open puzzles are

1. The existence of the Higgs field in the SM leads to the so-called **hierarchy problem**: Due to the Higgs field being scalar, quantum loop calculations predict a very large correction to the mass of the Higgs boson [4, 5]. Only by an unnatural fine-tuning of the bare Higgs mass the observed value $m_{\text{Higgs}} \simeq 125 \text{ GeV}$ [6] can be recovered in the SM.
2. **Dark matter**: Several cosmological observations such as rotational curves of galaxies [7], the bullet cluster [8] and large scale structure formation [9] provide evidence for the existence of electromagnetically non-interacting and therefore **dark matter**. In the SM the neutrinos are examples for such dark particles. Their abundance is, however, too low to explain the cosmological observations which suggest that approximately 85 % of the matter in the universe is dark matter. In fact, there is no known particle within the SM to explain these observations.
3. **Grand unification**: The quantization of electric charges and the exact cancellation of proton and the electron electric charges are not explained by the SM and suggest that strong and electroweak interactions should be combined in a *Grand Unified Theory* (GUT). This is supported further by the fact that, due to renormalization group running, the three coupling constants of the SM meet almost, but not exactly, at a common energy scale $\lambda_{\text{GUT}} \sim 10^{16} \text{ GeV}$ [10].
4. **Strong CP problem**: There exists a term in the QCD part of the SM Lagrangian that is allowed by the SM's symmetries, but whose coefficient $\theta \leq 10^{-9}$ is unnaturally small [11]

$$\mathcal{L}_{\text{CP}} = \theta \frac{n_f g^2}{32\pi^2} F_{\mu\nu} \tilde{F}^{\mu\nu} . \quad (1.1)$$

This term would lead to CP-violation in QCD which is not observed. Therefore, θ must be very small or zero. This fine-tuning problem suggests that there is an underlying mechanism, not yet know, that suppresses the value of θ , which would naturally be of the order of one. There are several proposals for such a mechanism, one of them is an additional pseudoscalar elementary particle, the so-called axion [12].

5. **Matter-Antimatter asymmetry**: The Λ -CDM model (**C**old **D**ark **M**atter), which is also called the Standard Model of Cosmology, is based on GR, the

SM, additional cold dark matter and a cosmological constant Λ . With only few assumptions it is able to explain the structure of our universe. However, no explanation has been found, yet, within the the Λ -CDM model for the much larger abundance of baryonic matter than anti-baryonic matter [13].

6. In the SM the **neutrinos** are **massless**. The observation of neutrino oscillations, which was awarded with the Nobel Price in 2015 for T. Kajita and A. B. McDonald, has proven that neutrinos do have a mass. While the squared mass differences Δm_{21}^2 and Δm_{23}^2 are known from experiments [6], only upper limits to the values of the masses themselves have been found. The most stringent limits have been obtained from cosmology on the basis of the Λ -CDM model to be $m_\nu < 0.17$ eV [14]. The KATRIN experiment aims to perform a direct measurement of the electron antineutrino mass. It is designed to be sensitive to a neutrino mass down to 0.2 eV [15] which is above the threshold excluded by cosmological observations.
7. The observation that the universe is expanding at an accelerating rate is parameterized in the Λ -CDM model by an exotic form of energy, so-called **dark energy** [16]. The Λ -CDM model predicts that dark energy contributes with 68 % to the energy content of the universe. However, it is presently still very unclear, what the nature of this dark energy is.

The failure of the SM to explain these puzzles shows that the SM is incomplete and needs to be extended to also incorporate so-called physics *Beyond the Standard Model* (BSM). The search for extensions of the SM has yielded many promising new ideas and concepts. Some of them tackle only specific problems of the SM, while others solve more than one problem at once.

One of the most promising and mathematically most elegant ideas is *supersymmetry* (SUSY) which postulates an additional symmetry between bosonic and fermionic degrees of freedom. Supersymmetric theories are interesting and useful from different perspectives. On the one hand, they elegantly solve several problems of the SM, see [10] for an overview. In particular, the hierarchy problem is solved naturally, SUSY theories provide different dark matter candidates, the running coupling constants meet much more precisely at a GUT scale $\Lambda_{GUT} \approx 10^{16}$ GeV and the strong CP problem can be solved within SUSY theories [17]. Furthermore, SUSY is an essential component of string theory. On the other hand, supersymmetric theories can serve as very useful toy models to theoretically understand the phenomena of quantum field theories because the additional symmetry simplifies investigations dramatically. A well known example is the *AdS/CFT* correspondence which is deduced from string theory and which in its original form relates $\mathcal{N} = 4$ super Yang-Mills theory to string theory in five-dimensional anti-de Sitter space times a five-sphere [18]. In this thesis we make use of the additional

1. Introduction

symmetry in the form of the Ward identities corresponding to the SUSY transformations (cf. Sec. 15).

The first studies of supersymmetric field theories have been done in the 1970's, with the Wess-Zumino model [19] being one of the first and most important toy models. A more realistic supersymmetric model is the *Minimally Supersymmetric extension of the Standard Model* (MSSM) [20]. There have been many studies of supersymmetric models and experimental searches for the particles predicted by supersymmetry. To date, no such particle has been found. Since unbroken SUSY predicts for each fermion a boson of the same mass and vice versa, it must be broken if it exists in nature. If this breaking is soft, such that no additional UV-divergences occur, the aforementioned hierarchy problem is still under control. However, it is not clear which mechanism is responsible for the breaking of supersymmetry.

In fact, despite the long ongoing investigation of supersymmetric models, most of the low energy phenomena of these theories are still largely unknown. The reason is that the most commonly used tool in QFT, perturbation theory, breaks down at small energies, where the running gauge couplings become large for strongly interacting (asymptotically free) theories. Other computational methods are needed to study low energy features like the spectrum of bound states or the phase diagram.

A technique that is particularly useful to investigate this non-perturbative realm of strongly interacting theories is *Lattice Quantum Field Theory*. Lattice QFT allows to calculate non-perturbative properties of strongly interacting QFTs from first principles. Amongst others, the correct prediction of the hadron spectrum [21] and the deconfinement phase transition of QCD [22] belong to the most important successes of lattice QFT.

Based on early theoretical work of Curci, Veneziano and Yankielowicz [23], [24] the Desy-Münster collaboration investigates non-perturbative properties of $\mathcal{N} = 1$ supersymmetric Yang-Mills theory (SYM) using the framework of lattice QFT. SYM is the simplest supersymmetric non-abelian gauge theory. It describes the interactions of gluons and their superpartners the gluinos. Since it does not include the other particles of the SM, it is not expected to describe the laws of nature, but it is rather used as a toy model to study supersymmetric gauge theories in the context of lattice QFT and should be viewed as a first step towards a more realistic theory, e.g. the supersymmetric extension of QCD, called *Super-QCD*. In the last decade the Desy-Münster collaboration has achieved considerable progress to perform lattice calculations of SYM. For SYM with the gauge group $SU(2)$ the masses of the lightest bound states have been computed [25, 26, 27, 28, 29, 30], the SUSY Ward identities have been studied [31, 32, 33, 29], and the deconfinement phase transition at finite temperature has been investigated [34, 35]. The results are consistent with theory predictions from effective models and confirm that, indeed, SYM can be studied in the framework of lattice QFT. Recently, the

collaboration has moved on to investigating SYM with the gauge group $SU(3)$, the gluon and gluino part of Super-QCD. First results have already been obtained [36, 37] and show many similarities to the results for the gauge group $SU(2)$.

This thesis is a contribution to the lattice simulations of SYM conducted by the Desy-Münster collaboration. It summarizes the recent progresses in the investigations of the spectrum of bound states in SYM with the gauge groups $SU(2)$ and $SU(3)$. A major improvement compared to earlier investigations of SYM with the gauge group $SU(2)$ is the utilization of the so-called *Variational Method*, which we use in combination with APE and Jacobi smearing. We have systematically optimized the techniques and the relevant parameters used within this approach. Consequently, we were not only able to increase the precision of the determined masses of the lightest bound states, but we have also extracted the corresponding first excited states as well as mixing properties of glueball and meson components of these states. The improved results for SYM with the gauge group $SU(2)$ have been published in [30]. Furthermore, the variational method is also successfully applied in the investigations of SYM with the gauge group $SU(3)$, where in addition to the masses and mixing properties we also study the influence of a soft supersymmetry breaking gluino mass on the spectrum of bound states. Moreover, recent investigations of the SUSY Ward identities are presented for the case of the gauge group $SU(3)$.

The thesis is structured as follows. In Sec. 2, SYM is briefly introduced and the theoretical expectations for the low energy bound states are discussed. In Sec. 3, the discretized formulation of SYM that we use to study SYM in the framework of lattice QFT is discussed. This formulation requires extrapolations of intermediate results to the so-called chiral and continuum limit. For this purpose, the simulated energy and length scales and the mass of the gluino need to be determined and the simulation parameters have to be tuned such that the extrapolations can be performed reliably. The procedure to estimate the scales and the gluino mass is discussed in Sec. 4.

The calculation of observables in lattice QFT is typically performed in several steps. First, field configurations are generated for different choices of simulation parameters. This step, called *Production*, is described in Sec. 5 and the generated field configurations are summarized in Sec. 6. In the second step, the so-called *Measurement*, correlation functions are determined from these field configurations. From these correlation functions, the observables are calculated in the third step (*Analysis*). The measurement and analysis steps, optimized for the variational investigation of the low energy spectrum, are described in detail in Secs. 7 to 12. In the last step, the observables, obtained from different sets of gauge configurations are extrapolated to the desired point in parameter space, here to the chiral and continuum limit. In Sec. 13, the details of these extrapolations are discussed and

1. Introduction

in Sec. 14 the extrapolated results are presented and discussed.

In addition to the variational analysis of the low energy spectrum, we also investigate supersymmetry restoration in the chiral and continuum limit by means of the SUSY Ward identities. Our findings are briefly summarized in Sec. 15. Finally, the conclusions and an outlook are presented in Sec. 16.

2. Supersymmetric Yang-Mills Theory

Symmetries have become the guiding principle to construct theories of the fundamental laws of physics. In fact, QFTs that aim to describe physics on a broad range of energy scales can be uniquely determined by defining their symmetries, their field content and a finite set of parameters. The Lagrangian of such a theory is given by the most general expression that can be formed from the given fields such that it is scalar, i.e. invariant under the demanded symmetries, and such that the theory is renormalizable. Renormalizability requires that all terms of the Lagrangian have a mass dimension of four or less. While the Lagrangian necessarily has to be invariant under the defining symmetries, this does not always guarantee that the quantum theory is also invariant because symmetries can be broken dynamically or anomalously. Therefore, it has to also be assured that the vacuum state as well as the measure of the path integral fulfill the demanded symmetries.

The framework of QFT itself is based on the requirement of Poincaré invariance. Therefore, every quantum field theory describing elementary particles is necessarily symmetric under the Poincaré group. Furthermore, quantum field theories are also invariant under CPT [38], which is the subsequent application of charge conjugation (C), parity transformation (P), and time conjugation (T).

The quantum field theory investigated in this thesis is $\mathcal{N} = 1$ supersymmetric Yang-Mills theory (SYM). It is defined to be invariant under $\mathcal{N} = 1$ global supersymmetry and under transformations of a gauge group G . Its field content is given by the gluon field $A_\mu^a(x)$ and its superpartner, the gluino field $\lambda^{a\alpha}(x)$, where α , a and μ are Dirac, gauge and space-time indices, respectively. In this thesis we consider the gauge groups $G = \text{SU}(2)$ and $G = \text{SU}(3)$. The corresponding theories are abbreviated as $\text{SU}(2)\text{-SYM}$ and $\text{SU}(3)\text{-SYM}$.

In the following, the most important aspects of SYM that are needed in this thesis are summarized. This includes a brief introduction of the two ingredients of SYM, Yang-Mills theory and supersymmetry. In addition, the expected low energy spectrum is discussed. For a more complete overview of supersymmetry the reader is referred to the literature, e.g. [10] and previous doctoral theses of the Desy-Münster collaboration [39, 40, 41, 25, 42, 43].

2.1. Yang-Mills Theory

Yang-Mills theories are quantum field theories that are invariant under non-abelian gauge group transformations. Gauge groups are generated by compact, reductive Lie algebras, most importantly the special unitary groups $\text{SU}(N)$. The field content of Yang-Mills theories consists of only the gauge fields, i.e. the fields that are

2. Supersymmetric Yang-Mills Theory

required to construct the gauge covariant derivative. For this reason Yang-Mills theories are also called pure gauge theories. Non-abelian Yang-Mills theories are confining at low temperatures, meaning that free particles, which are represented in QFT as asymptotic states, are not charged under the gauge group (color neutral). Hence, elementary particles that are charged under the gauge group are confined in color neutral bound states. Furthermore, these theories have a mass gap, i.e. the bound states are massive. Confinement is not yet completely understood theoretically and its existence in Yang-Mills theories has not been rigorously proven. In fact, the proof of a mass gap in Yang-Mills theories is one of the unsolved "Millennium Prize Problems" stated by the Clay Mathematics Institute in 2000 [44].

While, in general, semi-simple Lie groups, e.g. $U(1) \otimes SU(2) \otimes SU(3)$, are valid gauge groups of a Yang-Mills theory, we restrict ourselves here to the case of simple Lie groups which contain only one type of gauge field, e.g. $SU(N)$. The Lagrangian of such a Yang-Mills theory is given by

$$\mathcal{L} = -\frac{1}{4} F^{a\mu\nu} F_{\mu\nu}^a, \quad (2.1)$$

where $F_{\mu\nu}^a$ is the field strength tensor

$$F_{\mu\nu}^a = \partial_\mu A_\nu^a - \partial_\nu A_\mu^a + g f^{abc} A_\mu^b A_\nu^c \quad (2.2)$$

of the gauge field

$$A_\mu(x) = A_\mu^a(x) T^a \quad (2.3)$$

and where T^a and f^{abc} are the generators and the structure constants of the gauge group's Lie algebra, respectively.

Pure gauge theories are the simplest non-abelian gauge theories since they contain only gauge degrees of freedom, i.e. its elementary particles are only gluons. The particle spectrum therefore consists of bound states of gluons, so-called glueballs. Pure gauge theories can be studied very efficiently in the framework of lattice QFT. The necessary computations are much simpler compared to analogous computations for theories that contain fermion fields because of the absence of the fermion propagator, which is typically the most cost intensive part to be computed in lattice QFT calculations.

2.2. Supersymmetry

The next ingredient of SYM is supersymmetry which relates fermion and boson fields to one another. Actually, due to the Coleman-Mandula theorem [45], it

2.3. $\mathcal{N} = 1$ Supersymmetric Yang-Mills theory (SYM)

is not obvious that such a symmetry is realizable in quantum field theory. The theorem states under very general assumptions that in QFT, Poincaré space-time symmetry and internal symmetries cannot be combined in the form of Lie groups in any other but the trivial way, i.e. as a direct product. Later, Haag, Łopuszański and Sohnius discovered that the Poincaré space-time symmetry actually can be extended if the restriction to Lie groups is loosened [46]. By generalizing ordinary Lie algebras to \mathbb{Z}_2 -graded Lie algebras, also called *Lie superalgebras*, a new class of space-time symmetry is obtained: Supersymmetry. In fact, they also showed that the Lie superalgebra is the only possible non-trivial extension of the Poincaré algebra.

A Lie superalgebra has to fulfill two axioms:

1. $[A, B] = (-1)^{|A||B|+1} [B, A]$ (Skewsymmetry), (2.4)

2. $0 = (-1)^{|A||C|} [A, [B, C]] + (-1)^{|C||B|} [C, [A, B]] + (-1)^{|B||A|} [B, [C, A]]$,
(Super Jacobi Identity) (2.5)

where $|A|$ denotes the degree of the generator A and it can be either 0 or 1. Generators with degree 0 are called bosonic generators and generators with degree 1 are called fermionic generators or *supercharges*. The generators of the Poincaré group have charge 0. When restricted to generators of charge 0, the ordinary Lie algebra axioms are recovered.

2.3. $\mathcal{N} = 1$ Supersymmetric Yang-Mills theory (SYM)

$\mathcal{N} = 1$ supersymmetric Yang-Mills theory is the simplest supersymmetric extension of Yang-Mills theory. In addition to the Poincaré group, one Majorana supercharge Q^α is introduced, fulfilling the Majorana condition

$$\bar{Q} = Q^T C, \quad Q = C \bar{Q}^T, \quad (2.6)$$

where C is the charge conjugation operator

$$C = i\gamma_2\gamma_0. \quad (2.7)$$

The Lie superalgebra is then given by

$$[P^\mu, P^\nu] = 0, \quad (2.8)$$

$$[M^{\mu\nu}, P^\rho] = i(\eta^{\mu\rho} P^\nu - \eta^{\nu\rho} P^\mu), \quad (2.9)$$

$$[M^{\mu\nu}, M^{\rho\sigma}] = i(\eta^{\mu\rho} M^{\nu\sigma} - \eta^{\mu\sigma} M^{\nu\rho} - \eta^{\nu\rho} M^{\mu\sigma} + \eta^{\nu\sigma} M^{\mu\rho}), \quad (2.10)$$

2. Supersymmetric Yang-Mills Theory

$$[P^\mu, Q^\alpha] = 0, \quad (2.11)$$

$$[M^{\mu\nu}, Q^\alpha] = -\sigma^{\mu\nu, \alpha\beta} Q^\beta, \quad (2.12)$$

$$\{Q^\alpha, \bar{Q}^\beta\} = 2\gamma_\mu^{\alpha\beta} P^\mu, \quad (2.13)$$

with P^μ the generators of translations, $M^{\mu\nu}$ the generators of the Lorentz group, $\eta^{\mu\nu}$ the metric tensor of Minkowskian space-time, γ_μ the Dirac matrices and $\sigma_{\mu\nu} = \frac{i}{2}[\gamma_\mu, \gamma_\nu]$. Eqs. 2.8 to 2.10 define the Poincaré algebra and Eqs. 2.11 to 2.13 are introduced due to the \mathbb{Z}_2 -grading.

The Lagrangian of SYM is then constructed by including all renormalizable terms that can be formed from the gluon field $A_\mu^a(x)$ and the gluino field $\lambda^{a\alpha}(x)$ such that it is scalar under the supersymmetry group generated by the superalgebra defined in Eqs. 2.8 to 2.13. On-shell it is given by

$$\mathcal{L} = -\frac{1}{4}F_{\mu\nu}^a F^{\mu\nu, a} + \frac{i}{2}\bar{\lambda}^a (\not{D}\lambda)^a. \quad (2.14)$$

We neglect here a θ -term similarly to the θ -term of QCD which is mentioned in Sec. 1. Such a term would be consistent with the symmetries but it is not studied in this thesis, i.e. we consider $\theta = 0$.

Since the gluino is the superpartner of the gluon, their degrees of freedom have to match. Hence, the gluino field has to be in the same representation of the gauge group as the gluon, which is the adjoint representation. Thus, also the covariant derivative D_μ (Eq. 2.14) is the adjoint one

$$(D_\mu \lambda)^a = \partial_\mu \lambda^a + g f^{abc} A_\mu^b \lambda^c. \quad (2.15)$$

Furthermore, the gluino field is of Majorana nature, i.e. the gluino is its own anti-particle and the gluino field λ has to fulfill the Majorana condition (Eq. 2.6). The global infinitesimal supersymmetry transformation that relates gluon and gluino field is

$$\delta A_\mu^a = -2i\bar{\lambda}^a \gamma_\mu \epsilon, \quad \delta \lambda^a = -\sigma_{\mu\nu} F_{\mu\nu}^a \epsilon, \quad (2.16)$$

where ϵ is the Grassmann valued infinitesimal parameter of the transformation. The supersymmetry transformation yields a conserved Noether current at the classical level and corresponding Ward identities in the quantized theory. They are discussed in more detail in Sec. 15.

For the lattice simulations of SYM and to study supersymmetry breaking, it is useful to introduce a gluino mass term

$$\mathcal{L}_{\text{SUSY}} = -m_0 \bar{\lambda}^a \lambda^a, \quad (2.17)$$

2.3. $\mathcal{N} = 1$ Supersymmetric Yang-Mills theory (SYM)

which breaks supersymmetry softly, meaning that this term does not introduce additional ultraviolet divergences. The full SYM Lagrangian, including the supersymmetry breaking term is then given by

$$\mathcal{L}_{\text{SYM}} = -\frac{1}{4}F_{\mu\nu}^a F^{\mu\nu,a} + \frac{i}{2}\bar{\lambda}^a (\not{D}\lambda)^a - \frac{m_0}{2}\bar{\lambda}^a \lambda^a. \quad (2.18)$$

2.3.1. Symmetry breaking

The SYM Lagrangian (Eq. 2.14) is very similar to the QCD Lagrangian with only one flavor. The difference is that in SYM the fermion field λ is of Majorana type and in the adjoint representation of the gauge group, whereas in QCD the fermions are of Dirac type and in the fundamental representation. Due to this similarity, SYM features similar symmetries as one-flavor QCD at the level of the Lagrangian, i.e. at the classical level. In particular, for vanishing fermion mass, the Lagrangians of both theories have an accidental chiral symmetry and are conformally invariant. These two symmetries are broken anomalously by quantum corrections.

The aforementioned generation of a mass gap breaks the conformal symmetry. The chiral symmetry of SYM, whose infinitesimal transformation is given by

$$\delta\lambda = i\alpha\gamma_5\lambda, \quad (2.19)$$

with α the infinitesimal transformation parameter, is broken in different ways. Quantum corrections break it to the discrete subgroup \mathbb{Z}_{2N_C} [47]. Furthermore, when SYM is studied on the lattice, the discretization may break this discrete subgroup explicitly. Finally, a non-vanishing gluino mass, as it is introduced by the soft SUSY breaking term (Eq. 2.17), breaks this symmetry completely. The chiral symmetry breaking pattern is further discussed on the basis of the lattice discretization chosen for our investigations in Sec. 3.2.

In addition to the chiral and conformal symmetry breaking it is natural to ask whether supersymmetry could be broken spontaneously. However, in SYM this is not possible. This is demonstrated by considering the Witten index, which counts the number of bosonic minus the number of fermionic states with zero energy and which has to be necessarily zero for a broken SUSY phase to exist [48]

$$w = \text{Tr}[(-1)^F] = n_{\text{boson}} - n_{\text{fermion}}. \quad (2.20)$$

Witten further showed that in SYM the Witten index is non-zero

$$w = N_c. \quad (2.21)$$

2. Supersymmetric Yang-Mills Theory

2.3.2. Low energy spectrum

Using the methods of effective field theory, Veneziano and Yankielowicz have worked out candidates for the lightest bound states in SYM [23]. They claimed that the lightest bound states form a mass-degenerate multiplet, the *chiral supermultiplet*, consisting of a scalar meson, a pseudoscalar meson (0^{++} and 0^{-+} in J^{PC} -representation, respectively) and a spin- $1/2$ bound state of gluons and gluinos which we call *gluino-glue*. The scalar meson is closely related to the f_0 meson known from QCD. The difference is that in SYM the fermions are in the adjoint and not in the fundamental representation of the gauge group. Therefore, in SYM the scalar meson is called a- f_0 where a stands for adjoint. Analogously, the pseudoscalar meson is called a- η' due to its similarity to the η' meson of QCD. The gluino-glue does not have an analogue in QCD.

Later Farrar, Gabadadze and Schwetz extended this analysis by considering also glueballs [49, 50], which are bound states of gluons without any valence fermions. They argued that there is, a priori, no reason why these glueball states should be heavier than the meson states. Therefore, they considered another multiplet consisting of a scalar glueball (0^{++}), a pseudoscalar glueball (0^{-+}) and a gluino-glue bound state. These glueballs have the same quantum numbers as the respective mesons and therefore it is expected that the physical states are mixed states of glueballs and mesons of the same quantum numbers. Hence, when mixing is considered, the physical states are expected to be arranged in chiral supermultiplets, each formed of three mass degenerate states: A scalar and a pseudoscalar mixed state of glueball and meson states and a gluino-glue state. In the following, the states in the lightest multiplet are called the *ground states* and the corresponding states of the heavier multiplet are called the *first excited states*. Furthermore, the collection of all scalar states is abbreviated by the *scalar channel*, and similarly for the pseudo-scalar and spin- $1/2$ states.

The authors of [50] have also worked out the multiplet structure when soft supersymmetry breaking is considered, e.g. by a non-vanishing gluino mass. They found that the ground states become heavier when SUSY is broken softly. In that case, the mass of the scalar is shifted the least and the mass of the pseudoscalar the most. The masses of the excited states are shifted by the same amounts, but to lower values. Therefore, when SUSY is broken softly, the pseudoscalar becomes the lightest particle of the excited multiplet and the scalar particle becomes the heaviest. The structure of the two chiral supermultiplets is depicted in Fig. 2.1.

The investigation of the ground and first excited states of the chiral multiplet is the central subject of this thesis. The expected mass degeneracy is a crucial test if our lattice calculations are suited to investigate SYM. First results of investigations for SU(2)-SYM that have been performed before the scope of this thesis, have confirmed the expected mass degeneracy of the ground states in the limit

2.3. $\mathcal{N} = 1$ Supersymmetric Yang-Mills theory (SYM)

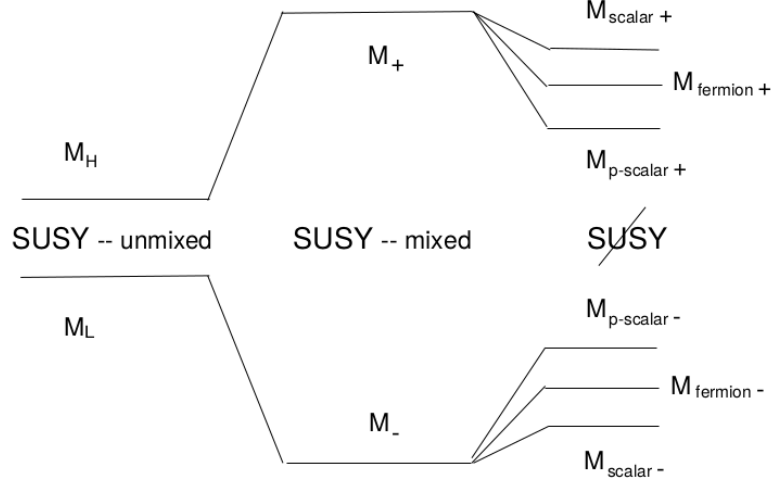


Figure 2.1.: Structure of the two considered chiral supermultiplets. When SUSY is not broken the scalar, pseudoscalar and gluino-gluon states form two degenerate multiplets (- and +). Soft supersymmetry breaking leads to mass shifts that break the degeneracy. Figure taken from [50].

of unbroken SUSY [28]. In fact, in these investigations, the glueball and meson components of the scalar and pseudoscalar channel have been considered separately. While the lowest masses, obtained from the analysis of the glueball and the meson components, agree approximately in the scalar channel, in the pseudoscalar channel the lowest masses obtained from the glueball components are significantly larger than the masses obtained from the meson component. This suggests that the physical ground state has only a small glueball component in the pseudoscalar channel, whereas in the scalar channel the mixing between glueball and meson states is considerably large in the ground state.

In the scope of this thesis, we have improved our methods and obtained more precise results for the ground state masses of SU(2)-SYM. Our findings not only confirm the degeneracy for the ground states, but we are now also able to observe the degeneracy in the first excited multiplet. Furthermore, we have been able to extract information about the glueball and meson contributions to the scalar and pseudoscalar states. The improved results for SU(2)-SYM have been published in [30] and the results for the gauge group SU(3) have been published in [36, 37]. The optimization of our methods and their application in the simulations of SYM with the gauge groups SU(2) and SU(3) are explained in much detail in Secs. 7 to 13. The final results for the bound state spectrum are discussed in Sec. 14.

2. *Supersymmetric Yang-Mills Theory*

The states belonging to the chiral supermultiplets are not the only bound states in SYM. There are, for example, baryons, i.e. states with three valence gluinos, vector mesons and more. In addition, there are also multi-particle states. The masses of these states have not been analyzed, yet, and they could be lighter than the first excited states of the chiral supermultiplet. In order to understand the spectrum of physical states in more detail, the Desy-Münster collaboration has started to investigate baryon states [51]. The investigations of such states are, however, beyond the scope of this thesis and we focus here only on the ground and first excited states of the chiral supermultiplet.

3. Lattice Formulation of SYM

Quantum field theories are usually defined in the continuum. The approach of lattice QFT is to discretize space-time on a finite hypercubic lattice with a non-zero lattice spacing a , see Fig. 3.1, and to calculate observables numerically on this lattice. Since computational resources are limited, the lattice has to be of finite extent. The results, obtained for different lattice spacings a and different lattice volumes V are then extrapolated to the thermodynamic limit of infinite lattice volume $V \rightarrow \infty$ and to the *continuum limit* of vanishing lattice spacing $a \rightarrow 0$. To obtain correct results in the continuum limit, it is necessary that, on the one hand, the lattice spacings are fine enough to resolve the observables of interest and that, on the other hand, the lattice sizes are large enough to sufficiently suppress so-called *finite volume effects*. For computations of particle masses the former requirement translates to

$$a \lesssim \frac{1}{m}. \quad (3.1)$$

The latter requirement means that the lattices need to be larger than the typical correlation lengths ξ , which are governed by the masses m of the lightest particles

$$\xi \sim \frac{1}{am}. \quad (3.2)$$

Limited computational resources restrict the number of lattice sites per spatial direction to be of the order $N_S = \mathcal{O}(10^1 - 10^2)$, which requires the lattice spacings to fulfill

$$N_S \gg \xi \stackrel{\text{Eq. 3.2}}{\Rightarrow} a \gg \frac{1}{N_S m} = \mathcal{O}(10^{-2} - 10^{-1})m^{-1}. \quad (3.3)$$

In QCD and similarly in SYM (cf. Sec. 4) this condition typically corresponds to lattice extents of

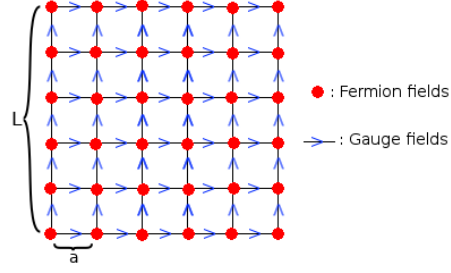
$$L = aN_S \gtrsim 1\text{-}2 \text{ fm}. \quad (3.4)$$

The extent aN_T in temporal direction is related to the temperature T via (for a derivation see, for example, [52], Chap. 12)

$$aN_T = 1/T. \quad (3.5)$$

3. Lattice Formulation of SYM

Figure 3.1: Two dimensional slice of the four dimensional hypercubic lattice. The lattice spacing is denoted by a and the lattice extent by L .



In this thesis we study the properties of SYM at low temperature and we therefore set for our simulations $N_T = 2N_S$. To account for translational invariance and the Grassmanian nature of fermion fields, we generally use periodic boundary conditions for all fields, but antiperiodic temporal boundary conditions for the fermion fields (for an explanation see [53], Chap. 4). Other choices are possible; the most prominent alternatives are periodic, Dirichlet [54] or open [55] temporal boundary conditions for the fermion fields.

Due to its similarity to QCD, the lattice calculations for SYM are very similar to the corresponding calculations of QCD which are explained in many textbooks about lattice QCD, e.g. [53, 52]. Therefore, in the following only the most important steps are explained, highlighting, in particular, the differences to QCD calculations.

3.1. Discretizing the action

In order to calculate observables on the lattice, a corresponding discretized formulation of SYM is required. For this purpose, a discretized action S^{latt} , which in the continuum limit $a \rightarrow 0$ agrees with the continuum action S^{cont} , is constructed. The choice of the discretized action S^{latt} is not unique. Any lattice discretization that yields the correct continuum limit is a valid discretization. Lattice QFT calculations are usually performed in Euclidean space-time and hence all calculations in the remainder of this thesis are done in the Euclidean formulation. It is obtained from the Minkowskian one by performing the Wick rotation of the temporal space-time component

$$x^0 \rightarrow -ix^4. \quad (3.6)$$

The most naïve lattice discretization is obtained by replacing the continuum gauge action

$$S_G^{\text{cont}} = \int d^4x \left(\frac{1}{4} F_{\mu\nu}^a F^{\mu\nu,a} \right) \quad (3.7)$$

3.1. Discretizing the action

and the continuum fermion action

$$S_F^{\text{cont}} = \int d^4x \text{Tr}_c [\bar{\lambda} (\not{D} + m_0) \lambda] \quad (3.8)$$

by the lattice actions

$$S_G^{\text{latt}} = \frac{\beta}{N_c} \sum_p \text{Re} (\text{Tr}_c [1 - U^{(p)}]) , \quad (3.9)$$

$$S_F^{\text{latt}} = \frac{a^4}{2} \sum_x \text{Tr}_c [\bar{\lambda} D \lambda] = \frac{a^4}{2} \sum_{x,a,\alpha} \bar{\lambda}_x^{\alpha a} D_{xy}^{\alpha a, \beta b} \lambda_y^{\beta b} , \quad (3.10)$$

where

$$D(x, y) = \sum_{\mu=1}^4 \gamma_\mu \frac{V_\mu(x) \delta_{x+\hat{\mu}, y} - V_\mu^\dagger(x - \hat{\mu}) \delta_{x-\hat{\mu}, y}}{2a} + m_0 \delta_{x, y} \quad (3.11)$$

is the so-called Dirac operator (Dirac and gauge indices suppressed), $\hat{\mu}$ denotes a unit vector in μ direction and

$$\beta = \frac{2N_c}{g^2} . \quad (3.12)$$

Furthermore, $V_\mu(x)$ is the parallel transporter from lattice site x to the neighboring lattice site in μ -direction. These parallel transporters, called *gauge links*, are required for gauge invariance of the action and represent the gauge field on the lattice. A derivation of these formulae can be found in almost any textbook on lattice QCD, e.g. [53, 52]. The main difference is, that here the gauge links $V_\mu(x)$ in the Dirac operator are in the adjoint representation of the gauge group in contrast to QCD, where the gauge links $U_\mu(x)$ are in the fundamental representation. The gauge links of the two representations are related via

$$V_\mu^{ab}(x) = 2\text{Tr}_c (U_\mu^\dagger(x) T^a U_\mu(x) T^b) . \quad (3.13)$$

Traces of closed loops of gauge links, called *Wilson loops*, are gauge invariant. The smallest possible Wilson loop is called *plaquette* $U_{\mu\nu}^{(p)}$ (see Fig. 3.2)

$$U_{\mu\nu}^{(p)} = \text{Tr}_c (U_\mu(x) U_\nu(x + \hat{\mu}) U_\mu^\dagger(x + \hat{\nu}) U_\nu^\dagger(x)) , \quad (3.14)$$

and the gauge action S_G^{latt} contains a sum over all possible plaquettes in the fundamental representation ($\sum_p U^{(p)}$).

It is simple to show that the naïve lattice action (Eqs. 3.9, 3.10) approaches

3. Lattice Formulation of SYM

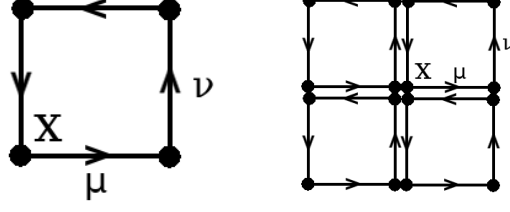


Figure 3.2.: Plaquette $U_{\mu\nu}^{(p)}(x)$ (left) and clover plaquette $Q_{\mu\nu}$ (right).

the continuum action (Eq. 2.18) in the limit $a \rightarrow 0$. However, it is unsuitable for lattice simulations. The reason is the so-called *fermion doubling problem*: The quark propagator, derived from the naïve lattice action, has 15 poles in the corners and on the edges of the first Brillouin zone in addition to the pole at $p = (0, 0, 0, 0)$ which is known from the continuum action. This means that the naïve lattice action leads to 15 additional unphysical modes. Therefore, lattice simulations using the naïve lattice action do not have the correct continuum limit.

This problem is avoided by choosing a more sophisticated lattice fermion action S_F^{latt} . Some of the most prominent fermion discretizations are known as *Wilson fermions*, *staggered fermions* [56], *domain wall fermions* [57] and *overlap fermions* [58]. Each of them has pros and cons.

For the lattice simulations of SYM we use the Wilson fermion discretization. In this discretization the fermion doubling problem is avoided by adding the so-called Wilson term to the Dirac operator

$$O_{\text{Wilson}}^{ab}(x, y) = -a \sum_{\mu=1}^4 \frac{V_{\mu}^{ab}(x) \delta_{x+\hat{\mu}, y} - 2\delta^{ab} \delta_{x, y} + V_{\mu}^{\dagger, ab}(x - \hat{\mu}) \delta_{x-\hat{\mu}, y}}{2a^2}, \quad (3.15)$$

which is a discretized version of $-(a/2)D_{\mu}D_{\mu}$. The Wilson term is an irrelevant operator, meaning that it vanishes in the naïve continuum limit. Due to this term, the fermion doublers acquire a mass which goes to infinity in the continuum limit. Therefore, in this limit, the fermion doublers decouple and the correct continuum limit is obtained. The Wilson fermion action of SYM reads

$$S_F^{(\text{Wilson})} = \frac{1}{2} \sum_x \text{Tr}_c [\bar{\lambda} D_W \lambda], \quad (3.16)$$

$$D_W^{ab}(x, y) = \delta_{x, y} \delta^{ab} - \kappa \sum_{\mu=1}^4 (V_{\mu}^{ab}(x) \delta_{x+\hat{\mu}, y} (\mathbb{1} + \gamma_{\mu}) + V_{\mu}^{\dagger, ab}(x - \hat{\mu}) (\mathbb{1} - \gamma_{\mu}) \delta_{x-\hat{\mu}, y}), \quad (3.17)$$

where D_W is the Dirac-Wilson operator (Dirac indices suppressed) and the fields

3.2. Breaking of SUSY on the lattice and its restoration

λ have been rescaled with respect to Eq. 3.10 to absorb the factor a^4 and such that the action can be written in terms the so-called hopping parameter κ

$$\kappa = \frac{1}{2am_0 + 8} . \quad (3.18)$$

The Dirac-Wilson operator can be written in matrix form $(D_W)_{MN}$ where M and N are multi-indices representing the space-time, gauge and spin indices x, a, α . An important property of the Dirac-Wilson matrix is that it is γ_5 -Hermitian

$$D_W^\dagger = \gamma_5 D_W \gamma_5 , \quad (3.19)$$

which implies that its eigenvalues are real or come in complex conjugate pairs. Furthermore, due to the adjoint representation of the gluino fields, each eigenvalue is doubly degenerate [35].

3.2. Breaking of SUSY on the lattice and its restoration

Discretizing quantum field theories on the lattice breaks some of their symmetries. Since the symmetries are one of the defining properties of a quantum field theory, it is crucial that this symmetry breaking is dealt with appropriately if one wants to obtain any meaningful result.

First and foremost, the introduction of a discrete space-time lattice breaks Poincaré invariance to a discrete hypercubic subgroup. Consequently, also supersymmetry is broken, which is directly clear from Eq. 2.13. In the continuum limit, Poincaré invariance is restored. From the Callan-Symanzik- β -function (not to be confused with β defined in Eq. 3.12), which for SYM is known exactly [59] to be ¹

$$\beta(g) = \mu \frac{d}{d\mu} g(\mu) = -\frac{g^3}{16\pi^3} \frac{3N_c}{1 - \frac{N_c g^2}{8\pi^2}} , \quad (3.20)$$

one can straightforwardly derive (see [52], Chap. 3 for a derivation for QCD) that the continuum limit corresponds to

$$a \rightarrow 0 \Leftrightarrow g^2 \rightarrow 0 , \quad (3.21)$$

and consequently

$$a \rightarrow 0 \Leftrightarrow \beta \rightarrow \infty , \quad (3.22)$$

¹Since the β function depends on the regularization scheme, the lattice β function might differ from this formula. When $\beta(g)$ is expanded in powers of g , however, the first two expansion coefficients are universal, i.e. independent of the regularization scheme.

3. Lattice Formulation of SYM

where β is defined in Eq. 3.12. Therefore, the results obtained for finite values of β have to be extrapolated to the limit $\beta \rightarrow \infty$.

However, this is not sufficient to simulate SYM. The reason is that the Wilson fermion discretization breaks chiral symmetry explicitly (for a derivation see [52], Chap. 7), but SYM is invariant under chiral rotations of \mathbb{Z}_{2N_C} as explained in Sec. 2.3.1. This breaking of chiral symmetry is reminiscent of the Nielsen-Ninomiya no-go theorem, which forbids a chirally invariant, doubler-free, local lattice discretization in even dimensions [60].

It would be desirable to find a lattice formulation of SYM that keeps full supersymmetry intact also on the lattice. However, the supersymmetry violation due to the absence of the Leibniz rule on the lattice can be amended only by giving up locality as has been proven in [61]. In our lattice investigations we adopt an idea proposed by Curci and Veneziano in 1987 [24] to simulate $\mathcal{N} = 1$ SYM on the lattice. They suggested to let the lattice discretization spoil both, Poincaré invariance and chiral symmetry, and to extrapolate the results to limit where the \mathbb{Z}_{2N_C} chiral symmetry and Poincaré invariance are restored. In this chiral and continuum limit also supersymmetry is restored. Hence, this limit is called supersymmetric limit.

In the extrapolation to the chiral limit, the soft SUSY breaking term (Eq. 2.17) comes into play. The breaking of chiral symmetry by the lattice formulation implies that the bare gluino mass receives an additive contribution and hence the gluino mass needs to be renormalized additively (and also multiplicatively). This additive contribution can be countered by a suitable value of the bare gluino mass m_0 . Thus, the chiral limit, i.e. the point where the renormalized gluino mass m_r vanishes, can be found by varying m_0 . In practice, m_0 is tuned implicitly by means of varying κ (cf. Eq. 3.18). The value of κ where m_r vanishes is called critical κ_c and it depends on the value of β which regulates the lattice spacing. As mentioned above, SYM cannot be studied directly in the chiral limit, i.e. at κ_c . This can also be observed by the fact that the condition number, which is the ratio of the largest to the smallest eigenvalue of the Dirac Wilson matrix D_W , approaches infinity in this limit which makes simulations impossible (cf. Sec. 8.4). Furthermore, there appears a sign problem when approaching the chiral limit (for further discussion see Secs. 3.4 and 5.5). Hence, the chiral extrapolation is unavoidable when using Wilson fermions. The extrapolations to the chiral and continuum limit are explained in more detail in Secs. 4 and 13.

In order to study the chiral properties of SUSY on the lattice, it is interesting to consider other fermion discretizations, such as the aforementioned domain wall fermions or overlap fermions. Domain wall fermions avoid the Nielsen-Ninomiya no-go theorem by introducing a fifth space-time dimension in such a way that the desired four dimensional theory of chiral fermions establishes as a domain wall in the five-dimensional space. The idea of overlap fermions goes back to early work

of Ginsparg and Wilson who formulated a lattice version of chiral symmetry which approaches chiral symmetry in the continuum limit [62] and which is kept intact on the lattice when overlap fermions are used. Lattice simulations using domain wall fermions or overlap fermions are computationally very expensive. The Desy-Münster collaboration has recently started first exploratory studies of using overlap fermions for the simulations of SYM. These studies are, however, beyond the scope of this thesis.

3.3. Improving the lattice action

The precision of the results, extrapolated to the continuum limit, depends crucially on the dependency of the observables on the lattice spacing a . A strong dependency drives the theory away from the continuum limit for finite values of a and usually leads to larger final errors of the extrapolated results. In order to tame these lattice discretization effects, we employ different techniques in our simulations. In the simulations of SU(2)-SYM we use a tree-level Symanzik improved gauge action and a Stout smeared fermion action. For the corresponding simulations for SU(3)-SYM we use an unimproved gauge action, but a one-loop clover improved fermion action. These improvements are explained in the following.

The lattice action (Eqs. 3.9, 3.16) can be expanded as a power series of the lattice spacing a

$$S^{\text{latt}} = S^{\text{cont}} + aS^{(1)} + a^2S^{(2)} + \mathcal{O}(a^3). \quad (3.23)$$

The terms $aS^{(1)} + a^2S^{(2)} + \mathcal{O}(a^3)$ lead to lattice discretization effects. Irrelevant operators (counterterms) can be added to the lattice action in order to cancel the leading order terms in a . Improving the action in this way improves automatically all on-shell observables, i.e. observables that fulfill the equations of motions, such as masses of particles. For a full improvement, not only the action, but also all discretized operators used for estimating (measuring) off-shell observables have to be improved similarly. The procedure to systematically remove the leading order lattice discretization effects is known as *Symanzik's improvement program* [63, 64].

When the SYM lattice action is expanded in a , it turns out that the Wilson gauge action S_G^{latt} is already free of lattice discretization effects proportional to a while the fermion action S_F^{latt} contains such a term (for a derivation see [52]):

$$S_G^{\text{latt}} = S_G^{\text{cont}} + a^2S_G^{(2)} + \mathcal{O}(a^4), \quad (3.24)$$

$$S_F^{\text{latt}} = S_F^{\text{cont}} + aS_F^{(1)} + a^2S_F^{(2)} + \mathcal{O}(a^3). \quad (3.25)$$

A single additional dimension five operator is sufficient to cancel the leading term

3. Lattice Formulation of SYM

$aS_F^{(1)}$ in the fermion action. This operator is the so-called *clover term*, defined as

$$O_{CL}(x) = -c_{sw} \frac{a}{4} \bar{\lambda}^a(x) \sigma_{\mu\nu} F_{\text{latt,adj}}^{\mu\nu,ab}(x) \lambda^b(x), \quad (3.26)$$

where c_{sw} is the so-called Sheikholeslami-Wohlert coefficient named after the authors who first proposed this improvement [65] for QCD. $F_{\text{latt}}^{\mu\nu}(x)$ is the lattice field strength tensor written in terms of the clover plaquette $Q_{\mu\nu}(x)$ (see Fig. 3.2)

$$F_{\text{latt}}^{\mu\nu}(x) = -\frac{i}{8a^2} (Q_{\mu\nu}(x) - Q_{\mu\nu}(x)), \quad (3.27)$$

$$Q_{\mu\nu}(x) = U_{\mu\nu}^{(p)}(x) + U_{\mu\nu}^{(p)}(x - \hat{\mu}) + U_{\mu\nu}^{(p)}(x - \hat{\mu} - \hat{\nu}) + U_{\mu\nu}^{(p)}(x - \hat{\nu}). \quad (3.28)$$

For the adjoint field strength tensor $F_{\text{latt,adj}}^{\mu\nu}(x)$, adjoint plaquettes $V^{(p)}$ constructed from adjoint gauge links (Eqs. 3.13, 3.14) have to be used in Eq. 3.28 instead of the plaquettes $U^{(p)}$ in the fundamental representation. For a complete cancellation of the $aS^{(1)}$ term, c_{sw} has to be tuned non-perturbatively. For QCD such a tuning has been done [66, 67, 68, 69]. The non-perturbative tuning is, however, rather complex and while a non-perturbative calculation of c_{sw} has been done for adjoint fermions in the gauge group SU(2) [70], such a calculation has not yet been performed for the gauge group SU(3). There exists, however, a perturbative calculation of c_{sw} at one-loop order for general gauge groups SU(N) which in the case of the gauge group SU(2) agrees within 5 % with the non-perturbative estimation [71]. The perturbative expansion of c_{sw} is given by

$$c_{sw} = c_{sw}^{(0)} + c_{sw}^{(1)} g^2 + \mathcal{O}(g^4). \quad (3.29)$$

The one-loop calculation of the improvement coefficients yields [71]

$$c_{sw}^{(0)} = 1, \quad c_{sw}^{(1)} = 0.16764(3)C_R + 0.01503(3)N_c, \quad (3.30)$$

where C_R is the quadratic Casimir invariant of the gauge group representation. For the adjoint representation of the gauge group SU(N), it is given by

$$C_R(\text{SU}(N), \text{adjoint}) = N. \quad (3.31)$$

For SU(3) this yields

$$c_{sw}^{(1)} = 0.54801(13). \quad (3.32)$$

We use this one-loop estimation for the clover improvement of the fermion action for our simulations of SU(3)-SYM.

For the simulations of SU(2)-SYM, which have been initiated prior to the in-

3.4. Calculation of observables in SYM on the lattice

vestigations of SU(3), clover improvement is not used. Instead, one level of Stout smearing is used in the fermionic action, i.e. the gauge links $V_\mu(x)$ in the fermion action (Eq. 3.16) are replaced by a smeared gauge links $\tilde{V}_\mu(x)$ using the Stout smearing technique introduced in [72] with a smearing parameter

$$\rho = 0.15. \quad (3.33)$$

The smearing reduces short range topological defects of the gauge field and removes the corresponding small eigenvalues of the Dirac-Wilson operator, as was pointed out in [25]. Furthermore, in the simulations of SU(2)-SYM a tree-level-Symanzik improved gauge action is used as it was introduced in [73, 74] to cancel the leading order lattice discretization term $a^2 S_G^{(2)}$ in the gauge action (cf. Eqs. 3.9, 3.24).

Based on the simulations of SYM with gauge group SU(2), it was demonstrated in [28] that using the clover-improvement in favor of the Stout smearing in the fermion action leads to a suppression of lattice discretization effects and therefore this option was chosen for our investigations of SU(3)-SYM.

3.4. Calculation of observables in SYM on the lattice

Using the discretized action, observables of SYM can be calculated in the framework of lattice QFT. Typically, in QFT observables are calculated from correlation functions C of field operators $O(x)$

$$C(x_1, x_2, \dots) = \langle O_1(x_1) O_2(x_2) \dots \rangle. \quad (3.34)$$

In the continuum the expectation value of an operator O (here $O = O_1(x_1) O_2(x_2) \dots$) in the Euclidean path integral formalism is given by

$$\langle O \rangle = \frac{1}{\mathcal{Z}} \int \mathcal{D}\Phi O e^{-S} \equiv \frac{1}{\mathcal{Z}} \text{Tr} [O e^{-S}], \quad \mathcal{Z} = \int \mathcal{D}\Phi e^{-S} \equiv \text{Tr} [e^{-S}], \quad (3.35)$$

where Φ stands for the collection of all fields. The Euclidean path integral formalism is closely related to the canonical ensemble in statistical mechanics where the partition function is given by

$$\langle O \rangle = \frac{1}{\mathcal{Z}_{\text{stat}}} \text{Tr} [O e^{-\beta \hat{H}}], \quad \mathcal{Z}_{\text{stat}} = \text{Tr} [e^{-\beta \hat{H}}]. \quad (3.36)$$

Thus, relating $S \leftrightarrow \beta \hat{H}$ and the path integral over the field configurations with the trace over all microstates, methods of statistical mechanics can be applied to Eq. 3.35, which is also discussed in Sec. 5.

3. Lattice Formulation of SYM

When discretized, the path integral is replaced by a finite number of integrals

$$\int \mathcal{D}\Phi \rightarrow \int \prod_x d\Phi(x) \doteq \int [d\Phi] , \quad (3.37)$$

where the product runs over all lattice points x . However, the number of lattice sites x and thus the number of integration variables is too large (cf. Sec. 3) to compute the integrals exactly. Thus, the standard approach in lattice QFT is to evaluate Eqs. 3.35, 3.37 numerically by *Monte Carlo integration* and *importance sampling*, which is explained in the following. Even though these techniques reduce the computational cost significantly, the computations are still very demanding and are performed on the largest computing clusters currently available.

The Euclidean action (Eqs. 3.9, 3.16) consists of boson and fermion fields. While boson fields are unproblematic, the Grassmannian nature of the fermion fields makes it non-trivial to simulate the theory on the computer. The fermion fields are therefore integrated out analytically. This is possible because fermions appear as bilinears in the fermionic action S_F^{latt} yielding a well known Gaussian function of Grassmann variables in the path integral. For convenience, the fermion action is repeated here

$$S_F^{\text{latt}} = \frac{1}{2} \sum_x \text{Tr}_c[\lambda D_W \lambda] . \quad (3.16)$$

In QCD, where the fermions Ψ are in the fundamental representation, integrating the fermions fields yields the so-called fermion determinant

$$\int [d\Psi d\bar{\Psi}] e^{-\bar{\Psi} D_W \Psi} = \det(D_W) , \quad (3.38)$$

while in the case of Majorana fermions λ , which are present in SYM, the fermion integration yields a Pfaffian (for a derivation see [33])

$$\int [d\lambda] e^{-\text{Tr}_c[\bar{\lambda} D_W \lambda]} = \text{Pf}(C D_W) , \quad (3.39)$$

where C is the charge conjugation operator. It can be shown that the eigenvalues λ_i of D_W come in degenerate pairs and that for each complex pair of eigenvalues, the complex conjugate pair is also a pair of eigenvalues [43]. The Pfaffian of the fermion matrix D_W is given by

$$\text{Pf}(C D_W) = \prod_i^{\text{no degeneracy}} \lambda_i , \quad (3.40)$$

3.4. Calculation of observables in SYM on the lattice

where the product only includes one of the doubly degenerate eigenvalues. Since these eigenvalues are real or come in complex conjugate pairs, this Pfaffian is real. Up to its sign, the Pfaffian is equivalent to the square root of the determinant

$$\text{Pf}(CD_W) = \text{sgn}(\text{Pf}(CD_W))\sqrt{\det(D_W)}, \quad (3.41)$$

where $\det(C) = 1$ was used.

After the fermion integration, the lattice action depends only on the gauge field $U(x)$ and the lattice path integral becomes

$$\langle O \rangle^{\text{latt}} = \frac{1}{\mathcal{Z}^{\text{latt}}} \int [dU] O w(U), \quad \mathcal{Z}^{\text{latt}} = \int [dU] w(U), \quad (3.42)$$

$$w(U) = \text{sgn}(\text{Pf}(CD_W(U)))\sqrt{\det(D_W(U))}e^{-S_{\text{boson}}(U)}, \quad (3.43)$$

where the x -dependency of $U(x)$ has been suppressed. In the Monte Carlo integration approach (without importance sampling) the integral over all gauge field configurations is approximated by a sum over randomly sampled gauge configurations U_i

$$\int [dU] f(U) \rightarrow \frac{1}{N} \sum_i^N f(U_i), \quad (3.44)$$

where N is the number of samples. The expectation value of an observable is then approximated by

$$\hat{O} = \frac{\frac{1}{N} \sum_i^N O(U_i) w(U_i)}{\frac{1}{N} \sum_i^N w(U_i)}. \quad (3.45)$$

Ignoring the sign of the Pfaffian for the moment, Eq. 3.45 shows that \hat{O} is obtained by a weighted average of $O(U_i)$ where the weight is given by $w(U_i)$. The efficiency of the Monte Carlo integration is improved drastically by a technique called importance sampling: Instead of using uniformly sampled random gauge configurations, random gauge configuration with a probability distribution given by the weight function $w(U_i)$ are generated and used for the Monte Carlo Integration. The generation of such gauge configurations is further discussed in Sec. 5. Using these gauge configurations \hat{O} is given by

$$\hat{O} = \frac{1}{N} \sum_i^N O(U_i), \quad (3.46)$$

The integration error of Monte Carlo integration decays with $1/\sqrt{N}$.

3. Lattice Formulation of SYM

The sign of the Pfaffian appearing in the weight is a problem and an incarnation of the infamous sign problem in lattice QFT: $w(U_i)$ can only be interpreted as a weight if it is strictly positive. The occurrence of negative signs in the weights for the importance sampling therefore spoils the interpretation of $w(U_i)$ as a weight for importance sampling. The sign problem can be circumvented if only a few gauge configurations have a negative Pfaffian (mild sign problem). In that case the sign of the Pfaffian can be ignored in the generation of the gauge configurations and this is corrected in the estimator of O

$$\hat{O} = \frac{\sum_i^N O(U_i) \operatorname{sgn}(U_i)}{\sum_i^N \operatorname{sgn}(U_i)}, \quad (3.47)$$

where

$$\operatorname{sgn}(U_i) \doteq \operatorname{sgn}(\operatorname{Pf}(CD_W(U_i))). \quad (3.48)$$

This correction technique is called *reweighting*. From Eq. 3.47 it is clear that reweighting only works well for a mild sign problem. If the number of positive and negative signs are approximately equal, the denominator of Eq. 3.47 becomes very small and therefore leads to large fluctuations and hence an unreliable determination of \hat{O} . The process of calculating observables in SYM using lattice QFT is then summarized as follows

1. For different values of β and κ , sets of random lattice gauge configurations distributed by the weight $w(U)$ are produced. A set of gauge configurations for fixed values of β and κ is called ensemble.
2. The correlators (here represented by $\langle O(U_i) \rangle$) are determined (measured) from the configurations of the gauge ensembles.
3. In the analysis step the observables are extracted from the measured correlators. Uncertainties are estimated using statistical methods.
4. The results obtained for different values of β and κ are extrapolated to the chiral and continuum limit.

4. Towards the supersymmetric limit: Scale setting and the adjoint pion

As explained in Sec. 3, supersymmetry is broken by the lattice discretization. It is restored in the limit of vanishing (renormalized) gluino mass $m_r \rightarrow 0$ (chiral limit) and vanishing lattice spacing $a \rightarrow 0$ (continuum limit). Neither the lattice spacing a nor the renormalized gluino mass m_r are input parameters of the simulations, but they are tuned by means of β and κ . In order to reliably extrapolate the results to the supersymmetric limit, a and m_r have to be estimated from the ensembles. The methods that we apply in our calculations to do this are summarized in the present section.

4.1. Tuning the renormalized gluino mass

For the chiral extrapolation it is not required to directly determine m_r , but an observable which is proportional to m_r is suitable as well to define the massless point. It is desirable that the measurement of this observable should be cheap and come with only a small error since this error propagates into all chirally extrapolated results.

In our project we employ two observables which fulfill these requirements: The squared mass of the adjoint pion $m_{a-\pi}^2$ and the subtracted gluino mass $m_S Z_S^{-1}$ defined from the supersymmetric Ward identities (where Z_S is a renormalization factor). While the adjoint pion is not a physical particle of SYM, it can be defined in the partially quenched limit of SYM with one additional flavor [27]. Based on the OZI-approximation of SYM it has been argued [23] that, analogously to the Gell-Mann-Oakes-Renner relation of QCD, the squared adjoint pion mass is proportional to the renormalized gluino mass

$$m_{a-\pi}^2 \propto m_r. \quad (4.1)$$

$m_{a-\pi}^2$ is a particularly useful observable because the signal-to-noise ratio is typically very high and the measurement of the corresponding correlation functions is required anyhow for the mass determination of the a - η' bound states (for details about the measurement, see Sec. 8.2). Therefore, we employ $m_{a-\pi}^2$ as a measure for the gluino mass to extrapolate to the chiral limit (for an example see Fig. 4.1). The supersymmetric Ward identities can then be used as an additional check of supersymmetry restoration in the chiral and continuum limit. This is further discussed in Sec. 15.

4. Towards the supersymmetric limit: Scale setting and the adjoint pion

For the simulations of SYM, we tune κ , such that the adjoint pion mass is in the range

$$0.15 \lesssim am_{a-\pi} \lesssim 0.7. \quad (4.2)$$

For larger values of $am_{a-\pi} > 0.7$, lattice artifacts are likely to become large (cf. Sec. 3) and the determination of the particle masses becomes difficult because the correlation functions decay very quickly (the technique to extract masses from correlation functions is explained in Sec. 7). Smaller values of $m_{a-\pi}$ are computationally very expensive to simulate because of the rapidly growing condition number of D_W (cf. Sec. 8.4) and the increasing sign problem (cf. Secs. 3.4, 5.5) when approaching the chiral limit.

4.2. Scale setting

The lattice spacing a is not an input parameter of the simulations, but can be controlled by the parameter β , as explained in Sec. 3.2. The continuum limit corresponds to $a \rightarrow 0 \Leftrightarrow \beta \rightarrow \infty$. The value of a in physical units has to be determined from the simulations.

Due to the lack of an external scale, dimensionful quantities determined from the lattice simulations, e.g. masses of particles, can only be expressed in units of scales defined within the simulation. In principle, any dimensionful observable can be used as a scale. The simplest scale available is the lattice spacing a and as a first step, dimensionful observables are typically measured in multiples of powers of the lattice spacing. Since we are interested in the continuum limit, where the lattice spacing vanishes, the observables have to be converted, in a second step, into units of a scale which does not vanish in the continuum limit. Ideally, that scale is also accessible from other calculations or experiments so that the final results can be compared.

The precision of the final results depends crucially on the precision of the scale determination, since all dimensionful observables are expressed in units of the scale. We conclude that, ideally, the observable used for the scale setting fulfills the following requirements

1. Its measurement is computationally inexpensive.
2. Its measurements comes with a small error (statistical and systematical).
3. It has a physical interpretation and ideally can be compared to experiments or other calculations.

In QCD simulations, hadron masses, which can be very well compared to experimental values, are often chosen for the scale setting. The disadvantage of using

hadron masses is that the measurements of hadron masses in lattice calculations can be computationally expensive and come with a sizable error.

In order to profit from the experience obtained in lattice QCD, it is desirable to choose an observable which is comparable to QCD calculations for the scale setting in SYM. However, the hadrons of SYM are different from the ones of QCD. Due to these reasons, we use purely gluonic scales, i.e. observables that can be obtained directly from expectation values of Wilson loops and no fermion propagators have to be calculated. Such scales are defined in QCD and in SYM since the gluon field is defined identically in SYM and in QCD. This scale could then also be used in investigations of Super QCD.

A commonly used gluonic scale is the Sommer parameter r_0 [75]. It can be measured efficiently and it has a clear physical interpretation in QCD since it is calculated from the static potential of two quarks. Its physical value

$$r_0 \simeq 0.5\text{fm} \tag{4.3}$$

can be used to compare the results of lattice calculations to experiments and we use this relation in SYM to convert the results to fm and GeV. However, r_0 is generally not the best choice since its computation requires smoothing and fitting procedures which make it prone to systematic and statistical errors.

Other scales which avoid these problems have been developed in the context of gradient flow, most prominently the scales t_0 [76] and w_0 [77], which also have the dimension of length. These scales share many advantages with the Sommer scale r_0 , while the measurements come with much smaller errors. The use of these scales in SYM has been analyzed in detail by the Desy-Münster collaboration [78]. The analysis showed, that these scales are suited for the scale setting as long as effects from different topological sectors are under control (cf. Sec. 5.4). As was pointed out in [77] w_0 is less affected by cutoff effects than t_0 and therefore we use w_0 for the scale setting in SYM.

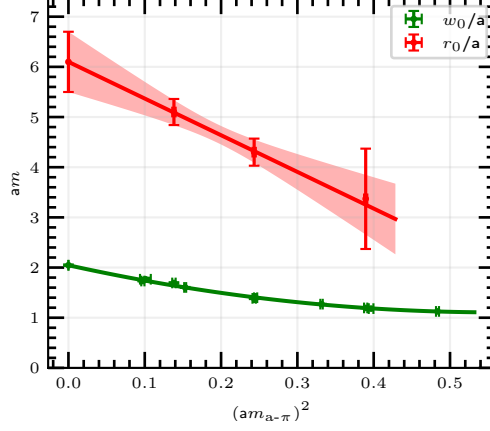
4.2.1. Mass dependent and mass independent scale setting

There exist different schemes for the scale setting. Similar to renormalization schemes, there are mass dependent and mass independent ones.

In the mass dependent scale setting scheme, all dimensionful quantities, determined from a given ensemble, are expressed in units of w_0 which is also measured from the same ensemble. In the mass independent scheme, on the contrary, the measured values of w_0 , determined at different values of κ and fixed values of β , are extrapolated first to a specified point and all dimensionful quantities at this value of β are expressed in units of this extrapolated value. In QCD one may, for example, use the value of w_0 extrapolated to the physical point (i.e. the point

4. Towards the supersymmetric limit: Scale setting and the adjoint pion

Figure 4.1: Chiral extrapolations of the scales w_0 and r_0 for SU(3), $\beta = 5.4$. r_0 has been determined on only a few ensembles since it is not used for the final results, but rather to get a rough estimate of the lattice spacing in the unit fm.



where the pion mass in terms of some scale agrees with the experimental value). Since SYM is defined in the chiral limit, we extrapolate w_0 to the chiral limit (see Fig. 4.1) and denote the chiral value with the index χ

$$w_{0,\chi}(\beta) = \lim_{m_{a-\pi}^2 \rightarrow 0} w_0(\beta, m_{a-\pi}^2). \quad (4.4)$$

Similarly $r_{0,\chi}$ denotes the chirally extrapolated value of r_0 . The extrapolations are performed by polynomial fits of the form

$$w_{0,\beta}(x) = w_{0,\chi,\beta} + c_1 x + c_2 x^2 + c_3 x^3 + \mathcal{O}(x^4), \quad (4.5)$$

where β is written as an index to stress that β is fixed in the extrapolation and $x = (am_{a-\pi})^2$, $w_{0,\chi,\beta} \equiv w_{0,\chi}(\beta)$. The c_i are the fit parameters. Note that both, x and $w_{0,\beta}(x)$, come with measurement uncertainties and we therefore use the ODR (Orthogonal distance regression) fitting routine provided by the SciPy library for Python.

It is not clear, a priori, which scale setting scheme is to be preferred. For infinite statistics, both schemes yield the same chiral limit (see App. A.5). The way this limit is approached, however, may be influenced by the choice of the scale setting scheme. Thus, for finite statistics the two procedures may lead to different uncertainties for the final results. In Sec. 13 the influence of the scale setting scheme on the extrapolated results is investigated on the basis of the ground states masses of SU(3)-SYM.

5. Generation of gauge configurations

In the previous sections, the basic concepts of simulating SYM in the framework of lattice QFT are explained, leaving out the details about generating gauge configurations, measuring the observables and extrapolating the results to the supersymmetric limit. These details are explained in the following sections, starting with the production of configurations.

The generation of gauge configurations, distributed according to the weight $w(U)$, is the most basic and therefore probably also the most important step in lattice QFT calculations. A lot of effort has been made to develop efficient algorithms for the production of such gauge configurations. For theories including dynamical fermions so-called *Hybrid Monte Carlo* (HMC) algorithms have proven to be useful. These algorithm are based on *Markov chains*, which means that each configuration is calculated from the previous one. This is done by evolving a molecular dynamics trajectory with randomized initial momenta, followed by an accept/reject step to guarantee the distribution according to the weight $w(U)$. Hence, the configurations are not completely independent of one another. HMC algorithms have become the standard in lattice gauge theory and details can be found in [79] and in many other textbooks on lattice QFT. The most important steps are:

1. A proposal for a new gauge field configuration is calculated by evolving the previous configuration on a molecular dynamics trajectory. This means that, in the spirit of classical Hamiltonian mechanics, conjugate momenta to the bosonic quantum fields are introduced, and the fields are integrated numerically along the equations of motion with Gaussian distributed random initial momenta for a time interval of length τ using N steps of length ϵ , i.e. $\tau = N\epsilon$. Except for numerical integrations errors, the energy of the molecular dynamics trajectory, and thus the action of the produced gauge configurations, stays constant. This step is called *Update*.
2. To achieve the correct distribution of configurations, the proposed configuration is accepted or rejected with a probability according to the weight $w(U)$.

The main requirement for Monte-Carlo algorithms is ergodicity, i.e. that starting from an arbitrary field configuration, every other field configuration can, in principle, be reached by the algorithm. Here, the numerical integration error of the molecular dynamics trajectory is important. If the integration were exact, the algorithm would only produce configurations of constant action (constant energy

5. Generation of gauge configurations

of the molecular dynamics trajectory) and thus the produced ensemble would be the microcanonical and not the canonical one (cf. Sec. 3.4).

The generation of gauge configurations for our investigations of SU(3)-SYM have been performed in the scope of this thesis, whereas the configurations of SU(2)-SYM were produced earlier. Also, the implementation of the HMC algorithms has been done earlier, so that the main task required for this thesis was setting up and monitoring the production of configurations. Therefore, only the most important aspects of the HMC-algorithms that we use and the setting of their parameters is outlined in this section. For more details the reader is referred to the cited references.

5.1. Polynomial and rational approximation

The main difficulty in HMC algorithms is handling the fermion determinant and its square root that arise from integrating out the fermion fields (Eqs. 3.39, 3.41) and thus encode the interactions of the gauge links at different lattice sites. This section briefly summarizes how the resulting non-local action is simulated by the algorithms used in our investigations.

It is convenient to work with the squared Hermitian Dirac-Wilson matrix

$$D_5^2 \doteq (\gamma_5 D_W)^2 \quad (5.1)$$

instead of the Dirac-Wilson matrix D_W because its eigenvalues are positive. This can be achieved by rewriting the inverse root of the fermion determinant as

$$\left(\sqrt{\det D_W}\right)^{-1} = (\det(D_W)^2)^{-\frac{1}{4}} = (\det(\gamma_5 D_W)^2)^{-1/4} = \det\left((D_5^2)^{-\frac{1}{4}}\right), \quad (5.2)$$

and using $\det(\gamma_5) = 1$. The fermion determinant is exponentiated as a bilinear of complex boson auxiliary fields ϕ , so-called *pseudofermions*, as

$$\left(\sqrt{\det D_W}\right)^{-1} = \det\left((D_5^2)^{-\frac{1}{4}}\right) = \int d\phi d\phi^\dagger e^{-S_{PF}(U, \phi, \phi^\dagger)}, \quad (5.3)$$

with

$$S_{PF}(U, \phi, \phi^\dagger) = -\phi^\dagger (D_5^2)^{-1/4} \phi. \quad (5.4)$$

Note that $S_{PF}(U, \phi, \phi^\dagger)$ implicitly depends on the gauge field U through $D_W(U)$. The lattice action in terms of the gauge field U and the pseudofermions ϕ is then

given by

$$S^{\text{latt}}(U, \phi, \phi^\dagger) = S_G(U) + S_{PF}(U, \phi, \phi^\dagger). \quad (5.5)$$

The pseudofermion fields ϕ are sampled according to the probability distribution $e^{-S_{PF}(\phi, \phi^\dagger)}$ by generating a vector R of random complex numbers with a probability distribution proportional to $\exp(-R^* R)$ at the beginning of each molecular dynamics trajectory. The pseudofermion fields ϕ are then given by

$$\phi = (D_5^2)^{1/8} R, \quad (5.6)$$

and they are kept fixed during the molecular dynamics integration of the gauge field. The operator $(D_5^2)^{1/8}$ in Eq. 5.6 cannot be directly computed since the dimension of D_5^2 are too large. Hence, in the *Polynomial Hybrid Monte Carlo algorithm* (PHMC) it is approximated by a polynomial functional of D_5^2 and in the *Rational Hybrid Monte Carlo algorithm* (RHMC) it is approximated by a rational functional. The error stemming from the approximation can be corrected in the accept/reject step or in the reweighting factors (cf. Sec. 3.4).

For the production of configurations for SU(2)-SYM, the so-called *Two step multi boson polynomial HMC* (TSMB) algorithm that has been developed by Montvay in [80] and a slightly modified version called (TS-PHMC) as described in [81] were used. As the name suggests it is based on a polynomial approximation in combination with multiple pseudofermions. For further details, see the reference. For the production of configurations for SU(3)-SYM we use the RHMC algorithm. For details see [43].

5.2. Running the algorithm

The TSMB, the TS-PHMC and the RHMC algorithms used for the production of the gauge configurations fulfill the so-called *detailed balance* condition, which guarantees the correct distribution of the gauge configurations in the limit of infinite statistics. In real simulations the number of configurations is, of course, always finite. In order to obtain configurations distributed according to $w(U)$, it is therefore important to ensure, that the algorithm can efficiently sample the entire configuration space and does not get stuck in specific regions. For this purpose, we monitor the production of gauge configurations and adjust the parameters of the HMC algorithm accordingly. The most important aspects are explained in the following.

5. Generation of gauge configurations

5.2.1. Tuning the parameters

A disadvantage of HMC algorithms is that the produced configurations are not independent of one another because they are generated as a Markov chain. The correlation between consecutive configurations is called *autocorrelation* and the typical number of subsequent configurations on which autocorrelations are measurable in the Markov chain is called autocorrelation time. For an efficient sampling of the configuration space, the produced configurations should ideally feature a small autocorrelation time. The most important parameter to tune the autocorrelation time is the trajectory length τ which controls the distance of two consecutive configurations in the configuration space. Therefore, τ should be chosen sufficiently large. For increasing τ , however, also the integration error increases, leading to large energy differences between two consecutive configurations and a low probability of being accepted in the accept/reject step (*acceptance rate*). For our simulations of SU(3)-SYM we therefore use the well established value

$$\tau = 1.0. \quad (5.7)$$

The integration error is, furthermore, controlled by the choice of the integration algorithm and number N of integration steps. A small step size $\epsilon = \tau/N$ leads to small integration errors and therefore to a larger acceptance rate. On the other hand, it increases the computational cost of the integration. In investigations of QCD, acceptance rates of 60-80 % have shown to lead to the best performance of the HMC algorithms and we therefore tune the step size to achieve such a rate.

We use the integration scheme proposed by Sexton and Weingarten [82]. It makes use of the fact that the gauge action S_G and the so-called gauge force stemming from S_G , which has to be calculated for the integration of the equations of motion, is much cheaper to compute numerically than S_{PF} and the corresponding fermion force. At the same time, the gauge force is usually much larger than the fermion force. Therefore, it is useful to separate the time scales for the gauge force integration and the fermion force integration, i.e. the fermion force is updated less often than the gauge force. Thus, a larger step size ϵ_F is used for the integration of the fermion force than the step size ϵ_G of the gauge force integration. The ratio of the step sizes should optimally be inverse to the ratio of the magnitude of the respective forces F_G and F_F

$$\frac{\epsilon_F}{\epsilon_G} = \frac{|F_G|}{|F_F|}. \quad (5.8)$$

For our simulations of SU(3) this ratio is typically

$$\frac{\epsilon_F}{\epsilon_G} \approx 4. \quad (5.9)$$

To achieve an acceptance rate of 60-80 %, $N_F = \tau/\epsilon_F$ is tuned in the interval

$$N_F \in [12, 18], \quad (5.10)$$

and correspondingly $N_G = \tau/\epsilon_G = \epsilon_F/\epsilon_G N_F \approx 4N_F$.

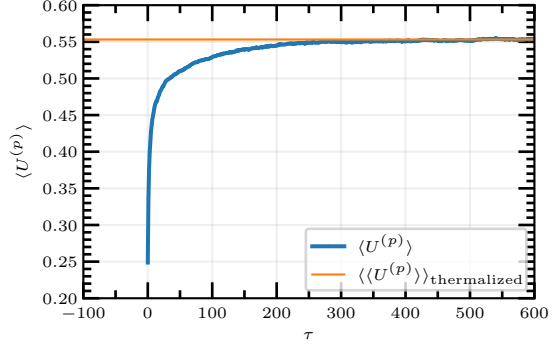
5.3. Thermalization

To start the production of gauge configurations, an initial configuration has to be provided and different choices are possible. In our runs we usually use a so-called hot start, which means that random SU(N) matrices are generated for the gauge links of SU(N)-SYM. As explained in Sec. 3.4, the configurations are sampled according to the canonical ensemble, which means that, in equilibrium, the configurations fluctuate around the minimum of Helmholtz free energy (in the statistical mechanics picture). The initial configuration consisting of random SU(N) matrices is far out of this equilibrium (and thus hot). Hence, starting from the hot configuration, the algorithm evolves towards configurations of minimal Helmholtz free energy. This process is called *thermalization*.

In order to obtain the desired distribution of gauge configurations, the hot configurations produced during thermalization should be discarded since they have been artificially introduced to start the run, but they are far out of equilibrium and thus do not fit into the distribution given by the weight $w(U)$. To determine, how many configurations are affected by the thermalization, one can monitor different observables calculated from the produced configurations. We usually use the average plaquette $\langle U^{(p)} \rangle$, which is given by the average over all possible plaquettes on the configuration, as a measure for the thermalization. Once the system has thermalized, $\langle U^{(p)} \rangle$ fluctuates around its expectation value. The thermalization time τ_{therm} can, hence, be identified as the number of configurations it takes until $\langle U^{(p)} \rangle$ reaches its average value (see Fig. 5.1).

5. Generation of gauge configurations

Figure 5.1: Thermalization of a gauge ensemble of SU(3)-SYM and $\beta = 5.4$, $\kappa = 0.1703$ and a lattice extent of $16^3 \times 32$. Depicted is the average plaquette $\langle U^{(p)} \rangle$ of each configuration and its expectation value $\langle \langle U^{(p)} \rangle \rangle_{\text{thermalized}}$ estimated from its average over the thermalized configurations. The thermalization takes ~ 500 HMC steps.



5.4. Potential barriers and topological freezing

Detailed balance guarantees that in the limit of infinite statistics, the configuration space is fully and correctly sampled. Due to potential barriers between different regions of the configuration space, the HMC algorithm can, however, become stuck in specific regions for a large number of subsequent configurations until it eventually tunnels to other regions. For low tunneling rates, many steps of the HMC algorithm are needed until the configuration space is sampled sufficiently well. The number of produced configurations is, however, limited by the computing resources available. Thus, a low tunneling rate may lead to an insufficient sampling of the configuration space and therefore to incorrect/biased results.

The most prominent source of potential barriers known in lattice QFT is due to topology. The topological charge of a field configuration is defined in the continuum as

$$Q_{\text{top}} = \frac{1}{32\pi^2} \int d^4x \epsilon_{\mu\nu\rho\sigma} F^{\mu\nu,a} F^{\rho\sigma,a}. \quad (5.11)$$

It can straightforwardly be discretized to be used on the lattice by replacing the field strength tensor $F^{\mu\nu,a}$ by its lattice version $F_{\text{latt}}^{\mu\nu,a}$ defined in Eq. 3.27

$$Q_{\text{top}}^{\text{latt}} = \frac{1}{32\pi^2} \sum_x \epsilon_{\mu\nu\rho\sigma} F_{\text{latt}}^{\mu\nu,a} F_{\text{latt}}^{\rho\sigma,a}. \quad (5.12)$$

Unlike the continuum version, $Q_{\text{top}}^{\text{latt}}$ is not necessarily integer. In [76] Lüscher describes that field configurations "between the sectors" have a rapidly decreasing weight in the path integral when the lattice spacing approaches zero. In other words, there are rapidly increasing potential barriers between field configurations of different values of the topological charge. The algorithm can therefore become stuck in the regions of fixed topological charge. This phenomenon is known as

5.5. Monitoring the sign of the Pfaffian

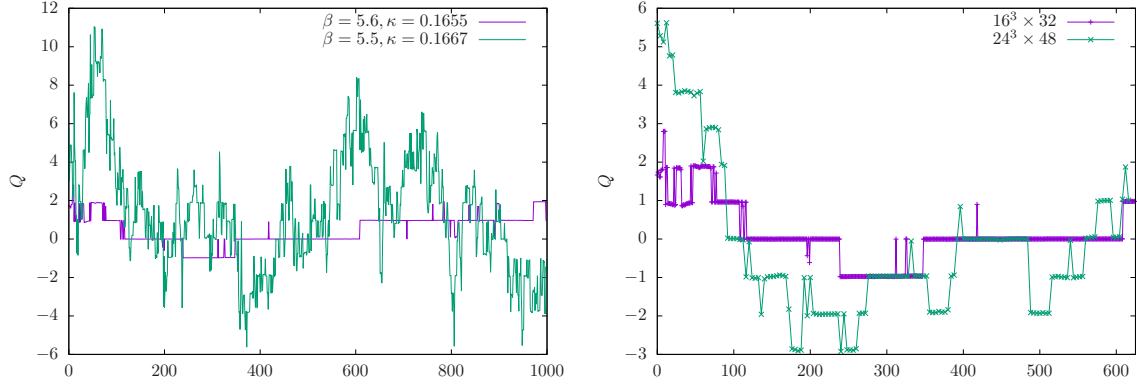


Figure 5.2.: Sampling of the topological sectors in SU(3)-SYM. While for $\beta = 5.5$ topological sampling is very efficient (left, green), at $\beta = 5.6$ fluctuations of the topological charge are rare (left, purple). This problem is overcome by choosing a larger lattice volume of $24^3 \times 48$ instead of $16^3 \times 32$ (right, green). The figure has been published in [36].

topological freezing.

To avoid topological freezing, open boundary conditions in the temporal direction can be used [83]. In our simulations we do not use this technique. Instead, we monitor the topological charge to make sure that this topological freezing does not lead to inefficient sampling of the configuration space. The measurement of the topological charge, which requires Wilson flow as a smoothing procedure, is described in [78].

In our investigations of SU(3)-SYM, we observe significant topological freezing only at the finest simulated lattice spacings ($\beta = 5.6$), when using the lattice volume $V = 16^3 \times 32$. The effect is overcome when the larger volume $V = 24^3 \times 48$ is considered, see Fig. 5.2.

5.5. Monitoring the sign of the Pfaffian

In order to properly handle the sign of the Pfaffian, we monitor the lowest eigenvalues λ_i of the Dirac-Wilson operator D_W , see Fig. 5.3. Since the λ_i are either real or come in complex conjugate pairs and the Pfaffian is given by the non-degenerate product of the eigenvalues (cf. Sec. 3.4), it can only be negative if there are real, negative eigenvalues. These negative eigenvalues appear only for values of κ near the critical value κ_c [84].

In the simulations of SU(2)-SYM a considerable number of negative Pfaffian signs are observed only for the two ensembles at $\beta = 1.75$ where $\kappa = 0.1494$ and $\kappa = 0.1495$, which are the ensembles where κ is closest to κ_c [26]. However, the

5. Generation of gauge configurations

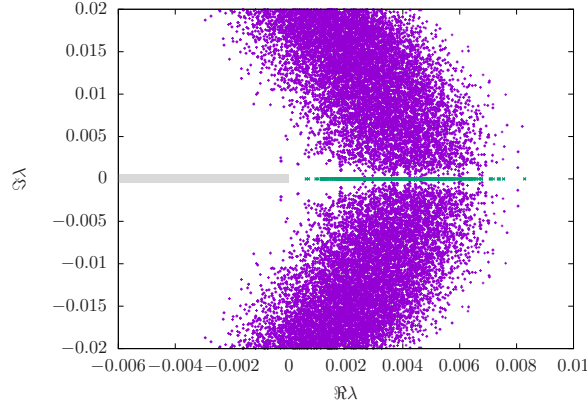


Figure 5.3.: Eigenvalues of the Dirac-Wilson matrix D_W from 1022 SU(3)-SYM configurations at $\beta = 5.5$, $\kappa = 0.1683$. The green points indicate eigenvalues close to the real axis ($\langle v | \gamma_5 | v \rangle > 0.001$ with $|v\rangle$ the corresponding eigenvector). Negative Pfaffian signs can only occur if there are real negative eigenvalues, i.e. green points in the shaded region. This is not the case here. The figure has been published in [36].

effect is still very mild at the 1-3 % level. The negative signs are handled using the reweighting method, as explained in Sec. 3.4. We do not observe significant negative eigenvalues in the investigations of SU(3)-SYM.

5.6. Finite size effects

Limited computing resources restrict the simulated lattice volumes in four dimensional hypercubic lattice QFT with dynamical fermions typically to only a few cubic fm. While analyzing quantum systems in finite boxes is interesting on its own, e.g. for the analysis of scattering states [85], here we are mainly interested in the limit of infinite volume. The deviations of the system from its infinite volume limit are called *finite size effects*. It is intuitive that states which have a small mass and therefore a large Compton wavelength are more affected by finite size effects than states of larger mass and, hence, shorter Compton wavelength.

There are two approaches to reduce impact of finite volume effects. The first approach is to run the simulation for different lattice sizes and to extrapolate the results to the infinite volume limit. The second approach is to work with lattice volumes that are already large enough such that finite size effects are smaller than the statistical errors for the investigated observables. In our simulations we use the latter approach. In order to ensure that our volumes are large enough, we have

5.6. Finite size effects

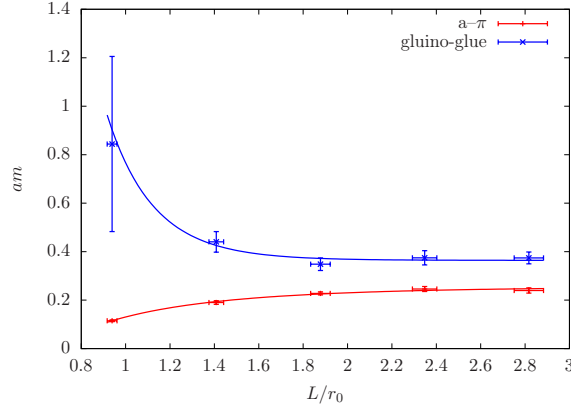


Figure 5.4.: Finite size analysis of the gluino-gluon ground state and the $a\pi$ masses at $\beta = 5.6$ in SU(3)-SYM and $\kappa = 0.1660$ for the different lattice sizes $8^3 \times 32$, $12^2 \times 32$, $16^3 \times 32$, $20^3 \times 40$, and $24^3 \times 48$. Lattices with a spatial extent $L > 2.4r_0$ show no significant finite size effects. The results have been fitted using the function $c \exp(-\alpha L)/L$ with the fit parameters c and α . Figure taken from [36]

tested the dependency of several observables on the (spatial) volume size [36]. We find that for lattices with a spatial extent

$$L \gtrsim 2.4r_{0_\chi}, \quad (5.13)$$

there are no significant finite size effects and hence for our simulations we use lattice volumes that fulfill this requirement. The analysis for the masses of the adjoint pion and of the gluino-gluon ground state is depicted Fig. 5.4.

6. Summary of the gauge ensembles

6.1. SU(2)-SYM

The ensembles of gauge configurations for the investigations of SYM with the gauge group SU(2) have been produced before the scope of this thesis using the TSMB and the TS-PHMC algorithm. They have been presented in [25], [26] and [28]. As explained in Sec. 3, the simulations of SYM with gauge group SU(2) are based on a Stout smeared action. For $\beta = 1.75$ the Desy-Münster collaboration has produced two different kinds of gauge configurations. One kind is based on a one level Stout smeared fermion action and the other kind is based on a three level Stout smeared fermion action. For consistency we only consider the gauge configurations with one level of Stout smearing in the scope of this thesis. Furthermore, for $\beta = 1.75$ there are simulations of two different lattice volumes ($V = 24^3 \times 48$ and $V = 32^3 \times 64$). Since finite volume effects are small for both studied volumes, we include both of them and treat them on the same footing when extrapolating the observables to the chiral and continuum limit.

The simulated parameters ranges of β and κ , as well as the corresponding lattice spacings, lattice volumes and adjoint pion masses are summarized in Tabs. 6.1 and 6.2. The chirally extrapolated values of the scales $w_{0,\chi}$ and $r_{0,\chi}$, needed for the scale setting and the continuum extrapolations (cf. Sec. 4.2), are summarized in Tab. 6.3. Further details are provided in Tab. A.1 in App. A.6.

6.2. SU(3)-SYM

The gauge configurations for the investigations of SU(3)-SYM have been produced in the scope of this thesis and first results have been published in [36] and [37]. We have attempted to produce gauge configurations for different values of $\beta \in \{5.2, 5.3, 5.4, 5.45, 5.5, 5.6, 5.8\}$. The lattices for $\beta = 5.2$ and $\beta = 5.3$ appeared to be too coarse and we have not been able to tune κ towards the chiral limit. The smallest pion mass obtained for $\beta = 5.3$ was $am_{a-\pi} = 0.600(6)$ for $\kappa = 0.1750$. Upon increasing κ further, the conjugate gradient solver converged only very slowly (after ~ 15.000 iterations). We have therefore excluded $\beta = 5.2$ and $\beta = 5.3$ from our simulations. For $\beta = 5.8$ the simulations were significantly affected by finite volume effects and simulations with lattice volumes large enough to suppress these effects are prohibitively expensive.

We have therefore chosen to use $\beta \in \{5.4, 5.45, 5.5, 5.6\}$ for our simulations. For each value of β we have produced gauge ensembles for at least four different values of κ corresponding to $am_{a-\pi}$ between 0.2 and 0.7. On average ~ 4700 con-

figurations have been produced for each ensemble. The lattice volumes have been chosen large enough, such that finite volume effects are sufficiently suppressed. A summary of the simulated parameter ranges, lattice volumes, and the corresponding physical values of the lattice spacings and of the adjoint pion masses are presented in Tabs. 6.1 and 6.2. Further details are provided in Tab. A.3 in App. A.6. Similarly to the case of SU(2)-SYM discussed above, we have simulated two different lattice volumes for $\beta = 5.6$ ($V = 12^3 \times 24$ and $V = 16^3 \times 32$). Finite volume effects are suppressed sufficiently on both volumes. This is supported by the fact that both volumes fulfill the finite volume condition formulated in Eq. 5.13. Thus, the simulations from both volumes are taken into account and they are treated on the same footing in the chiral and continuum extrapolations.

The measurements of the scales r_0 and w_0 have been mainly performed by our collaboration members Georg Bergner, Philipp Scior and Istvan Montvay. While the lattice spacings in units of fm have been determined via r_0 , we use the more precise scale w_0 for all other purposes. For the chiral extrapolations of the two scales we have used second order polynomials (cf. Sec. 4.2) and the resulting values are presented in Tab. 6.3. Note that the values of χ_r^2 obtained in the chiral extrapolations of the scale w_0 are rather large. We have therefore also tested to use a third order polynomial for the extrapolations. However, this has not reduced the value of χ_r^2 . We therefore conclude that a second order polynomial is sufficient for a reliable extrapolation. The most probable explanation for the large values of χ^2 is a slight underestimation of the uncertainties of w_0 .

The simulated physical lattice spacings and lattice volumes are comparable to the ones of the simulations for SU(2)-SYM. Since the simulations of SU(3)-SYM are significantly more expensive (the number of gauge degrees of freedom in the adjoint representation is $N_C^2 - 1 = 3$ for SU(2) and $N_C^2 - 1 = 8$ for SU(3)), the finest lattice spacing ($a = 0.0496(13)$ fm) is ~ 38 % larger than the finest lattice spacing of the SU(2)-SYM simulations ($a = 0.0358(6)$ fm). This is, however, well compensated by the clover-improvement used in the SU(3)-SYM simulations.

6. Summary of the gauge ensembles

β	V	a [fm]	L [fm]	$\#\kappa$	κ_{\min}	κ_{\max}
1.6	$24^3 \times 48$	0.0865(44)	2.1(1)	3	0.1550	0.1575
1.75	$24^3 \times 48$	0.0528(16)	1.267(37)	4	0.1490	0.1493
1.75	$32^3 \times 64$	0.0704(21)	2.253(67)	2	0.1494	0.1495
1.9	$32^3 \times 64$	0.03584(61)	1.146(20)	4	0.1433	0.14435
5.4	$12^3 \times 24$	0.0820(81)	0.984(97)	4	0.1695	0.1705
5.4	$16^3 \times 32$	0.0820(81)	1.31(12)	6	0.1692	0.1705
5.45	$16^3 \times 32$	0.0691(21)	1.106(33)	5	0.1685	0.1693
5.5	$16^3 \times 32$	0.0535(39)	0.856(62)	4	0.1667	0.1680
5.6	$24^3 \times 48$	0.0496(13)	1.1904(31)	4	0.1645	0.1660

Table 6.1.: Summary of the simulation parameters and the corresponding lattice spacings a and spatial extents L determined from the chirally extrapolated scale $r_{0,\chi}$ (cf. Tab. 6.3). The last three columns provide information on the number of different values of κ as well as the minimal and maximal values of κ studied for the given value of β . Top: Values for SU(2) taken from earlier investigations [28]. Bottom: Values for SU(3) obtained in the scope of this thesis.

β	$(am_{a-\pi})_{\min}$	$(am_{a-\pi})_{\max}$	$(w_{0,\chi}m_{a-\pi})_{\min}^2$	$(w_{0,\chi}m_{a-\pi})_{\max}^2$
1.6	0.201(10)	0.5757(41)	0.140(14)	1.146 (17)
1.75	0.1263(65)	0.2380(14)	0.186(19)	0.659(10)
1.9	0.1498(32)	0.2255(72)	0.770(40)	2.825(81)
5.4	0.3123(33)	0.6954(14)	0.402(12)	1.607(36)
5.45	0.2282(36)	0.4748(22)	0.346(16)	1.497(51)
5.5	0.2606(29)	0.5468(13)	0.555(20)	2.445(67)
5.6	0.22819(86)	0.51380(42)	0.610(18)	3.082(87)

Table 6.2.: Ranges of the simulated adjoint pion masses in units of the lattice spacing and of the physical scale $w_{0,\chi}$ for each β . Top: SU(2)-SYM simulations, bottom: SU(3)-SYM simulations.

β	$w_{0,\chi}/a$	χ_r^2	$w_{0,\chi}^{(3)}/a$	χ_r^2	$r_{0,\chi}/a$	χ_r^2
1.6	1.8595(39)	-	-	-	5.78(15)	-
1.75	3.411(18)	-	-	-	9.47(14)	-
1.9	5.858(84)	-	-	-	13.95(12)	-
5.4	2.031(22)	3.13	2.045(64)	3.74	6.10(60)	0.0215
5.45	2.577(43)	3.22	2.41(11)	3.70	7.24(22)	0.4730
5.5	2.860(39)	5.06	3.13(13)	-	9.35(68)	1.6496
5.6	3.422(48)	1.42	3.54(11)	-	10.07(26)	0.6248

Table 6.3.: Chirally extrapolated values of the scales r_0 and w_0 . Top: Values for $SU(2)$ taken from [28]. Bottom: Values for $SU(3)$ obtained by using a second order polynomial ($w_{0,\chi}/a$) and a third order polynomial ($w_0^{(3)}, \chi/a$) for the fit. For $\beta = 5.5$ and $\beta = 5.6$ there are only four ensembles each. The third order polynomial has also four fit parameters and therefore χ_r^2 cannot be determined here.

7. Measuring bound state masses

The masses of the bound states belong to the most interesting observables in non-perturbative investigations of gauge theories. In particular, in SYM the expected mass degeneracy of the supermultiplets provides a non-trivial measure for supersymmetry restoration in the chiral and continuum limit (cf. Sec. 2.3.2). After suitable gauge ensembles have been produced (cf. Secs. 5, 6), the masses of the bound states in the chiral multiplet can be extracted from these ensembles. For this purpose, suitable correlation functions need to be measured. The present section provides an overview of the extraction of particle masses from these correlation functions and the determination of their uncertainties.

The details concerning measuring the correlation functions and improved techniques to increase the precision of the results are explained in Secs. 8 to 11.

7.1. Extracting bound state masses from the correlation function

The correlation function $C_{ij}(t_1, t_2)$ of two operators $O_i(t_1)$ and $O_j(t_2)$, localized at times t_1 and t_2 , respectively, is defined as

$$C_{ij}(t_1, t_2) = \left\langle O_i(t_1) O_j^\dagger(t_2) \right\rangle = \langle \Omega | O_i(t_1) O_j^\dagger(t_2) | \Omega \rangle, \quad (7.1)$$

with $|\Omega\rangle$ the vacuum state. Due to translational invariance, it only depends on the relative time distance $t = t_1 - t_2$, hence

$$C_{ij}(t) = \left\langle O_i(t) O_j^\dagger(0) \right\rangle, \quad (7.2)$$

which is also to be interpreted as the i - j component of the *correlation matrix* of the operators O_i . The correlation functions (correlators) decay exponentially with the energies of the physical states $|n\rangle$ above the vacuum state $|\Omega\rangle$. This is demonstrated by inserting a full set $\{|\Omega\rangle, |n\rangle\}$ of the Hamiltonian's eigenstates

$$C_{ij}(t) = \sum_{\phi=\{\Omega, n\}} \langle \Omega | O_i(t) | \phi \rangle \langle \phi | O_j^\dagger(0) | \Omega \rangle \quad (7.3)$$

$$= \langle O_i \rangle \langle O_j \rangle + \sum_n \langle \Omega | e^{tH} O_i(0) e^{-tH} | n \rangle \langle n | O_j^\dagger(0) | \Omega \rangle \quad (7.4)$$

$$= \langle O_i \rangle \langle O_j \rangle + \sum_n a_i^{(n),*} a_j^{(n)} e^{-t(E^{(n)} - E^\Omega)} \quad (7.5)$$

$$= \langle O_i \rangle \langle O_j \rangle + \sum_n a_i^{(n),*} a_j^{(n)} e^{-tE^{(n)}}, \quad (7.6)$$

7.1. Extracting bound state masses from the correlation function

with

$$a_i^{(n)} = \langle n | O_i^\dagger(0) | \Omega \rangle . \quad (7.7)$$

In Eq. 7.6 the vacuum energy $E_\Omega = 0$ has been normalized to zero and for notational convenience a discrete spectrum of physical states is assumed. In lattice calculations with finite lattice volumes this assumption is certainly fulfilled. The calculation can be straightforwardly generalized to continuous spectra. The first term in Eq. 7.6 is usually avoided by subtracting the expectation value in the definition of O_i if it is non-zero

$$O_i = O'_i - \langle O'_i \rangle \quad (7.8)$$

and therefore this term is neglected in the following. The diagonal elements of the correlation matrix are given by

$$C_{ii}(t) = \sum_n \left| a_i^{(n)} \right|^2 e^{-tE^{(n)}} . \quad (7.9)$$

The coefficient $|a_i^{(n)}|^2$ is the overlap of the state $|n\rangle$ with the the state created by O_i^\dagger acting on the vacuum, or in short, the overlap of the operator O_i with the state $|n\rangle$. In order to determine the mass of a physical state $|n\rangle$ with high precision, the operator O_i needs to have a sufficiently large overlap with this state and should ideally have only small overlap with other states. In other words, the state created by the operator O_i should be as similar as possible to the state $|n\rangle$. The operators are therefore called *interpolating operators* or interpolating fields and they have to have the same quantum numbers as the states that they interpolate. Otherwise the overlap would be zero.

Furthermore, to estimate masses of bound states, the states created by the operators should have vanishing momentum $\vec{p} = \vec{0}$, such that the energy of the interpolated state is identical to the mass $E^{(n)} = m^{(n)}$. Corresponding operators can be obtained by constructing interpolating operators in coordinate space and Fourier transforming them with $\vec{p} = \vec{0}$

$$O_i(\vec{p}, t) = \frac{1}{L^3} \sum_{\vec{x}} e^{i\vec{p}\vec{x}} O_i(\vec{x}, t) , \quad (7.10)$$

$$O_i(t) \doteq O_i(\vec{0}, t) = \frac{1}{L^3} \sum_{\vec{x}} O_i(\vec{x}, t) . \quad (7.11)$$

Inserting these operators back into the correlation function shows that the correlator can be obtained from the correlation function $C(x, y)$ in position space

7. Measuring bound state masses

summed over all spatial indices

$$C_{ij}(t) \stackrel{\text{Eqs. 7.2}}{\stackrel{7.11}{=}} \frac{1}{L^6} \sum_{\vec{x}, \vec{y}} \left\langle O_i(\vec{x}, t) O_j^\dagger(\vec{y}, 0) \right\rangle = \frac{1}{L^6} \sum_{\vec{x}, \vec{y}} C_{ij}(x, y) \Big|_{y^4=0} = \frac{1}{L^3} \sum_{\vec{x}} C_{ij}(x, y_0), \quad (7.12)$$

where in the last step translational invariance was used and $t = x^4 - y_0^4$. The space-time coordinate y_0 is arbitrary and can be chosen freely.

The finite size of the lattice and the (anti-)periodicity in the temporal direction is not taken into account in the discussion above. Due to these boundary conditions, the correlator has contributions that are even or odd under $t \rightarrow T - t$ (for a discussion, see [53], Secs. 4.2.5 and 5.2.1). Projected to the even or the odd part, the correlator is given by

$$C_{ij}(t) = \sum_n a_i^{(n),*} a_j^{(n)} \left(e^{-tm^{(n)}} \pm e^{-(T-t)m^{(n)}} \right). \quad (7.13)$$

Thus, in addition to the forward propagating mode described in Eq. 7.9, the lattice correlator has also backward propagating modes. In principle, there are also contributions from wrapping once or several times around the lattice. Since these are exponentially suppressed, they are neglected here.

The procedure to extract masses of a bound states from a given ensemble is then summarized as follows.

1. Construct an operator in position space that has sufficient overlap with the bound state of interest; sum over the spatial indices according to Eq. 7.12.
2. Measure the correlation function $C_{ii}(t)$ (Eq. 7.2) on the ensemble. To improve the precision of in the estimation of $C_{ii}(t)$, the measured values are (anti-)symmetrized, depending on whether the even or the odd part shall be analyzed

$$C_{ii}(t) = \frac{1}{2} (C_{ii}(t) \pm C_{ii}(T - t)). \quad (7.14)$$

3. Extract the decay parameter $m^{(n)}$ from the correlation function.

The mass $m^{(0)}$ of the ground state $|0\rangle$ is the simplest one to extract. For sufficiently large time separations t , all contributions of heavier states to the correlator $C_{ii}(t)$ have decayed and, hence, the ground state mass is given by the decay parameter of the correlator at large t . The so-called *effective mass* provides a first

7.2. Fitting the correlator

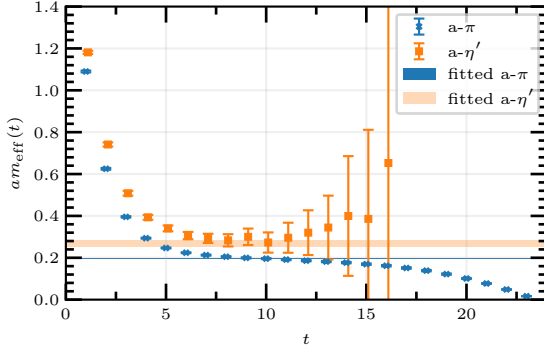


Figure 7.1: Effective mass of the $a\text{-}\pi$ and of the $a\text{-}\eta'$ for SU(2)-SYM, $\beta = 1.75$, $\kappa = 0.14925$. The effect of the backward propagation mode is visible from the effective mass of the $a\text{-}\pi$ at large values of t . For comparison, the corresponding masses, estimated from fits of the correlators are depicted as shaded bands.

estimate for $m^{(0)}$ from the time separations t and $t + 1$

$$m_{\text{eff}}^{(0)}(t) \doteq \ln \frac{C_{ii}(t)}{C_{ii}(t+1)}. \quad (7.15)$$

Since at small values of t also heavier states contribute to the correlator, the effective mass is larger than the ground state mass for small time separations t . For larger values of t , the effective mass approaches the mass of the ground state from above, see Fig. 7.1. Thus, once the higher states have decayed the effective mass forms a plateau. For very large values of t two effects let the effective mass deviate from this plateau:

1. The definition of the effective mass in Eq. 7.15 does not take into account the backward propagation mode, which becomes important at very large values of t .
2. There are always statistical uncertainties due to the limited number of configurations. At large t the correlator decays to very small values, often resulting in a poor signal-to-noise ratio. In this case the measured effective mass fluctuates strongly at large t .

A better method to estimate the particle masses is to fit the correlator $C_{ii}(t)$ using a suitable fit function. The advantage of a fit over the effective mass estimate is twofold. Fitting the correlator takes into account data of more than two time separations and heavier states than the ground state are accessible by using different fit functions (multi state fit).

7.2. Fitting the correlator

Fitting is the procedure of finding the most probable set of parameters $\{c_k\}$ for a given functional form $f_{c_k}(x)$ to resemble the measured data points (x_i, y_i) . Thus,

7. Measuring bound state masses

the masses of bound states can be extracted from the correlation functions by treating them as fit parameters. Fitting is a standard numerical method in science and therefore only the relevant details are summarized here.

Assuming Gaussian distributed data points about the expectation values, the most probable set of fit parameters $\{c_k\}$ is obtained by finding c_k that minimizes

$$\chi^2 = \sum_{i,j} (f_{c_k}(\bar{x}_i) - \bar{y}_i) \text{Cov}_{ij}^{-1} (f_{c_k}(\bar{x}_j) - \bar{y}_j). \quad (7.16)$$

Here \bar{x}_i , \bar{y}_i are the data points averaged over repeated measurements and Cov_{ij} is the covariance matrix of the data. It can be estimated from the data points of repeated measurements

$$\text{Cov}_{ij} = \frac{1}{N-1} \sum_n^N (y_{i,n} - \bar{y}_i)(y_{j,n} - \bar{y}_j). \quad (7.17)$$

where N is the number of measurements. This method of determining the parameter set c_k is called a *correlated fit*. If the data points are not correlated among each other, then the covariance matrix Cov_{ij} is diagonal. In this case the parameters c_k can be determined from an *uncorrelated fit* where only the diagonal elements of the covariance matrix are determined and all other elements are set to zero ($C_{ij} = 0$ for $i \neq j$).

For the extraction of masses, the functional form of the correlators is known analytically (Eq. 7.13). Thus, to determine the mass of the ground state, the correlator is fitted at large values of t using the fit ansatz

$$f(t) = \begin{cases} c \cosh((t - T/2)m^{(0)}) \\ c \sinh((t - T/2)m^{(0)}) \end{cases}, \quad (7.18)$$

depending on whether the correlator is even or odd in $t \rightarrow T - t$. c and $m^{(0)}$ are the fit parameters.

It is possible to extract also heavier states than the ground state by performing a so-called multi state fit, i.e. by using fit functions of the form

$$f(t) = \begin{cases} \sum_n^N c_n \cosh((t - T/2)m^{(n)}) \\ \sum_n^N c_n \sinh((t - T/2)m^{(n)}) \end{cases}, \quad (7.19)$$

to determine the masses of the N lowest states. Since these multi state fits have many fit parameters, they require a good signal-to-noise ratio of the measured data and are often unstable. A better method to determine the masses of excited states is the so-called *variational method* which is explained in Sec. 7.3.

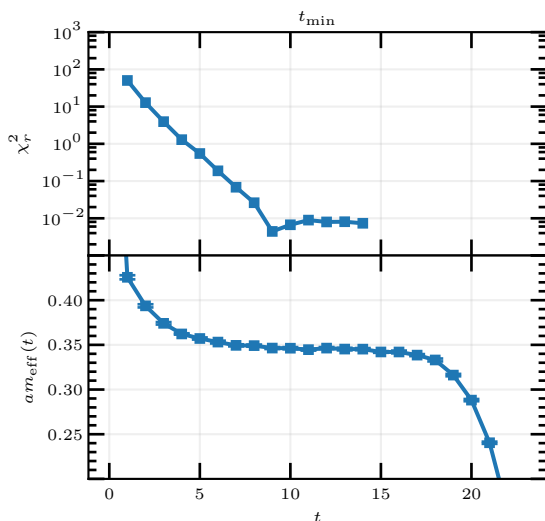


Figure 7.2: Effective mass (bottom) and χ_r^2 of an uncorrelated mass fit with a fixed fit length $t_{\max} - t_{\min} = 10$ and varying values of t_{\min} (top) of the a - π determined from the SU(3)-SYM ensemble $\beta = 5.6$, $\kappa = 0.1655$. From the effective mass it is difficult to estimate t_{\min} . It can be determined more reliably by means of χ_r^2 which stabilizes around $t = 9$.

In addition to the functional form, also the t -interval of the fit has to be chosen with care. Especially the choice of the lower limit t_{\min} is crucial. If t_{\min} is too small, the fit is affected by unwanted contaminations of heavier states. On the other hand, choosing a too large value for t_{\min} leads to poor precision because the signal-to-noise ratio drops quickly for increasing values of t . The choice of the upper limit of the fit interval t_{\max} is not as critical because, due the small signal-to-noise ratio at large values of t , those data points have only a small influence on the fitted value for the mass m . For a fit of the correlator, the maximal value $t_{\max} = T/2$ can be used for the upper limit. For advanced methods like the variational method, this might not necessarily be the case (cf. Sec. 11.4).

There are different ways to estimate the lower limit of the fit interval. One method is to take the value of t where the effective mass plateau sets in, see Fig. 7.2. This estimate is, however, not very precise because there is no unique way to determine the beginning of the plateau and it is especially difficult if fluctuations of the effective mass, due to limited statistics, are large. Another way to determine the appropriate fitting interval is to perform fits using different values of t_{\min} and to judge the goodness of the fit interval by the reduced chi squared

$$\chi_r^2 = \frac{\chi^2}{\text{d.o.f.}} \quad (7.20)$$

$$\# \text{d.o.f.} \hat{=} \text{number of degrees of freedom} \quad (7.21)$$

$$= \text{number of datapoints} - \text{number of parameters}. \quad (7.22)$$

If the fit function describes the data correctly and the data points are Gaussian

7. Measuring bound state masses

distributed, then the expected value of χ_r^2 for a correlated fit is of order one

$$\chi_r^2 = \mathcal{O}(1). \quad (7.23)$$

This is only fulfilled for t -intervals, for which the heavier states have decayed sufficiently. Otherwise χ_r^2 grows quickly with decreasing t_{\min} . Therefore the procedure to find the minimal value for t_{\min} is to increase t_{\min} until χ_r^2 stabilizes at a value of $\mathcal{O}(1)$.

As was demonstrated in [86], a correlated fit is often unstable for small data sets. The author suggests that, to reliably perform correlated fits, the data set should have a size

$$N > \max(D^2, 10(D + 1)), \quad (7.24)$$

where N is the number of estimators, here the number of independent configurations, and D is the number of data points to fit. In lattice calculations this condition is often not fulfilled and thus it is recommended to perform uncorrelated fits, instead. Therefore we always use uncorrelated fits in the determination of the bound state masses.

In this case, the condition $\chi_r^2 = \mathcal{O}(1)$ has to be loosened. In practice, it is often sufficient to find the region where χ_r^2 stabilizes for increasing t_{\min} , see Fig. 7.2. As a consequence of using uncorrelated fits, the uncertainty estimates, provided by the fitting algorithms, are not correct. Therefore, the uncertainties of the results are determined using the *Jackknife* resampling method which is explained in Sec. 7.4. Furthermore, instead of using Eq. 7.17, we also employ the Jackknife method to estimate the (diagonal) entries of the covariance matrix Cov_{ij} used in the fit of the masses.

7.3. The variational method

Interpolating operators have, in general, non-vanishing overlap with more than just one physical state. In Sec. 7.2, it is explained that the contribution of the lightest states to the correlator can be separated by multi state fits or by considering large values of t for the ground state. This procedure, however, has disadvantages. For large values of t , the signal-to-noise ratio of the correlator is typically much worse than for small values of t . Secondly, multi state fits become unstable very quickly for large numbers of fit parameters. These effects lead to low precision of the final data. It is therefore desirable to isolate the contribution of a single physical state to the correlator and to extract its mass from this isolated part.

A method which has proved to be very useful in this regard is the so-called *variational method* which was first suggested by Wilson [87] to improve the signal

7.3. The variational method

of the ground state. This idea was soon after generalized to also isolate the contributions of higher excited states. The main idea is to systematically construct an operator which has optimal overlap with the physical state to be analyzed and only small overlap with the other states. This is achieved by forming a linear combination of several different interpolating operators $O_i(x)$

$$O(x) = \sum_i \alpha_i O_i(x), \quad (7.25)$$

and optimizing the coefficients α_i such that the overlap with the state is maximized. For the ground state this amounts to maximizing [88]

$$\lambda^{(0)}(t - t_0) = \max_{\{\alpha_i\}} \frac{\langle \Omega | O(t) O(t_0) | \Omega \rangle}{\langle \Omega | O(0) O^\dagger(0) | \Omega \rangle} \stackrel{\text{Eq. 7.9}}{=} \max_{\{\alpha_i\}} \frac{\sum_n |a^{(n)}(\alpha_i)|^2 e^{-(t-t_0)m^{(n)}}}{\sum_n |a^{(n)}(\alpha_i)|^2}, \quad (7.26)$$

where now the overlaps $|a^{(n)}(\alpha_i)|^2$ depend on the coefficients α_i . For $t > t_0$ the expression is clearly maximal when the overlap with the ground state $|a^{(0)}(\alpha_i)|^2$ is maximal. It was quickly realized [89] that this extremal solution can be obtained equivalently from solving the generalized eigenvalue problem (GEVP)

$$C(t) \vec{v}^{(n)}(t, t_0) = \lambda^{(n)}(t, t_0) C(t_0) \vec{v}^{(n)}(t, t_0), \quad (7.27)$$

where $C(t)$ is the matrix of cross-correlation functions, defined in Eq. 7.2, $\lambda^{(n)}(t, t_0)$ are the generalized eigenvalues, sorted by their magnitude and $\vec{v}^{(n)}(t, t_0)$ are the corresponding generalized eigenvectors. In Ref. [90] it has been shown that the generalized eigenvalues $\lambda^{(n)}(t, t_0)$ satisfy

$$\lim_{t \rightarrow \infty} \lambda^{(n)}(t, t_0) \propto e^{-m^{(n)}(t-t_0)} (1 + O(e^{-\Delta m_n(t-t_0)})), \quad (7.28)$$

$$\Delta m_n = \min_{l \neq n} |m_l - m_n|. \quad (7.29)$$

Since the functional form of the eigenvalues $\lambda^{(n)}(t, t_0)$ (Eq. 7.28) and of the correlator $C_{ii}(t)$ (Eq. 7.9) are similar, the masses $m^{(n)}$ of not only the ground state, but also of the next heavier states, can be extracted from $\lambda^{(n)}(t, t_0)$ using the same methods (effective mass, fitting) as explained for extracting the masses from the correlator $C_{ii}(t)$. A multi state fit is not necessary.

Besides its benefits to extract higher excited state masses, the variational method also increases the precision of the ground state mass estimation by allowing to use smaller values of t_{\min} , due to the reduced excited state contaminations in $\lambda^{(0)}(t)$ compared to $C_{ii}(t)$.

There are several parameters to be optimized in the variational approach such

7. Measuring bound state masses

as the choice of the operators O_i (sometimes called *variational basis*), the value of t_0 , the fitting intervals, etc. A systematic optimization of these parameters is described in Secs. 9 and 11.

7.4. Determining uncertainties, Jackknife method

As for all numerical calculations, it is important to determine the uncertainties of observables calculated in lattice QFT. This can be achieved by means of statistical methods. For this purpose, autocorrelations among the configurations (cf. Sec. 5.2.1) have to be properly taken into account, which is explained in Sec. 7.5. In the present section, the data is considered to be free of autocorrelations.

This simplest approach to statistically estimate uncertainties is called *Data Blocking*. It is, however, often unstable for small data sets and therefore it is not commonly used in lattice computations. This stability problem is circumvented by resampling methods. The two most popular resampling approaches are *Jackknife* and *Bootstrap*. They are very similar. In both methods the estimator \hat{O} for the observable O is calculated from the full data set, while the estimator for its error $\Delta\hat{O}$ is obtained from resampled data sets of the original data. The two methods differ in the way the original data set is resampled. The three methods, data blocking, Jackknife and Bootstrap are standard statistical methods and they are explained in many textbooks, e.g. [52], Chapter 4. In this thesis we use the Jackknife method which is summarized in the following.

From the original data, consisting of N configurations, a new data set, called *Jackknife sample*, is constructed by removing one configuration from the original set. This way, N Jackknife samples are obtained by removing each configuration once. On each Jackknife sample i , an estimator \tilde{O}_i for the observable O is calculated in the usual way (Eq. 3.47). The Jackknife error estimate is then given by

$$(\Delta\hat{O})^2 = \frac{N-1}{N} \sum_{i=1}^N (\tilde{O}_i - \hat{O})^2, \quad (7.30)$$

where \hat{O} is the estimator calculated from the original data set. A potential bias can be eliminated by means of

$$\hat{O}_{\text{unbiased}} = \hat{O} - (N-1)(\tilde{O} - \hat{O}), \quad (7.31)$$

where

$$\tilde{O} = \frac{1}{N} \sum_i^N \tilde{O}_i. \quad (7.32)$$

The bias correction, however, is known to sometimes lead to stability problems and it is therefore not performed in this thesis. Instead, \hat{O} is used as the final result.

7.5. Eliminating autocorrelations, Binning

The uncertainty estimate from the Jackknife method can be spoiled if autocorrelations are present in the data set. Therefore, autocorrelations need to be properly handled. The simplest solution to eliminate autocorrelations is to take only every n -th configuration and discard the configurations in between where n is larger than the autocorrelation time scale. A more elaborate alternative, which takes into account all configurations and which is used in this thesis, is a procedure called *Binning*. In this method the data set is divided into bins, each containing B consecutive configurations. The Jackknife samples are then constructed by removing a whole bin instead of removing only one configuration. Hence, $N_B = N/B$ Jackknife samples are obtained, where N is the number of configurations.

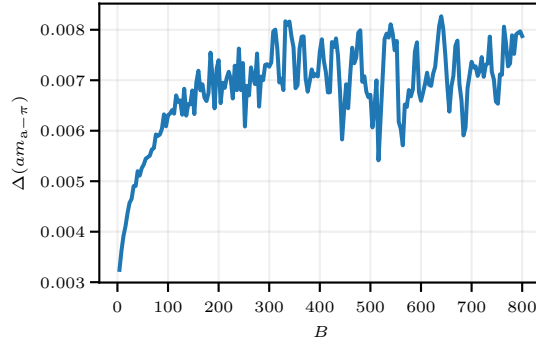
The proper bin size required to eliminate autocorrelations can be estimated by calculating the Jackknife error estimates for different bin sizes B . For increasing bin sizes, the effect of autocorrelations is successively reduced. Therefore, the error estimates $(\Delta\hat{O})_B$ plotted against B stabilize and form a plateau once autocorrelations are eliminated. The bin size B , where the plateau begins, is then used for the final estimation of the uncertainty, see Fig. 7.3.

An even more elaborate method to take into account autocorrelations, is the so-called Γ -method which has been developed in [91]. However, the Γ -method is not used in the scope of this thesis.

In general, the autocorrelation time varies for different observables and therefore the determination of the proper bin size needs to be performed for each observable individually. The longest autocorrelation times are typically observed for the topological charge (cf. Sec. 5.4).

7. Measuring bound state masses

Figure 7.3: Jackknife error estimates for $am_{a-\pi}$ using different bin sizes B . We read off a bin size $B \simeq 200$ required to eliminate autocorrelation.



8. Constructing variational bases and measuring correlation functions

As outlined in the previous section, the variational method is a very useful technique to investigate the ground and excited states of the SYM spectrum. In this thesis the variational method is employed for the investigation of the states belonging to the chiral multiplet. For this purpose, variational bases of suitable interpolating operators have to be constructed for the scalar, the pseudoscalar, and the spin- $1/2$ channel. Our approach is to use a set of local interpolating operators on which smearing techniques are applied to construct the variational bases. The definition of the basic interpolating fields and the smearing techniques used to construct the variational bases are explained in the present section. Furthermore, the details of measuring the corresponding correlation functions are described.

The techniques introduced in this section come with several parameters. The tuning of these parameters to obtain high signal-to-noise ratios is explained in Sec. 9.

8.1. Local interpolating operators

Interpolating operators are gauge invariant operators which are constructed from fields on the lattice and which carry the quantum numbers of the respective state. In principle, every operator that meets this condition is a valid operator to be used in the variational method. In this section we define the set of local operators used for the construction of the variational bases. We differentiate between different kind of operators

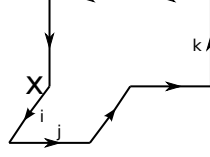
- Operators which are constructed solely from gluonic fields (Wilson loops) are called glueball operators.
- Operators that are bilinears of fermion fields are called meson operators.
- There are also operators constructed from both, gluon and fermion fields, the prime example being the gluino-gluon operator defined below.

The states in the scalar and in the pseudoscalar channel are expected to be mixed states of glueballs and mesons. Hence, it is expected that both, glueball operators as well as meson operators have non-vanishing overlap with these states.

The local glueball and meson interpolating operators used in our investigations are commonly known from lattice QCD (with the difference the fermions of QCD

8. Constructing variational bases and measuring correlation functions

Figure 8.1: Wilson loop $\mathcal{C}_{ijk}(x)$ used in the interpolating field of 0^{-+} -glueball.



are in the fundamental representation of the gauge group) and therefore the definitions are simply stated here without much discussion. The glueball operator for the 0^{++} channel is defined as

$$O_{\text{gb}^{++}}(x) = \text{Tr}_c \left[U_{12}^{(p)}(x) + U_{23}^{(p)}(x) + U_{31}^{(p)}(x) \right], \quad (8.1)$$

where $U_{ij}^{(p)}$ denotes a plaquette in the i - j direction. The corresponding local operator for the 0^{-+} glueball is given by

$$O_{\text{gb}^{-+}}(x) = \sum_{R \in \mathbf{O}_h} [\text{Tr}_c [\mathcal{C}(x)] - \text{Tr}_c [P\mathcal{C}(x)]], \quad (8.2)$$

$$\begin{aligned} \mathcal{C}_{ijk} = & U_i(x) U_j(x + \hat{i}) U_i^\dagger(x + \hat{j}) U_j(x + \hat{j}) \\ & U_k(x + 2\hat{j}) U_j^\dagger(x + \hat{j} + \hat{k}) U_j^\dagger(x + \hat{k}) U_k(x + \hat{k}), \end{aligned} \quad (8.3)$$

where the sum runs over all rotations of the cubic group \mathbf{O}_h and $P\mathcal{C}$ is the parity conjugate of the Wilson loop \mathcal{C} , see Fig. 8.1. The meson interpolating operators are given by

$$O_{\text{a-f}_0}(x) = \bar{\lambda}^a(x) \lambda^a(x), \quad O_{\text{a-}\eta'}(x) = \bar{\lambda}^a(x) \gamma_5 \lambda^a(x). \quad (8.4)$$

The interpolating field of the gluino-gluon state is obtained by discretizing the continuum interpolator

$$O_{\text{gg}}^{\text{cont}}(x) = \frac{1}{2} \sigma_{\mu\nu}^{\alpha\beta} \text{Tr}_c [F^{\mu\nu}(x) \lambda^\beta(x)], \quad (8.5)$$

which has already been used in early works of SYM [23]. This is achieved by replacing the field strength tensor with the lattice version (cf. Eq. 3.27) and restricting the sum to the spatial components (indicated by the indices i, j)

$$O_{\text{gg}}^\alpha(x) = \frac{1}{2} \sigma_{ij}^{\alpha\beta} \text{Tr}_c [F_{\text{latt}}^{ij}(x) \lambda^\beta(x)]. \quad (8.6)$$

8.2. Evaluating the correlators and the a - π

Measuring the glueball correlation functions

$$C_{\text{gb}}(x, y) = \left\langle O_{\text{gb}}(x) O_{\text{gb}}^\dagger(y) \right\rangle \quad (8.7)$$

by means of Eq. 3.47 is straightforward because the glueball interpolators $O_{\text{gb}}(x)$ can be evaluated directly on the gauge configurations.

Correlation functions of interpolating operators that include fermion fields are more difficult to measure. As explained in Sec. 3.4, the fermion fields are integrated out and not stored in the configurations. Therefore, the fermion fields appearing in the correlation functions have to be Wick contracted for the measurement. Note that due to the Majorana nature of the gluino, contractions of the form

$$\overline{\lambda}\lambda \stackrel{\text{Eq. 2.6}}{=} \overline{\lambda}\lambda^T C \quad \text{and} \quad \overline{\lambda}\lambda \stackrel{\text{Eq. 2.6}}{=} C \overline{\lambda}^T \lambda \quad (8.8)$$

are non-vanishing and have to be taken into account. In the case of the meson correlators, Wick contractions lead to connected and disconnected pieces

$$C_{\text{m}}(x, y) = \langle O_{\text{m}}(x) O_{\text{m}}^\dagger(y) \rangle = \langle \bar{\lambda}^a(x) \Gamma \lambda^a(x) \bar{\lambda}^b(y) \Gamma \lambda^b(y) \rangle \quad (8.9)$$

$$\begin{aligned} &= \langle \overbrace{\bar{\lambda}^a(x) \Gamma \lambda^a(x)} \overbrace{\bar{\lambda}^b(y) \Gamma \lambda^b(y)} \rangle + \langle \overbrace{\bar{\lambda}^a(x) \Gamma \lambda^a(x) \bar{\lambda}^b(y) \Gamma \lambda^b(y)} \rangle \\ &\quad + \langle \overbrace{\bar{\lambda}^a(x) \Gamma \lambda^a(x) \bar{\lambda}^b(y) \Gamma \lambda^b(y)} \rangle \end{aligned} \quad (8.10)$$

$$= \langle \text{Tr}_c [\Gamma D_W^{-1}(x, x)] \rangle \langle \text{Tr}_c [\Gamma D_W^{-1}(y, y)] \rangle - 2 \langle \text{Tr}_c [\Gamma D_W^{-1}(x, y) \Gamma D_W^{-1}(y, x)] \rangle, \quad (8.11)$$

where $D_W^{-1}(x, y)$ denotes the propagator from x to y (spin and group indices suppressed) and Γ represents $\mathbb{1}$ or γ_5 . The first term in Eq. 8.11 is the disconnected piece and the second term is the connected piece. A graphical representation of the meson correlator is shown in Fig. 8.2.

The correlator for determining the mass of the adjoint pion is defined to be the connected piece of the a - η' -correlator

$$C_{a-\pi}(x, y) = \langle \text{Tr} [\gamma_5 D_W^{-1}(x, y) \gamma_5 D_W^{-1}(y, x)] \rangle. \quad (8.12)$$

The adjoint pion is not a physical particle of SYM because its correlator cannot be obtained from Wick contractions of interpolating operators. This is because in SYM all interpolating operators are necessarily flavor singlets since SYM has only one fermion species ($1/2$ flavor). Hence, the Wick contractions of fermion bilinears always contain disconnected pieces.

8. Constructing variational bases and measuring correlation functions

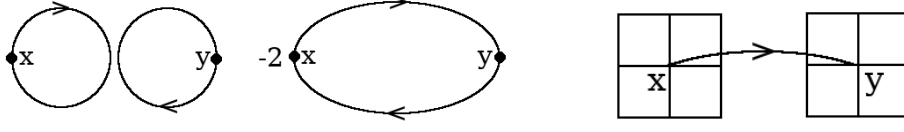


Figure 8.2.: Graphical representations of the meson correlator (left) and of the gluino-gluon correlator (right). The meson correlator consists of a disconnected and a connected piece. The gluino-gluon correlator consists of a fermion propagator connecting two antisymmetrized clover plaquettes representing the lattice field strength tensor F_{ij}^{latt} .

Wick contracting the gluino-gluon correlator yields

$$C_{\text{g-g}}^{\alpha\beta}(x, y) = \langle O_{\text{g-g}}^{\alpha}(x) \bar{O}_{\text{g-g}}^{\beta}(y) \rangle \quad (8.13)$$

$$= \frac{1}{4} \left\langle \sigma_{ij}^{\alpha\alpha'} \text{Tr}_c \left[F_{ij}^{\text{latt}}(x) \overline{\lambda^{\beta'}(x)} \right] \text{Tr}_c \left[F_{kl}^{\text{latt}}(y) \bar{\lambda}^{\beta'}(y) \right] \sigma_{kl}^{\beta'\beta} \right\rangle \quad (8.14)$$

$$= \frac{1}{4} \left\langle \sigma_{ij}^{\alpha\alpha'} \text{Tr}_c \left[F_{ij}^{\text{latt}}(x) T^a \right] (D_W^{-1})_{xy}^{\alpha'a, \beta'b} \text{Tr}_c \left[F_{kl}^{\text{latt}}(y) T^b \right] \sigma_{kl}^{\beta'\beta} \right\rangle, \quad (8.15)$$

where T^a are the generators of the gauge group.

It is simple to show that the the glueball and the meson correlators considered here are symmetric in $t \rightarrow T - t$ and, hence, cosh functions (Eq. 7.18) are used for fitting the correlators. The gluino-gluon correlator can be expanded in the basis of the Dirac matrices $\Gamma_i = \{\mathbb{1}, \gamma_5, \gamma_\mu, \gamma_m u \gamma_5, i\sigma_\mu \nu\}$. By studying the transformation properties of the correlator, it can be shown [92] that only two terms are non-vanishing

$$C_{\text{gg}}^{\alpha\beta}(t) = C_1(t) \delta^{\alpha\beta} + C_{\gamma_4}(t) \gamma_4^{\alpha\beta}, \quad (8.16)$$

where $C_1(t)$ and $C_{\gamma_4}(t)$ are real components. They are anti-symmetric and symmetric under $t \rightarrow T - t$

$$C_1(t) = -C_1(T - t), \quad C_{\gamma_4}(t) = C_{\gamma_4}(T - t). \quad (8.17)$$

The two correlators $C_1(t) = \frac{1}{4} \text{Tr}_D[C_{\text{gg}}(t)]$ and $C_{\gamma_4}(t) = \frac{1}{4} \text{Tr}_D[\gamma_4 C_{\text{gg}}(t)]$ can be used separately for the mass estimation using a sinh or a cosh fit function, respectively (Eq. 7.18).

8.3. Smearing techniques

The interpolating fields defined in Sec. 8.1 are ultralocal in the sense that they are defined from the smallest possible Wilson loops and fermion fields at single space-time points. It is well known, however, that bound states have a finite spatial extent. Therefore, ultralocal interpolating fields have only small overlaps with these states. Even worse: Since heavier states have a smaller Compton wave length compared to lighter states it is intuitive that the signals for the light states are very contaminated by contributions of heavier states when using ultralocal operators.

In order to improve the spatial overlap with the light states, we use smearing techniques on the ultralocal operators to construct spatially extended operators. By varying the smearing parameters, and in particular the so-called *smearing level*, different interpolating operators are constructed from the ultralocal operators. In this thesis we use these different operators, obtained from different smearing levels, as the operator basis in the variational method.

As an alternative, extended operators can be constructed manually, e.g. by considering Wilson loops of larger extent in the case of the glueball interpolators (cf. Eqs. 8.1, 8.2). These extended operators could then also be smeared. This approach is, however, not investigated in this thesis.

Many different smearing techniques have been explored in lattice QFT. In our investigations we apply *APE smearing* [93] and *Jacobi smearing* [94, 95] to smear the gauge and the gluino field, respectively. The spatially extended (smeared) interpolating operators are then constructed by replacing the unsmeared fields with the smeared fields.

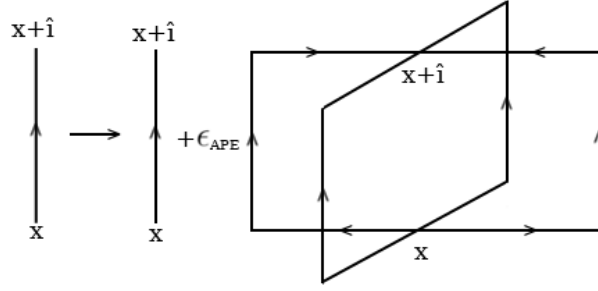
Smearing does not only increase the spatial extent of local operators, but it also smoothens short ranged (ultraviolet) fluctuations of the fields and hence it may reduce noise. Besides the use of smearing in the construction of interpolating operators, Stout smearing is applied to the gauge field in the fermionic part of the action in our simulations of SU(2)-SYM to reduce the fluctuations of the gauge field and correspondingly the fluctuations of the eigenvalues of D_W , as explained in Sec. 3.3.

8.3.1. APE smearing

As the name suggests, APE smearing was developed by the APE collaboration [93]. It is used to smear the gauge field by adding to each gauge link its surrounding

8. Constructing variational bases and measuring correlation functions

Figure 8.3: Graphical representation of APE smearing



staples times a real smearing parameter ϵ_{APE} , see Fig. 8.3

$$U_i(x) \rightarrow U'_i(x) = U_i(x) + \sum_{j=\pm 1, j \neq i}^{\pm 3} \epsilon_{\text{APE}} U_j(x) U_i(x + \hat{j}) U_j^\dagger(x + \hat{i}). \quad (8.18)$$

Here the spatial smearing function is given, which is used in this work. It can be generalized to four dimensional smearing straightforwardly. The modified link $U'(x)$ is not necessarily an element of the gauge group any more. Therefore, it has to be projected back to the gauge group

$$\tilde{U}(x) = P_G U'(x), \quad (8.19)$$

where P_G represents the projector to the gauge group G . The projection is straightforwardly done by normalizing the first row of the matrix $U'(x)$ and then applying the Gram-Schmidt method to reconstruct the remaining rows.

By iterative application of the two smearing steps (Eqs. 8.18, 8.19), the gauge field is progressively smoothened. At the same time the smeared link becomes successively non-local, in the sense that it includes contributions from distant links. The number of smearing iterations N_{APE} , called smearing level, is the second parameter of APE smearing.

8.3.2. Jacobi smearing

In order to smear the fermion field λ , we use a modified version of the gauge invariant Jacobi smearing which has been developed by the Wuppertal group [94] and the UKQCD collaboration [95]. The idea is to use for the smearing function $F(\vec{x}, \vec{y})$ the three-dimensional scalar propagator $M^{-1}(\vec{x}, \vec{y})$

$$\lambda(x) \rightarrow \tilde{\lambda}(x) = \sum_{\vec{y}} F(\vec{x}, \vec{y}) \lambda(y) = \sum_{\vec{y}} M^{-1}(\vec{x}, \vec{y}) \lambda(y), \quad (8.20)$$

where M is given by

$$M_{ab}(\vec{x}, \vec{y}) = \delta_{\vec{x}, \vec{y}} \delta_{ab} - H_{ab}(\vec{x}, \vec{y}), \quad (8.21)$$

and the hopping matrix H is defined by

$$H_{ab}(\vec{x}, \vec{y}) = \kappa_J \sum_{i=1}^3 \left[\delta_{\vec{y}, \vec{x} + \hat{i}} V_{i,ab}(\vec{x}) + \delta_{\vec{y}, \vec{x} - \hat{i}} V_{i,ab}^\dagger(\vec{x} - \hat{i}) \right]. \quad (8.22)$$

Here, $V(\vec{x})$ are the gauge links in the adjoint representation (cf. Eq. 3.13). Since the smearing function is defined from the scalar propagator, the dependence on the Dirac indices is simply given by an overall factor of $\delta_{\alpha\beta}$ which is suppressed here. The smearing function $F(\vec{x}, \vec{y})$ is given by the solution of three-dimensional Klein-Gordon equation which can be constructed in the form of a power series

$$\sum_{\vec{y}'} M_{ab}(\vec{x}, \vec{y}') F_{bc}(\vec{y}', \vec{y}) = \delta_{\vec{x}, \vec{y}} \delta_{ac} \quad (8.23)$$

$$\Rightarrow F_{ab}(\vec{x}, \vec{y}) = \delta_{\vec{x}, \vec{y}} + \sum_{i=1}^{\infty} (H^i)_{ab}(\vec{x}, \vec{y}). \quad (8.24)$$

For small values of the hopping parameter κ_J this solution converges. However, in this case the spatial extent of the smearing function is small and many terms of the smearing function have to be calculated to obtain a good approximation. In fact, the sum does not have to converge to be used as a smearing function. In the Jacobi smearing method, one therefore uses a larger value of κ_J , outside of the convergent regime, and truncates the sum after N_J terms [95], where N_J is the smearing level.

It was already realized in [95] that fluctuations of the gauge field are enhanced and introduce unacceptably large noise when using large smearing levels. To overcome this issue, we use a procedure which we call *pre-smearing*. Instead of using the gauge links V in the hopping matrix H (Eq. 8.22), we use APE smeared gauge links \tilde{V} , as has also been done in [96]. \tilde{V} is obtained by applying APE smearing to the gauge links U in the fundamental representation and calculating \tilde{V} from the smeared gauge links \tilde{U} using Eq. 3.13. The hopping matrix defined from the smeared gauge links is labeled \tilde{H} .

Furthermore, we introduce an overall normalization factor C_J in order to suppress exponential growth of the smearing function which can lead to numerical issues in the calculations. The normalization factor cancels out in physical observables.

With these two modifications, the Jacobi smearing operator used in our invest-

8. Constructing variational bases and measuring correlation functions

igations is given by

$$F_{\alpha a, \beta b}(\vec{x}, \vec{y}) = (C_J)^{N_J} \delta_{\alpha\beta} \left(\delta_{\vec{x}, \vec{y}} + \sum_{i=1}^{N_J} (\tilde{H}^i)_{ab}(\vec{x}, \vec{y}) \right), \quad (8.25)$$

$$\tilde{H}_{ab}(\vec{x}, \vec{y}) = \kappa_J \sum_{i=1}^3 \left[\delta_{\vec{y}, \vec{x} + \hat{i}} \tilde{V}_{i,ab}(\vec{x}) + \delta_{\vec{y}, \vec{x} - \hat{i}} \tilde{V}_{i,ab}^\dagger(\vec{x} - \hat{i}) \right]. \quad (8.26)$$

To optimize the signal-to-noise ratio of the correlation functions, suitable values for the pre-smearing parameters ϵ_{APE} , N_{APE} and for the Jacobi smearing parameters κ_J , N_J and C_J have to be used. The systematical tuning of these parameters is discussed in detail in Sec. 9.1.

As explained in Sec. 8.2, the fermion fields in the correlation functions have to be Wick contracted before the correlation functions can be measured on the configurations, i.e. they are replaced by propagators D_W^{-1} . A short calculation shows (App. A.2) that smearing the fermion fields is equivalent to replacing the propagator D_W^{-1} with the smeared propagator

$$D_W^{-1} \rightarrow \tilde{D}_W^{-1} = F D_W^{-1} F^\dagger. \quad (8.27)$$

Since the Jacobi smearing operator is Hermitian $F^\dagger = F$, the Hermitian conjugation can be dropped.

8.4. Calculation of the propagators

The measurements of the meson and the gluino-gluon correlation functions require the determination of the propagator D_W^{-1} . While the Dirac-Wilson matrix D_W is sparse, its inverse D_W^{-1} is not. Furthermore, D_W^{-1} has

$$(\text{Volume} \times \text{Gauge components} \times \text{Dirac components})^2 = (L^3 \times T \times (N_c^2 - 1) \times 2)^2 \quad (8.28)$$

entries and quickly becomes very large for increasing lattice volumes. With current computing resources it is impossible to calculate all elements of D_W^{-1} or even to store the complete matrix in memory for reasonably large lattice volumes. Instead, in lattice QFT, correlators including fermion propagators are approximated by methods that rely on iterative solvers which numerically solve the linear equation

$$D_W |S_i\rangle = |S_o\rangle \quad (8.29)$$

$$\Rightarrow |S_i\rangle = D_W^{-1} |S_o\rangle. \quad (8.30)$$

$|S_o\rangle$ and $|S_i\rangle$ are called source and sink vectors, respectively and solving Eq. 8.29 numerically is called *inversion*. The inversions are the most computation-intensive part of lattice calculations. The iterative solvers repeatedly apply the matrix-vector multiplication $D_W |v\rangle$. Hence, to achieve a good performance it is important that

- $D_W |v\rangle$ is computed efficiently.
- The iterative solver is efficient, i.e. it needs as few matrix-vector multiplications as possible to converge. The convergence of iterative solvers depends crucially on the condition number of D_W (ratio of largest to smallest eigenvalue). The larger the condition number is, the more iterations are required by the solver. This effect is observed, in particular, when κ approaches κ_c .

In our investigations of SYM we use the well-established conjugate gradient (CG) solver for the inversion [97]. In order to speed up the matrix-vector multiplication $D_W |v\rangle$, we have, in the scope of this thesis, implemented a data structure that allows vectorized multiplications. This is discussed in App. A.1.

In the following, the methods to calculate the correlation functions by means of using the conjugate gradient solver are explained.

8.4.1. Connected piece

A short calculation shows that for the connected piece of the meson correlator it is sufficient to calculate the forward propagator $\text{Tr}[\Gamma\gamma_5 D_W^{-1}(x, y)]$ (see [52], Chap. 6 for a derivation)

$$C_{\text{conn}}(x, y) = \langle \text{Tr}[\Gamma(D_W^{-1})(x, y)\Gamma(D_W^{-1})(y, x)] \rangle = \left\langle \sum_{\alpha, a, \beta, b} |(\Gamma\gamma_5 D_W^{-1})^{\alpha, a, \beta, b}(x, y)|^2 \right\rangle. \quad (8.31)$$

Projecting to zero momentum (Eq. 7.12) leads to

$$C_{\text{conn}}(t) = \left\langle \sum_{\vec{x}, \alpha, a, \beta, b} |(\Gamma\gamma_5 D_W^{-1})^{\alpha a, \beta b}(x, y_0)|^2 \right\rangle. \quad (8.32)$$

Thus, the correlator is given by summing the absolute squares of the column entries of $\Gamma\gamma_5 D_W^{-1}$ for a fixed position $y = y_0$. These are in total $(N_C^2 - 1) \times 2$ columns (all combinations of color indices and Dirac indices).

The columns of D_W^{-1} can be calculated efficiently using so-called δ -sources with

8. Constructing variational bases and measuring correlation functions

fixed position y_0 , Dirac-index α_0 and color-index a_0

$$|S_0\rangle_M = \delta_{MN_0}, \quad (8.33)$$

where the multi-index notation $N_0 = (y_0, \alpha_0, a_0)$ was used. The sink $|S_i\rangle = D_W^{-1} |S_0\rangle$, which is obtained using the iterative solver, provides the column of D_W^{-1} with the multi-index N_0

$$(D_W^{-1})_{MN_0} = (D_W)_{MN}^{-1} \delta_{NN_0} = (D_W^{-1} |S_0\rangle)_M = |S_i\rangle_M. \quad (8.34)$$

Jacobi smearing can be included straightforwardly by replacing the propagator D_W^{-1} with the smeared propagator \tilde{D}_W^{-1}

$$(\tilde{D}_W^{-1})_{MN_0} = (F D_W^{-1} F^\dagger |S_0\rangle)_M. \quad (8.35)$$

Thus, the smeared propagator is calculated from a δ -source on which subsequently F^\dagger , D_W^{-1} and F are applied.

To calculate $C(t)$, a corresponding δ -source is inverted for all values of color and spin indices a_0, α_0 . The source position y_0 is arbitrary and in our investigations we choose a random position y_0 for each configuration. To increase the precision, one could also average over several source positions per configuration. Using one source position, the signal-to-noise ratio of the connected piece is usually already higher than the one for the disconnected piece of the correlator and we therefore use only one source position per configuration.

8.5. Disconnected piece and SET

For the disconnected piece of the meson correlator a different technique is needed than for the connected piece. The reason is that in the disconnected piece the sum for the zero momentum projection runs over the diagonal of the propagator

$$C_{\text{disc}}(t) = \left\langle \sum_{\vec{x}} \text{Tr}[\Gamma D_W^{-1}(x, x)] \text{Tr}[\Gamma D_W^{-1}(y_0, y_0)] \right\rangle, \quad (8.36)$$

which is very hard to compute. We therefore use the well-established *stochastic estimator technique* (SET) to approximate D_W^{-1} .

The idea of SET is to solve the Dirac equation on a set of source noise vectors

$|\eta^i\rangle$ fulfilling the relation

$$\frac{1}{N_S} \sum_i^{N_S} |\eta^i\rangle \langle \eta^i| = \mathbb{1} + \mathcal{O}\left(1/\sqrt{N_S}\right). \quad (8.37)$$

We use \mathbb{Z}_4 random complex numbers of the form $(\pm 1 \pm i)/\sqrt{2}$ for the entries of the noise vectors $|\eta^i\rangle$. Other choices are possible. The propagator D_W^{-1} is then approximated by

$$D_W^{-1} = \frac{1}{N_S} \sum_i^{N_S} |s^i\rangle \langle \eta^i| + \mathcal{O}\left(1/\sqrt{N_S}\right), \quad \text{with} \quad |s^i\rangle = D_W^{-1} |\eta^i\rangle, \quad (8.38)$$

and $|s^i\rangle$ is calculated using the conjugate gradient solver. To calculate the disconnected piece of the correlator, we first compute

$$D_{\Gamma, \text{Tr}}^{\text{SET}}(x^4) \doteq \frac{1}{N_S} \sum_{\vec{x}} \text{Tr} \left[\sum_i^{N_S} \Gamma |s^i\rangle \langle \eta^i| \right] \quad (8.39)$$

from a set of stochastic estimators and then calculate the disconnected piece via

$$C_{\text{disc}}(t) \approx \frac{N_S^2}{N_S^2 - N_S} \left(\langle D_{\Gamma, \text{Tr}}^{\text{SET}}(x^4) D_{\Gamma, \text{Tr}}^{\text{SET}}(y^4) \rangle - \frac{1}{N_S} C_{\text{conn}}(t)(1 - \delta_{t0}) \right),$$

where $t = x^4 - y^4$. The latter term and the prefactor correct a bias that is introduced because the same set of stochastic noise sources is used for both propagators. The bias correction is derived in detail in App. A.4.

Jacobi smearing can be included according to Eq. 8.27 by smearing the source and the sink vector in Eq. 8.38

$$\tilde{D}_W^{-1} \approx \frac{1}{N_S} \sum_{i, \vec{x}}^{N_S} F |s^i\rangle \langle \eta^i| F^\dagger. \quad (8.40)$$

8.5.1. Gluino-glue

The calculation of the gluino-glue correlator is rather similar to the calculation of the connected piece of the meson correlator. The main difficulty is to calculate

$$(D_W^{-1})_{xy}^{\alpha' a, \beta' b} \text{Tr}_c [F_{kl}^{\text{latt}}(y) T^b]. \quad (8.41)$$

For this purpose, we use a so-called wall-source, which means that not only one space-time point, but a whole time-slice (all sites for fixed value of y_0^4) is filled. It

8. Constructing variational bases and measuring correlation functions

is given by

$$(|S_0\rangle)_y^{\alpha a} = \text{Tr}_c [F_{kl}^{\text{latt}}(y) T^{a_0}] \delta^{\alpha\alpha_0} \delta_{y^4 y_0^4}. \quad (8.42)$$

The inversion is performed for each value of color and spin indices, a_0 and α_0 , similarly to the case of the δ -sources used in the calculation of the connected piece. Having inverted the sources, the gluino-gluon correlator $C_{\text{gg}}^{\alpha\beta}(x, y)$ can be calculated straightforwardly by evaluating Eq. 8.15.

Both, Jacobi and APE smearing can be applied to the gluino-gluon correlator. Jacobi smearing is implemented the same way as in the connected piece of the meson correlator (cf. Eq. 8.35). APE smearing can be applied to the gauge field in the field strength tensor F_{ij}^{latt} (cf. Eq. 3.27). In the scope of this thesis we use only APE smearing for the smearing of the gluino-gluon correlator which has turned out to be as effective as using Jacobi smearing or a combination of APE and Jacobi smearing [98].

8.6. Speeding up the inverter

The inversions are by far the most time-consuming part in lattice QFT calculations. Therefore, the lattice QFT community has spent considerable effort to find algorithms that reduce the computational effort and therefore speed up the inversions. In this work we use two of these techniques that can be combined efficiently, namely *even-odd preconditioning* and the *truncated eigenmode approximation*. In this section the details of these techniques are explained. Furthermore, we have restructured the data layout of our simulation code to utilize vector instructions, which is discussed in App. A.1.

8.6.1. Truncated Eigenmode approximation

For the determination of the mass spectrum and other observables, many different correlation functions are calculated. Hence, inversions of many different source vectors are performed. The truncated eigenmode approximation makes use of the fact that D_W does not change for a given gauge configuration. The idea is to calculate the N_E lowest eigenmodes of the Hermitian Dirac operator $\gamma_5 D_W$, given by its lowest eigenvalues λ_i and the corresponding eigenvectors $|v_i\rangle$, and use these to speed up all inversions. The computation of the eigenmodes is done efficiently using an accelerated Arnoldi algorithm as described in [84]. The propagator can be then approximated by

$$D_W^{-1} \gamma_5 \approx \sum_{i=1}^{N_E} \frac{1}{\lambda_i} |v_i\rangle \langle v_i|, \quad (8.43)$$

and D_W^{-1} can be obtained by multiplying this expression from the right with γ_5 .

The truncated eigenmode approximation becomes exact if all $N_E = V \times (N_c^2 - 1) \times 2$ eigenmodes are calculated, which is, however, impossible with current computing resources. Due to the factor λ_i^{-1} in Eq. 8.43, the lowest eigenmodes provide the largest contribution to the propagator and therefore truncating the sum to the lowest N_E eigenmodes could lead to a good approximation of D_W^{-1} .

The quality of the approximation, when used for the calculation of correlators, has to be studied individually for each correlator by comparing with other methods, e.g. with SET (cf. Sec. 8.5). In practice, we have found that the disconnected piece of the meson correlators converges only slowly with increasing N_E .

Therefore, the truncated eigenmode approximation is combined with the methods discussed in Secs. 8.4 to calculate the correlators. For this purpose, the source vectors $|S_0\rangle$ are projected to the subspace orthogonal to the lowest eigenmodes before the inversion

$$|S_{o\perp}\rangle = |S_o\rangle - \sum_{i=1}^{N_E} \langle v_i | \gamma_5 | S_o \rangle |v_i\rangle \quad (8.44)$$

and only $|S_{o\perp}\rangle$ is inverted. The sink vector is then given by

$$|S_i\rangle = D_W^{-1} |S_o\rangle = \sum_{i=1}^{N_E} \frac{1}{\lambda_i} |v_i\rangle \langle v_i | \gamma_5 | S_o \rangle + D_W^{-1} |S_{o\perp}\rangle . \quad (8.45)$$

For the disconnected piece this amounts to

$$D_W^{-1} \gamma_5 \approx \sum_{i=1}^{N_E} \frac{1}{\lambda_i} |v_i\rangle \langle v_i| + \frac{1}{N_S} \sum_{i=1}^{N_S} |s_{\perp}^i\rangle \langle \eta_{\perp}^i| \doteq \sum_{i=1}^{N_E+N_S} a_i |u_i\rangle \langle u'_i| . \quad (8.46)$$

The inversion of the projected source $|S_{o\perp}\rangle$ converges faster than the inversion of the original source because the condition number of D_W is effectively reduced by removing the lowest modes. Furthermore, the precision is increased in the disconnected piece because the contribution to the propagator from the lowest eigenmodes is computed exactly (up to the numerical precision of the computed eigenmodes) and only the remainder is approximated stochastically. For the investigations presented in this thesis we have used between 20 and 40 eigenmodes (depending on the used machine) which has turned out to be a good compromise between the cost of calculating the eigenmodes and the gained speed up.

8. Constructing variational bases and measuring correlation functions

8.6.2. Even Odd preconditioning

Even-odd preconditioning exploits the fact, that D_W contains only nearest neighbor interactions. By choosing a coordinate system, such that all coordinates are positive and indexing (idx) the sites of the lattice in a four dimensional checker-board pattern

$$\text{idx}(x^\mu) = \begin{cases} \lfloor 0.5(x^1 + x^2 L + x^3 L^2 + x^4 L^3) \rfloor, & \text{mod}(x^1 + x^2 + x^3 + x^4, 2) = 0 \\ \lfloor 0.5(L^3 + x^1 + x^2 L + x^3 L^2 + x^4 L^3) \rfloor, & \text{mod}(x^1 + x^2 + x^3 + x^4, 2) = 1 \end{cases}, \quad (8.47)$$

the lattice is decomposed into two sub-lattices; the so-called even sites are labeled by the lower half of the indices and the odd sites are labeled by the higher half of the indices. A lattice vector can then be written as

$$|v\rangle = \begin{pmatrix} v_e \\ v_o \end{pmatrix}, \quad (8.48)$$

where v_e contains the even and v_o contains the odd sites. In this basis the Dirac-Wilson matrix is written as

$$D_W = \begin{pmatrix} M_{ee} & M_{eo} \\ M_{oe} & M_{oo} \end{pmatrix}. \quad (8.49)$$

In the next step the D_W is factorized using the Schur complement technique into a product of lower triangular, diagonal, and upper triangular block matrices

$$D_W = LDU = \begin{pmatrix} \mathbb{1} & 0 \\ M_{oe}M_{ee}^{-1} & \mathbb{1} \end{pmatrix} \begin{pmatrix} M_{ee} & 0 \\ 0 & D_p \end{pmatrix} \begin{pmatrix} \mathbb{1} & M_{ee}^{-1}M_{eo} \\ 0 & \mathbb{1} \end{pmatrix}, \quad (8.50)$$

where the even-odd preconditioned Dirac-Wilson matrix D_p is given by

$$D_p = M_{oo} - M_{oe}M_{ee}^{-1}M_{eo}. \quad (8.51)$$

The inverse of the full Dirac-Wilson matrix D_W can be reconstructed from the preconditioned matrix D_p by

$$D_W^{-1} = U^{-1}D^{-1}L^{-1} = \begin{pmatrix} \mathbb{1} & -M_{ee}^{-1}M_{eo} \\ 0 & \mathbb{1} \end{pmatrix} \begin{pmatrix} M_{ee}^{-1} & 0 \\ 0 & D_p^{-1} \end{pmatrix} \begin{pmatrix} \mathbb{1} & 0 \\ -M_{oe}M_{ee}^{-1} & \mathbb{1} \end{pmatrix}. \quad (8.52)$$

Thus, instead of D_W^{-1} , only M_{ee}^{-1} and D_p^{-1} have to be computed which is more efficient because the matrix D_p has only half the number of rows and columns as D_W and M_{ee} can be exactly inverted without much effort because it is diagonal in

8.6. Speeding up the inverter

the space-time components ($M_{ee}(x, y) \propto \delta_{xy}$). In fact, in the plain Wilson action without the clover term $M_{ee} = M_{oo} = \mathbb{1}$.

In order to simplify the smearing of D_W^{-1} in the estimation of the disconnected piece, we use the SET method with $N_S = 100$ stochastic sources to approximate M_{ee}^{-1} , which is computed very efficiently. For the disconnected piece, even-odd preconditioning is combined with the other methods by estimating D_p^{-1} using the truncated eigenmode approximation and SET

$$D_p^{-1}\gamma_5 = \sum_{i=1}^{N_E+N_S} a_i |u_i\rangle \langle u'_i| . \quad (8.53)$$

and inserting the result into Eq. 8.52, yielding

$$D_W^{-1}\gamma_5 \approx \begin{pmatrix} M_{ee}^{-1}\gamma_5 + \sum_i a_i |w_i\rangle \langle w'_i| & \sum_i a_i |w_i\rangle \langle u'_i| \\ \sum_i a_i |u_i\rangle \langle w'_i| & \sum_i a_i |u_i\rangle \langle u'_i| \end{pmatrix} , \quad (8.54)$$

where the vectors $|w_i\rangle$ are related to the vectors $|u_i\rangle$ by

$$|w_i\rangle = -M_{ee}^{-1}M_{eo}|u_i\rangle \quad \Rightarrow \quad \langle w_i| = -\langle u_i|(M_{ee}^{-1}M_{eo})^\dagger = -\langle u_i|\gamma_5 M_{oe} M_{ee}^{-1}\gamma_5 , \quad (8.55)$$

and correspondingly for $|w'_i\rangle$ and $|u'_i\rangle$.

9. Optimizing the variational bases

In the previous Secs. 7 and 8 the procedures to extract the masses of bound states from the gauge ensembles are outlined. In order to get the best possible signal for the ground and the first excited states of the chiral supermultiplet with minimal computational effort, the relevant parameters have to be optimized. The tuning of these parameters is subject of the present section.

Our investigations are based on the variational method. The variational bases are constructed from different smearing levels of the interpolating operators defined in Sec. 8.1. For the 0^{++} and the 0^{-+} channels, two different types of operators are available for each channel: Glueball and meson interpolators (Eqs. 8.1, 8.2 and 8.4). Since the physical states are expected to be mixtures of glueball and meson states, it is sensible to use a combined basis of glueball and meson interpolating fields in these channels. For the spin- $1/2$ channel (gluino-glue) we consider only one type of interpolator (Eq. 8.6). Therefore, in this case, the variational basis consists of different smearing levels of the basic interpolator; for the investigations in the present section we consider the $C_1(t)$ correlator (cf. Sec. 8.2).

The optimization of the parameters is carried out as follows. In the first step, the smearing parameters are tuned to guarantee efficient smearing and a low noise level. Then, the dependency of the statistical fluctuations on the number of stochastic estimators, used for the estimation of disconnected piece of the meson correlator, is studied. Based on the optimized parameters, the choice of interpolators to be used in the variational bases is optimized. For this purpose, first, separate variational bases of only glueball, only meson, and only gluino-glue operators are considered and the influence of using different smearing levels is investigated. Then, also mixed bases of glueball and meson operators are taken into account.

The optimization of the methods is also described in our publication [30] and therefore the present section has some overlap with the cited reference. However, the tuning of the parameters is described in much more detail in this thesis.

9.1. Smearing parameters

Smearing is used to create extended operators from the local interpolating fields. The spatial extent of the smeared operators can be estimated by the so-called

smearing radius R_S . For the smearing function $F(x, y)$ it is defined as

$$R_S^2 = \frac{\sum_{\vec{x}} |\vec{x}|^2 |F(\vec{x}, 0)|^2}{\sum_{\vec{x}} |F(\vec{x}, 0)|^2}. \quad (9.1)$$

In order to generate interpolating operators that have large overlaps with the physical states, it is reasonable to choose smearing radii that are not much larger than the size of the states' wave functions, which can be estimated by the Compton wavelengths. The proton of QCD, for example, has a Compton wavelength of $\lambda^{(p)} \simeq 1.321$ fm and a (charge-)radius of $r^{(p)} \simeq 0.88$ fm [6] (when measured from electron scattering). The minimal bound state masses in our investigations, excluding the a - π , which is not a physical particle, are given by $am_{\min} \simeq 0.2$ (see Tabs. A.1, A.3, A.4 in App. A.6). Using this value, the maximal radius to be used is approximately given by

$$R_S \lesssim 1/m_{\min} \simeq 5a. \quad (9.2)$$

9.1.1. APE smearing

APE-smearing, used for smearing the gluon field, has two parameters. The strength of the smearing steps is modulated by ϵ_{APE} and the number of smearing steps is given by the smearing level N_{APE} . The tuning of ϵ_{APE} is not performed in the scope of this thesis. Instead, we use standard values which have also been used in previous investigations [42], [98]

$$\epsilon_{\text{APE}} = \begin{cases} 0.4 & \text{for smearing gluino-gluon interpolators} \\ 0.5 & \text{otherwise} \end{cases}. \quad (9.3)$$

The smearing radius gives a hint for suitable values for N_{APE} . There are different estimates for R_S as a function of ϵ_{APE} and N_{APE} . Demmouche [81] proposed ¹

$$R_{\text{APE}}^{\text{Dem.}} = \sqrt{N_{\text{APE}} \epsilon_{\text{APE}}} a, \quad (9.4)$$

whereas Bernard and DeGrand proposed an estimate for the smearing radius that is smaller by a constant factor $R_{\text{APE}}^{\text{B.D.}} = R_{\text{APE}}^{\text{Dem.}}/\sqrt{3}$ [99]. For the gluon field we use smearing levels up to $N_{\text{APE}} = 80$, which results in estimated smearing radii $R_{\text{APE}}^{\text{Dem.}} \simeq 6.3a$ and $R_{\text{APE}}^{\text{B.D.}} \simeq 3.7a$. Hence, Eq. 9.2 is approximately fulfilled. For the gluino-gluon, smearing levels up to $N_{\text{APE}} = 95$ are considered due to the smaller

¹In the reference [81], the definition of the smearing radius is missing a square root. This has been corrected here, resulting in the square root in Eq. 9.4.

9. Optimizing the variational bases

value of ϵ_{APE} in this case.

9.1.2. Jacobi smearing

Jacobi smearing has more parameters than APE smearing due to the additional pre-smearing. The tuning of the parameters cannot be done independently for each parameter since the optimal value for one parameter might change, when the other parameters are varied. Therefore, the parameters are tuned in a hierarchical order, readjusting the parameters in between. The order is given as follows.

1. The smearing parameters κ_J and N_J have the largest influence on the smearing function since κ_J determines whether the smearing function is in the convergent or divergent regime (cf. Sec. 8.3.2) and N_J regulates how much smearing is applied and has therefore direct influence on the smearing radius. Furthermore, it is expected that the pre-smearing procedure has only minor influence on the smearing radius since it smoothens fluctuations, but does not drastically change the gauge links. The first step is therefore to find suitable values of κ_J and N_J . This is done by studying the smearing radius R_s and the shape of the smearing functions. For this purpose, pre-smearing is switched off in this step and the normalization factor is set to $C_J = 1$.
2. Using the suitable values for κ_J and N_J , estimated in step 1, the pre-smearing parameter N_{APE} is tuned by studying the connected and disconnected pieces of the meson correlation functions. The parameter ϵ_{APE} is set to $\epsilon_{\text{APE}} = 0.5$ as discussed in Sec. 9.1.1.
3. The tuning of κ_J and the range for N_J are readjusted using the pre-smearing parameters determined in step 2.
4. The value of the normalization constant C_J is determined by studying the norm of the smearing function $\|F\|$. The other smearing parameters do not need to be readjusted because C_J is merely a normalization factor which does not change the effect of the smearing but only suppresses potential numerical issues.

The tuning is done on the basis of the SU(2)-SYM ensemble with the parameters $\beta = 1.75$, $\kappa = 0.14925$. This ensemble was chosen because it is situated in the center of the simulated parameter range, i.e. it has a medium lattice spacing and a medium value of the adjoint pion mass. The four tuning steps are explained in the following.

1. κ_J and N_J :

In order to find reasonable values for κ_J and N_J , we measured the smearing radius R_S for different values of κ_J and for smearing levels in the interval $N_J \in [0, 100]$.

As expected, R_S is a monotonously increasing function of the hopping parameter κ_J and of the smearing level N_J , see Fig. 9.1. Furthermore, the convergence behavior of the smearing function becomes apparent: For $\kappa_J < 0.2$ the smearing radius approaches rather small constant values ($R_s < 1a$) with increasing values of N_J . For $\kappa_J \geq 0.2$ the smearing radius does not approach constant values within the interval $N_J \in [0, 100]$. We conclude that the critical value of κ_J that separates the convergent and the divergent regime is $\kappa_{J,\text{crit.}} \approx 0.2$. A precise estimation of $\kappa_{J,\text{crit.}}$ is not needed here.

Interestingly, the dependence of the smearing radius on κ_J is small, as long as κ_J is sufficiently larger than $\kappa_{J,\text{crit.}}$ (see $\kappa_J = 0.25, \kappa_J = 0.3$ in Fig. 9.1). The smearing radii are $R_S < 5a$ for all considered smearing levels N_J and hence the parameter range $N_J \in [0, 100]$ is appropriate according to Eq. 9.2. In Fig. 9.2 the norm of the smearing function

$$\|F(x, 0)\| \doteq \text{Tr}[F(x, 0)F^\dagger(x, 0)] \quad (9.5)$$

is shown in the x^1 - x^2 plane for a fixed smearing level $N_J = 40$ and varying values of κ_J . It is noticeable that the overall shape (envelope) of the smearing function does not depend much on κ_J as long as κ_J is in the divergent regime. This is consistent with the observation that the smearing radius depends only mildly on κ_J in this regime. However, for increasing values of κ_J , spikes appear in $\|F(x, 0)\|$ because $\|F(x, 0)\|$ grows in an alternating pattern with the number of smearing levels. Even smearing levels contribute only to the even sites and odd smearing levels contribute only to the odd sites in $\|F(x, 0)\|$, see Fig. 9.3. This can be explained by the hopping nature of the Jacobi smearing kernel $H(\vec{x}, \vec{y})$ (Eq. 8.22), which in each step connects neighboring sites. In odd smearing iterations only odd sites are connected to the even site $y = 0$ and thus contribute to $\|F(x, 0)\|$ and similarly in even iterations only even sites contribute. Since in the divergent regime the smearing function grows exponentially with N_J , the contributions to the even or to the odd sites from each smearing levels are so large that they overshoot the smearing function of the previous smearing level, causing spikes. This effect increases for increasing values of κ_J .

The wave functions of the low lying states are expected to be smooth and not spiky. Thus, we prefer a value of κ_J that is just above $\kappa_{J,\text{crit}}$ rather than a larger value of κ_J . The smearing radius can then be controlled by the parameter N_J .

9. Optimizing the variational bases

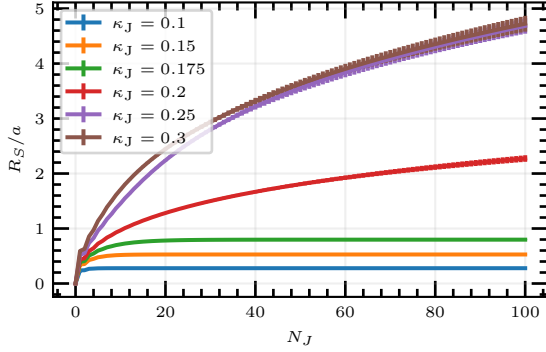


Figure 9.1.: Smearing radius as a function of κ_J and N_J for the ensemble SU(2) $\beta = 1.75$, $\kappa = 0.14925$, no pre-smearing was used.

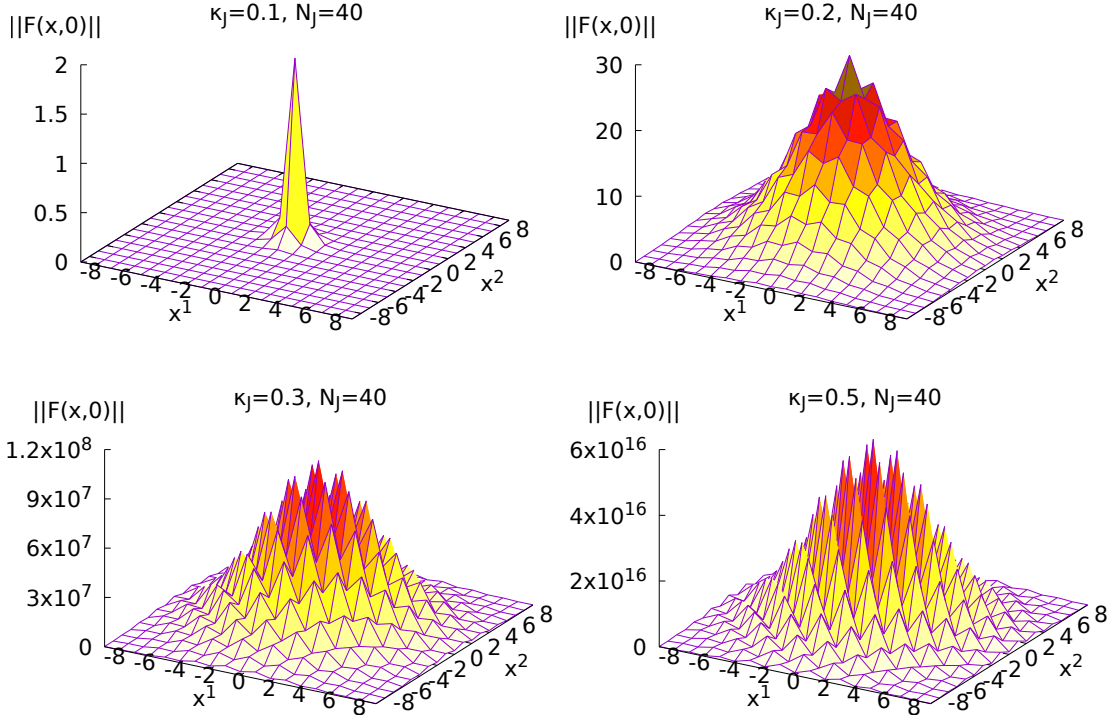


Figure 9.2.: Smearing functions for different values of the smearing parameter κ_J (see legend) and fixed smearing level $N_J = 40$, pre-smearing was enabled ($N_{\text{APE}} = 20$, $\epsilon_{\text{APE}} = 0.5$); a corresponding plot for the case of disabled pre-smearing is very similar. For increasing κ_J the smearing function develops sharp spikes while the overall shape (envelope) is similar. The smearing function was not normalized ($C_J = 1$). The SU(2)-SYM ensemble $\beta = 1.75$, $\kappa = 0.14925$ was used.

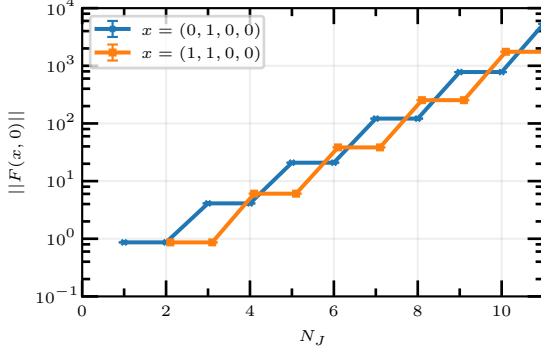


Figure 9.3: Every odd smearing step contributes only to the odd sites and every even smearing step contributes only to the even sites. This is shown here for the odd site $x = (0, 1, 0, 0)$ and for the even site $x = (1, 1, 0, 0)$ using pre-smeared, non-normalized Jacobi smearing with $\kappa_J = 0.5$. The SU(2)-SYM ensemble $\beta = 1.75$, $\kappa = 0.14925$ was used.

2. Pre-smearing parameter N_{APE}

The next step is to tune the pre-smearing parameter N_{APE} . First tests indicated that $\kappa_{J,\text{crit.}}$ is lowered slightly when pre-smearing is enabled. We therefore chose a value of $\kappa_J = 0.2$ for the tuning of the pre-smearing parameter, which for all considered pre-smearing levels $1 \leq N_{\text{APE}} \leq 160$ is large enough to assure a smearing radius $R_S > 4a$ at $N_J = 100$. Furthermore, the normalization is set to $C_J = 0.9$ in this step.

To investigate the noise suppression of the pre-smearing technique, the correlation functions of the scalar meson $a\text{-}f_0$ and the pseudoscalar meson $a\text{-}\eta'$ are studied using different pre-smearing levels N_{APE} . The noise is determined by means of the Jackknife error estimate of the correlation function averaged over the t -interval $t \in [3, 10]$, which is the relevant interval for the extraction of the masses

$$\langle \Delta C \rangle \doteq \frac{1}{8} \sum_{t=3}^{10} C(t). \quad (9.6)$$

The noise of the $a\text{-}f_0$ correlator grows with N_J if no pre-smearing is applied, especially in the disconnected piece (see Fig. 9.4). The noise is suppressed when using pre-smearing with pre-smearing levels in the interval $N_{\text{APE}} \in [10, 80]$. The results are not very sensitive to the value of N_{APE} and values of N_{APE} between 10 and 80 all lead to comparable noise suppression. For larger values of N_{APE} the signal degrades again.

The $a\text{-}\eta'$ correlator is less affected by noise stemming from Jacobi smearing at large smearing levels N_J . Using pre-smearing does not significantly suppress this noise (see Fig. 9.5). However, when pre-smearing is used, Jacobi smearing more effectively suppresses excited state contributions to the $a\text{-}\eta'$ correlator. Again, the results are not very sensitive to the exact value of N_{APE} as long as it is in a suitable range $N_{\text{APE}} \in [10, 80]$. Considering both correlators ($a\text{-}f_0$ and $a\text{-}\eta'$), we choose the smearing level $N_{\text{APE}} = 20$ for our investigations, as it appears to be a good choice

9. Optimizing the variational bases

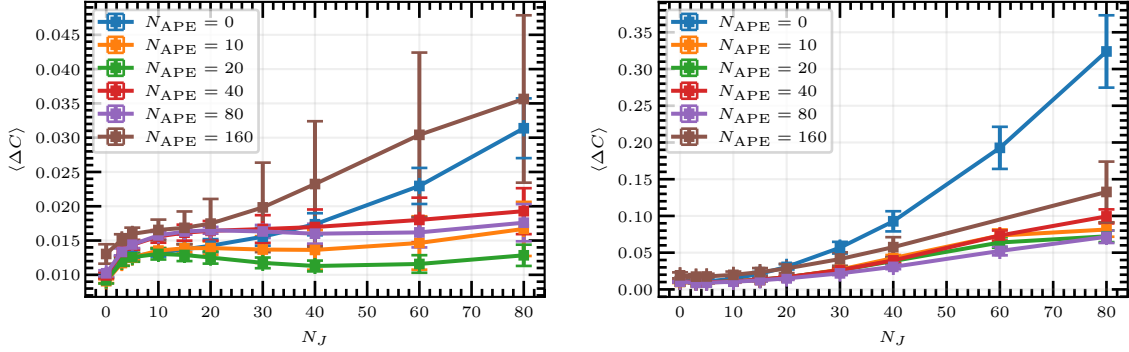


Figure 9.4.: Jackknife-error of the full a - f_0 correlator (left) and of the disconnected piece (right) averaged over the interval $t \in [3, 10]$ and plotted against N_J using different pre-smearing levels N_{APE} . Larger Jacobi smearing levels lead to large statistical uncertainties (blue). Using pre-smearing suppresses those significantly. The SU(2)-SYM ensemble $\beta = 1.75$, $\kappa = 0.14925$ was used. A similar figure has been published in [30].

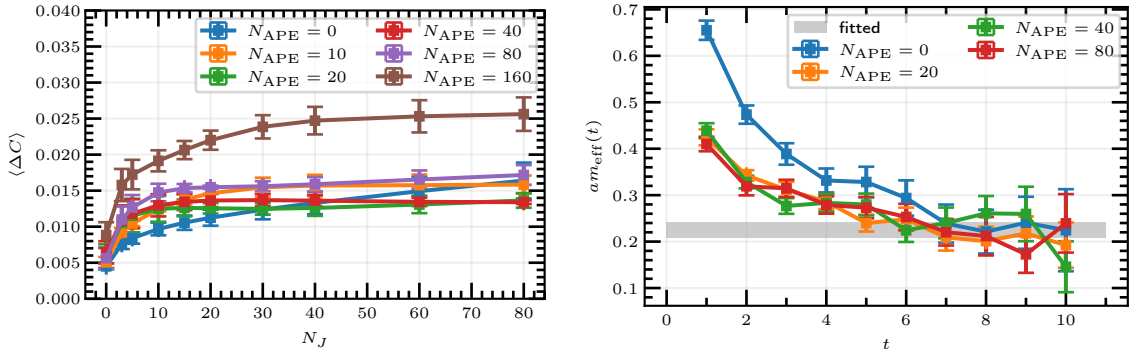


Figure 9.5.: Left: Jackknife-error of the a - η' correlator averaged over the interval $t \in [3, 10]$ and plotted against N_J using different pre-smearing levels N_{APE} . Right: Effective mass of the a - η' correlator using different pre-smearing levels N_{APE} . The Jacobi smearing level is fixed to $N_J = 20$. When pre-smearing is applied, excited state contributions are more effectively suppressed compared to not using pre-smearing (blue). The SU(2)-SYM ensemble $\beta = 1.75$, $\kappa = 0.14925$ was used. A similar figure has been published in [30].

for suppressing noise and excited state contributions.

As an additional test, we have also tested Stout smearing instead of APE smearing. It did not improve the noise suppression further and we therefore stay with APE pre-smearing.

3. Re-tuning κ_J and N_J :

In this third step, suitable ranges of N_J are determined and we verify whether the previously used value of $\kappa_J = 0.2$ needs to be modified when the pre-smearing parameter is set to the optimal value $N_{\text{APE}} = 20$. For this purpose, the smearing functions and the smearing radius are studied on five different ensembles of different simulation parameters κ and β , including SU(2)-SYM and SU(3)-SYM ensembles. The considered ensembles are listed in the legend of Fig. 9.6. We find that for all of the five ensembles the critical value κ_J is $\kappa_{J,\text{crit}} \approx 0.175(20)$ and thus $\kappa_J = 0.2$ is in the divergent regime for all of these ensembles. Apparently, in the simulated parameter range the value of $\kappa_{J,\text{crit}}$ depends only very mildly on the simulation parameters N_c , β and κ . This is also apparent from the smearing radius, plotted as a function of N_J , which is very similar for the tested ensembles, see Fig. 9.6. Furthermore, with $\kappa_J = 0.2$ the smearing function develops only minor wrinkles and no sharp spikes (see Fig. 9.7). We therefore stay with this value of κ_J .

Concerning the smearing levels we consider smearing levels up to $N_J = 80$ which provides smearing radii $R_S < 6a$, which is approximately in accordance with Eq. 9.2.

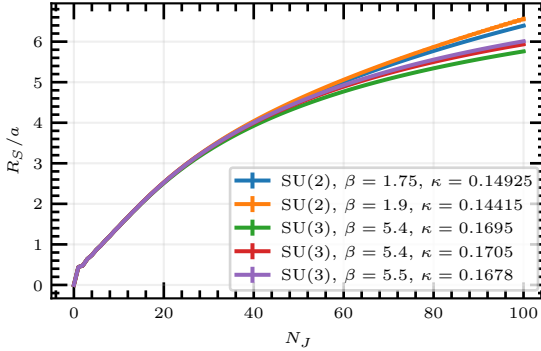


Figure 9.6: Smearing radius for fixed $\kappa_J = 0.2$ as a function of N_J for different ensembles. The pre-smearing parameters are $N_{\text{APE}} = 20$, $\epsilon_{\text{APE}} = 0.5$.

9. Optimizing the variational bases

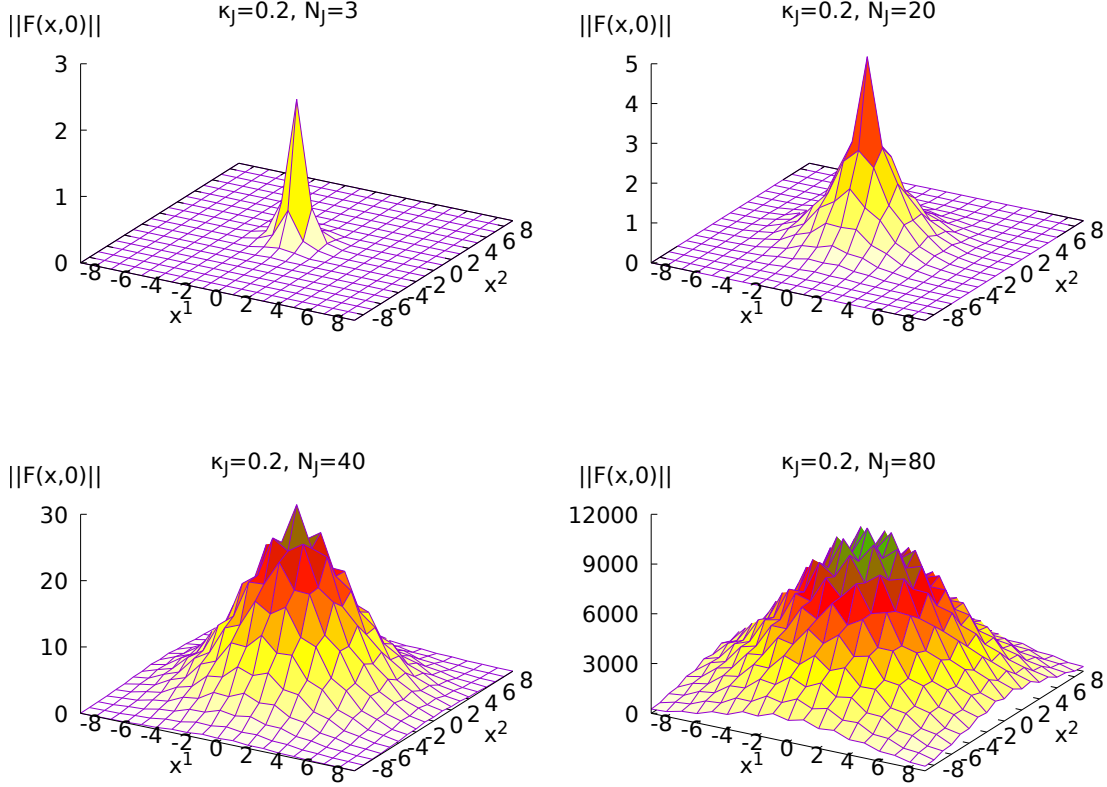


Figure 9.7.: Smearing functions for fixed value of the smearing parameter $\kappa_j = 0.2$ and different smearing levels N_J (see legend), pre-smearing was enabled ($N_{\text{APE}} = 40$, $\epsilon_{\text{APE}} = 20$). The smearing function was not normalized ($C_J = 1$). The SU(2)-SYM ensemble $\beta = 1.75$, $\kappa = 0.14925$ was used.

4. C_J

As a final step, the normalization constant C_J needs to be determined, so that exponential growth of the correlators for large values of N_J is avoided. For this purpose, we calculate $\|F\|$ for different smearing levels using stochastic noise vectors $|\eta\rangle$ similarly to the SET method explained in Sec. 8.5

$$\|F\|^2 = \text{Tr} [F^\dagger F] \approx \sum_i \text{Tr} [F |\eta^{(i)}\rangle \langle \eta^{(i)}| F^\dagger] = \sum_i \|F |\eta^{(i)}\rangle\|^2, \quad (9.7)$$

where the trace runs over Dirac and color indices and over all lattice sites. Already a single noise vector evaluated on five gauge configurations provides a very precise estimate of $\|F\|$ (see Fig. 9.8). $\|F\|$ grows close to exponentially with the smearing

level N_J . We therefore determine C_J by a fit to $\|F\|$ in the interval $N_J \in [10, 100]$ using the fit function

$$f(N_J) = aC_J^{-N_J}. \quad (9.8)$$

The region $t < 10$ is excluded from the fit since $\|F\|$ is not exactly exponential and the normalization is more important for larger smearing levels where the smearing function grows rapidly if not normalized. The fit returns the parameters

$$a \approx 4.6 \cdot 10^6, C_J \approx 0.87. \quad (9.9)$$

When $C_J = 0.87$ is used in the Jacobi smearing, $\|F\|$ stays within the same order of magnitude in the interval $N_J \in [0, 100]$. Thus, the smearing function is successfully normalized. Since, as discussed above, the smearing function does not change drastically, when other values of the simulation parameters β , κ , N_c are considered, we use $C_J = 0.87$ throughout all our investigations.

In summary the optimized Jacobi smearing parameters are given by

$$\kappa_J = 0.2, \quad C_J = 0.87, \quad \epsilon_{\text{APE}} = 0.5, \quad N_{\text{APE}} = 20. \quad (9.10)$$

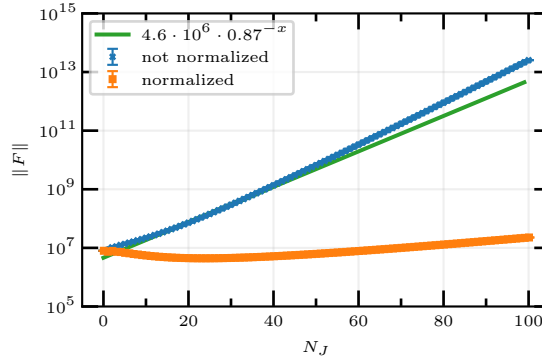


Figure 9.8.: $\|F\|$ as a function of N_J . Each data point is evaluated from five independent gauge configurations of the SU(2)-SYM ensemble $\beta = 1.75$, $\kappa = 0.14925$ using one stochastic noise vector. The error bars are too small to be visible. The data obtained from non-normalized smearing ($C_J = 1$) is plotted in blue. It was fitted in the interval $N_J \in [10, 100]$ using the functional form $f(N_J) = aC_J^{-N_J}$. The fitted function is displayed in green. The orange data points show $\|F\|$ obtained from normalized smearing with the normalization factor $C_J = 0.87$.

9.2. Number of stochastic estimators

After the optimized Jacobi smearing parameters have been determined, the number of stochastic estimators N_S , used for the estimation of the disconnected pieces of the meson correlators, can be optimized. For this purpose, we normalize the disconnected pieces $C_{\text{disc}}(t = 1) = 1$ and consider the averaged Jackknife error estimates of $\langle \Delta C_{\text{disc}} \rangle$ similarly as in step 2 of Sec. 9.1.2.

We have estimated the dependence of $\langle \Delta C_{\text{disc}} \rangle$ on N_S using every fourth configuration of our SU(2)-SYM test ensemble with the parameters $\beta = 1.75$, $\kappa = 0.14925$. We find that higher smearing levels require less stochastic estimators, see Fig. 9.9, and the scalar correlator requires more stochastic estimators than the pseudoscalar one. At around 20 stochastic estimators the error is dominated by the gauge noise (the stochastic error is smaller than 15 % of the gauge noise) for all tested smearing levels except for the unsmeared scalar correlator.

Thus, at the level of our statistics, it is sufficient to use 20 stochastic estimators. For the investigations in the scope of this thesis we stayed, however, with the more conservative choice of

$$N_S = 40. \quad (9.11)$$

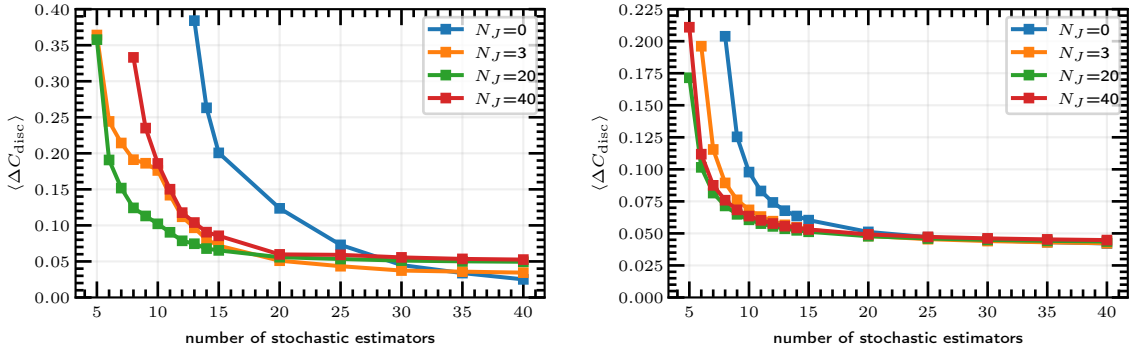


Figure 9.9.: Jackknife error estimates of the disconnected piece averaged over $t \in [3, 10]$ for the scalar (left) and the pseudoscalar (right) meson as a function of the number of stochastic estimators. The statistical uncertainties stemming from the stochastic estimation decrease quickly with an increasing number of stochastic estimators. At around 20 stochastic estimators, the statistical uncertainties approach plateaus. The plateau values represent the gauge noise, stemming from the fluctuations of the gauge field in the ensemble. The disconnected pieces are normalized to 1 at $t = t_0$. A similar figure has been published in [30].

9.3. Optimizing the variational operator bases

In the previous sections, the systematic optimization of the parameters for the smearing techniques and the stochastic estimator technique are discussed. Using the optimal parameters, the next step is to systematically optimize the operator bases of the variational method. Our approach is to construct the operator bases from different smearing levels of the basic interpolating operators.

The optimization is done in three successive steps.

1. To identify the most relevant smearing levels for each interpolating operator, only the minimal choice of smearing levels is considered, i.e. only single smearing levels for the determination of the ground state and two smearing levels for the determination of the excited state.
2. For each basic interpolating operator, variational bases of several different smearing levels are investigated.
3. In the scalar and pseudoscalar channel, mixed variational bases consisting of both, smeared glueball and smeared meson operators are studied.

The three steps are discussed in detail in the following sections.

For the optimization we consider gluino-gluon and meson interpolating operators with the smearing levels $N_S \in \{0, 5, 15, \dots, 95\}$ and glueball interpolating operators with the smearing levels $N_{APE} \in \{8, 16, \dots, 48\}$, where N_S represents N_{APE} in the case of the gluino-gluon and N_J in the case of the mesons. The maximal smearing level of the glueball operators considered here is smaller than suggested in Sec. 9.1.1. The reason is that while we have measured the meson correlators specifically for this analysis, the glueball correlation functions have already been measured in the scope of previous investigations [26] and we reanalyze those correlation functions here. The considered smearing levels are still large enough to get an impression which smearing levels are relevant. In the case of the gluino-gluon, an investigation of the smearing levels has already been done in [98]. In order to get a complete picture of all three channels of the chiral multiplet, we reanalyze the gluino-gluon correlation functions of the SU(2)-SYM ensemble $\beta = 1.9$, $\kappa = 0.14415$ that have been measured in the scope of the previous analysis. The investigations of the glueball and meson smearing levels are based on the SU(2)-SYM ensemble with the parameters $\beta = 1.75$, $\kappa = 0.14925$, which is also used in Sec. 9.1.2.

9. Optimizing the variational bases

9.3.1. Single Smearing Levels

The first step of the systematic optimization is to consider only single smearing levels for the estimation of ground states. To judge the quality of the interpolation by the smeared operators, we study the effective masses of the corresponding correlators at fixed time distances t . The effective mass at small values of t is expected to be smaller, the stronger higher excited states are suppressed. To find the smearing level for each operator that optimally interpolates the ground state, we therefore search for the minimum of the effective mass when the smearing level is varied. In addition, the noise level of the optimal smearing level should be low, i.e. the effective mass should have a small statistical uncertainty.

Except for the case of the $a\text{-}f_0$, the effective masses of all studied correlators decrease monotonically with increasing smearing level, while their errors stay almost constant (in the case of the 0^{-+} glueball, the noise even reduces for increasing smearing level), see Figs. 9.10, 9.11, 9.12. This suggests that in these cases, the largest considered smearing levels are optimal because they provide the strongest suppression of higher excitations, while featuring a low noise level. In fact, the analysis indicates that even larger smearing levels could provide an even better signal. However, in the scope of this thesis we have not considered larger smearing levels because the smearing radii are already quite large for the smearing levels considered here (cf. Secs. 9.1.1, 9.1.2). The effective mass calculated from $a\text{-}f_0$ correlator shows a minimum around $N_J = 25$, also its uncertainty is minimal here.

The corresponding analysis for the first excited states requires to use at least two operators, i.e. two smearing levels, in the variational approach. Thus, for the first operator we assign the smearing level that has been found to be optimal for the ground state and vary the smearing level of the second operator. The effective mass of the first excited state is then calculated from the corresponding eigenvalue of the GEVP.

Similarly to the study of the ground states, we observe monotonously decreasing effective masses with increasing smearing levels, see Figs. 9.10, 9.11, 9.12. The uncertainties of the effective masses are almost constant except for the case of the glueball operators where the uncertainties grows rather strongly with increasing smearing level. This increased noise could have two reasons. Either the additional noise is a direct consequence of using large smearing levels, or the two used smearing levels are too similar and a large difference between the two used smearing levels is favored (the smearing level of the first operator was set to the maximal choice $N_{\text{APE}} = 48$ and, hence, it might be favorable if the smearing level of the second operator is small). This is further investigated in Sec. 9.3.2.

9.3. Optimizing the variational operator bases

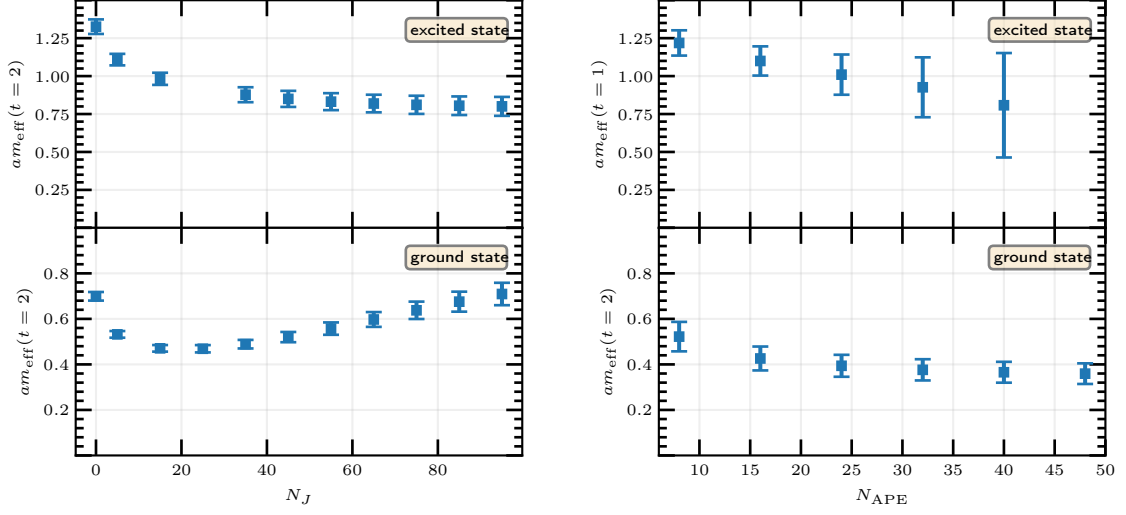


Figure 9.10.: Effective masses at fixed t of ground and first excited state in the 0^{++} channel. Left: $a-f_0$ correlator, Right: Glueball correlator. For the ground state, only single smearing levels were used (abscissa), whereas for the first excited state two different smearing levels were used and one of the two smearing levels was set to the optimal smearing level of the ground state ($N_J = 25$ for the $a-f_0$ -correlator and $N_{\text{APE}} = 48$ for the glueball-correlator), the other smearing level is labeled at the abscissa.

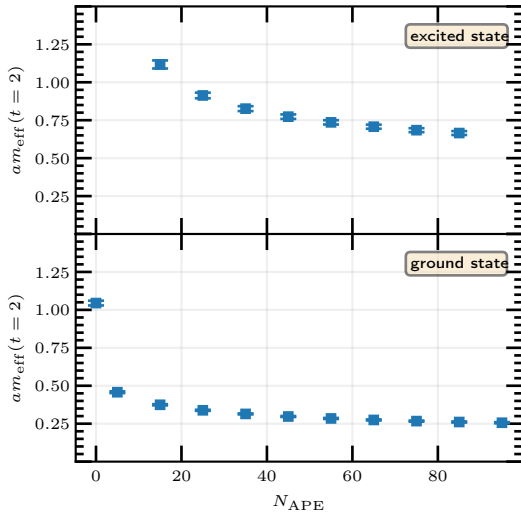


Figure 9.11: Similar plot for the gluino-gluon channel as in Fig. 9.10. The optimal smearing level of the ground state is $N_{\text{APE}} = 95$.

9. Optimizing the variational bases

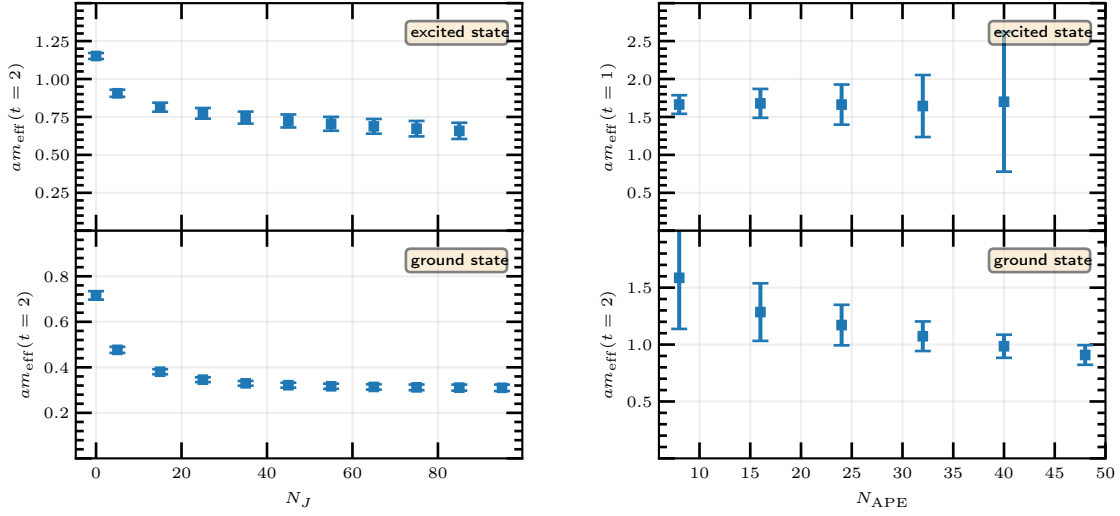


Figure 9.12.: Similar plots for the 0^{-+} channel as in Fig. 9.10. Left: $a\text{-}\eta'$ correlator, Right: Glueball correlator. The optimal smearing level of the ground states are $N_J = 95$ for the $a\text{-}\eta'$ -correlator and $N_{\text{APE}} = 48$ for the glueball-correlator.

9.3.2. Combining several smearing Levels

In the present section, combinations of different smearing levels are studied to find the optimal ones for each basic interpolator. Mixed operator bases of glueball and meson operators for the analysis of the scalar and the pseudoscalar channels are subject of Sec. 9.3.3.

In principle, it is expected that the interpolation of the physical states is improved with every additional operator in the GEVP. However, each additional operator typically requires to measure further correlation functions and thus increases the computational cost. In particular, for the gluino-glue correlator and for the connected piece of the meson correlator, every considered smearing level requires the inversions of the smeared sources (cf. Secs. 8.4.1, 8.5.1). If the additional information of the new operator is small, it might be better to spend the computing time elsewhere, e.g. to increase the statistics. Furthermore, stability problems may arise if too many operators are considered in the GEVP. Two such problems are discussed in Secs. 11.1 and 11.4. For these reasons, it is desirable to find a small set of smearing levels for each channel, which includes the most relevant operators and hence allows efficient and precise estimations of the bound state masses.

To find these optimal combinations of smearing levels we systematically choose different subsets of the sets of smeared operators that are also studied in the

9.3. Optimizing the variational operator bases

previous Sec. 9.3.1.

For each number n of operators we consider the following sets:

1. Small smearing levels: Only the smallest n smearing levels of the full set are taken into account.
2. Large smearing levels: Only the largest n smearing levels of the full set are taken into account.
3. Uniformly distributed: Out of the full set, the smallest and the largest smearing levels and $n - 2$ additional smearing levels, uniformly distributed in between, are taken into account.
4. Mid-large, uniformly distributed: Out of the full set, a medium and the largest smearing level, and $n - 2$ additional smearing levels, uniformly distributed between them, are considered. For the medium smearing level we choose $N_{\text{APE}} = 35$ for the gluino-gluon and the $a\text{-}\eta'$ operators, and $N_{\text{APE}} = 24$ for the glueball operators. For the $a\text{-}f_0$ operator we choose $N_J = 25$ for the medium level because the analysis of the previous Sec. 9.3.1 suggests that this smearing level is optimal for the ground state.

Similarly to the analysis in Sec. 9.3.1, we employ the effective masses of the lowest two states at fixed time distances t to judge the quality of the interpolation. The results for the two lowest eigenvalues of the GEVP are shown in Figs. 9.13, 9.14 and 9.15 together with the best estimate for the masses obtained by fitting the eigenvalues using the optimal choice of interpolating operators. The dependency of the effective masses on the smearing levels is mostly similar for all five interpolators: Considering the set of smallest smearing levels obviously leads to unwanted contributions of higher excitations so that the effective masses at small t are significantly higher than the best estimate. Using only the largest smearing levels leads to the strongest suppression of these excited state contributions. The uniformly distributed subsets also suppress excited state contributions, but not quite as much as the large smearing levels. Furthermore, with the exception of the glueball interpolators, the error of the effective masses is almost constant for the different combinations of the smearing levels.

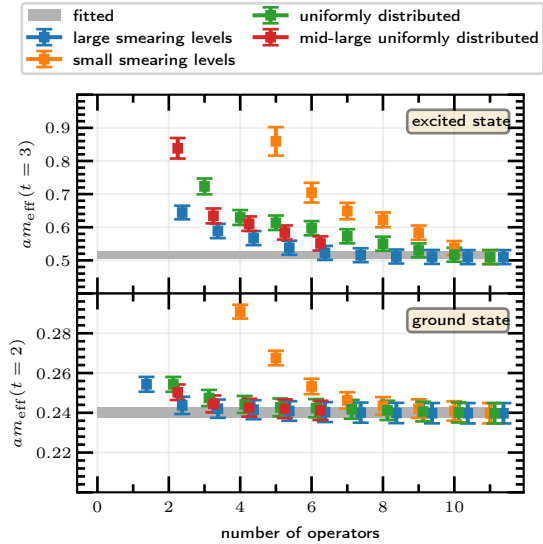
Hence, using a set of rather large smearing levels for the mass estimations generally appears to be the optimal choice. With this choice, even a few operators seem to interpolate the states efficiently and additional smearing levels do not lower the effective mass further. The optimal number of different smearing levels depends on the interpolator and the physical state to be analyzed. While for the ground states typically 2-3 different smearing levels seem to be optimal, some of the excited states (gluino-gluon, $a\text{-}\eta'$) benefit from up to six different operators. The fact

9. Optimizing the variational bases

that the largest smearing levels are optimal even for the ground state estimated from the $a\text{-}f_0$ interpolator is a bit surprising in view of the result from Sec. 9.3.1 where a medium smearing level $N_J \approx 25$ was found to be optimal.

The effective masses from the glueball operators become very noisy with increasing number of interpolating operators. In the case of the first excited states of the pseudoscalar glueball correlator, the set of uniformly distributed smearing levels seems to be better suited than the set of large smearing levels as it leads to smaller statistical fluctuations and a lower effective mass. However, this state appears to be significantly heavier than the other considered states and it is therefore not investigated further. The excited state of the scalar channel cannot be extracted reliably from the glueball interpolators because the signal is too noisy.

Figure 9.13: Effective masses at fixed values of t of the ground and first excited state of the gluino-gluon channel using the different sets of interpolating operators described in Sec. 9.3. The final result of the fit to the eigenvalues is shown for comparison. For better visualization, small offsets have been used in the abscissa for the different sets. A similar figure has been published in [30].



9.3. Optimizing the variational operator bases

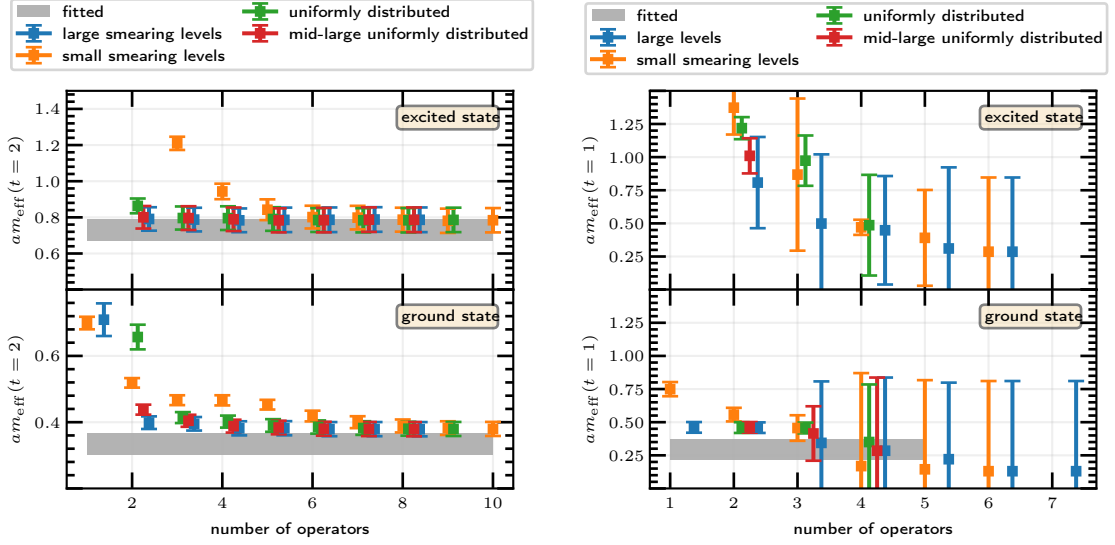


Figure 9.14.: Similar plots for the 0^{++} channel as in Fig. 9.13. Left: $a-f_0$ interpolators. Right: Glueball interpolators. A similar figure has been published in [30].

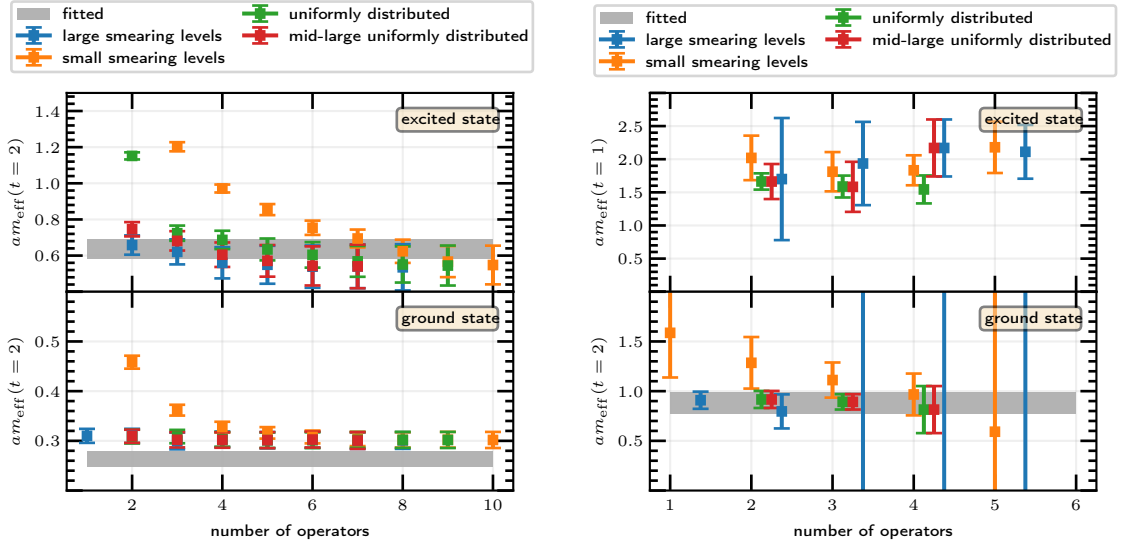


Figure 9.15.: Similar plots for the 0^{+-} channel as in Fig. 9.13. Left: $a-\eta'$ interpolators. Right: Glueball interpolators. A similar figure has been published in [30].

9. Optimizing the variational bases

9.3.3. Mixed operator bases

In the previous section only variational bases from different smearing levels of single basic interpolating operators are considered. As discussed in Sec. 2.3.2, earlier investigations [28] suggest that in the pseudoscalar channel the ground state seems to be rather meson-like, i.e. it has only a very small glueball component, whereas there is considerably large mixing in the ground state of the scalar channel between glueball and meson states. Such mixed physical states are expected to be best interpolated by extended operator bases consisting of both, glueball and meson interpolators in the variational method. This extended variational approach serves two purposes. Firstly, due to the better interpolation of the physical states, cleaner signals are expected, which consequently improves the precision of the computed masses. Secondly, using mixed operator bases in the variational method allows to investigate quantitatively how much mixing is present in the physical states. The present section focuses on the optimization of the variational bases to obtain clean signals for the extraction masses in the scalar and in the pseudoscalar channel. In addition, the mixing is assessed qualitatively. The corresponding quantitative analysis is discussed in Secs. 10 and 14.4.

The mixed operator bases are constructed from different smearing levels of glueball operators O_{gb} and meson operators O_{m} . The full correlation matrix is then written in the following form

$$C(t) = \begin{pmatrix} \langle O_{\text{gb}}(t) O_{\text{gb}}^\dagger(0) \rangle & \langle O_{\text{gb}}(t) O_{\text{m}}^\dagger(0) \rangle \\ \langle O_{\text{m}}(t) O_{\text{gb}}^\dagger(0) \rangle & \langle O_{\text{m}}(t) O_{\text{m}}^\dagger(0) \rangle \end{pmatrix} \quad (9.12)$$

where each entry is a submatrix consisting of the correlators among the different smearing levels of two basic interpolators. While the correlators in the diagonal blocks are the ordinary glueball and meson correlators, which are discussed in Sec. 8.2, the correlators in the off-diagonal blocks are mixed correlation functions of glueball and meson interpolators. Wick contraction of the fermion fields leads to a disconnected propagator in the mixed correlation functions

$$\langle O_{\text{m}}(0) O_{\text{gb}}^\dagger(0) \rangle = \left\langle \sum_{\vec{x}} \overline{\lambda}(x) \Gamma \lambda(x) O_{\text{gb}}^\dagger(y_0) \right\rangle = \left\langle \sum_{\vec{x}} \text{Tr}[\Gamma D_W^{-1}(x, x)] O_{\text{gb}}^\dagger(y_0) \right\rangle. \quad (9.13)$$

A graphical representation of the mixed correlation matrix is depicted in Fig. 9.16.

Similarly to the analyses in Sec. 9.3.1 and 9.3.1 we explore variational bases consisting of differently smeared operators and use the effective masses at a fixed time distance t as a measure to judge the quality of the interpolation. In the scalar channel even the minimal set of only one meson smearing level $N_J = 80$ and one

9.3. Optimizing the variational operator bases

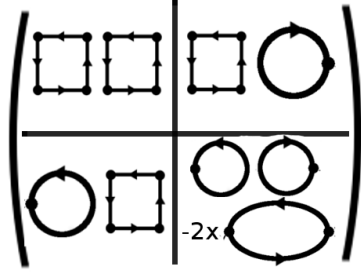


Figure 9.16: Graphical representation of the correlation matrix when a mixed basis of glueball and meson operators is considered. The glueball components are represented by the plaquette and the meson components by the disconnected and connected loops

glueball smearing level $N_{\text{APE}} = 48$ provides a better suppression of higher excited states at a low noise level than using solely meson or solely glueball operators, see Fig. 9.17. The signal from the mixed basis is also quite independent of the used smearing levels. The addition of further meson or glueball operators to the minimal basis does not improve the signal further. Instead, higher excitations become accessible. We conclude that it is crucial to include both, meson and glueball operators in the variational basis to reliably extract the ground state mass in the scalar channel.

The corresponding analysis of the pseudoscalar channel yields much different results. The mass estimation of the ground state does not improve when the mixed basis is considered. In fact, the signal is identical to the one from the $a\text{-}\eta'$ interpolator, see Fig. 9.18. Furthermore, the off-diagonal blocks of the correlation matrix (Eq. 9.12), which contain the mixed correlation functions (Eq. 9.13) and hence encode the mixing of the glueball and meson states, turn out to be zero within rather large uncertainties, indicating only small mixing in the pseudoscalar channel. This confirms the earlier supposition that the ground state in the pseudoscalar channel is predominantly of mesonic type [28].

There are two separate excited states of very similar mass in the pseudoscalar channel. The signal of one of these two states is very similar to signal of the lowest state obtained from using solely glueball operators, whereas the other signal is very similar to the one of the first excited state estimated from the meson interpolators, see Fig. 9.18. These states are further discussed in Sec. 10.

We conclude that for the mass determination of the ground and first excited states in the scalar channel it is optimal to use a mixed basis of glueball and meson operators. In the pseudoscalar channel the mass determination does not benefit from the mixed basis and we therefore extract the masses by separately using purely mesonic variational bases or purely gluonic variational bases.

9. Optimizing the variational bases

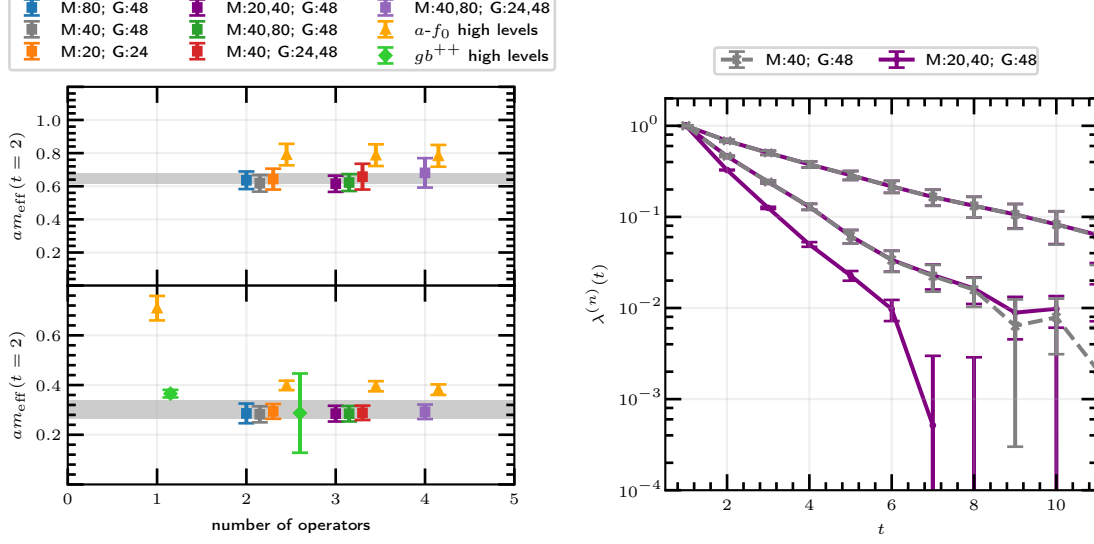


Figure 9.17.: Left: The ground state and the first excited state of the 0^{++} channel are accessible with the mixed basis of one meson and one glueball operator (blue, gray, orange). The signal is insensitive to the used smearing levels which are indicated by M: meson smearing levels, G: glueball smearing levels in the legend. Also adding further meson or glueball operators does not further suppress excited states. If solely meson or only glueball operators are used (orange and light green), the effective mass at $t = 2$ is larger compared to the mixed bases, suggesting that the states are interpolated worse in this case.

Right: The first two generalized eigenvalues are plotted for the minimal mixed basis of one meson and one glueball operator (gray). Adding another operator to the mixed basis does not change the signal for the ground state and the first excited state, but a signal for a second excited state appears (purple).

A similar figure has been published in [30].

9.3. Optimizing the variational operator bases

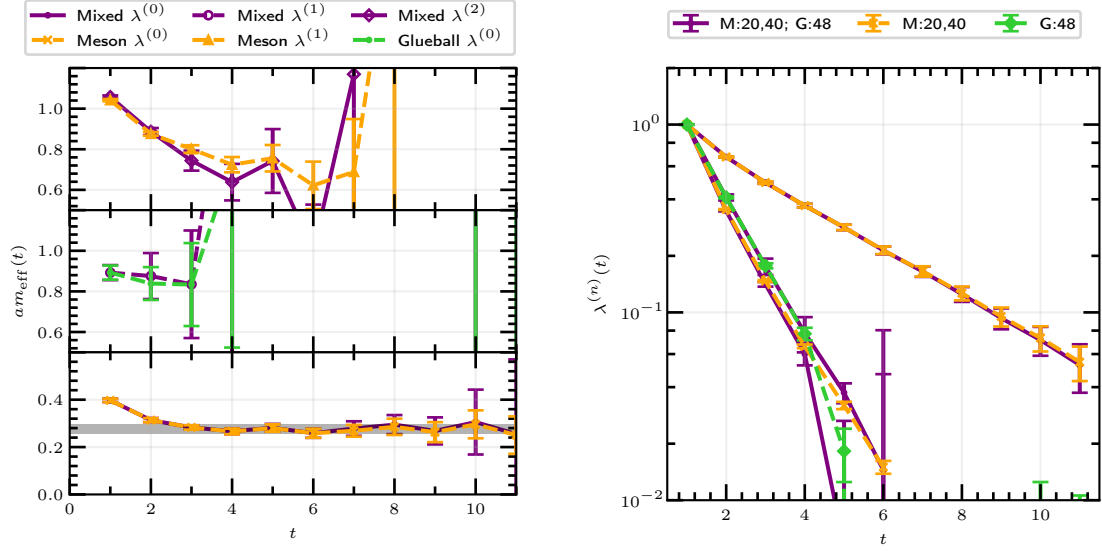


Figure 9.18.: Comparison of the enlarged basis in the 0^{-+} channel to using solely meson operators or solely glueball operators. The smearing levels are the same both plots (left and right) and they are labeled in the legend of the right-hand-side plot (same notation as in Fig. 9.17). The signal of the ground state does not improve by including glueball operators compared to using only meson operators. The mixed approach yields two excited states of very similar mass. One of them can be also obtained by from using solely glueball operators and the other one can be also obtained by using solely meson operators. The figure has been published in [30].

10. Glueball and meson mixing in the two lowest chiral supermultiplets

The variational method provides approximations of the entire physical states. Hence, it does not only give insight into the masses of these states, but also other properties such as the predicted mixing of meson and glueball components in the scalar and pseudoscalar channel [49, 50] can be investigated. First results of the extended variational approach, discussed in detail in Sec. 9.3.3, indicate only a small mixing in the 0^{-+} channel, but a rather large mixing in the lowest two states of the 0^{++} channel. The details of studying the mixing in the scalar channel quantitatively are discussed in the present section. They have also been presented in [30].

The approximation of a physical state $|n\rangle$ is given by the scalar product of the generalized eigenvector \vec{v}_n of the GEVP with the interpolating operators \vec{O}^\dagger acting on the vacuum $|\Omega\rangle$

$$|n\rangle \approx |\phi_n\rangle = \vec{v}_n \vec{O}^\dagger |\Omega\rangle = \sum_i v_{ni} O_i^\dagger |\Omega\rangle = \sum_i v_{ni} |\varphi_i\rangle . \quad (10.1)$$

It can be decomposed into a glueball contribution $|\phi^{(g)}\rangle$ and a meson contribution $|\phi^{(m)}\rangle$

$$|\phi_n\rangle = \sum_{i=1}^{n_g} v_{ni}^{(g)} O_i^{(g),\dagger} |\Omega\rangle + \sum_{i=1}^{n_m} v_{ni}^{(m)} O_i^{(m),\dagger} |\Omega\rangle \quad (10.2)$$

$$= \sum_{i=1}^{n_g} v_{ni}^{(g)} |\varphi_i^{(g)}\rangle + \sum_{i=1}^{n_m} v_{ni}^{(m)} |\varphi_i^{(m)}\rangle \doteq |\phi_n^{(g)}\rangle + |\phi_n^{(m)}\rangle , \quad (10.3)$$

where $v_{ni}^{(g)}$ and $v_{ni}^{(m)}$ are the components of the eigenvectors \vec{v}_n corresponding to the glueball operators $O_i^{(g)}$ and the meson operators $O_i^{(m)}$, respectively, and $|\Omega\rangle$ is the vacuum state. Note that $|\phi_n\rangle$, $|\phi_n^{(g)}\rangle$ and $|\phi_n^{(m)}\rangle$ are not normalized here.

We define the glueball content $c_n^{(g)}$ and the meson content $c_n^{(m)}$ of the physical state $|n\rangle$ as the overlap of this state with its glueball and meson contributions

$$c_n^{(g)} \doteq \langle n^{(g)} | n \rangle \approx \frac{1}{N_n^{(g)} N_n} \langle \phi_n^{(g)} | \phi_n \rangle = \frac{1}{N_n^{(g)} N_n} \sum_i v_{ni}^{*(g)} c_{ni}^{(g)} , \quad (10.4)$$

$$c_n^{(m)} \doteq \langle n^{(m)} | n \rangle \approx \frac{1}{N_n^{(m)} N_n} \langle \phi_n^{(m)} | \phi_n \rangle = \frac{1}{N_n^{(m)} N_n} \sum_i v_{ni}^{*(m)} c_{ni}^{(m)} , \quad (10.5)$$

where $N_n^{(g)}$, $N_n^{(m)}$ and N_n are normalization factors. The coefficients $c_{ni}^{(g)}$ and $c_{ni}^{(m)}$ are the restrictions of the inner products

$$c_{ni} \doteq \langle \varphi_i | n \rangle \approx \langle \varphi_i | \phi_n \rangle \quad (10.6)$$

to the glueball and the meson components. They can be calculated as the components of the vectors dual to the generalized eigenvectors \vec{v}_n [88]

$$\sum_i v_{ni}^* c_{ni} = \delta_{mn} . \quad (10.7)$$

So they are given by the components of the row vectors of M^{-1} , where M is the matrix formed by the column vectors \vec{v}_n . The normalization factors can be obtained by inserting a full set of states

$$N_n^2 = \langle \phi_n | \phi_n \rangle = \sum_k \langle \phi_n | k \rangle \langle k | \phi_n \rangle \stackrel{\text{Eqs. 10.1}}{=} \sum_{ij} v_{ni}^* v_{nj} \sum_k c_{ki} c_{kj}^* . \quad (10.8)$$

$$N_n^{(g)2} = \langle \phi_n^{(g)} | \phi_n^{(g)} \rangle = \sum_{ij} v_{ni}^{*(g)} v_{nj}^{(g)} \sum_k c_{ki}^{(g)} c_{kj}^{*(g)} , \quad (10.9)$$

$$N_n^{(m)2} = \langle \phi_n^{(m)} | \phi_n^{(m)} \rangle = \sum_{ij} v_{ni}^{*(m)} v_{nj}^{(m)} \sum_k c_{ki}^{(m)} c_{kj}^{*(m)} , \quad (10.10)$$

Note that glueball contribution $|\phi^{(g)}\rangle$ and the meson contribution $|\phi^{(m)}\rangle$ are not necessarily orthogonal to each other and therefore $|c_n^{(g)}|^2$ and $|c_n^{(m)}|^2$ in general do not add up to 1.

The calculation above shows that the meson content $c^{(m)}$ and glueball content $c^{(g)}$ can be fully calculated from the eigenvectors \vec{v}_n of the GEVP. Since these can be determined for any value of t individually, also the $c^{(m)}$ and $c^{(g)}$ are determined for each value of t . For the best estimate of $c^{(m)}$ and $c^{(g)}$, the values obtained from different values of t are averaged, weighted by their corresponding Jackknife uncertainty estimates, which is equivalent to determining $c^{(m)}$ and $c^{(g)}$ by fitting a constant to the respective data.

In order to verify the correctness of the calculation, we have determined $c^{(m)}$ and $c^{(g)}$ from the test ensemble $\text{SU}(2)$, $\beta = 1.75$, $\kappa = 0.14925$ for the ground state and the first excited state of the scalar channel using different combinations of smeared glueball and meson interpolators. In Fig. 10.1 the expected formation of a plateau in the interval $t \in [2, 7]$ is clearly visible. For larger values of t , the estimates deviate from the plateau value, which is expected because the contribution of excited states decay exponentially and hence the eigenvectors \vec{v}_n are not resolvable reliably for large values of t . Fig. 10.2 shows the result obtained from fits in the interval $t \in [2, 7]$ for different combinations of smeared glueball and meson

10. Glueball and meson mixing in the two lowest chiral supermultiplets

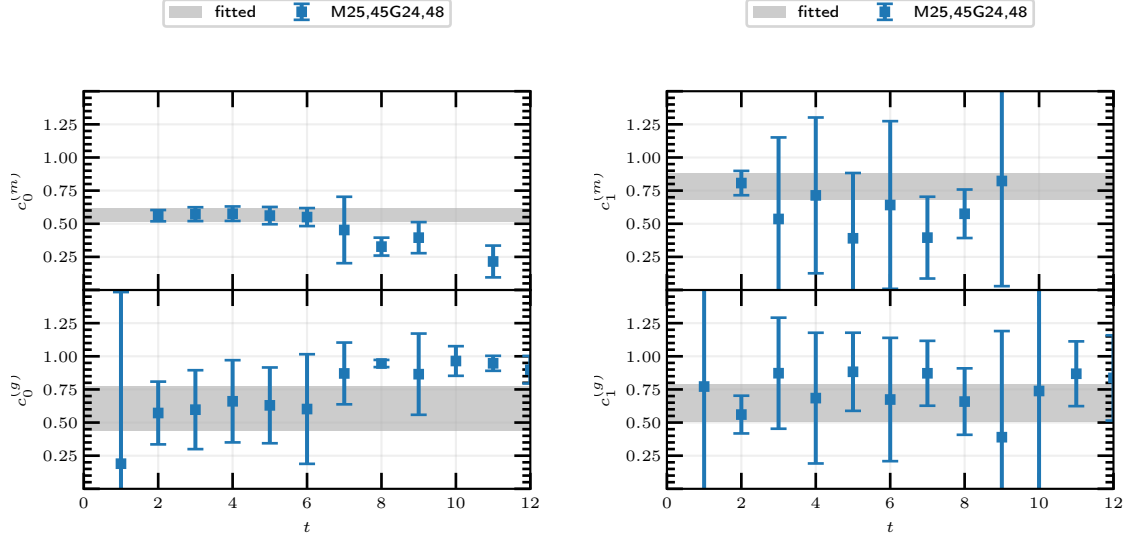


Figure 10.1.: Glueball content $c_{0^{++}}^{(g)}$ and meson content $c_{0^{++}}^{(m)}$ of the ground state (left) and the excited state (right) of the 0^{++} channel determined at different time separations t . The values fitted in the interval $t \in [2, 7]$ are plotted in gray.

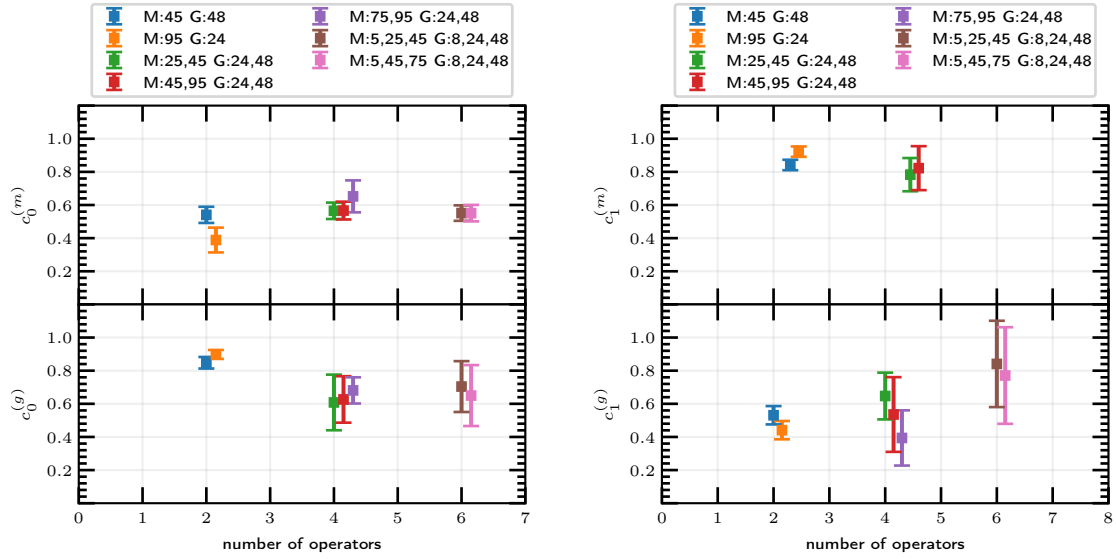


Figure 10.2.: Glueball content $c_{0^{++}}^{(g)}$ and meson content $c_{0^{++}}^{(m)}$ of the ground state (left) and the excited state (right) of the 0^{++} channel determined from different sets of interpolating operators and weighted averages over time separations $t \in [2, 7]$.

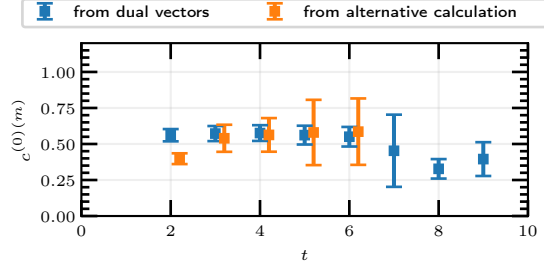


Figure 10.3.: Comparison of the two methods to calculate the mixing components. The results are more precise, when $c_{0++}^{(0)(m)}$ is calculated by means of Eq. 10.7 (blue) in comparison to using Eq. 10.14 (orange).

interpolators. It is apparent that, when using at least two glueball interpolators and two meson interpolators, the final results are stable (within errors) against varying the interpolators. We conclude that the meson content $c_{0++}^{(m)}$ and glueball content $c_{0++}^{(g)}$ of the ground state and first excited state of the scalar channel can be extracted using two meson interpolators and two glueball interpolators.

We have, furthermore, explored an alternative to calculate the coefficients c_{ni} by means of

$$c_{ni} = \langle \varphi_i | n \rangle \approx \langle \varphi_i | \phi_n \rangle \quad (10.11)$$

$$= \langle \Omega | v_{im}^* O_m v_{nj} O_j^\dagger | \Omega \rangle \quad (10.12)$$

$$= \vec{v}^{(i),\dagger} C(0) \vec{v}^{(n)} \quad (10.13)$$

$$= \frac{1}{\lambda^{(n)}(t, 0)} \vec{v}^{(i),\dagger} C(t) \vec{v}^{(n)}, \quad (10.14)$$

where in the last step the defining equation of the GEVP (Eq. 7.27) was used. The exponentially decreasing denominator in Eq. 10.14 leads to large fluctuations and hence this method is less precise than calculating the c_{ni} by means of Eq. 10.7; a comparison of the two calculations is shown for $c_{0++}^{(0)(m)}$ in Fig. 10.3. Thus, we use Eq. 10.7 to calculate the mixing coefficients.

In the pseudoscalar channel the mixing coefficient indeed turn out to be $c_{0-+}^{(0)(g)} = -0.03(2)$, $c_{0-+}^{(0)(m)} = 1.000(1)$ on the test ensemble, confirming that the ground state is meson-like. A first analysis of the the mixing coefficients of the corresponding excited states indicates considerable mixing $c_{0-+}^{(1)(g)} = 0.86(8)$, $c_{0-+}^{(2)(m)} = 0.24(7)$, $c_{0-+}^{(2)(g)} = 0.70(4)$, $c_{0-+}^{(2)(m)} = 0.94(2)$. In the scope of this thesis we have, however, not further analyzed the mixing of the excited states in the pseudoscalar channel and leave the subject open for future investigations.

11. Further details of the variational analysis

The optimization of the variational bases to extract the masses and the mixing properties of lowest bound states using the variational approach are discussed in detail in the previous sections. There are further parameters to adjust and additional techniques that can be used to improve the precision of the results. They are explained in the following.

11.1. Solving the GEVP and the truncation method

The GEVP (Eq. 7.27) can be solved using different methods. It can, for example, be reformulated as an ordinary eigenvalue problem by multiplying both sides of the equation from the left with $C(t_0)^{-1}$

$$C(t_0)^{-1}C(t)\vec{v}^{(n)} \doteq M(t, t_0)\vec{v}^{(n)} = \lambda^{(n)}(t, t_0)\vec{v}^{(n)}. \quad (11.1)$$

A similar method is to apply the Cholesky decomposition $C(t_0) = LL^T$ where L is a lower triangular matrix. The GEVP can then be reformulated as

$$L^{-1}C(t)L^{-1,T}L^T\vec{v}^{(n)} = \lambda^{(n)}(t, t_0)L^T\vec{v}^{(n)}, \quad (11.2)$$

$$M(t, t_0)\vec{\tilde{v}}^{(n)} = \lambda^{(n)}(t, t_0)\vec{\tilde{v}}^{(n)}, \quad (11.3)$$

with

$$M(t, t_0) \doteq L^{-1}C(t)L^{-1,T}, \quad \vec{\tilde{v}}^{(n)} \doteq L^T\vec{v}^{(n)}. \quad (11.4)$$

The Cholesky decomposition has the advantage that $M(t, t_0)$ in Eq. 11.4 is symmetric in contrast to $M(t, t_0)$ in Eq. 11.1 and thus easier to handle. Solving the GEVP via the Cholesky decomposition is implemented in the GSL C++-library, which we usually use.

Both methods require that $C(t_0)$ has full rank since otherwise it is not invertible. Thus, linearly independent interpolating operators O_i should be chosen. In practice, it is, due to limited statistics, already problematic if the variational basis is approximately linearly dependent, indicated by very small eigenvalues that fluctuate in the vicinity of zero. In [90] it has therefore been suggested to limit the number of interpolating operators to $r < N_S/2$, where N_S is the spatial extent of the lattice in units of the lattice spacing a .

In order to automatize the selection of linearly independent operators, the *truncation method* can be applied. The idea is to diagonalize $C(t_0)$ by a unitary matrix

transformation and discard the rows and columns whose diagonal elements are approximately zero. For this purpose, the eigenvectors $\vec{v}_0^{(n)}$ and the corresponding eigenvalues $\lambda_0^{(n)}$ of $C(t_0)$ are calculated. The truncated correlation matrix is then given for all values of t by

$$(C_{\text{trunc}})_{ij}(t) = \vec{v}_0^{(i),\dagger} C(t) \vec{v}_0^{(j)}, \quad (11.5)$$

where only those eigenvectors are used whose corresponding eigenvalues fulfill

$$\lambda_0 < \epsilon, \quad (11.6)$$

and where ϵ is the truncation threshold that can be adjusted to obtain reliable results.

The truncated correlation matrix $C_{\text{trunc}}(t)$ can then be used in the GEVP. The new basis vectors are given by linear combinations of the old basis. Since a linear combination of interpolating operators forms again an interpolating operator, the new basis is a valid variational basis. The truncation method thus discards (truncates) those parts of the operators that have no (or very small) overlap with the physical states.

The truncation method is only necessary when correlation functions among many different interpolating operators are considered. However, the measurements of correlators that include fermion propagators are typically computationally expensive and thus only the glueball correlators are cheap to compute. Furthermore, as explained in Sec. 9, in our investigations it is not beneficial to use more than ~ 5 interpolating operators and in the scope of this thesis we include only the few most relevant interpolators. These small variational bases are usually not linearly dependent and thus it is not necessary to utilize the truncation method.

11.2. t_0

We have investigated the influence of the parameter t_0 of the GEVP on the results. In [88] it is argued that $t_0 \geq t/2$ should be chosen to suppress excited state contributions. In Figs. 11.1 and 11.2 the dependence of the effective mass on the value of t_0 is shown for the different channels. The effective masses from different values of t_0 vary only very slightly and a suppression of excited states is hardly visible. For large values of t_0 two problems appear. Firstly, the signals become very noisy. Secondly, due to the increased noise, some of the eigenvalues of $C(t_0)$ fluctuate in the vicinity of zero, resulting in a breakdown of the methods to solve the GEVP, as explained in Sec. 11.1. For the gluino-gluon correlator $C_1(t)$ the method already breaks down for $t_0 \geq 1$ at the SU(2)-SYM ensemble $\beta = 1.9$, $\kappa = 0.14415$. Since the excited state suppression by using large values of t_0 is

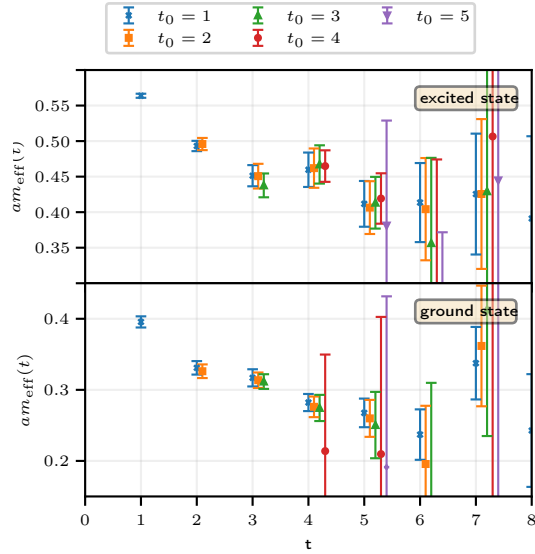
11. Further details of the variational analysis

only very small and problems arise if t_0 is chosen too large, we chose rather small values for t_0 that worked reliably for all investigated ensembles. The values of t_0 used for the different channels are collected in Tab. 11.1.

Channel	t_0/a
0^{++} -mixed	1
$a\text{-}\eta'$	1
Gluino-gluon $C_1(t)$	0
Gluino-gluon $C_{\gamma_4(t)}$	1
0^{-+} glueball	0

Table 11.1.: Values of t_0 used in the GEVP for the different channels.

Figure 11.1: Effective masses of the 0^{++} channel for different values of t_0 measured from the SU(2)-SYM ensemble $\beta = 1.9$, $\kappa = 0.14415$. The suppression of higher excited states by using large values of t_0 is not observed. The variational basis consists of $a\text{-}f_0$ operators with the smearing levels $N_J \in \{20, 40\}$ and glueball operators with the smearing levels $N_{\text{APE}} \in \{40, 80\}$.



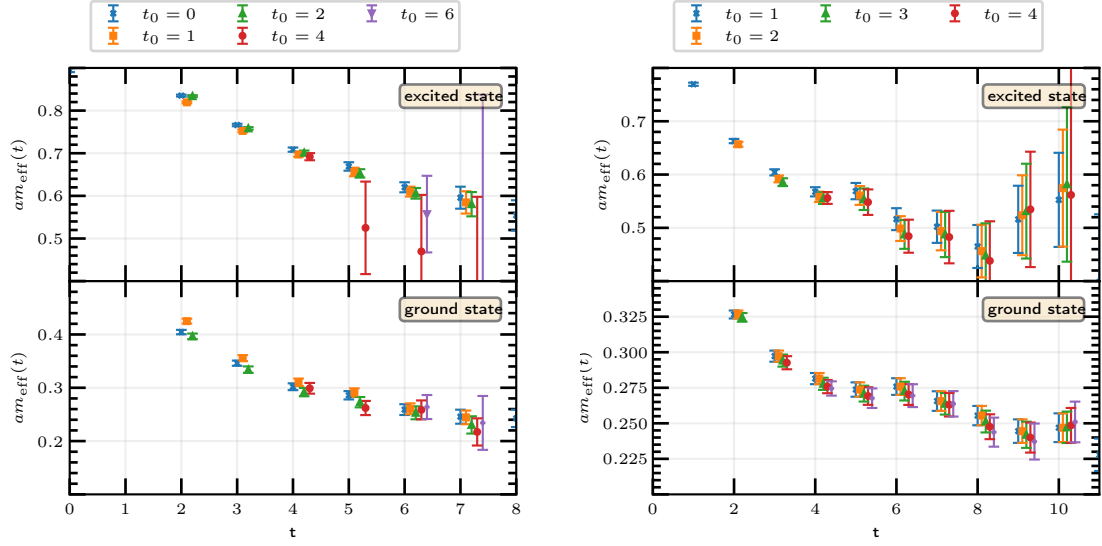


Figure 11.2.: Effective masses of the ground state and first excited state of the $a\text{-}\eta'$ channel (left) and the gluino-gluon channel (right) using different values for t_0 . The suppression of higher excited states by using large values of t_0 is negligible. The variational bases consist of the smearing levels $N_J \in \{0, 3, 20, 40\}$ for the $a\text{-}\eta'$ channel and of the $C_{\gamma_4}(t)$ correlators from the smearing levels $N_{\text{APE}} \in \{55, 65, 75, 85, 95\}$ for the gluino-gluon channel, respectively.

11.3. Offset Handling / Derivative Trick

Due to limited statistics, it may happen, that the correlators do not properly decay to zero. Instead, they approach finite constants (offsets), see Fig. 11.3, or show other unexpected behavior such as going to negative values, see Fig. 11.4. If these effects are not handled properly, the masses of the states may be over or underestimated. If the correlator approaches a positive constant, the corresponding effective mass does not form a plateau, but decays to zero, and the mass of the particle is likely to be underestimated (see Fig. 11.3). Contrarily, if the correlator approaches negative values, the effective mass is pushed to too large values, leading to a fake plateau at small values of t where higher excitations have not sufficiently decayed. Therefore, in this case the mass of the particle is likely to be overestimated (see Fig. 11.4). In our simulations we observe such effects in some of the data. They could be overcome by simply producing more statistics. However, due to limited computing resources, this is not always possible and therefore other methods are required to handle these effects. For this purpose, we have studied two such techniques, the *offset subtraction method*, and the *derivative trick*.

11. Further details of the variational analysis

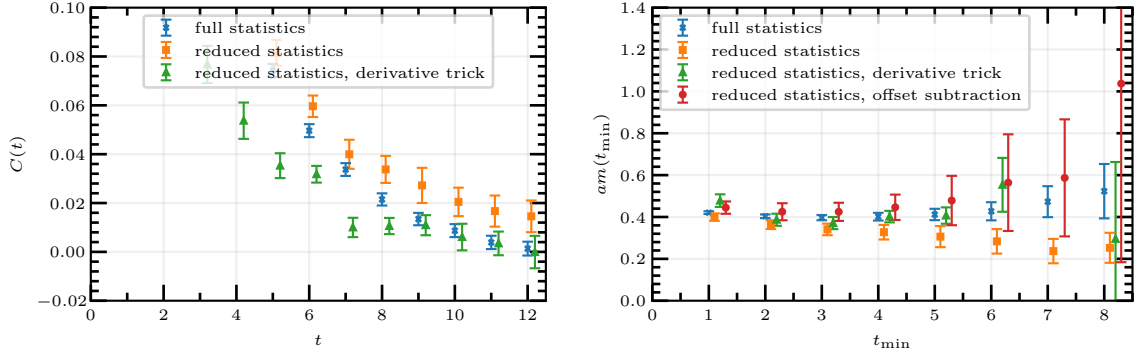


Figure 11.3.: In the case of low statistic, the correlator might not decay to zero. To demonstrate this effect, the $a\text{-}\eta'$ correlator, estimated from only 200 configurations (orange), is compared to using the full statistics of 7736 configurations (blue). The plot on the right shows mass fits of fit length 5 with different values of the lower limit t_{\min} of the fit interval. Due to the finite offset, the mass would be underestimated from the reduced statistics. In fact, a plateau is not even visible. Using the derivative trick removes the offset and reproduces the correct mass estimates of the full statistics. The offset subtraction method leads to a slight overestimation of the mass and larger uncertainties in comparison to the derivative trick. The ensemble $SU(3)$, $\beta = 5.5$, $\kappa = 0.1678$ was used. Note that the error bars might be slightly underestimated for the case of the reduced statistics because, due to the small statistics, the bin size could not be chosen large enough to eliminate all autocorrelations.

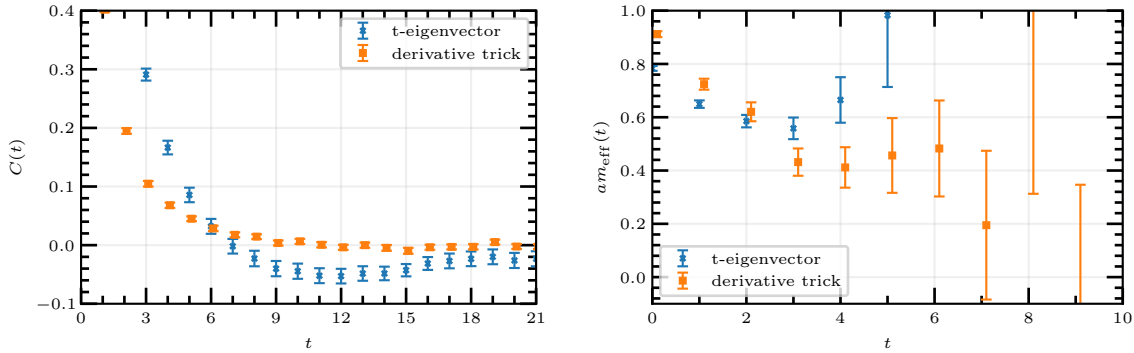


Figure 11.4.: Smeared 0^{-+} glueball correlator $C(t)$ and its derivative $\frac{d}{dt}C(t)$ measured from the ensemble $SU(2)$, $\beta = 1.9$, $\kappa = 0.14435$, using $N_{\text{APE}} = 80$. The unphysical decay to negative values is mitigated by using the derivative trick. The effective mass corresponding to $C(t)$ has a fake plateau around $am_{\text{eff}} \approx 0.6$. The derivative trick leads to a mass plateau $am_{\text{eff}} \approx 0.4$.

11.3. Offset Handling / Derivative Trick

In the offset subtraction method, the unphysical offset c of the correlator is estimated by a weighted average of the correlator at the largest n values of t . The weights are given by the squared Jackknife error estimate of the correlator

$$c = \frac{\sum_{i=0}^{n-1} w_i C(T/2 - i)}{\sum_{i=0}^{n-1} w_i}, \quad w_i = \frac{1}{(\Delta C(T/2 - i))^2}, \quad (11.7)$$

where T is the number of lattice sites in the temporal direction. The offset c is then subtracted globally from the correlator

$$C_{\text{subtracted}}(t) = C(t) - c. \quad (11.8)$$

The offset subtraction method can be used in the variational method by applying it to the eigenvalues $\lambda^{(n)}(t)$ of the GEVP. The parameter n can be varied to improve the precision of the estimation. While the offset subtraction method is able to reduce the effect of a finite offset, it does have several disadvantages.

1. If the mass of the particle is small, the correlation function may correctly be finite at large t , even if it is not affected by an offset. The offset subtraction method would erroneously subtract this finite value leading to an overestimation of the mass.
2. The offset might not be estimated reliably if n is small and uncertainties are large. If n is increased, however, the error discussed in 1. is more likely to set in.
3. The offset subtraction method is not able handle unphysical effects of the correlator that are not constant offsets (see, for example, Fig. 11.4).

To overcome the disadvantages of the offset subtraction method, the derivative trick can be used. The idea is to use the time-derivative of the correlator instead of the correlator itself for the mass extraction. A potential constant offset would then drop out. The derivative of the correlator is also a sum of exponential functions that decay with the energy of the physical states

$$\frac{d}{dt} C_{ij}(t) \stackrel{\text{Eq. 7.6}}{=} - \sum_n m^{(n)} a_i^{(n)} a_j^{(n)*} e^{-tm^{(n)}}, \quad (11.9)$$

and thus the usual techniques can be applied to extract the mass from $\frac{d}{dt} C_{ij}(t)$. On the lattice, the derivative has to be discretized and we choose the forward derivative here

$$\frac{d}{dt} C_{ij}(t) \rightarrow \frac{C_{ij}(t+1) - C_{ij}(t)}{a}. \quad (11.10)$$

11. Further details of the variational analysis

Since the lattice derivative agrees with the continuum derivative only up to order a , it is better to use a modified fit function $f_{\text{der}}(t)$ for the extraction of the masses that correctly resembles the lattice derivative

$$f_{\text{der}}(t) = \frac{f(t+1) - f(t)}{a}, \quad (11.11)$$

where $f(t)$ is the original fit function (cf. Eq. 7.18). In the variational method the derivative trick is applied to the generalized eigenvalues of the GEVP. The disadvantage of the derivative trick is that contributions of higher excitations to the correlator are enhanced due to the additional factor m_n in Eq. 11.9.

The two offset handling methods can be demonstrated on the example of the $a\text{-}\eta'$ correlator, estimated on a small subset which consists of only 200 out of the 7736 configurations of the SU(3)-SYM ensemble $\beta = 5.5$, $\kappa = 0.1678$, see Fig. 11.3. While the correlator determined from the full statistics properly decays to zero, the correlator determined from the subset approaches a positive offset. In the latter case it would be very difficult to correctly estimate the $a\text{-}\eta'$ ground state mass without any offset handling because, due to the positive offset, no mass plateau is visible. Both, the offset subtraction method and the derivative trick allow a correct mass estimation within uncertainties. The offset subtraction method leads to a slight overestimation of the mass and to larger uncertainties compared to the derivative trick. These two effects can be explained by the aforementioned disadvantages 1. and 2. of the offset subtraction method. The enhancement of excited state contributions by using the derivative trick only affects the mass fits with $t_{\text{min}} = 1$. The mass fits with $t_{\text{min}} \geq 2$ are consistent with the correct result from full statistics.

Besides removing constant offsets, the derivative trick seems to even mitigate other unphysical behavior of the correlator such as becoming negative (see Fig. 11.4) or not decaying to exponentially to zero.

Due to the several advantages of the derivative trick over the offset subtraction method we apply the derivative trick in the cases when the correlator does not properly decay to zero.

Yet another method would be to introduce a constant as an additional fit parameter. We have not tested this method, but we don't expect any further improvement since this method can only deal with constant offsets, similarly to the offset subtraction method, and additional fit parameters often lead to unstable fits.

11.4. Ordering and fixed vector method

The generalized eigenvalues of the GEVP decay exponentially with the masses of the physical states. The statistical fluctuations of the correlators, however, usually decrease more slowly with t , leading to an exponential decay of the signal-to-noise ratio, see Fig. 11.5. Thus, for sufficiently large values of t , the noise of the correlators is larger than the signal. The same is true for the generalized eigenvalues. The statistical fluctuations can then lead to a wrong ordering of the eigenvalues. This can be best explained by the following example. Let the true eigenvalues at $t = 10$ be

$$\hat{\lambda}^{(0)} = 0.2, \quad \hat{\lambda}^{(1)} = 0.01, \quad (11.12)$$

and let the statistical fluctuations, induced by finite statistics, to be of the order

$$\sigma(\hat{\lambda}^{(0)}) = 0.1, \quad \sigma(\hat{\lambda}^{(1)}) = 0.5. \quad (11.13)$$

Due to the statistical fluctuations, the eigenvalues, determined on an ensemble could then, for example, be

$$\lambda^{(0)} = 0.1, \quad \lambda^{(1)} = 0.51. \quad (11.14)$$

Now, if the eigenvalues are sorted by their magnitude, one would erroneously deduce

$$\lambda^{(0)} = 0.51, \quad \lambda^{(1)} = 0.1. \quad (11.15)$$

The determined value for $\lambda^{(0)}$ deviates significantly from the true value, far outside the statistical uncertainty. The ordering may even fluctuate on the different Jackknife samples.

There are different techniques to avoid such errors. In the following we discuss, in particular, different sorting algorithms for the eigenvalues, the *fixed vector method* and reducing the number of interpolating operators.

Sorting by eigenvectors:

An alternative to sorting the eigenvalues by their magnitude is to sort the eigenvalues by their corresponding eigenvectors as follows.

1. Choose a small time separation t_1 where the statistical uncertainties of the eigenvalues $\lambda(t_1)$ do not overlap. Calculate the eigenvectors $\vec{v}(t_1)$ and sort eigenvalues and eigenvectors as usual by the eigenvalues' magnitudes.
2. Identify the eigenvectors and the corresponding eigenvalues at all other values

11. Further details of the variational analysis

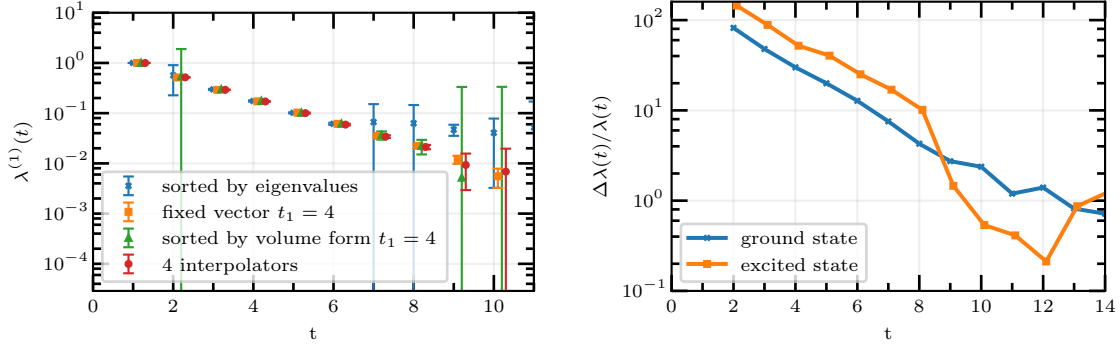


Figure 11.5.: Comparison of different methods to sort the eigenvalues on the example of the first excited state of the 0^{++} channel, using the SU(2)-SYM ensemble $\beta = 1.9$, $\kappa = 0.1433$. If the eigenvalues are sorted by their magnitude, they are misidentified for $t \geq 7$. All three methods, the fixed vector method, sorting by volume forms and reducing the number of operators to four interpolators lead to correct estimations for larger values of t . Right: The signal-to-noise ratio decays exponentially with t .

of t by using the eigenvectors $\vec{v}(t_1)$ as a reference.

There are different possibilities to identify the eigenvectors. One method is to calculate the scalar products of all $\vec{v}(t)$ at fixed t with all reference vectors $\vec{v}(t_1)$, identify the pair that has the largest scalar product, and repeat until all vectors are identified. Another method is to calculate all volume forms V at fixed t

$$V = |\det M|, \quad (11.16)$$

where the columns of the matrix M are given by the reference vectors $\vec{v}(t_1)$ and one of the reference vectors is replaced with one of the vectors $\vec{v}(t)$. One then identifies the pair of vector and reference vector that leads to the largest volume form V upon replacement. The process is then repeated until all vectors are identified. This method is more stable compared to the identification based on scalar products, which can be intuitively understood because the volume forms takes into account all reference vectors in contrast to the scalar product which is calculated from only one reference vector.

Fixed Vector Method

In the fixed vector method, instead solving the GEVP for each time separation t individually, the GEVP is solved only at a fixed time separation t_1 . The generalized

eigenvalues for the values of t are then obtained via

$$\lambda^{(n)}(t) = \vec{v}^{(n),T}(t_1)C(t)\vec{v}^{(n)}(t_1), \quad (11.17)$$

which avoids the sorting issues at larger values of t . The fixed vector method is correct because the generalized eigenvectors are, in general, independent of t if only a finite number of physical states is accessible [88]. A disadvantage of the fixed vector method, compared to solving the GEVP for every value of t , is that the statistical fluctuations of the eigenvectors do not average out over several different values of t .

A comparison of the two methods is displayed in Fig. 11.5 on the example of the first excited state in the 0^{++} channel, estimated from three glueball and three meson interpolators. It is visible, that both methods, sorting by the volume form and the fixed vector method, lead to a more consistent estimation of the generalized eigenvalues for large values of t . It is, however, similarly efficient to reduce the number of interpolating operators to two glueball and two meson operators. Indeed, we observe in our investigations that incorrect ordering of the eigenvalues appears less often, the fewer operators are used in the variational basis. In Secs. 9 and 10, it is explained that we generally consider variational bases consisting of only the few most relevant operators. With this choice, false ordering of the eigenvalues is rare and we therefore do not use the fixed vector method (which has a disadvantage, as discussed above) and only use the sorting by volume forms if necessary. Note that incorrect ordering of the eigenvalues usually only appears in the region of large values of t , which is of small importance when extracting the masses from the fits since the signal-to-noise ratio is small at large values of t .

Another alternative, that could overcome the disadvantage of the fixed vector method, but which we have not tested, is to apply the fixed vector method using several values of t_1 and averaging the final results.

11.5. Normalization and Symmetrization

The correlation matrices are in general Hermitian (cf. App. A.3). Due to finite statistics, the measured correlation functions might, however, turn out to be not exactly Hermitian. To stabilize the computations, they are therefore Hermitianized

$$C_{ij}(t) \rightarrow C'_{ij}(t) = 0.5(C_{ij}(t) + C_{ji}^*(t)). \quad (11.18)$$

In principle, this technique can be applied to all three channels. However, we have only used the symmetrization in the scalar and pseudoscalar channels and not for the gluino-gluon channel. Furthermore, we normalize the correlation matrices such

11. Further details of the variational analysis

that the diagonal elements become unity at t_0 to eliminate potential numerical issues

$$C_{ij}(t) \rightarrow C'_{ij}(t) = \frac{C_{ij}(t)}{\sqrt{C_{ii}(t_0)}\sqrt{C_{jj}(t_0)}} \quad (\text{no index sum}). \quad (11.19)$$

This is a valid procedure because it simply amounts to normalizing the interpolating operators.

12. Summary of the measurements

Using the improved techniques explained in Secs. 7 to 11, we have extracted the masses of the ground and first excited states of the chiral multiplet and the mixing coefficients $c^{(g)}$ and $c^{(m)}$ in the scalar channel from the produced gauge ensembles of SYM with the gauge groups SU(2) and SU(3) (The ensembles are discussed in Sec. 6.). For this purpose, we have chosen the smearing levels $N_J \in \{0, 3, 20, 40\}$ for the meson interpolators and smearing levels up to $N_{\text{APE}} = 80$ for the glueball operators using the optimized smearing parameters which are summarized in Eqs. 9.3 and 9.10.

In the scalar channel, the analysis is based on mixed variational bases including glueball and meson interpolators. We have mostly used two meson and two glueball operators for the analysis of masses and mixing properties, choosing smearing levels that led to clean signals (e.g. the combination $N_J \in 20, 40$, $N_{\text{APE}} \in 40, 80$). On the finest lattices, it was in some cases also possible to include three meson and three glueball operators without running into the problems discussed in Sec. 11.4. The inclusion of these additional operators produced consistent results.

In the pseudoscalar channel, on the contrary, we have not used mixed variational bases, but extracted the masses separately from the meson and the glueball operators since the mixed operator bases did not give rise to improved signals (cf. Sec. 9.3.3). The analysis based on pseudoscalar glueball interpolators was only possible in the case of the SU(2)-SYM simulations. In the SU(3)-SYM simulations, the signal was too noisy to reliably estimate effective mass plateaus and appropriate fitting intervals.

Note that the used smearing levels of the meson interpolators are chosen more conservatively, also including smaller smearing levels than the ones discussed in Sec. 9. For the case of the scalar channel this does not have a large influence, as the choice of smearing level has only a small influence on the results (cf. Secs. 9.3.3 and 10). In the pseudoscalar channel, this choice might not be optimal, but it was compensated by choosing the lower limit of the fit intervals t_{min} sufficiently large.

Throughout the analysis, we have made sure that systematical uncertainties are under control, i.e. they are not larger than the statistical ones. This includes the estimation of proper bin sizes to eliminate autocorrelations and to guarantee the correct estimation of the statistical uncertainties (cf. Secs. 7.4 and 7.5), as well as choosing suitable values t_{min} of the fitting intervals based on the criteria of χ_r^2 and the formation of effective mass plateaus as discussed in Secs. 7.1 and 7.2.

The results of our analyses are collected in Tabs. A.1, A.2, A.3 and A.4 in App. A.6. They have partly been published in [30] and [37].

13. Extrapolations

Ultimately, we are interested in the supersymmetric limit, i.e. the chiral and continuum limit (cf. Sec. 3.2). The next step is therefore to extrapolate the collected data to this limit. There are different approaches to perform these extrapolations. In the following, the two methods that we use and which we call *two-step extrapolation* and *combined extrapolation* are discussed on the basis of the measured ground state masses of the chiral supermultiplet of SU(3)-SYM. This data is ideally suited to study the extrapolations because the ground state masses feature small uncertainties compared to the other observables which we have considered (excited states, mixing coefficients) and the parameter space spanned by β and κ is sampled more uniformly than in the case of the SU(2)-SYM simulations.

The present section is devoted to exploring and optimizing the two extrapolation approaches. The final results for the different observables are discussed in Sec. 14.

13.1. Two-step and combined extrapolations

In the two-step approach, the observables are first extrapolated to the chiral limit for each value of β individually, similarly to the chiral extrapolations of the scales w_0 and r_0 (cf. Sec. 4.2). In a second step, the resulting chiral values are extrapolated to the continuum limit. In the combined approach, on the contrary, the extrapolation to the chiral and continuum limit is done simultaneously.

To explain these two approaches in more detail and to discuss how they are related to each other, some notation is introduced first. As explained in Sec. 4, we use the squared mass of the adjoint pion $m_{a-\pi}^2$ and the lattice spacing a to tune towards the chiral and continuum limit, respectively. Furthermore, all dimensionful observables are expressed in units of a scale s , where the scale can be the lattice spacing $s = a$ or a dimensionful observable such as w_0 or $w_{0,\chi}$. The lattice spacing is not a suitable scale for the extrapolation to the continuum limit since it vanishes in this limit. Therefore, we use $s = w_0$ or $s = w_{0,\chi}$ in the continuum extrapolations. We label the squared pion mass and the lattice spacing in units of the scale s as

$$x = (sm_{a-\pi})^2, \quad y = \frac{a}{s}, \quad (13.1)$$

where s is assumed to have the mass dimension $[s] = -1$. If an observable with a different mass dimension is chosen for the scale setting, it has to be raised to an appropriate power, such that the results has mass dimension -1 and can be used as the scale s . We furthermore denote the observable which shall be extrapolated

13.1. Two-step and combined extrapolations

to the supersymmetric point by O . It should also be formulated dimensionless and in terms of the scale s , e.g.

$$O = \begin{cases} sm, & \text{(particle mass)} \\ c^{(g)}, & \text{(glueball mixing coefficient)} \end{cases} . \quad (13.2)$$

The extrapolations of the observables to the supersymmetric point are based on the assumption that the observables can be described by analytic functions $O(x, y)$ in the simulated vicinity near the supersymmetric point. The function $O(x, y)$ can be approximated by a Taylor expansion in x and y

$$O(x, y) = O_{\chi, \text{cont}} + c_1 x + c_2 y + c_3 xy + c_4 x^2 + c_5 y^2 + c_6 xy^2 + \mathcal{O}(\text{higher}), \quad (13.3)$$

where $O_{\chi, \text{cont}}$ and the c_i are Taylor coefficients. Here, all terms that we consider for the extrapolations are included.

While the Taylor expansion in Eq. 13.3 is appropriate for the extrapolations of the SU(2)-SYM results, the ansatz can be improved further for the simulations of SU(3)-SYM because these are based on a one-loop clover improved action (cf. Sec. 3.3). The leading discretization effects are therefore expected to be of the order $\mathcal{O}(ag^4) = \mathcal{O}(a/\beta^2)$. Thus, in this case, y can be replaced with

$$y \rightarrow \tilde{y} = \frac{a}{s\beta^2} \quad (13.4)$$

in the terms of the Taylor series that are linear in y . The ansatz used in the extrapolations for the SU(3)-SYM simulations is then given by

$$O(x, y) = O_{\chi, \text{cont}} + c_1 x + c_2 \tilde{y} + c_3 x \tilde{y} + c_4 x^2 + c_5 y^2 + c_6 xy^2 + \mathcal{O}(\text{higher}). \quad (13.5)$$

13.1.1. Combined extrapolation

The combined extrapolation is then straightforward. The extrapolated value $O_{\chi, \text{cont}}$ of the observable O in the supersymmetric point is obtained by performing a two dimensional fit (in x and y) of the Taylor polynomial (Eq. 13.3 or 13.5) to the data, where c_i and $O_{\chi, \text{cont}}$ are the fit parameters. For this purpose, we use the ODR fitting routine provided by the SciPy library for Python. In Figs. 13.1 and 13.2 these fits are visualized for the mass of gluino-glue ground state in SU(3)-SYM.

In order, to keep the error of the extrapolated value $O_{\chi, \text{cont}}$ small and to prevent overfitting (which means fitting the noise rather than the actual data), the fit function should include only the dominating terms of the Taylor series, which lead to an acceptable χ_r^2 of the fit. We therefore consider only subsets of the coefficients c_i and set the others to zero. While in the case of the SU(2)-SYM simulations we

13. Extrapolations

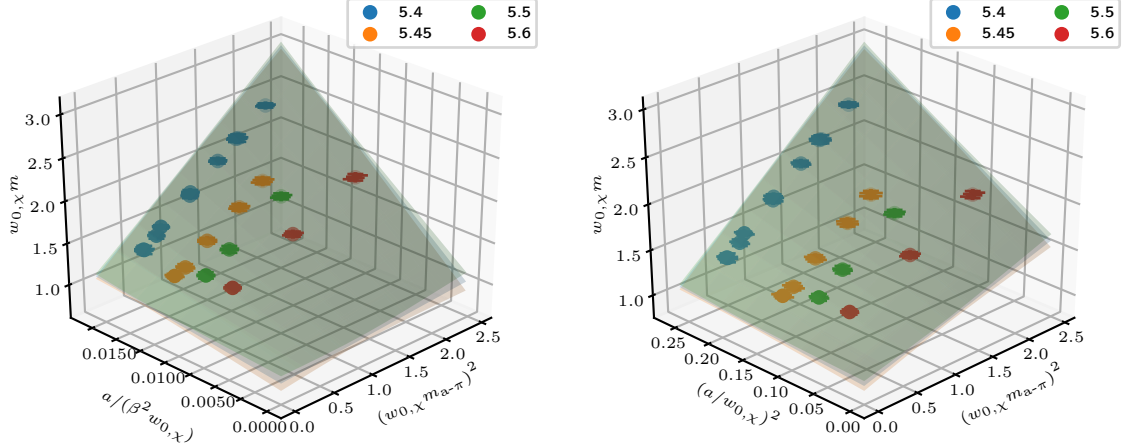


Figure 13.1.: Combined chiral and continuum extrapolation of the gluino-glue ground state mass using the chirally extrapolated observable $w_{0,\chi}$ for the scale setting. The data points are color coded for the different values of β (see legends). Left: Linear extrapolation in \tilde{y} (fit coefficients c_1, c_2, c_3), Right: Quadratic extrapolation in \tilde{y} (fit coefficients c_1, c_5 and c_6).

expect the linear terms in x and y to be dominating, in the SU(3)-SYM the linear terms in \tilde{y} might be very small due to the clover improvement, i.e. $c_2 \ll 1$, $c_3 \ll 1$. In this case, the next higher order $\mathcal{O}(y^2)$ is expected to be dominating. To find the most suitable extrapolations, we test different fit functions and compare the corresponding values of χ_r^2 and the resulting uncertainties of $O_{\chi,\text{cont}}$. We label these extrapolations as

- Linear extrapolation: Neglect quadratic terms in y , i.e. $c_5 = c_6 = 0$.
- Quadratic extrapolation: Neglect linear terms in \tilde{y} , i.e. $c_2 = c_3 = 0$.
- Linear + quadratic extrapolation: Consider both, linear terms in \tilde{y} and quadratic terms in y .

Instead of using a single observable for the scale setting, principally, one may use different observables s_1 , s_2 and s_3 for the scale setting of $m_{a-\pi}$, a and O , respectively. The value $O_{\chi,\text{cont}}$ of the observable at the supersymmetric point does not depend on the choice of the scales s_1 and s_2 , which can be demonstrated easily (see App. A.5). The coefficients c_i , which determine how this limit is approached, however, may differ and therefore one could try to find for each observable the combination of scales that leads to the best fit result, i.e. to a small value of χ_r^2 and to a small uncertainty $\Delta O_{\chi,\text{cont}}$. However, this would not only be very time consuming, but it is also error prone because fluctuations of the data can randomly

13.1. Two-step and combined extrapolations

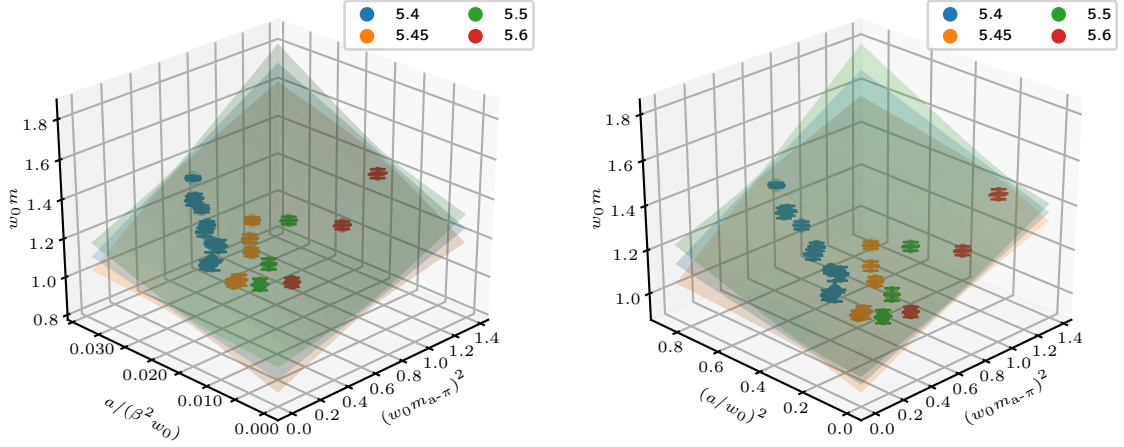


Figure 13.2.: Similar plots as in Fig. 13.1. The difference is that here the values w_0 measured at the individual ensembles were used as the scale.

lead to small values of χ_r^2 and $\Delta O_{\chi, \text{cont}}$, even for non-optimal choices of the fit parameters. We have therefore decided to use one common scale $s = s_1 = s_2 = s_3$. We test both, using the chirally extrapolated scale $s = w_{0, \chi}$ and the scale $s = w_0$ measured at each ensemble for the scale setting. Note that the extrapolated value $O_{\chi, \text{cont}}$ does not depend on this choice because in the supersymmetric point (and also in the chiral limit) both scales agree.

A detailed discussion about the choice of the fitting coefficients and of the scale setting is provided in Secs. 13.2 and 13.3.

13.1.2. Two-step extrapolation

In the two-step extrapolation approach, the observables are first extrapolated to the chiral limit and the obtained data is then extrapolated to the continuum limit. This approach has the advantage, that different scales s_χ and s_{cont} can be used for the chiral and continuum extrapolations, respectively. In particular, the lattice spacing $s_\chi = a$ may be used for the scale setting in the chiral extrapolations, which avoids the additional error stemming from the measurement of the scale setting observable. It is, of course, not possible to use the lattice spacing a for the scale setting in the combined extrapolation because the lattice spacing vanishes in the continuum limit. The chiral extrapolation is performed for each value of β individually by fitting a polynomial to the data

$$O_y(x) = O_{\chi, y} + \tilde{c}_{1, y} x + \tilde{c}_{2, y} x^2 + \mathcal{O}(\text{higher}), \quad (13.6)$$

13. Extrapolations

where the dependency on y is written as an index to stress that y is kept fixed in the chiral extrapolation. The coefficients \tilde{c}_i are related to the coefficients of Eq. 13.3 by

$$O_{\chi,y} = O_{\chi,\text{cont}} + c_2 y + c_5 y^2, \quad (13.7)$$

$$\tilde{c}_{1,y} = c_1 + c_3 y + c_6 y^2, \quad (13.8)$$

$$\tilde{c}_{2,y} = c_4. \quad (13.9)$$

To prevent overfitting, the set of fitting parameters should be chosen minimally. In contrast to the combined extrapolation, different sets of fitting coefficients can be used for different values of β which is a further advantage of the two-step approach.

In the second step, the chiral values $O_\chi(y)$ of the observables are extrapolated in a similar fashion to the continuum limit. For this purpose, the values of $O_\chi(y)$, obtained from the chiral extrapolation, are first converted to the scale s_{cont} used for the continuum extrapolation by multiplying with a suitable power of s_{cont}/s_χ . Then, the extrapolation is performed by a polynomial fit

$$O_\chi(y) = O_{\chi,\text{cont}} + c_2 y + c_5 y^2 + \mathcal{O}(\text{higher}). \quad (13.10)$$

13.1.3. Theoretical comparison of the two approaches

Based on the assumption that the observable $O(x, y)$ is analytic in the simulated vicinity of the supersymmetric point (in the quadrant $x \geq 0, y \geq 0$), both, the two-step and the combined extrapolation should provide correct results because then

$$O_{\chi,\text{cont}} = \lim_{(x,y) \rightarrow (0,0)} O(x, y) = \lim_{x \rightarrow 0} \lim_{y \rightarrow 0} O(x, y), \quad (13.11)$$

and the two limits on the r.h.s commute. However, both approaches have advantages and disadvantages, which may lead to different statistical and systematical uncertainties. These are discussed in the following.

The combined approach takes into account all data points in a single fit. Therefore, it requires less fitting parameters in total. Consider, for example, a set of 20 ensembles consisting of four different values of β and five different values of κ for each β . The two-step approach would require four chiral extrapolations and one continuum extrapolation. If only the constant term and the linear orders in x and y are considered, this would amount to $2(4 + 1) = 10$ fitting parameters. The corresponding combined approach requires only four fitting parameters ($O_{\chi,\text{cont}}, c_1, c_2, c_3$). Hence, it is expected to be much more stable against fluctuations of the data. Furthermore, the combined approach returns the most probable values of the fit parameters because it minimizes the global χ_r^2 in the x - y -plane.

13.2. Optimizing the two-step extrapolation

The two-step approach, on the contrary, minimizes χ_r^2 for the chiral and the continuum extrapolations subsequently. Thus, in general, it does not minimize the global χ_r^2 and hence does not find the most likely value of the $O_{\chi,\text{cont}}$. This deviation can be thought of as a bias that vanishes in the limit of infinite statistics.

Besides its shortcomings, the two-step approach also features advantages compared to the combined fit. Firstly, the lattice spacing a can be used for the scale setting in the chiral extrapolations which avoids the additional uncertainty stemming from the measurement of the scale setting observable. Secondly, the set of fit parameters can be adjusted for each extrapolation individually.

13.2. Optimizing the two-step extrapolation

We have tested both extrapolation approaches on the basis of the ground states masses of the chiral multiplet of SU(3)-SYM to optimize the choice of the fit parameters and the scale setting observable. In order disentangle any possible issues appearing in the chiral and continuum extrapolations it is useful to first consider the two-step extrapolations where the chiral and continuum extrapolations are performed separately.

The first step is the chiral extrapolation which is performed individually for the different values of β . As a first attempt, we have tested linear extrapolations ($\tilde{c}_{2,y} = 0$ in Eq. 13.6) using the lattice spacing for the scale setting $s_\chi = a$. We find acceptable values of $0.1 < \chi_r^2 < 3$ in most of the cases, see Tab. 13.1. Larger values of χ_r^2 occur in the extrapolations of the gluino-gluon ground state mass at the two finer lattice spacings

$$\beta = 5.5 : \chi_r^2 = 4.07, \quad (13.12)$$

$$\beta = 5.6 : \chi_r^2 = 7.08. \quad (13.13)$$

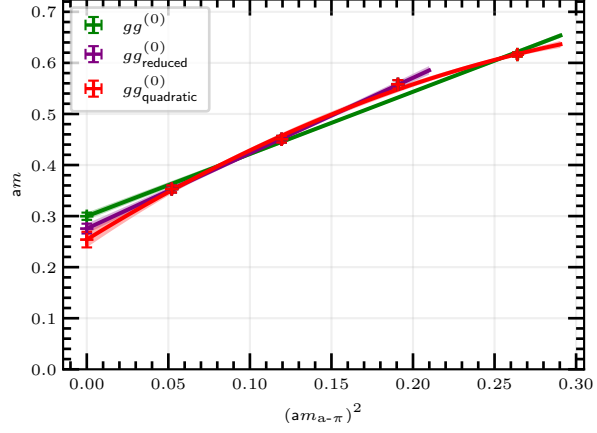
Using a second order polynomial for the fit function in these cases ($\tilde{c}_{1,y} \neq 0 \neq \tilde{c}_{2,y}$)

β	$am_{gg}^{(0)}$	χ_r^2	$am_{a-\eta'}^{(0)}$	χ_r^2	$am_{0^{++}}^{(0)}$	χ_r^2
5.4	0.5272(86)	0.32	0.364(10)	2.19	0.363(32)	0.43
5.45	0.4040(81)	0.37	0.322(22)	0.36	0.310(39)	1.30
5.5	0.366(12)	4.07	0.288(11)	0.09	0.292(51)	0.77
5.6	0.2997(71)	7.08	0.270(14)	2.80	0.298(53)	0.47

Table 13.1.: Chirally extrapolated ground state masses of SU(3)-SYM using all available ensembles and only linear extrapolations in $x = (am_{a-\pi})^2$.

13. Extrapolations

Figure 13.3: Chiral extrapolation of the gluino-gluon ground state mass at $\beta = 5.6$. A first order polynomial (green) cannot accurately resemble all data points. A second order polynomial fits the data much better (red). Alternatively the data point with the largest adjoint pion mass may be neglected, leading to an acceptable first order polynomial fit.



leads to acceptable values of

$$\beta = 5.5 : \chi_r^2 = 0.0170, \quad (13.14)$$

$$\beta = 5.6 : \chi_r^2 = 2.75. \quad (13.15)$$

Closer inspection of the fits for $\beta = 5.6$ shows that the data is best described by a convex function, i.e. $\tilde{c}_{2,y} < 0$, see Fig. 13.3. Apparently, a linear fit function does not suffice to describe the data points at large values of $m_{a-\pi}^2$ accurately enough at the level of our precision and higher orders of the Taylor series become important. The data shows a similar behavior for $\beta = 5.5$ and also for the $a-\eta'$ mass at $\beta = 5.6$ whose extrapolation leads to an acceptable, but rather large value of $\chi_r^2 = 2.80$ when using a linear fit.

A disadvantage of using a second order polynomial for the chiral extrapolation, is that due to the additional fit parameter, the uncertainty of the extrapolated result is larger compared to a linear fit and the extrapolation is more prone to overfitting. As an alternative we have tested to neglect the mass estimates that are outside of the linear regime. This way, the values of χ_r^2 , obtained from the extrapolations of the gluino-gluon ground state mass, significantly reduce to

$$\beta = 5.5 : \chi_r^2 = 0.14, \quad (13.16)$$

$$\beta = 5.6 : \chi_r^2 = 0.06. \quad (13.17)$$

The chirally extrapolated masses, obtained from both methods (second order polynomial or neglecting the ensembles outside of the linear regime) are compatible within their errors, see Tab. 13.2. Due to the considerably larger value of χ_r^2 at $\beta = 5.6$, the method to use using a second order polynomial is slightly disfavored.

13.2. Optimizing the two-step extrapolation

Poly.	Order	\tilde{c}_1	\tilde{c}_2	s_χ	$\kappa = 0.1645$	$w_0 m_{\text{gg}}^{(0)}$	χ_r^2
	1	✓	-	a	✓	1.026(28)	7.08
	1	✓	-	$w_{0,\chi}$	✓	0.994(36)	2.18
	1	✓	-	w_0	✓	0.929(33)	2.38
	2	✓	✓	a	✓	0.869(54)	2.75
	2	✓	✓	$w_{0,\chi}$	✓	0.877(73)	1.11
	2	✓	✓	w_0	✓	0.84(10)	3.88
	1	✓	-	a	-	0.943(35)	0.06
	1	✓	-	$w_{0,\chi}$	-	0.944(44)	0.03
	1	✓	-	w_0	-	0.879(43)	1.38

Table 13.2.: Comparison of chiral extrapolations at $\beta = 5.6$ of the gluino-gluon ground state mass using different polynomial orders and scales. Using the scale w_0 does not reduce the statistical error nor the value of χ_r^2 compared to using $w_{0,\chi}$. The fifth column marks whether the ensemble with $\kappa = 0.1645$ is included in the extrapolation or not. The extrapolation considered for the final results is highlighted in blue.

In order to understand, when the linear description of the data breaks down, it is useful to consider the adjoint pion masses in physical units rather than units of the unphysical lattice spacing, cf. Tab. 6.2. The squared pion masses in units of $w_{0,\chi}$ at the ensembles that are apparently outside the linear regime, are given by $(m_{a-\pi} w_{0,\chi})^2 = 2.445(67)$ and $(m_{a-\pi} w_{0,\chi})^2 = 3.082(87)$ for $\beta = 5.5$, $\kappa = 0.1667$ and $\beta = 5.6$, $\kappa = 0.1645$, respectively. Since these are the largest squared physical pion masses of all ensembles, this suggests that for

$$(m_{a-\pi} w_{0,\chi})^2 \gtrsim 2.5 \quad (13.18)$$

quadratic terms become important. Of course, this value is only a rough estimate that depends on the precision of the data and on the observable. The mass in 0^{++} channel might, for example also be affected, but due to the larger statistical uncertainties the effect is not observed there. We conclude, that at our precision, it is necessary to use a second order polynomial for the chiral extrapolations if ensembles with such large adjoint pion masses are included. In hindsight, it would have therefore been better to only simulate ensembles with $(m_{a-\pi} w_{0,\chi})^2 \lesssim 2.5$.

Another alternative that we have tested is to use the scale $s_\chi = w_0$, i.e. the non-extrapolated values of w_0 , in the chiral extrapolation, which might suppress the effect of higher orders in x , as discussed in Sec. 13.1. Due to the additional error from the measurements of w_0 , the uncertainties are larger in this case. These

13. Extrapolations

Extr. Type	c_2	c_5	$w_0 m_{gg}^{(0)}$	χ_r^2	$w_0 m_{a-\eta'}^{(0)}$	χ_r^2	$w_0 m_{0^{++}}^{(0)}$	χ_r^2
Lin	✓	-	0.782(72)	0.75	0.991(93)	0.18	1.07(31)	0.03
Quad	-	✓	0.887(45)	0.99	0.907(57)	0.11	0.95(19)	0.04
Lin + Quad	✓	✓	0.56(34)	1.03	0.66(62)	0.06	1.4(1.7)	0.004
Lin	✓	-	0.689(94)	2.56	0.95(10)	1.01	1.17(29)	0.21
Quad	-	✓	0.837(58)	3.14	0.884(63)	0.89	1.01(18)	0.27
Lin + Quad	✓	✓	0.00(44)	2.60	-0.20(84)	0.11	2.1(1.5)	0.05

Table 13.3.: Ground state masses of the chiral multiplet, extrapolated to the continuum limit using different fit functions in the two-step approach. The top and bottom tables differ in the way how the data outside the linear regime has been handled in the chiral extrapolations. Top: Data outside of the linear regime has been discarded and a linear fit was used in the chiral extrapolations. Bottom: All data points have been taken into account and a second order polynomial was used in the chiral extrapolations for $\beta = 5.5$ and $\beta = 5.6$. The data considered for the final results is highlighted in blue.

larger uncertainties may hide the effects stemming from higher orders. For better comparison, we have therefore also performed the chiral extrapolations using $s_\chi = w_{0,\chi}$ which should provide very similar results to the case $s_\chi = a$ since it amounts to just multiplying all masses by a common factor, but takes into account the additional uncertainty of $w_{0,\chi}$. The results for the gluino-gluon at $\beta = 5.6$ are shown in Tab. 13.2. Indeed, the extrapolated mass and its uncertainty using $s_\chi = w_{0,\chi}$ is very similar to the case $s_\chi = a$, while the value χ_r^2 , is smaller for $s_\chi = w_{0,\chi}$ since the data points are essentially unchanged, but have larger uncertainties. Using the scale w_0 does not reduce the error of the extrapolated results, nor does it reduce χ_r^2 , but in fact χ_r^2 appears to be larger compared to using $w_{0,\chi}$. We therefore stay with $s_\chi = a$ for the scale setting in the chiral extrapolations.

The second step of the two-step approach is the continuum extrapolation. For this purpose, we convert the chirally extrapolated values to units of w_0 ¹ and fit a polynomial (Eq. 13.10) to extract $O_{\chi,\text{cont}}$. As discussed in Sec. 13.1, we test different fit functions: Linear, quadratic and linear + quadratic extrapolations. The extrapolated values, their uncertainties and the corresponding values of χ_r^2 are presented in Tab. 13.3. The values of χ_r^2 for the linear and the quadratic continuum extrapolations are quite similar. Hence, we cannot deduce whether the linear or the quadratic order in y is dominant in the simulated parameter range. Using both, linear and quadratic orders in y , leads to very large uncertainties in

¹Note that after the chiral extrapolation we do not need to distinguish between w_0 and $w_{0,\chi}$ anymore, because in this limit $w_0 = w_{0,\chi}$ per definition.

13.3. Optimizing the combined extrapolation

the continuum extrapolations and should not be used.

From the continuum extrapolations we can also gain additional information about the question, discussed above, whether to use second order polynomials or to discard data outside the linear regime in the chiral extrapolations. For this purpose, we have performed the continuum extrapolations for the differently chirally extrapolated data sets; the results are also included in Tab. 13.3. The values of χ_r^2 of the continuum extrapolations are smaller when the data outside the linear regime is discarded. As discussed above, this method is also favored by the values of χ_r^2 in the chiral extrapolations. It therefore seems more consistent to discard the data affected by quadratic effects and to always use linear fits in the chiral extrapolations than to use second order polynomials.

We conclude that it is optimal to use the scale $s_\chi = a$ and $s_{\text{cont}} = w_{0\chi}$, and to discard the mass estimates outside the linear regime at large values of $(w_{0,\chi} m_{a-\pi})^2$, namely

- $\beta = 5.6$, $\kappa = 0.1645$: All three channels.
- $\beta = 5.5$, $\kappa = 0.1667$: Gluino-gluon.

Since it is not clear, whether the linear or the quadratic continuum extrapolation is to be favored, we consider both for the final results.

13.3. Optimizing the combined extrapolation

Similarly to the case of the two-step approach, we have tested several different combinations of fitting parameters and scales in the combined extrapolations. Of course, the fitting parameter $O_{\chi,\text{cont}}$ is always included. Based on our experience in the two-step extrapolation, we have excluded the masses, estimated from ensemble $\beta = 5.6$, $\kappa = 0.1645$, and the gluino-gluon mass at $\beta = 5.5$, $\kappa = 0.1667$, when not using the quadratic term in x , i.e. when $c_4 = 0$. The extrapolated masses, their uncertainties and the χ_r^2 of the fits are collected in Tab. 13.4.

We first consider the results obtained using the chirally extrapolated scale $w_{0,\chi}$. The minimal sensible choice of fitting parameters is to allow only terms proportional to x and \tilde{y} , i.e. only the fit parameters c_1 and c_2 . This leads to a rather large value of $\chi_r^2 = 3.35$ in the linear extrapolation of the gluino-gluon mass, which indicates that it is not sufficient to consider only these two terms. The reason becomes clear when visualizing the data, see Fig. 13.4. The slope in x -direction changes with β and therefore with y . Hence, the mixed term $c_3 x \tilde{y}$ needs to be included in the fit function for a reliable extrapolation. This reduces χ_r^2 to an acceptable value $\chi_r^2 = 0.67$. For the $a-\eta'$ and the 0^{++} channels, the reduction of χ_r^2 , when the c_3 term is included, is not as drastic as for the gluino-gluon because

13. Extrapolations

the slopes do not vary so much with β (see Fig. 13.5) and the uncertainties of the data points in the 0^{++} channel are much larger than the ones of the gluino-gluon.

We have also tested to include the term proportional to x^2 (c_4) and not neglecting any data points. However, we find that it lowers the precision of the final results. This is intuitive because only very few data points are outside the linear regime. Therefore, it is not beneficial to include these data points at the cost of having to use an additional fit parameter that results in larger uncertainties of the extrapolated results.

Since it is not clear, a priori, whether the linear order in \tilde{y} or the quadratic order in y is dominating in the simulated parameter range, we have also performed quadratic extrapolations, i.e. instead of c_2 and c_3 , the fit parameters c_5 and c_6 are used. The results are very similar to the linear extrapolations, i.e. the masses are compatible within errors with the corresponding ones from the linear extrapolations and also the values of χ_r^2 are very similar. Also in the quadratic extrapolations it turns out to be optimal to use three fitting parameters c_1 , c_5 and c_6 .

Based on the values of χ_r^2 we cannot conclude if the linear or quadratic order in y is dominating in the simulated parameter range, in agreement with the discussion of the two-step approach in Sec. 13.2. This suggests that the linear order might still be important, but one would need more data points and/or higher precision to make a clear statement. Principally, it could even depend on the observable. Unfortunately, the linear + quadratic fit in y does not provide any further information regarding this point since the resulting uncertainties are very large due to the larger number of coefficients.

Additionally, we have tested to use the scale $s = w_0$ instead of $s = w_{0,\chi}$. Interestingly, even the minimal choice of using only the c_1 and c_2 terms leads to an acceptable value of $\chi_r^2 = 1.14$ for the gluino-gluon. This suggests, that the coefficient of the mixed term (c_3) is not as large compared to the case of using $w_{0,\chi}$ for the scale setting. One could therefore be tempted to use only c_1 and c_2 for the final results. However, the quadratic extrapolation (c_1 and c_4) also yields acceptable values of χ_r^2 , but different results for the masses, which are incompatible with the ones from the linear extrapolation (far outside of the uncertainties). We therefore prefer the more conservative choice to also include in this case the terms c_3 and c_6 for the linear and the quadratic extrapolation, respectively. Moreover, when using $s = w_0$ for the scale setting, also extrapolations using the linear and the quadratic order in y are stable as long as only one of the mixed terms (c_3 or c_6) is used.

In summary, we have found that the different extrapolations with the fitting parameters (c_1, c_2, c_3) and (c_1, c_5, c_6) lead to reliable extrapolations. The results of these extrapolations are all compatible within their uncertainties. The ones using the scale $s = w_{0,\chi}$ have slightly smaller values of χ_r^2 compared to $s = w_0$. We therefore consider these for the final results. In addition, we also include the

13.3. Optimizing the combined extrapolation

linear + quadratic extrapolation with the coefficients (c_1, c_2, c_5, c_6) and using the scale w_0 into the considerations for the final results.

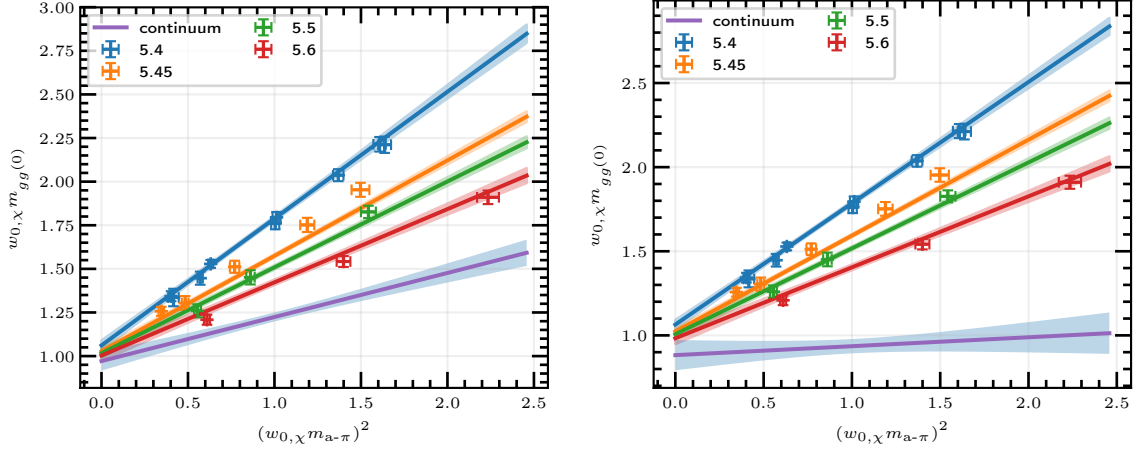


Figure 13.4.: Projection of the plots in Fig. 13.1 to the continuum plane $a/w_0 = 0$ for the gluino-gluon ground state mass. Shown are the data points and slices of the fit for each value of β (see legend) together with the extrapolated fit function at vanishing lattice spacing $a/w_0 = 0$. Left: Linear extrapolation. Right: Quadratic extrapolation.

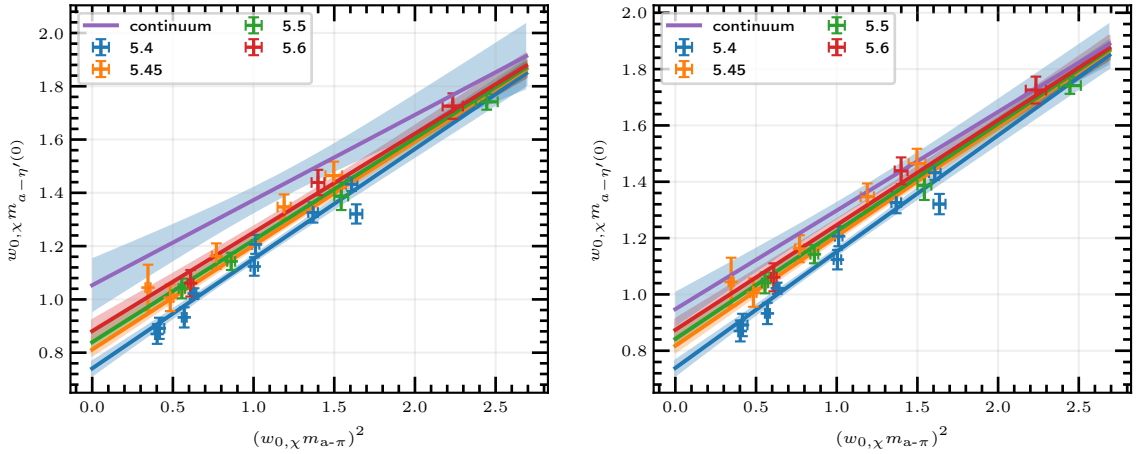


Figure 13.5.: Similar plot for the $a-\eta'$ ground state mass as in Fig. 13.4.

s	y -Order	c_1	c_2	c_3	c_4	c_5	c_6	$sm_{gg}^{(0)}$	χ_r^2	$sm_{a-\eta'}^{(0)}$	χ_r^2	$sm_{0++}^{(0)}$	χ_r^2
w_{0_x}	Lin	✓	✓	-	-	-	-	0.282(46)	3.35	0.955(52)	1.32	1.83(14)	0.89
w_{0_x}	Lin	✓	✓	✓	-	-	-	0.847(87)	0.67	1.04(10)	1.34	1.13(31)	0.55
w_{0_x}	Lin	✓	✓	✓	✓	-	-	0.819(96)	0.70	0.93(13)	1.22	1.29(32)	0.63
w_{0_x}	Quad	✓	-	-	-	✓	-	0.594(30)	4.01	0.889(35)	1.29	1.403(93)	0.91
w_{0_x}	Quad	✓	-	-	-	✓	✓	0.951(54)	1.19	0.943(62)	1.31	0.97(18)	0.52
w_{0_x}	Quad	✓	-	-	✓	✓	✓	0.911(64)	1.17	0.853(86)	1.19	1.05(21)	0.59
w_{0_x}	Lin+Quad	✓	✓	✓	-	✓	-	0.23(25)	0.28	0.74(32)	1.36	0.56(97)	0.56
$w_{0,x}$	Lin+Quad	✓	✓	-	-	✓	✓	0.06(24)	0.34	0.72(31)	1.35	0.80(92)	0.55
w_0	Lin	✓	✓	-	-	-	-	0.886(26)	1.14	0.807(30)	1.33	1.150(87)	0.46
w_0	Lin	✓	✓	✓	-	-	-	0.991(76)	1.66	0.81(12)	1.42	1.26(37)	0.51
w_0	Lin	✓	✓	✓	✓	-	-	1.009(74)	1.64	0.85(12)	1.51	1.46(33)	0.58
w_0	Quad	✓	-	-	-	✓	-	0.957(16)	1.53	0.695(20)	1.69	0.757(61)	0.77
w_0	Quad	✓	-	-	-	✓	✓	0.976(36)	1.61	0.768(51)	1.65	1.02(15)	0.61
w_0	Quad	✓	-	-	✓	✓	✓	1.039(48)	1.97	0.756(81)	1.66	1.10(21)	0.62
w_0	Lin+Quad	✓	✓	✓	-	✓	-	0.889(74)	1.47	0.96(11)	1.47	1.40(32)	0.60
w_0	Lin+Quad	✓	✓	-	-	✓	✓	0.847(66)	1.36	0.940(91)	1.44	1.29(29)	0.57

Table 13.4.: Extrapolations of the ground state masses of the chiral supermultiplet to the supersymmetric point using the combined fitting approach and different choices of fitting functions and scales s . The ticks in the c_i -columns mark which terms have been taken into account (cf. Eq. 13.5). The rows with the combinations of fit parameters and scale considered for the final results are highlighted in blue. In the extrapolations that include c_4 (quadratic order in $(sm_{a-\pi})^2$), all data points are included, whereas for the other ones, the estimated masses outside the linear regime in x have been discarded (all three channels at $\beta = 5.6$, $\kappa = 0.1645$, and the gluino-gluon mass at $\beta = 5.5$, $\kappa = 0.1667$).

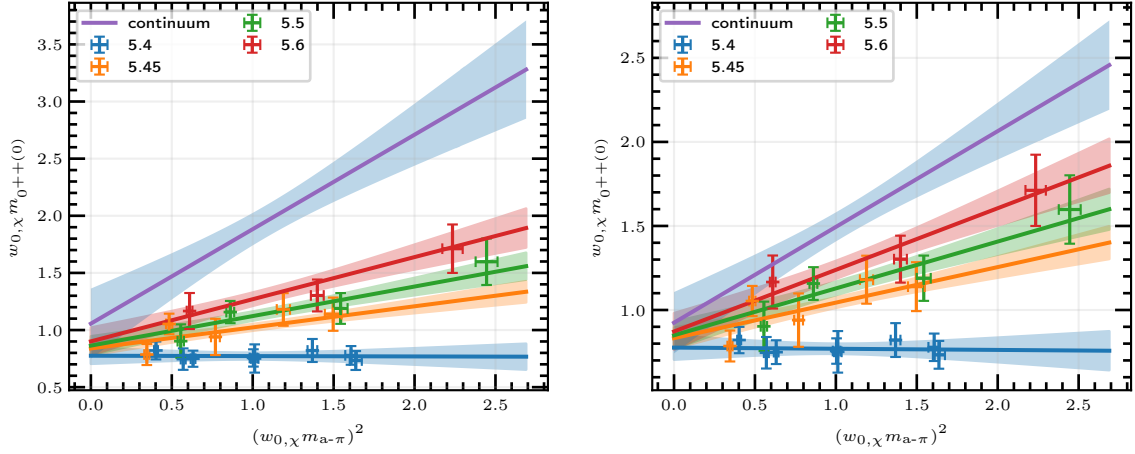


Figure 13.6.: Similar plot for the scalar ground state mass as in Fig. 13.4.

13.4. Summary of the extrapolations

The tests and optimization of the two extrapolation approaches show that it is optimal to include only the linear order in x and discard the few data points that are outside of the linear regime. For our the ground state masses of SU(3)-SYM, this corresponds to discarding mass estimates from the ensembles with $(m_{a-\pi} w_{0,\chi})^2 \gtrsim 2.5$. It is not clear whether the linear or the quadratic order in the lattice spacing is dominating in the simulated parameter range.

We have found several reasonable procedures for the extrapolation to the chiral and continuum limit out of which we consider five for the final results. They are listed in Tab. 13.5. The mass estimates from these extrapolation procedures are compatible within the statistical uncertainties for each of the channels. This indicates that the systematic error, resulting from the choice of the extrapolation approach, is under control, i.e. it is not larger than the statistical uncertainties obtained from the fits. It is not clear which of the extrapolation procedures is to be favored. One could argue that the combined approach has theoretical advantages as discussed in Sec. 13.1.3. However, also the two-step extrapolation has advantages, such as the possibility to choose $s_\chi = a$ in the chiral extrapolations. For the final results, which are discussed in Sec. 14, we therefore average the masses and their errors obtained from the five different extrapolations. We do not weight the average by the uncertainties because the deviations of the results are rather systematic errors than statistical ones since the results are all obtained from the same data set. Hence, it does not seem consistent to use the statistical uncertainties as weights.

13. Extrapolations

Approach	Extrapolation type	s_χ	s_{cont}	Fit parameters
Two-step	Linear	a	$w_{0,\chi}$	$\tilde{c}_{1,y}, c_2$
Two-step	Quadratic	a	$w_{0,\chi}$	$\tilde{c}_{1,y}, c_5$
Combined	Linear	$w_{0,\chi}$	$w_{0,\chi}$	c_1, c_2, c_3
Combined	Quadratic	$w_{0,\chi}$	$w_{0,\chi}$	c_1, c_5, c_6
Combined	Linear + Quadratic	w_0	$w_{0,\chi}$	c_1, c_2, c_5, c_6

Table 13.5.: Collection of the extrapolation approaches that have turned out to be most useful and that are considered for the final results

Note that for the tests of the different extrapolation techniques we have considered the ground states of SU(3)-SYM, which has been simulated using a clover-improved action. The simulations of SU(2)-SYM, however, were performed without clover improvement. Therefore, in the case of SU(2)-SYM, we expect the linear term in y to be dominating and do not include the quadratic order in y for the extrapolations.

14. Results of the mass spectra and the mixing in the scalar channel

Using the two-step and combined extrapolation approaches, discussed in Sec. 13, we have extrapolated the masses of the ground and excited states of the chiral supermultiplet as well as the mixing coefficients of the scalar channel to the supersymmetric point. The extrapolations yield also first insights into supersymmetry breaking by a non-vanishing gluino mass. In the following, the results from the extrapolations are summarized (Secs. 14.1 to 14.4) and discussed (Sec. 14.5). Some parts of these results have been published in [30] and [37]. Here, an updated and much more detailed discussion is provided.

14.1. Light bound state masses of SU(2)-SYM

The results for the masses of the ground and first excited states of the chiral supermultiplet of SU(2)-SYM, extrapolated to the chiral and continuum limit, are collected in Tabs. 14.1 and 14.2. Similarly to the case of SU(3), we have neglected the data for gluino-gluon ground state mass of the ensemble $\beta = 1.9, \kappa = 0.1433$, which appeared to be outside the linear regime ($(w_0 m_{a-\pi})^2 = 2.825(81)$). Since the SU(2)-SYM simulations were performed without clover improvement, we have only taken into account the two linear extrapolations out of the five approaches summarized in Tab. 13.5. The continuum extrapolations of the two approaches are depicted in Fig. 14.1. Further plots can be found in Fig. A.2 in App. A.7.1. The results from the two-step and from the combined approach are consistent within their uncertainties except for the mass of the ground state in the scalar channel where the results from the combined fit deviates from the result of the two-step approach by 2.3σ . When neglecting the outlier from the combined approach, we find the expected degeneracy of the ground states masses in the supersymmetric point

$$w_0 m_{\text{gg}}^{(0)} = 0.945(62), \quad w_0 m_{a-\eta'}^{(0)} = 0.978(61), \quad w_0 m_{0^{++}}^{(0)} = 1.12(21). \quad (14.1)$$

To estimate the mass of the supermultiplet we use a weighted average of the masses in the three channels

$$w_0 m^{(0)} = 0.968(43), \quad (14.2)$$

where the weights are given by the inverse of the squared uncertainties. The uncertainty of the weighted average is estimated by standard error propagation.

14. Results of the mass spectra and the mixing in the scalar channel

For simplicity, we have not taken into account correlations among the different channels. The masses of all three channels are compatible with this estimate within uncertainties.

If, on the other hand, the outlier is not neglected, we obtain

$$w_0 m_{0^{++}}^{(0)} = 1.36(18) \quad (14.3)$$

leading to a modified result for the mass of the supermultiplet

$$w_0 m^{(0)} = 0.984(42). \quad (14.4)$$

In this case, the mass of the $0^{(++)}$ channel deviates by 2.1σ from this average.

Let us discuss the outlier. Unfortunately, the SU(2)-SYM ensembles are very inhomogeneously distributed in the parameter space spanned by β and κ . For $\beta = 1.6$ there are only ~ 1500 thermalized configurations on average for each ensemble, while for $\beta = 1.75$ and $\beta = 1.9$ there are 7000 and 13000 thermalized configurations, respectively, on average for each ensemble. Furthermore, the range of simulated physical pion masses is very different for each value of β (see Fig. 14.2 and Tab. 6.2). Due to the inhomogeneous sampling of the parameter space, it is plausible that the fit of the masses, especially in the scalar channel, in which the uncertainties are much larger than in the other channels, could be unstable. In particular, the estimation of the mixed term ($c_3 xy$) which determines the change of the slope in the x -direction with varying y , could be poor because there are only very few data points in the region $(w_{0,\chi m_{a-\pi}})^2 > 1$. From the present data it is, hence, not unambiguously clear whether the outlier should be taken seriously or not.

Fortunately, such an ambiguity does not occur in the extrapolations of the excited state masses. Here, the two-step extrapolation and the combined approach yield compatible results that are degenerate within errors among the three channels

$$w_0 m_{\text{gg}}^{(1)} = 3.07(24), \quad w_0 m_{a-\eta'}^{(1)} = 2.89(22), \quad (14.5)$$

$$w_0 m_{0^{++}}^{(1)} = 2.87(28), \quad w_0 m_{\text{gb}^{--}}^{(0)} = 3.20(33). \quad (14.6)$$

As already observed in Sec. 9.3.3, the lowest mass, determined from the pseudo-scalar glueball interpolator, is compatible with the excited state multiplet at all values of β and also in the continuum limit, see Fig. 14.1. It is therefore very likely that the first excited state in the pseudoscalar channel is a mixed state that includes glueball and meson components. However, a detailed mixing analysis has only been performed for the scalar channel in the scope of this thesis.

The weighted average of the three channels yields an estimate for the supermul-

14.1. Light bound state masses of SU(2)-SYM

triplet of excited states

$$w_0 m^{(1)} = 2.98(13) , \quad (14.7)$$

where, before calculating the weighted average over all three channels, the mass of the pseudoscalar channel has been determined by a weighted average of the results from the glueball and the meson analysis. The masses of all three channels are compatible with this value within errors.

β	$am_{gg}^{(0)}$	χ_r^2	$am_{a-\eta'}^{(0)}$	χ_r^2	$am_{0^{++}}^{(0)}$	χ_r^2
1.6	0.623(22)	1.23	0.362(36)	0.31	0.374(70)	0.10
1.75	0.3122(93)	0.94	0.193(32)	0.28	0.252(35)	1.74
1.9	0.167(11)	0.01	0.1511(51)	0.22	0.173(30)	3.70
Extr. type	$w_0 m_{gg}^{(0)}$	χ_r^2	$w_0 m_{a-\eta'}^{(0)}$	χ_r^2	$w_0 m_{0^{++}}^{(0)}$	χ_r^2
Lin (two-step)	0.930(69)	0.21	0.979(57)	1.96	1.12(21)	3.06
Lin (combined)	0.959(54)	0.65	0.976(64)	0.42	1.60(15)	2.71
Average	0.945(62)	-	0.978(61)	-	1.36(18)	-

Table 14.1.: Ground state masses of the chiral supermultiplet of SU(2)-SYM extrapolated to the chiral limit (upper table), and to the continuum limit (lower table). The outlier in the scalar channel is highlighted in red. The last row, highlighted in green, summarizes the final results (averages of both extrapolation approaches).

β	$am_{gg}^{(1)}$	χ_r^2	$am_{a-\eta'}^{(1)}$	χ_r^2	$am_{0^{++}}^{(1)}$	χ_r^2	$am_{gb^{++}}^{(0)}$	χ_r^2
1.6	1.08(23)	-	0.932(89)	-	0.53(42)	-	1.014(14)	-
1.75	0.663(52)	2.33	0.678(52)	3.00	0.594(61)	0.75	0.69(14)	0.79
1.9	0.457(15)	1.52	0.455(30)	4.77	0.389(17)	0.39	0.502(45)	0.49
Extr. t.	$w_0 m_{gg}^{(1)}$	χ_r^2	$w_0 m_{a-\eta'}^{(1)}$	χ_r^2	$w_0 m_{0^{++}}^{(1)}$	χ_r^2	$w_0 m_{gb^{++}}^{(0)}$	χ_r^2
Lin (2s)	3.06(23)	0.64	3.08(25)	0.04	2.75(31)	0.28	3.37(37)	0.19
Lin (c)	3.07(24)	1.63	2.70(18)	3.13	2.98(25)	0.62	3.03(29)	0.78
Average	3.07(24)	-	2.89(22)	-	2.87(28)	-	3.20(33)	-

Table 14.2.: Table for the first excited states corresponding to Tab. 14.1 . In the first column 2s and c abbreviate two-step and combined, respectively.

14. Results of the mass spectra and the mixing in the scalar channel

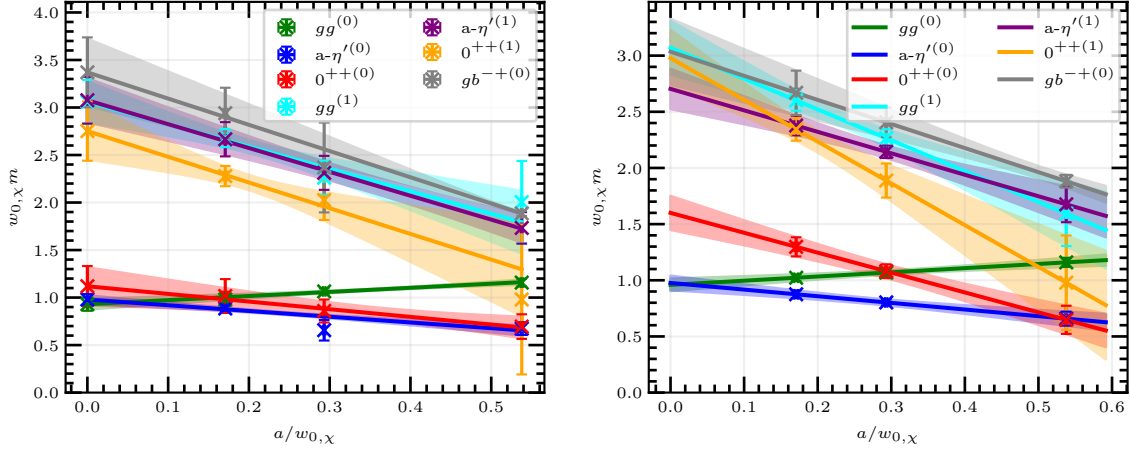


Figure 14.1.: Extrapolations to the supersymmetric point of the ground and first excited states of the chiral supermultiplet of SU(2)-SYM. Left: Continuum extrapolation of the two-step approach. Right: Combined extrapolation, projected to the chiral plane, i.e. to the plane where the gluino mass vanishes. The data points in the plot on the right mark the chirally extrapolated values at the simulated lattice spacings. Since the chiral and continuum extrapolation is done simultaneously, they align completely with the fit curves.

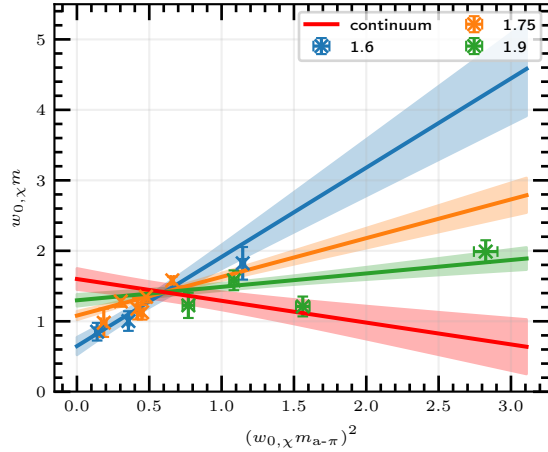


Figure 14.2: Combined extrapolation of the ground state in the scalar channel of SU(2)-SYM projected to the continuum plane where $a/w_{0,\chi} = 0$.

14.2. Light bound state masses of $SU(3)$ -SYM

The results of the extrapolations of the ground and first excited state masses of $SU(3)$ -SYM are collected in Tabs. 14.3 and 14.4. As explained in Sec. 13, we have neglected the masses estimated from the ensemble $\beta = 5.6$, $\kappa = 0.1645$ completely and also discarded the gluino-gluon ground state mass at $\beta = 5.5$, $\kappa = 0.1667$.

Averaging the results over the different extrapolations we obtain estimates for the masses of the ground states

$$w_0 m_{\text{gg}}^{(0)} = 0.863(65), \quad w_0 m_{\text{a-}\eta'}^{(0)} = 0.964(81), \quad w_0 m_{0^{++}}^{(0)} = 1.08(26), \quad (14.8)$$

of the chiral supermultiplet. The weighted average yields an estimate for the ground state mass of the chiral supermultiplet

$$m^{(0)} w_0 = 0.909(50). \quad (14.9)$$

Within their errors, the ground state masses obtained in all three channels are compatible with this value. Hence, we have found the expected degeneracy.

The corresponding analysis of the first excited states yields

$$w_0 m_{\text{gg}}^{(1)} = 2.90(18), \quad w_0 m_{\text{a-}\eta'}^{(1)} = 2.59(14), \quad w_0 m_{0^{++}}^{(1)} = 1.78(47), \quad (14.10)$$

The mass of the first excited state in the $0^{(++)}$ channel is considerably lower ($m_{0^{++}}^{(1)} = 1.78(47)$) than the ones of the gluino-gluon and the $\text{a-}\eta'$. The weighted average over only the gluino-gluon and the $\text{a-}\eta'$ channels yields

$$w_0 m_{\text{gg,a-}\eta'}^{(1)} = 2.71(11), \quad (14.11)$$

and the masses from both channels are compatible with this estimate. Including also the scalar channel yields a weighted average

$$w_0 m^{(1)} = 2.62(11) \quad (14.12)$$

and the mass of the scalar $0^{(++)}$ channel deviates by 1.8σ from this weighted average. This deviation can still be explained by statistical fluctuations. A more detailed discussion is provided in Sec. 14.5.

14. Results of the mass spectra and the mixing in the scalar channel

β	$am_{gg}^{(0)}$	χ_r^2	$am_{a-\eta'}^{(0)}$	χ_r^2	$am_{0^{++}}^{(0)}$	χ_r^2
5.4	0.5272(86)	0.32	0.364(10)	2.19	0.363(32)	0.43
5.45	0.4040(81)	0.37	0.322(22)	0.36	0.310(39)	1.30
5.5	0.332(17)	0.13	0.288(11)	0.09	0.292(51)	0.77
5.6	0.2755(96)	0.06	0.244(18)	1.05	0.271(66)	0.46
Extr. type	$w_0m_{gg}^{(0)}$	χ_r^2	$w_0m_{a-\eta'}^{(0)}$	χ_r^2	$w_0m_{0^{++}}^{(0)}$	χ_r^2
Lin (two step)	0.782(72)	0.75	0.991(93)	0.18	1.07(31)	0.03
Quad (two step):	0.887(45)	0.99	0.907(57)	0.11	0.95(19)	0.04
Lin (combined)	0.847(87)	0.67	1.04(10)	1.34	1.13(31)	0.55
Quad (combined)	0.951(54)	1.19	0.943(62)	1.31	0.97(18)	0.52
Lin+Quad (combined)	0.847(66)	1.36	0.940(91)	1.44	1.29(29)	0.57
Average	0.863(65)	-	0.964(81)	-	1.08(26)	-

Table 14.3.: Ground state masses of the chiral supermultiplet of SU(3)-SYM, extrapolated to the chiral limit (upper table), and to the continuum limit (lower table). The last row, highlighted in green, summarizes the final results (averages of the different extrapolation approaches)

β	$am_{gg}^{(1)}$	χ_r^2	$am_{a-\eta'}^{(1)}$	χ_r^2	$am_{0^{++}}^{(1)}$	χ_r^2
5.4	1.106(49)	1.54	0.889(19)	1.99	0.71(17)	1.77
5.45	0.910(46)	6e-4	0.761(29)	1.34	0.67(11)	0.42
5.5	0.883(27)	0.80	0.741(17)	1.09	0.61(11)	1.73
5.6	0.747(20)	0.04	0.649(32)	1.84	0.459(53)	0.90
Extr. type	$w_0m_{gg}^{(1)}$	χ_r^2	$w_0m_{a-\eta'}^{(1)}$	χ_r^2	$w_0m_{0^{++}}^{(1)}$	χ_r^2
Lin (two step)	2.96(21)	0.33	2.73(16)	0.28	1.68(59)	0.29
Quad (two step)	2.73(12)	0.33	2.40(10)	0.44	1.67(34)	0.28
Lin (combined)	3.03(22)	0.90	2.84(18)	1.33	1.90(59)	1.97
Quad (combined)	2.77(13)	0.90	2.47(11)	1.29	1.86(34)	2.00
Lin+Quad (combined)	3.00(21)	0.88	2.53(15)	1.11	0.95(60)	1.54
Average	2.90(18)	-	2.59(14)	-	1.78(47)	-

Table 14.4.: Table for the first excited states corresponding to Tab. 14.3. The linear + quadratic extrapolation (red) was unstable for the first excited state of the scalar channel and thus has been neglected for the final results.

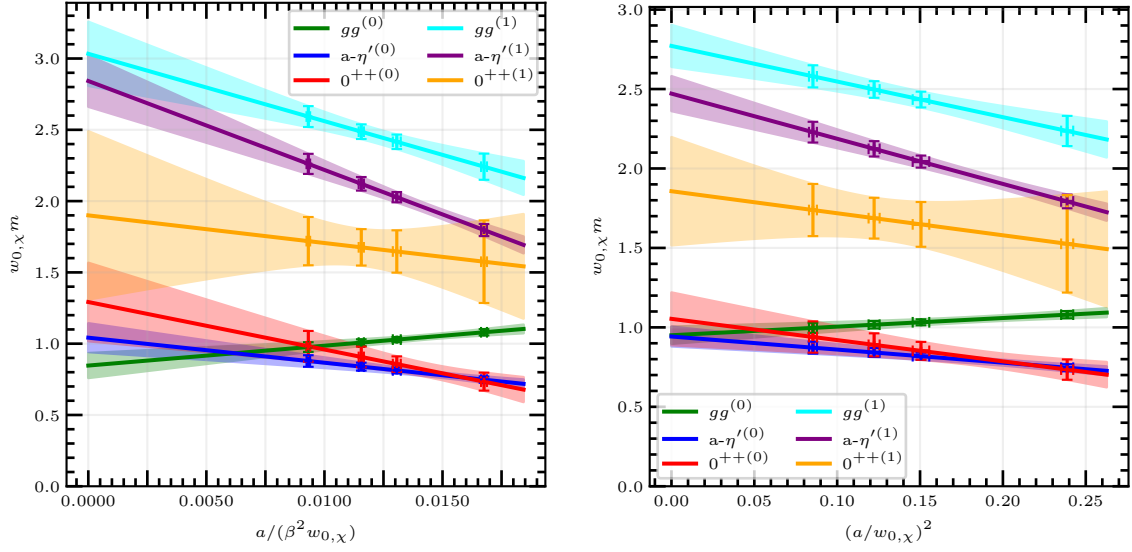


Figure 14.3.: Fit functions of the combined extrapolations, projected to the chiral plane ($(w_0 m_{a-\pi})^2 = 0$) for the ground and first excited states masses of chiral multiplet. Left: Linear extrapolation. Right: quadratic extrapolation. The data points mark the chirally extrapolated values at the simulated lattice spacings. Since the chiral and continuum extrapolation is done simultaneously, they align completely with the fit curves.

14.3. Soft supersymmetry breaking

If supersymmetry exists in nature, it must be broken since no supersymmetric particles have been observed, yet. The breaking mechanisms are still unknown. One possibility, is a dynamically generated gluino-mass, which breaks supersymmetry softly. The fit parameter c_1 of the combined extrapolation approach provides insight into the symmetry breaking by a non-vanishing gluino-mass and is, hence, of special interest. The parameters c_2 and c_5 quantify the supersymmetry breaking by lattice discretization artifacts.

We have collected the numerical results for c_1 in Tabs. 14.5 and 14.6 for the ground and first excited states of SU(3)-SYM. Since the parameter space spanned by β and κ is sampled not very homogeneously in the case of the SU(2)-SYM simulations, we have not performed such an analysis for SU(2)-SYM.

When employing the chirally extrapolated scale $w_{0,\chi}$, the results are not very consistent, which is most pronounced in the case of the gluino-glue ground state where the results from linear, quadratic and linear+quadratic extrapolations are not compatible within their uncertainties. Using the scale $s = w_0$, however, provides consistent results. This is most likely due to the fact that the slopes

14. Results of the mass spectra and the mixing in the scalar channel

of $O(x, y)$ in x -direction vary only slowly with y when using $s = w_0$, i.e. the cross terms $c_3 x \tilde{y}$ and $c_6 x y^2$ are small, which is also observed in Sec. 13.3. Therefore, the extrapolation of the slope c_1 is much more stable in this case. The final results for the ground states (also displayed in Tab. 14.5) have been obtained from a weighted average over the three different extrapolations. We find that the scalar ground state is affected the least by a non-zero gluino mass and the pseudoscalar ground state is affected the most, while the gluino-gluon ground state is between the two. This is consistent with the ordering predicted in [50] on the basis of an effective field theory model (cf. Sec. 2.3.2).

The analysis of the slopes c_1 of the corresponding first excited states yields rather large uncertainties. Hence, it is difficult to interpret this data and no clear statement on the ordering of the states by a SUSY breaking gluino mass can be made based on our analysis. The results do, however, favor a positive contribution to the bound state masses, in contrary to the analysis in [50] which predicts a negative mass contribution in this case.

s	Extrapolation	$c_{1,gg}^{(0)}$	$c_{1,a-\eta'}^{(0)}$	$c_{1,0^{++}}^{(0)}$
$w_{0,\chi}$	Lin (combined)	0.079(73)	0.325(72)	0.74(24)
$w_{0,\chi}$	Quad (combined)	0.267(46)	0.353(44)	0.53(15)
$w_{0,\chi}$	Lin+Quad (combined)	0.322(49)	0.360(45)	0.44(13)
w_0	Lin (combined)	0.252(99)	0.35(13)	-0.02(44)
w_0	Quad (combined)	0.291(53)	0.378(78)	0.06(24)
w_0	Lin+Quad (combined)	0.261(55)	0.387(78)	0.14(25)
w_0	Average	0.278(69)	0.372(95)	0.06(31)

Table 14.5.: Extrapolated results for the slopes c_1 of the ground states of SU(3)-SYM. The results using the scale $w_{0,\chi}$ (red) do not seem trustworthy because using different extrapolations result in very different results for the gluino-gluon. The results when using the scale w_0 seem to be stable and the average over the different extrapolations of these stable results is provided in the last row.

14.4. Mixing coefficients in the scalar channel

s	Extrapolation	$c_{1,gg}^{(1)}$	$c_{1,a-\eta'}^{(1)}$	$c_{1,0^{++}}^{(1)}$
$w_{0,\chi}$	Lin (combined)	0.16(18)	0.17(14)	-0.10(54)
$w_{0,\chi}$	Quad (combined)	0.33(10)	0.369(86)	0.13(30)
$w_{0,\chi}$	Lin+Quad (combined)	0.36(11)	0.406(89)	0.27(31)
w_0	Lin (combined)	0.10(29)	-0.02(22)	0.63(94)
w_0	Quad (combined)	0.24(16)	0.22(13)	0.37(52)
w_0	Lin+Quad (combined)	0.19(16)	0.33(13)	0.48(53)

Table 14.6.: Slopes c_1 of the first excited states corresponding to Tab. 14.5. The uncertainties are rather large.

14.4. Mixing coefficients in the scalar channel

In addition to the extrapolation of the masses and the slopes c_1 , we have extrapolated the mixing coefficients $c_{0^{++}}^{(0)(g)}, c_{0^{++}}^{(0)(m)}$ of the scalar ground states and $c^{(1)(g)}, c^{(1)(m)}$ of the corresponding first excited states to the supersymmetric limit. The results are listed in Tabs. 14.7 and 14.8. The corresponding plots of the extrapolations are presented in Figs. A.4 and A.5 in App. A.7.2. The results indicate a rather large mixing of glueball and meson components in the ground and first excited state of the scalar channel.

The mixing coefficients come with much larger uncertainties than the masses, which makes the extrapolations difficult. Some of the fits have very large values of χ_r^2 up to $\chi_r^2 = 10.10$ in the case of two-step extrapolations for the gauge group SU(2). This indicates that the uncertainties are underestimated in some cases. A possible explanation is that in addition to the statistical errors that we have considered, there are also systematic errors that we have not taken into account. As explained in Sec. 10, the calculation of the mixing coefficients requires that the physical state is described reasonably well by the interpolating fields. This may not always be the case and this is hence a source of systematic errors. Due to the large uncertainties, we have decided to use all data points, including the ones that are outside of the linear regime when considering the masses, to obtain more stable fits. Possible quadratic effects are most likely only relevant at a much higher precision than the one achieved with our statistics.

In the case of SU(2)-SYM we have used the same techniques for the extrapolations as for the extrapolation of the masses. In the case of SU(3)-SYM, however, due to the limited statistics, we had to restrict the fit function in the chiral plane ($m_{a-\pi}^2 = 0$) to a constant; i.e. in the combined extrapolations we have only used the fitting coefficients c_1 and c_3 in Eq. 13.5 and for the continuum extrapolation of the two-step approach we fitted a constant to the chirally extrapolated data.

14. Results of the mass spectra and the mixing in the scalar channel

One might argue that such fits are unreasonable. As an alternative one could therefore also take the coefficients obtained from the finest lattice spacing as the final results.

Due to the large and possibly underestimated uncertainties, the results for the mixing coefficients should be considered rather qualitatively than quantitatively. We find for both gauge groups SU(2) and SU(3) rather large mixing coefficients between 0.4 and 0.95, indicating a considerably large mixing of glueballs and mesons in the ground and first excited state of the 0^{++} channel.

Note that for the pseudoscalar channel we have found no apparent mixing in the ground state which is manifested by the vanishing off-diagonal blocks (mixing terms) in the correlation matrix (Eq. 9.12), cf. Sec. 10. A full quantitative mixing analysis for the corresponding first excited state has not been performed in the scope of this thesis.

β / Extr.	$c^{(0)(g)}$	χ_r^2	$c_{0^{++}}^{(0)(m)}$	χ_r^2	$c_{0^{++}}^{(1)(g)}$	χ_r^2	$c_{0^{++}}^{(1)(m)}$	χ_r^2
1.6	0.883(93)	0.13	0.569(77)	6e-4	0.76(28)	-	0.56(21)	-
1.75	0.78(15)	0.39	0.704(51)	4.27	0.43(15)	3.65	0.775(44)	4.58
1.9	0.828(28)	7.60	0.602(32)	8.64	0.593(38)	7.97	0.826(16)	10.1
Lin (2s)	0.804(60)	0.21	0.620(59)	3.44	0.59(13)	1.41	0.913(62)	0.18
Lin (c)	0.730(66)	2.48	0.657(58)	4.10	0.83(11)	4.14	0.669(45)	5.88
Average	0.767(63)	-	0.639(59)	-	0.71(12)	-	0.791(54)	-

Table 14.7.: Meson and glueball contents of the scalar ground (0) and first excited state (1), extrapolated to the chiral limit (top) and to the supersymmetric limit (bottom) for SU(2)-SYM.

14.5. Summary and discussion of the extrapolated mass spectra

β / Extr.	$c_{0^{++}}^{(0)(g)}$	χ_r^2	$c_{0^{++}}^{(0)(m)}$	χ_r^2	$c_{0^{++}}^{(1)(g)}$	χ_r^2	$c_{0^{++}}^{(1)(m)}$	χ_r^2
5.4	0.573(69)	2.16	0.638(36)	1.14	0.55(13)	0.77	0.667(58)	3.25
5.45	0.21(11)	0.51	0.714(48)	1.11	0.68(17)	1.35	0.896(53)	0.28
5.5	0.62(15)	1.45	0.520(80)	0.99	0.960(87)	0.41	0.918(70)	0.63
5.6	0.49(10)	0.26	0.822(83)	0.05	0.883(88)	0.70	0.767(45)	0.10
Lin (2)	0.31(22)	4.00	0.85(15)	3.42	1.40(25)	1.41	0.94(12)	5.23
Lin (c)	-0.09(19)	2.18	0.92(12)	1.17	2.23(19)	2.22	0.53(10)	4.68
Const (2)	0.491(48)	0.66	0.665(26)	0.84	0.837(53)	2.68	0.802(27)	3.95
Const (c)	0.444(45)	2.52	0.677(24)	1.34	1.003(50)	4.99	0.861(24)	5.09
Average	0.468(47)	-	0.671(25)	-	0.920(52)	-	0.832(26)	-

Table 14.8.: Extrapolated mixing coefficients for SU(3)-SYM corresponding to Tab. 14.7. The data is not precise enough for a linear continuum extrapolation (red) and leads to wrong values, e.g. $c_{0^{++}}^{(g)(1)} \gg 1$. Therefore, fit functions that are constant in the chiral limit have been chosen (cf. discussion in Sec. 14.4). Alternatively the values from the finest lattice spacing ($\beta = 5.6$) can be considered as the final results.

14.5. Summary and discussion of the extrapolated mass spectra

We observe the degeneracies in the supersymmetric limits of the ground states in SYM with the gauge groups SU(2) and SU(3) as predicted in [50]. This is strong evidence that, indeed, our lattice simulations are suitable to provide information about the supersymmetric theory in the continuum. The observed degeneracy of the corresponding first excited states supports this further. These heavier states are naturally affected stronger by lattice artifacts, which is also visible in the larger slopes of the excited states compared to the ground state in Figs. 14.1 and 14.3.

There are two outliers that do not fit into the expected degenerate supermultiplets: The scalar ground state of SU(2)-SYM when the combined extrapolation is considered, and the excited state mass in the scalar channel of SU(3)-SYM. As discussed in Sec. 14.1, the reason for the outlier in the case of SU(2) could be insufficient sampling of the parameter space, which is supported by the fact that the two-step and the combined approach provide significantly different results.

In the case of the excited scalar state in SU(3)-SYM, the results of the two-step and the combined extrapolations are consistent with each other. The deviation of 1.8σ from the multiplet can be explained by multiple reasons. It could be a statistical fluctuation of the data. A different explanation could be, that the state that we observe in the 0^{++} channel does not belong to the same multiplet as the

14. Results of the mass spectra and the mixing in the scalar channel

other two states. In fact, two-particle states would be expected to have a mass of about twice the ground state mass. In the case of SU(2) we do not observe such states with the operators that we have considered, which suggests that these operators have very small overlap with such states. It is possible that the state observed in the scalar channel of the SU(3)-SYM simulations is, in fact, such a multi-particle state. The observed mass is certainly in the expected range of two-particle states. However, at the moment we can only speculate. Including multi-particle state operators in the GEVP could be a first step to gain more information regarding this question. A phase shift analysis [85] could also provide further insights regarding multi-particle states. Such an analysis is, however, beyond the scope of this thesis and most probably also not doable with our current statistics since it requires very precise data.

In this thesis, we only consider the ground states and the first excited states of the chiral supermultiplet. The full spectrum consists of many more states, such as vector mesons, baryons, etc. It is an interesting question, how such states fit into the spectrum that we have found so far. Therefore, the Desy-Münster collaboration has started to also consider baryonic states [51]. These investigations are still in an early stage and quantitative results are so far not available.

Qualitatively and quantitatively the spectrum appears to be very similar for the gauge groups SU(2) and SU(3). Not only are the resulting supermultiplet masses in the supersymmetric limit in units of w_0 very similar, but the spectra are also affected almost identically by the lattice discretization, cf. Figs. A.2 and A.3 in App. A.7.1.

Using the combined extrapolation, we have also attempted to study, how the ground state masses are affected by a soft supersymmetry breaking gluino mass in SU(3)-SYM. Only the extrapolations using the scale w_0 provided consistent results. We find that the ground state masses of all three channels become larger with an increasing gluino mass. The data suggests that the $a\text{-}\eta'$ is affected the most by a gluino-mass term and the 0^{++} the least, while the gluino-gluon is in the middle. This ordering is consistent with the prediction of [50]. A similar analysis has not been carried out for SU(2)-SYM.

In addition, rather large mixing coefficients of glueball and meson components in the range $0.4 < c_i < 0.95$ have been found for the ground and first excited state of the scalar channel. In the pseudoscalar channel such a mixing is not observed for the ground state, but it appears to be meson-like. The corresponding first excited seems to be a mixed state with glueball and meson contents. However, a full quantitative mixing analysis has not been carried in this case.

15. SUSY Ward Identities

The main focus of this thesis lies on the investigation of the chiral supermultiplet spectrum of SYM, and Secs. 7 to 14 are devoted to this investigation. The fact that we have found the expected mass degeneracies in chiral and continuum limit is a strong evidence that this limit is indeed the supersymmetric limit of the theory. Another important check of supersymmetry restoration in this limit can be performed by studying the supersymmetric Ward identities. The analysis of the Ward identities in SU(3)-SYM is primarily done by our collaboration member Sajid Ali in the scope of our common supersymmetry project and our findings are briefly summarized here. A corresponding analysis for SU(2)-SYM has been done earlier and it has been presented in [28].

Ward identities arise from symmetries of a theory. For each continuous symmetry there is a conserved Noether current $j^\mu(x)$ and corresponding Ward identities. The Ward identities derived from the supersymmetry transformation (cf. Eq. 2.16) have been worked out in [100] and [31]. In the continuum and before renormalization they are given by

$$\langle \partial^\mu S_\mu(x) Q(y) \rangle = m_0 \langle \chi(x) Q(y) \rangle - \left\langle \frac{\delta Q(y)}{\delta \bar{\epsilon}(x)} \right\rangle, \quad (15.1)$$

where $Q(y)$ is an arbitrary insertion operator, $\bar{\epsilon}$ is the infinitesimal parameter of the supersymmetry transformation and $S_\mu(x)$ is the Noether current, also called supercurrent. The last term is a contact term that vanishes for $x \neq y$ and we restrict the analysis to this case. $S_\mu(x)$ and $\chi(x)$ are given by

$$S_\mu(x) = -\frac{1}{2} \text{Tr} [F_{\rho\nu}(x) \sigma_{\rho\nu} \gamma_\mu \lambda(x)], \quad (15.2)$$

$$\chi(x) = \frac{1}{2} \text{Tr} [F_{\rho\nu}(x) \sigma_{\rho\nu} \lambda(x)]. \quad (15.3)$$

Already from these equations it is clear that the supersymmetric Ward identities relate the gluino mass m_0 to correlators of the gauge fields, represented by $F_{\mu\nu}$, and the gluino fields, represented by λ . To be used in the lattice calculations, these formulae have to be properly discretized and renormalized. Furthermore, another current of mass dimension 7/2 that mixes with S_μ has to be taken into account. This calculation is described in detail in [31]. In the end, an overdetermined system of equations of correlation functions with two unknown parameters is obtained. The two parameters are

$$A = Z_T Z_S^{-1} \quad \text{and} \quad B = am_S Z_S^{-1}, \quad (15.4)$$

15. SUSY Ward Identities

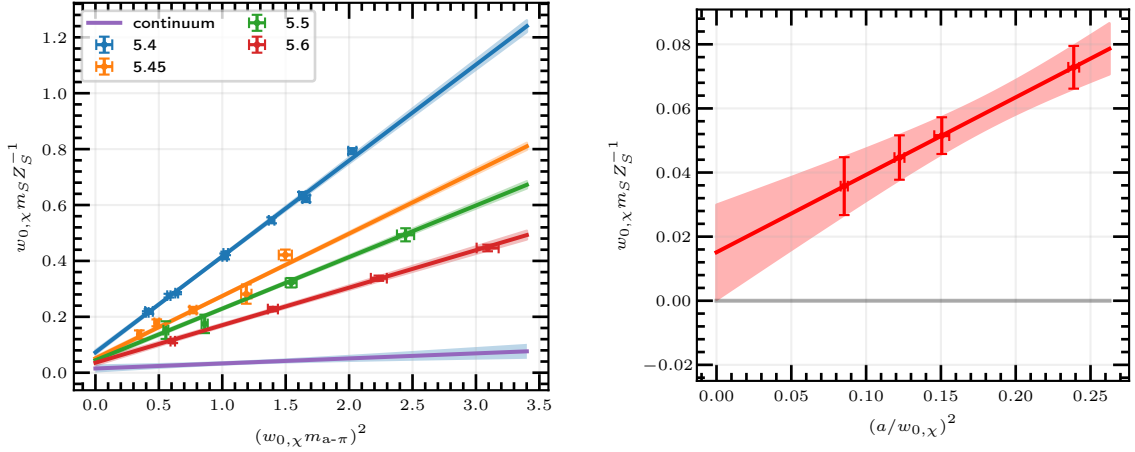


Figure 15.1.: Renormalized gluino mass from the Ward identities for SU(3)-SYM using the quadratic combined extrapolation. Left: Projection of the data points and the fit function at each simulated value of β to the continuum plane. Right: Projection of the fit function to the chiral plane (The data points resemble the fit and are only included to indicate the simulated lattice spacings).

where Z_T and Z_S^{-1} are renormalization coefficients and m_S is the additively renormalized, so-called subtracted, gluino-mass

$$m_S = m_0 - a^{-1} Z_\chi, \quad (15.5)$$

with the additional renormalization parameter Z_χ . The parameter B in Eq. 15.4 therefore defines the renormalized (multiplicatively and additively) gluino mass in lattice units on the basis of the supersymmetric Ward identities. The correlation functions required to estimate the parameters A and B can be directly measured from the gauge ensembles. For the insertion operator, the choice

$$Q(y) = \chi(y) \quad (15.6)$$

leads to a good signal-to-noise ratio which we improve further by applying APE and Jacobi smearing to the gauge and gluino fields, similarly as for the estimations of the mass spectrum (cf. Sec. 8.3). The parameters A and B are then determined by a linear fitting procedure of the parameters that minimizes the squared deviations of the system of equations. We use an elaborate version that has been worked out in [29] and that fully takes into account all correlations among the different time slices and correlators.

We have determined the renormalized gluino masses from the supersymmetric Ward identities for SU(3)-SYM and the data is presented in Tab. A.4 in App. A.6.

β	$am_S Z^{-1}$	χ_r^2
5.4	0.0326(23)	1.75
5.45	0.0214(57)	1.58
5.5	0.011(11)	0.30
5.6	0.0098(23)	0.56
Lin (two step)	-0.008(18)	0.12
Quad (two step):	0.016(12)	0.17
Lin (combined)	-0.022(23)	0.77
Quad (combined)	0.015(15)	0.62
Lin + Quad (combined)	-0.072(21)	1.42
Average	-0.014(18)	

Table 15.1: Renormalized subtracted gluino mass in lattice units calculated from the SUSY Ward identities, extrapolated to the chiral (top) and to the supersymmetric limit (bottom).

Furthermore, we have extrapolated the results to the chiral and continuum limit using the two-step and combined extrapolations, analogously to the extrapolation of the mass spectrum, see Fig. 15.1 and Tab. 15.1. Indeed, the gluino mass calculated from the Ward identities is consistent with zero within uncertainties in the supersymmetric limit $am_S Z^{-1} = -0.014(18)$. Thus, the SUSY Ward identities hold, which is an important, non-trivial confirmation of supersymmetry restoration in this limit.

16. Conclusions and Outlook

In this thesis the recent progress of the Desy-Münster collaboration to study the chiral supermultiplet in SU(2)-SYM and SU(3)-SYM is presented in detail. We have not only increased the precision significantly compared to earlier investigations of the ground states in SU(2)-SYM [28], but we have also studied the sector of the first excited states. Furthermore, we have successfully extended our investigations to SYM with the gauge group SU(3), which is computationally much more demanding.

For this purpose, we have greatly improved the algorithms and techniques for our lattice simulations and, in particular, for determining the properties of the bound states. I have personally performed most of the recent optimizations and measurements associated to the studies of the bound state masses and their extrapolations to the supersymmetric limit. Furthermore, I have contributed significantly to the generation of the gauge ensembles for the investigations of SU(3)-SYM, including setting up and monitoring the runs, as well as tuning the simulation parameters to accurately sample the theory and to utilize the computing time most efficiently. Moreover, I have contributed to optimizations that speed up the simulation code. For example, I have implemented a new data structure that allows vectorized computations, cf. App. A.1.

The analysis of the bound states has been performed on the basis of the variational method where the operator bases have been constructed from APE and Jacobi smeared interpolating fields. We have optimized the relevant parameters to obtain high signal-to-noise ratios. Using these improved techniques, we have found the predicted degeneracies of the ground and first excited states of the chiral supermultiplet in the supersymmetric limit [50]. Including mixed variational bases of smeared glueball and meson interpolators in our investigations allowed to perform quantitative analyses of the glueball and meson mixing in the scalar channel. The mixing coefficients c_i of the ground and first excited states have turned out to be considerably large, ranging from 0.4 to 0.95 and indicating significant mixing in these states, cf. Sec. 14.5. In the pseudoscalar channel, such mixing is not observed in the ground state which appears to be meson-like. The corresponding first excited seems to feature mixing, but a full quantitative analysis has not been performed in the scope of this thesis and this point is left open for future investigations.

The extrapolations to the chiral and continuum limit allow first insights into the effects of a (soft) supersymmetry breaking gluino mass in the case of SU(3)-SYM. They indicate positive mass shifts of the ground states, induced by the non-vanishing gluino mass, that are consistent with the predictions from [50]. The

results are, however, not completely unambiguous and depend on the scale setting method cf. Sec. 14.3.

Further evidence of supersymmetry restoration in the chiral and continuum limit is provided by means of the supersymmetric Ward identities (cf. Sec. 15), which we have investigated with very high precision and which hold in this limit.

In the future, the techniques presented in this thesis can be further improved. For instance, the variational bases could be complemented by adding further operators, e.g. multi-particle operators, glueball operators constructed from larger Wilson loops or operators including derivatives. The techniques are not restricted to SYM and we expect that they can be applied similarly in lattice studies of other theories, such as QCD or technicolor theories.

In this thesis only a tiny part of the non-perturbative phenomena of SYM has been studied. There are many more interesting topics that are currently under investigation or that can be studied in the future, such as the phase structure at finite temperature [101] or the other constituents of the particle spectrum, e.g. baryons and vector mesons. In fact, the Desy-Münster collaboration has started to investigate baryonic states in $SU(2)$ -SYM [51]; the studies are still in an early stage.

The investigations of SYM represent the first step towards understanding even more complex and more realistic supersymmetric theories, such as the supersymmetric extension of QCD (Super QCD). First consideration towards this direction have been presented by the Desy-Münster collaboration at the Lattice 2018 symposium [36]. The techniques, developed in this thesis, could be very useful for these future investigations, in particular in Super QCD which contains SYM as a subsector and in which mixing can occur between many more states, for instance between mesons of gluinos and quarks as well as glueballs and squark bound states.

A. Appendix

A.1. Data layout and vectorization

In order to utilize the computing time most efficiently, we have restructured our simulation code to increase its performance by utilizing so-called vector instructions. Vector instructions are a feature of modern CPUs that allows for parallel computation of floating point operations such as addition and multiplication. The instruction sets go by the name of SIMD, AVX, AVX2, AVX-512, etc. and modern CPU cores are capable of processing up to 64 single precision floating point operations in parallel (for AVX-512). To enable the compiler to use these vector instructions we have changed the data layout of our simulation code, which is explained in the following.

Let N be the size of the vector registers R in units of the size of a floating point number

$$N = \text{sizeof}(R)/\text{sizeof}(\text{float}) . \quad (\text{A.1})$$

A vectorized instruction is then able to perform N similar floating point operations in a single instruction (i.e. N additions, N multiplications, etc.). For example, instead of multiplying two of real numbers $a * b$, N pairs of real numbers can be multiplied simultaneously

$$a^N * b^N = (a^1 * b^1, a^2 * b^2, \dots, a^N * b^N) , \quad (\text{A.2})$$

where a^N and b^N denote vectors of N real numbers with coefficients a^i , b^i . In order to perform vector operations efficiently, the operands have to be stored contiguous in memory and aligned to specific boundaries, so that a full vector register can be loaded and stored with a single instruction (the requirement of alignment depends on the size of the vector registers).

In lattice simulations the quantum fields are usually stored as complex numbers, i.e. pairs of two floating point numbers representing the real part \Re and the imaginary part \Im . Hence, the most used basic operations are complex multiplication and complex addition. The complex multiplication

$$z_1 * z_2 = \Re_1 * \Re_2 - \Im_1 * \Im_2 + i (\Re_1 * \Im_2 + \Im_1 * \Re_2) . \quad (\text{A.3})$$

does not straightforwardly benefit from vector instructions because it consists of different floating point operations and the operands are usually not stored in the correct order in memory, such that they can be loaded with a single instruction.

A.1. Data layout and vectorization

However, if several complex multiplications of independent operands have to be performed, these multiplications can be parallelized by vectorizing each of the basic floating point operations contained in the complex multiplication (multiplication, addition and subtraction) according to Eq. A.2. For this purpose, the operands \Re^N and \Im^N have to be contiguous in memory such that they can be loaded and stored efficiently. Then, N complex multiplications can be performed in parallel, needing only as many compute cycles as a single complex multiplication.

The most computing intensive of lattice simulations is usually the Dirac-Wilson matrix-vector multiplications which run over the complete lattice-volume and therefore it is useful to parallelize the loop over the lattice sites. The simulation code used in previous studies of the Desy-Münster collaboration was based on a data structure called array of structures (AOS). A lattice vector, i.e. the object that the Dirac-Wilson matrix acts upon, was implemented as a three-dimensional array of complex numbers with the following structure

$$[\text{Volume}][\text{Spin}][\text{Group}][2], \quad (\text{A.4})$$

where $[2]$ denotes the inner structure storing the complex number. That is, the outermost array runs over all lattice sites, the second array runs over the spin indices and the third array runs over the group indices. This layout is, however, not optimal for using vector instructions because the real and the imaginary parts of the complex numbers are contiguous in memory and not blocks of N real and N imaginary parts as required for the vectorized complex multiplications.

In order to utilize vector instructions, it is better to use a data layout called structure of arrays (SOA), such as

$$[2][\text{Spin}][\text{Group}][\text{Volume}], \quad (\text{A.5})$$

where the real parts of the lattice sites are stored contiguously followed by the imaginary parts and hence the Dirac-Wilson matrix-vector multiplication can be parallelized over several sites of the lattice.

Following [102], we chose a hybrid data structure called AOSOA where the x^1 direction of the lattice is subdivided into blocks of block length B

$$[\text{Volume}][\text{Spin}][\text{Group}][2] \Rightarrow [\text{Volume}/B][\text{Spin}][\text{Group}][2][B]. \quad (\text{A.6})$$

This way, the real and the imaginary parts of one block are contiguous in memory, respectively, and the vector operations can be performed efficiently. The other three space-time directions are parallelized using the OpenMP and MPI frameworks. The operations, such as the Dirac-Wilson matrix-vector multiplication, then effectively run over the blocks instead of the lattice sites. The block length B can be adjusted according to the used machine and lattice size.

A. Appendix

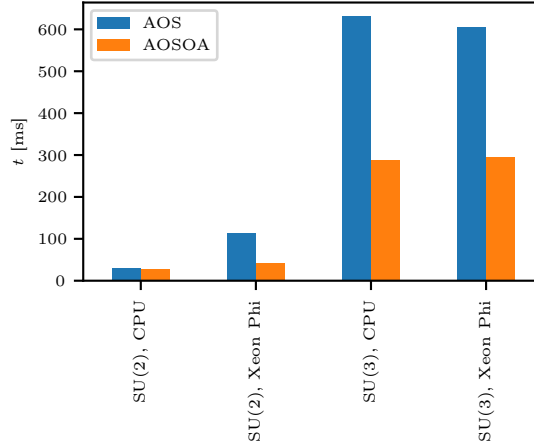


Figure A.1.: Comparison of the timings for one Dirac-Wilson matrix-vector multiplication using the old data layout (AOS) and the new data layout (AOSOA). The clover term was only used in SU(3). The test was performed on the NWZPHI compute cluster of the WWU Münster that is equipped with Intel Ivy Bridge CPUs and Xeon Phi 5110p (Knights Corner) accelerators. Note that the benchmark was carried out by averaging over many identical matrix-vector multiplications. The benchmark may differ from real application since, due to the repeated multiplications in the benchmark, the data can be stored in the caches of the CPUs and Xeon Phi accelerators.

Using the new data layout, we have increased the performance of the simulation code considerably, see Fig. A.1.

A.2. Jacobi smearing the fermion fields and the propagator

Smearing the fermion fields using Jacobi smearing

$$\lambda \rightarrow F\lambda \tag{A.7}$$

is equivalent to smearing the propagator

$$D_W^{-1} \rightarrow F D_W^{-1} F^\dagger. \tag{A.8}$$

A.3. Hermiticity of the correlation matrix $C(t)$

This can be demonstrated best by considering the following expression that appears in the disconnected piece

$$\bar{\lambda}_X \Gamma_{XY} \lambda_Y = -\lambda_Y \Gamma_{XY} \bar{\lambda}_X = -\Gamma_{XY} (D_W^{-1})_{YX} = -\text{Tr}(\Gamma D_W^{-1}), \quad (\text{A.9})$$

where A and B are multi indices denoting the collection of color and spin indices and the space-time dependence has been suppressed. If the fermion fields are smeared, we find

$$\overline{F\lambda} \Gamma F \lambda = \overline{F_{XX'} \lambda_{X'}} (\Gamma F)_{XY'} \lambda_{Y'} = \bar{\lambda}_{X'} (F^\dagger)_{X'X} (\Gamma F)_{XY'} \lambda_{Y'} \quad (\text{A.10})$$

$$= -(D_W^{-1})_{Y'X'} (F^\dagger)_{X'X} (\Gamma F)_{XY'} = -\text{Tr}(\Gamma F D_W^{-1} F^\dagger). \quad (\text{A.11})$$

It is simple to realize, that a similar calculation can be done for any other contraction of two smeared fermion fields. Comparing Eqs. A.9, A.11 concludes the calculation.

A.3. Hermiticity of the correlation matrix $C(t)$

A short calculation shows that the correlation matrix is Hermitian

$$C_{ij}(t) = \langle \phi_i(t) | \phi_j(0) \rangle = \langle \Omega | O_i(t) O_j^\dagger(0) | \Omega \rangle = \langle \Omega | e^{Ht} O_i(0) e^{-Ht} O_j^\dagger(0) | \Omega \rangle \quad (\text{A.12})$$

$$= \langle \Omega | O_i(0) e^{-Ht} O_j^\dagger(0) e^{Ht} | \Omega \rangle = \langle \Omega | O_i(0) O_j^\dagger(t) | \Omega \rangle = \langle \phi_i(0) | \phi_j(t) \rangle \quad (\text{A.13})$$

$$= \langle \phi_j(t) | \phi_i(0) \rangle^* = C_{ji}^*(t), \quad (\text{A.14})$$

where the time independence of the vacuum state and the skew-symmetry of the scalar product were used.

A.4. SET bias

As explained in Sec. 8.5, the disconnected piece of the correlator is computed using the SET method which amounts to approximating

$$\sum_{\vec{x}} \text{Tr}[\Gamma D_W^{-1}(x, x)] \approx \frac{1}{N_S} \sum_{\vec{x}} \text{Tr} \left[\sum_i^{N_S} \Gamma |s^i\rangle \langle \eta^i| \right] \doteq D_{\Gamma, \text{Tr}}^{\text{SET}}(t), \quad (\text{A.15})$$

where $|\eta^i\rangle$ are Z_4 noise source vectors and $|s^i\rangle = D_W^{-1} |\eta^i\rangle$ are the corresponding sink vectors. One might be tempted to use the same approximation, i.e. calculated from the same set of stochastic estimators, for both propagators in the disconnected

A. Appendix

piece

$$\sum_{\vec{x}} \text{Tr}[\Gamma D_W^{-1}(x, x)] \sum_{\vec{y}} \text{Tr}[\Gamma D_W^{-1}(y, y)] \approx D_{\Gamma, \text{Tr}}^{\text{SET}}(x^4) D_{\Gamma, \text{Tr}}^{\text{SET}}(y^4). \quad (\text{A.16})$$

However, this leads to a bias, which is shown below. To circumvent the bias, different sets of stochastic estimators can be used for both propagators. This would be not very efficient because both sets of stochastic estimators would have to be inverted. Instead, we subtract the bias, which is explained in the following.

For this purpose we use the multi-index notation to represent Dirac, color and lattice-site indices. Furthermore, the sum over \vec{X} shall denote a summation over all indices except the time component x^4 :

$$\sum_{\vec{X}} \doteq \sum_{x^1, x^2, x^3, \alpha, a} \quad (\text{A.17})$$

To understand the source of the bias, it is useful to first consider the expectation values of the components of the noise vectors. Using Z_4 noise leads to the following expectation values [103]

$$E[\eta_X^* \eta_Y] = \delta_{XY}, \quad (\text{A.18})$$

$$E[\eta_X^* \eta'_X \eta_Y^* \eta'_Y] = \delta_{XX'} \delta_{YY'} + \delta_{XY'} \delta_{X'Y} - \delta_{XX'YY'}, \quad (\text{A.19})$$

where

$$\delta_{XX'YY'} = \begin{cases} 1 & \text{if } X = Y = X' = Y' \\ 0 & \text{otherwise} \end{cases}. \quad (\text{A.20})$$

Furthermore, we calculate

$$\sum_{i,j}^{N_S} (\eta^i)_{X'} (\eta^i)_X^* (\eta^j)_{Y'} (\eta^{*,j})_Y \quad (\text{A.21})$$

$$= \sum_i^{N_S} (\eta^i)_{X'} (\eta^i)_X^* \sum_{j \neq i}^{N_S} (\eta^j)_{Y'} (\eta^{*,j})_Y + \sum_i^{N_S} (\eta^i)_{X'} (\eta^i)_X^* (\eta^i)_{Y'} (\eta^i)_Y^* \quad (\text{A.22})$$

$$\approx N_S(N_S - 1) \delta_{XX'} \delta_{YY'} + N_S(\delta_{XX'} \delta_{YY'} + \delta_{XY'} \delta_{X'Y} - \delta_{XX'YY'}) \quad (\text{A.23})$$

$$= N_S^2 \delta_{XX'} \delta_{YY'} + N_S(\delta_{XY'} \delta_{X'Y} - \delta_{XX'YY'}), \quad (\text{A.24})$$

where in line A.23 Eqs. A.18 and A.19 were used. If the two propagators in the

disconnected piece are approximated by the same set of noise vectors, one finds

$$D_{\Gamma, \text{Tr}}^{\text{SET}}(x^4) D_{\Gamma, \text{Tr}}^{\text{SET}}(y^4) \quad (\text{A.25})$$

$$= \frac{1}{N_S^2} \sum_{\vec{X}, \vec{Y}} \sum_{i,j}^{N_S} (\Gamma s^i)_X (\eta^i)_X (\Gamma s^j)_Y (\eta^j)_Y \quad (\text{A.26})$$

$$= \frac{1}{N_S^2} \sum_{\vec{X}, \vec{Y}} \sum_{i,j}^{N_S} (\Gamma D_W^{-1} \eta^i)_X (\eta^i)_X^* (\Gamma D_W^{-1} \eta^j)_Y (\eta^j)_Y^* \quad (\text{A.27})$$

$$= \frac{1}{N_S^2} \sum_{\vec{X}, \vec{Y}, X', Y'} (\Gamma D_W^{-1})_{XX'} (\Gamma D_X^{-1})_{YY'} \sum_{i,j}^{N_S} (\eta^i)_{X'} (\eta^i)_X^* (\eta^j)_{Y'} (\eta^j)_Y^* \quad (\text{A.28})$$

$$\stackrel{\text{Eq. A.24}}{=} \frac{1}{N_S^2} \sum_{\vec{X}, \vec{Y}, X', Y'} (\Gamma D_W^{-1})_{XX'} (\Gamma D_W^{-1})_{YY'} (N_S^2 \delta_{X'X} \delta_{Y'Y} \quad (\text{A.29})$$

$$+ N_S (\delta_{XY} \delta_{X'Y'} - \delta_{X'XY'}))$$

$$= \sum_{\vec{X}, \vec{Y}} \left[(\Gamma D_W^{-1})_{XX}^{-1} (\Gamma D_W^{-1})_{YY} + \frac{1}{N_S} (\Gamma D_W^{-1})_{XY} (\Gamma D_W^{-1})_{YX}^{-1} (1 - \delta_{XY}) \right]. \quad (\text{A.30})$$

The latter term is the aforementioned unwanted bias. It has the form of the connected piece of the correlator. The connected piece is estimated for the calculation of the bound state masses and we can use the measured value here to correct for the bias by subtracting the connected piece from the naïve stochastic estimation as follows

$$C_{\text{disc}}(t) = \left\langle \sum_{\vec{X}, \vec{Y}} (\Gamma D_W^{-1})_{XX} (\Gamma D_W^{-1})_{YY} \right\rangle \quad (\text{A.31})$$

$$\approx \frac{N_S^2}{N_S^2 - N_S} \left(\langle D_{\Gamma, \text{Tr}}^{\text{SET}}(x^4) D_{\Gamma, \text{Tr}}^{\text{SET}}(y^4) \rangle - \frac{1}{N_S} C_{\text{conn}}(t) (1 - \delta_{t0}) \right),$$

where $t = x^4 - y^4$.

A.5. Independence of the results of the scale setting observables

One may use different dimensionful observables s_1 , s_2 and s_3 for the scale setting of $m_{a-\pi}$, a and O , respectively. Let s_1 , s_2 and s_3 have mass dimension -1 . If the chosen observable for the scale does not have this mass dimension, it can be raised to a suitable power, such that the results has mass dimension -1 .

The results, extrapolated to the supersymmetric limit are independent of the choice of the scales s_1 and s_2 . Furthermore, the result does not depend on whether the chirally extrapolated $s_{3,\chi}$ value or whether the scale s_3 is used directly in the extrapolations. This is demonstrated in the following. For this purpose, the following notation is introduced

$$x \doteq s_1 m_{a-\pi}, \quad y \doteq \frac{a}{s_2}, \quad O \doteq (s_3)^d O_d, \quad (\text{A.32})$$

where O_d is the observable with mass dimension d and thus O is dimensionless. Correspondingly, upon changing the observables used for the scales we use the following notation

$$x' = s'_1 m_{a-\pi}, \quad y' = \frac{a}{s'_2}, \quad O' = (s'_3)^d O_d. \quad (\text{A.33})$$

The extrapolation of the observable O to the supersymmetric limit relies on Taylor expansion in x and y

$$O(x, y) = O_{\chi, \text{cont.}} + d_1 x + d_2 y + d_3 xy + \mathcal{O}(\text{higher}). \quad (\text{A.34})$$

In the following, we only consider the first terms of the Taylor expansions as in Eq. A.34 and drop all higher orders. The calculations, considering also higher orders, are similar. To understand the effect of changing the scale setting observables, it is useful consider the following Taylor expansions

$$x(x', y) = a_1 x' + a_2 y + a_3 x' y, \quad (\text{A.35})$$

$$y(x, y') = b_1 x + b_2 y' + b_3 x y', \quad (\text{A.36})$$

$$\left(\frac{s'_3}{s_3} \right)^d = s + c_1 x + c_2 y + c_3 xy, \quad (\text{A.37})$$

where

$$s \doteq \left(\frac{s'_3}{s_3} \right)_{\chi, \text{cont.}}^d. \quad (\text{A.38})$$

A.5. Independence of the results of the scale setting observables

By inserting Eq. A.35 into Eq. A.34 we find

$$O(x, y) = O_{\chi, \text{cont.}} + d_1(a_1x' + a_2y + a_3x'y) + d_2y + d_3(a_1x' + a_2y + a_3x'y)y \quad (\text{A.39})$$

$$= O_{\chi, \text{cont.}} + d_1a_1x' + (d_1a_1 + d_2)y + (d_1a_3 + a_1d_3)x'y \quad (\text{A.40})$$

$$\doteq O_{\chi, \text{cont.}} + d'_1x' + d'_2y + d'_3x'y. \quad (\text{A.41})$$

Thus, we have replaced $x \rightarrow x'$, or conversely $s_1 \rightarrow s'_1$. The value of the observable in the chiral and continuum limit $O_{\chi, \text{cont.}}$ remains unchanged, but the Taylor coefficients change. Replacing $y \rightarrow y' \Leftrightarrow s_2 \rightarrow s'_2$ has a similar effect, which can be shown by inserting Eq. A.36 into Eq. A.34

$$O(x, y) = O_{\chi, \text{cont.}} + d_1x + d_2(b_1x + b_2y' + b_3xy') + d_3x(b_1x + b_2y' + b_3xy') \quad (\text{A.42})$$

$$= O_{\chi, \text{cont.}} + (d_1 + b_1d_2)x + d_2b_2y' + (d_2b_3 + b_2d_3)xy' \quad (\text{A.43})$$

$$\doteq O_{\chi, \text{cont.}} + d''_1x + d''_2y' + d''_3xy'. \quad (\text{A.44})$$

The observable O' , expressed in terms of the new scale s'_3 can be obtained from the observable O in terms of the old scale s_3 by

$$O' = (s'_3)^d O_d = \left(\frac{s'_3}{s_3}\right)^d (s_3)^d O_d = \left(\frac{s'_3}{s_3}\right)^d O. \quad (\text{A.45})$$

Inserting Eqs. A.34 and A.37 into Eq. A.45 we find

$$O'(x, y) = (s + c_1x + c_2y + c_3xy) (O_{\chi, \text{cont.}} + d_1x + d_2y + d_3xy) \quad (\text{A.46})$$

$$= sO_{\chi, \text{cont.}} + sd_1x + sd_2y + (sd_3 + c_1d_2 + c_2d_1)xy \quad (\text{A.47})$$

$$\doteq O'_{\chi, \text{cont.}} + d'''_1x + d'''_2y + d'''_3xy, \quad (\text{A.48})$$

where

$$O'_{\chi, \text{cont.}} = sO_{\chi, \text{cont.}} = \left(\frac{s'_3}{s_3}\right)^d_{\chi, \text{cont.}} O_{\chi, \text{cont.}}. \quad (\text{A.49})$$

If $s_3 = w_0$ and $s'_3 = w_{0, \chi}$, then $s = 1$ and hence the chiral value $O_{\chi, \text{cont.}}$ is the same in both cases.

A.6. Summary tables of the ensembles and measured data

ID	β	κ	V	#Conf	$am_{a-\pi}$	$am_{gg}^{(0)}$	$am_{a-\eta'}^{(0)}$	$am_{0^{++}}^{(0)}$
A	1.6	0.15500	$24^3 \times 48$	1404	0.5757(41)	0.929(28)	0.626(13)	0.98(12)
B	1.6	0.15700	$24^3 \times 48$	1324	0.3208(38)	0.730(16)	0.459(35)	0.540(75)
C	1.6	0.15750	$24^3 \times 48$	1612	0.201(10)	0.633(31)	0.378(43)	0.458(68)
D	1.75	0.14900	$24^3 \times 48$	9300	0.2380(14)	0.4043(88)	0.319(12)	0.463(15)
E	1.75	0.14920	$24^3 \times 48$	9816	0.2026(18)	0.3709(90)	0.292(14)	0.395(24)
F	1.75	0.14925	$24^3 \times 48$	6428	0.1968(20)	0.3714(69)	0.270(17)	0.330(30)
G	1.75	0.14930	$24^3 \times 48$	10228	0.1897(26)	0.336(21)	0.265(20)	0.346(45)
H	1.75	0.14940	$32^3 \times 64$	4956	0.1615(14)	0.3575(57)	0.258(23)	0.376(22)
I	1.75	0.19450	$32^3 \times 64$	1692	0.1263(65)	0.3347(75)	-	0.287(59)
J	1.9	0.14330	$32^3 \times 64$	10176	0.28694(42)	0.3312(46)	0.3165(34)	0.336(24)
K	1.9	0.14387	$32^3 \times 64$	10144	0.21330(92)	0.2842(25)	0.2447(58)	0.204(21)
L	1.9	0.14415	$32^3 \times 64$	20704	0.17780(63)	0.2482(44)	0.2126(43)	0.288(20)
M	1.9	0.14435	$32^3 \times 64$	10648	0.1498(32)	0.2255(72)	0.1978(50)	0.204(19)

Table A.1.: Summary of the gauge configurations and the measured masses of the SU(2)-SYM simulations. The cases where the measurements could not be performed reliably, e.g. when the fit interval could not be determined reliably, are marked by “-”. The table is continued in Tab. A.2.

A.6. Summary tables of the ensembles and measured data

ID	$am_{\text{gg}}^{(1)}$	$am_{\text{a-}\eta'}^{(1)}$	$am_{0^{++}}^{(1)}$	$c_{0^{++}}^{(0)(g)}$	$c_{0^{++}}^{(0)(m)}$	$c_{0^{++}}^{(1)(g)}$	$c_{0^{++}}^{(1)(m)}$
A	1.31(11)	1.398(46)	-	0.42(25)	0.71(13)	-	-
B	1.15(16)	1.077(60)	0.84(17)	0.82(22)	0.616(91)	0.44(11)	0.853(30)
C	-	-	0.65(25)	0.822(77)	0.586(74)	0.63(17)	0.68(13)
D	-	0.724(24)	0.741(31)	0.602(71)	0.615(20)	0.787(75)	0.750(21)
E	0.756(23)	0.689(28)	0.715(44)	0.685(98)	0.604(35)	0.591(79)	0.784(24)
F	0.663(39)	0.764(21)	0.645(29)	0.718(67)	0.516(38)	0.523(44)	0.827(19)
G	0.621(44)	0.669(29)	0.688(58)	0.715(93)	0.654(39)	0.700(54)	0.732(30)
H	0.725(31)	0.688(35)	0.673(38)	0.650(84)	0.702(31)	0.70(10)	0.734(25)
I	0.695(75)	-	0.69(10)	0.49(11)	0.686(55)	0.754(58)	0.685(76)
J	0.618(12)	0.708(15)	0.524(12)	0.922(16)	0.311(17)	0.262(29)	0.904(10)
K	0.560(10)	0.550(48)	0.451(16)	0.925(15)	0.358(23)	0.317(24)	0.9008(83)
L	0.503(13)	0.497(27)	0.440(15)	0.796(31)	0.542(28)	0.497(29)	0.826(14)
M	0.505(14)	0.589(30)	0.435(19)	0.796(39)	0.572(42)	0.574(49)	0.796(29)

Table A.2.: Continuation of Tab. A.1. Here, the measurements of the corresponding masses of the first excited states as well as the mixing coefficients c_i are summarized.

A. Appendix

ID	β	κ	V	#Conf	$am_{a-\pi}$	w_0/a	r_0/a	$am_{gg}^{(0)}$	$am_{a-\eta'}^{(0)}$	$am_{0^{++}}^{(0)}$
A	5.4	0.1692	$16^3 \times 32$	8284	0.6954(14)	1.1259(42)	-	1.2164(79)	0.771(16)	0.443(37)
B	5.4	0.1695	$12^3 \times 24$	7628	0.6241(17)	1.1955(87)	3.4(10)	1.090(17)	0.705(10)	0.383(40)
C	5.4	0.1695	$16^3 \times 32$	3980	0.6298(24)	1.1819(38)	-	1.089(20)	0.650(16)	0.361(41)
D	5.4	0.1697	$16^3 \times 32$	3892	0.5759(14)	1.2711(53)	-	1.003(13)	0.653(17)	0.404(49)
E	5.4	0.1700	$12^3 \times 24$	5964	0.4933(22)	1.386(14)	4.30(27)	0.866(14)	0.553(16)	0.372(37)
F	5.4	0.1700	$16^3 \times 32$	5856	0.4952(21)	1.3988(91)	-	0.884(12)	0.594(16)	0.370(61)
G	5.4	0.1703	$12^3 \times 24$	4028	0.3718(30)	1.693(15)	5.10(26)	0.712(17)	0.459(18)	0.367(46)
H	5.4	0.1703	$16^3 \times 32$	9820	0.3911(16)	1.6039(93)	-	0.7523(78)	0.5029(82)	0.369(35)
I	5.4	0.1705	$12^3 \times 24$	3300	0.318(11)	1.767(30)	-	0.657(24)	0.439(19)	-
J	5.4	0.1705	$16^3 \times 32$	8052	0.3123(33)	1.7316(83)	-	0.661(12)	0.428(18)	0.404(38)
K	5.45	0.1685	$16^3 \times 32$	1312	0.4748(22)	1.6733(64)	5.04(18)	0.7579(92)	0.568(18)	0.442(56)
L	5.45	0.1687	$16^3 \times 32$	2564	0.4232(18)	1.778(10)	5.48(13)	0.680(11)	0.523(16)	0.458(55)
M	5.45	0.1690	$16^3 \times 32$	2480	0.3404(21)	2.036(11)	5.98(17)	0.5867(93)	0.451(17)	0.365(61)
N	5.45	0.1692	$16^3 \times 32$	1648	0.2699(31)	2.184(12)	6.82(31)	0.506(13)	0.390(18)	0.409(34)
O	5.45	0.1693	$16^3 \times 32$	2280	0.2282(36)	2.306(26)	6.71(22)	0.4876(60)	0.405(33)	0.305(35)
P	5.5	0.1667	$16^3 \times 32$	4116	0.5468(13)	1.881(12)	5.56(14)	0.7573(79)	0.6090(61)	0.559(71)
Q	5.5	0.1673	$16^3 \times 32$	3732	0.4344(13)	1.996(12)	6.15(16)	0.6387(89)	0.485(17)	0.416(47)
R	5.5	0.1678	$16^3 \times 32$	7736	0.3245(11)	2.247(10)	6.82(33)	0.507(12)	0.3996(99)	0.405(34)
S	5.5	0.1680	$16^3 \times 32$	1888	0.2606(29)	2.470(17)	8.06(34)	0.440(12)	0.364(12)	0.316(51)
T	5.6	0.1645	$24^3 \times 48$	5952	0.51380(42)	2.3316(95)	6.940(46)	0.6164(42)	0.5660(72)	0.479(69)
U	5.6	0.1650	$24^3 \times 48$	5728	0.43677(70)	2.548(15)	7.329(52)	0.5581(82)	0.504(12)	0.500(62)
V	5.6	0.1655	$24^3 \times 48$	4688	0.34561(76)	2.794(17)	8.005(58)	0.4506(65)	0.420(13)	0.381(40)
W	5.6	0.1660	$24^3 \times 48$	4096	0.22819(86)	3.141(25)	9.13(16)	0.3531(68)	0.310(14)	0.341(46)

Table A.3.: Summary of the gauge configurations and the measured masses of the SU(3)-SYM simulations. The cases where the measurements could not be performed reliably, e.g. when the fit interval could not be determined reliably, are marked by "-". The table is continued in Tab. A.4.

A.6. Summary tables of the ensembles and measured data

ID	$am_{\text{gg}}^{(1)}$	$am_{\text{a-}\eta'}^{(1)}$	$am_{0^{++}}^{(1)}$	$c_{0^{++}}^{(0)(g)}$	$c_{0^{++}}^{(0)(m)}$	$c_{0^{++}}^{(1)(g)}$	$c_{0^{++}}^{(1)(m)}$	$am_S Z_S^{-1}$
A	1.71(10)	1.5661(93)	1.85(92)	0.82(18)	0.75(14)	-	-	0.3874(43)
B	1.445(92)	1.4623(98)	1.25(40)	0.79(11)	0.722(88)	-	-	0.3095(60)
C	1.69(13)	1.479(13)	1.06(29)	0.76(12)	0.81(11)	-	-	0.3042(55)
D	1.59(15)	1.373(43)	0.76(23)	-	-	-	-	0.2664(48)
E	1.43(13)	1.234(40)	1.24(47)	0.852(61)	0.668(46)	0.14(12)	0.975(50)	0.2033(49)
F	1.493(87)	1.244(28)	1.52(49)	0.902(58)	0.613(49)	0.12(10)	0.924(85)	0.2086(27)
G	1.229(78)	0.996(36)	0.84(15)	0.595(50)	0.595(50)	0.19(12)	0.960(44)	0.1347(31)
H	1.345(41)	1.134(26)	1.18(21)	0.693(97)	0.633(32)	0.186(81)	0.855(39)	0.1391(16)
I	1.368(93)	0.89(13)	0.36(20)	-	-	0.48(11)	0.713(39)	0.1071(41)
J	1.114(56)	1.020(22)	1.36(34)	0.649(99)	0.688(27)	0.40(12)	0.850(56)	0.1054(19)
K	1.292(69)	1.208(30)	1.109(80)	0.79(17)	0.72(15)	0.57(25)	0.757(95)	0.1635(69)
L	1.212(47)	1.101(25)	1.066(92)	0.55(12)	0.662(38)	0.50(13)	0.79(12)	0.109(13)
M	1.105(38)	1.007(24)	0.886(81)	0.375(84)	0.619(40)	0.77(14)	0.840(90)	0.0870(42)
N	1.033(26)	0.936(28)	0.90(12)	0.42(13)	0.734(44)	0.44(14)	0.858(24)	0.0692(46)
O	-	0.819(31)	0.69(13)	0.345(92)	0.693(43)	0.76(17)	0.73(15)	0.0528(58)
P	1.299(36)	1.187(30)	0.74(12)	0.710(68)	0.638(66)	0.709(57)	0.566(47)	0.1726(78)
Q	1.190(30)	1.054(22)	0.839(71)	0.798(88)	0.521(44)	0.593(89)	0.702(65)	0.1126(57)
R	1.040(28)	0.9083(76)	0.733(94)	0.50(14)	0.581(50)	0.793(32)	0.824(51)	0.061(11)
S	0.974(22)	0.828(20)	0.54(11)	0.68(20)	0.53(19)	0.77(15)	0.74(11)	0.053(11)
T	1.054(15)	1.046(10)	0.701(47)	0.975(19)	0.309(60)	0.175(43)	0.953(28)	0.1304(29)
U	1.041(13)	0.974(27)	0.709(65)	0.799(64)	0.439(32)	0.352(99)	0.896(28)	0.0988(24)
V	0.928(13)	0.821(20)	0.673(48)	0.721(71)	0.585(45)	0.511(64)	0.855(23)	0.0666(21)
W	0.828(16)	0.747(23)	0.527(34)	0.63(16)	0.75(12)	0.83(10)	0.76(11)	0.0329(19)

Table A.4.: Continuation of Tab. A.3. Here, the measurements of the corresponding masses of the first excited states as well as the mixing coefficients c_i and the renormalized subtracted gluino mass $am_S Z_S^{1-}$ are summarized.

A. Appendix

A.7. Plots

A.7.1. Spectra

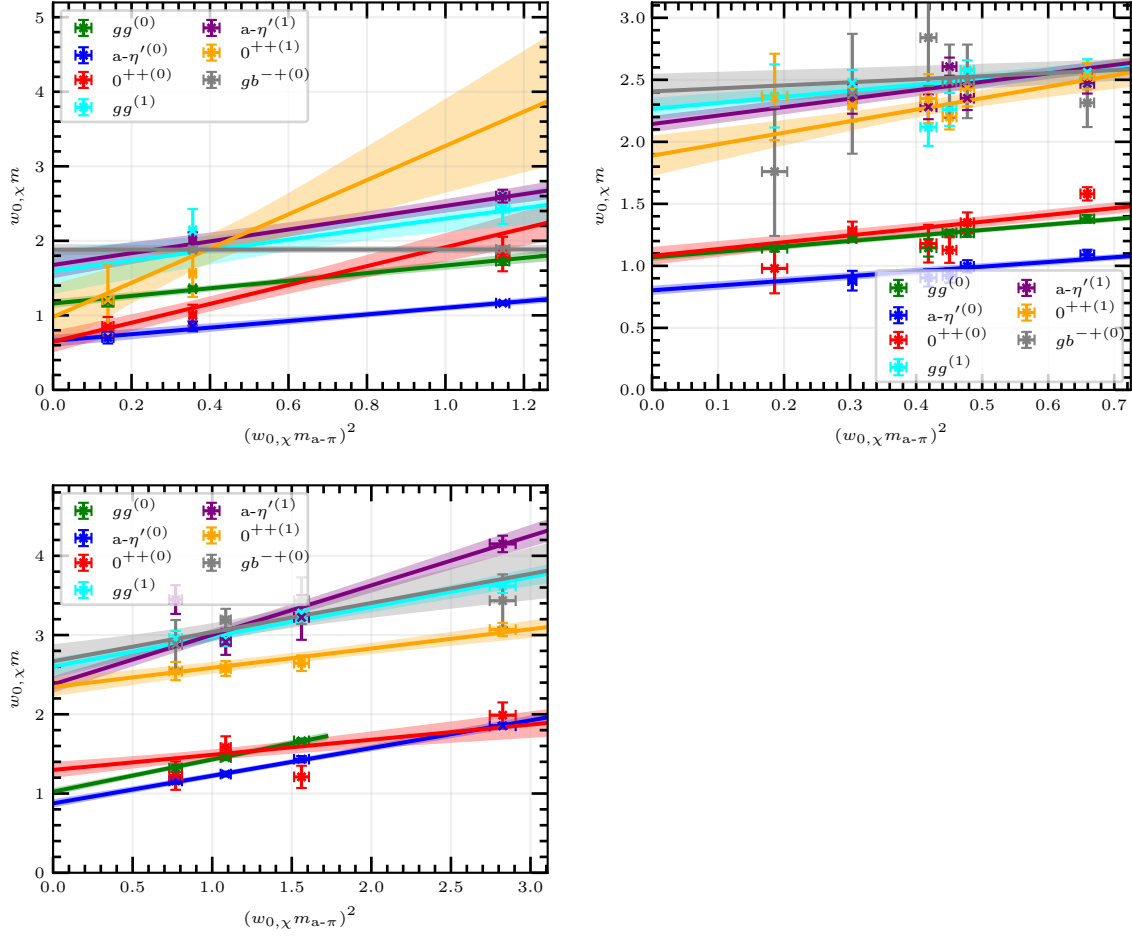


Figure A.2.: Measured mass spectrum of SU(2)-SYM and combined linear extrapolations, projected to the continuum plane ($a/w_{0,\chi}=0$) for the different simulated values of β . Top-left: $\beta = 1.6$. Top-right: $\beta = 1.75$. Bottom-left: $\beta = 1.9$.

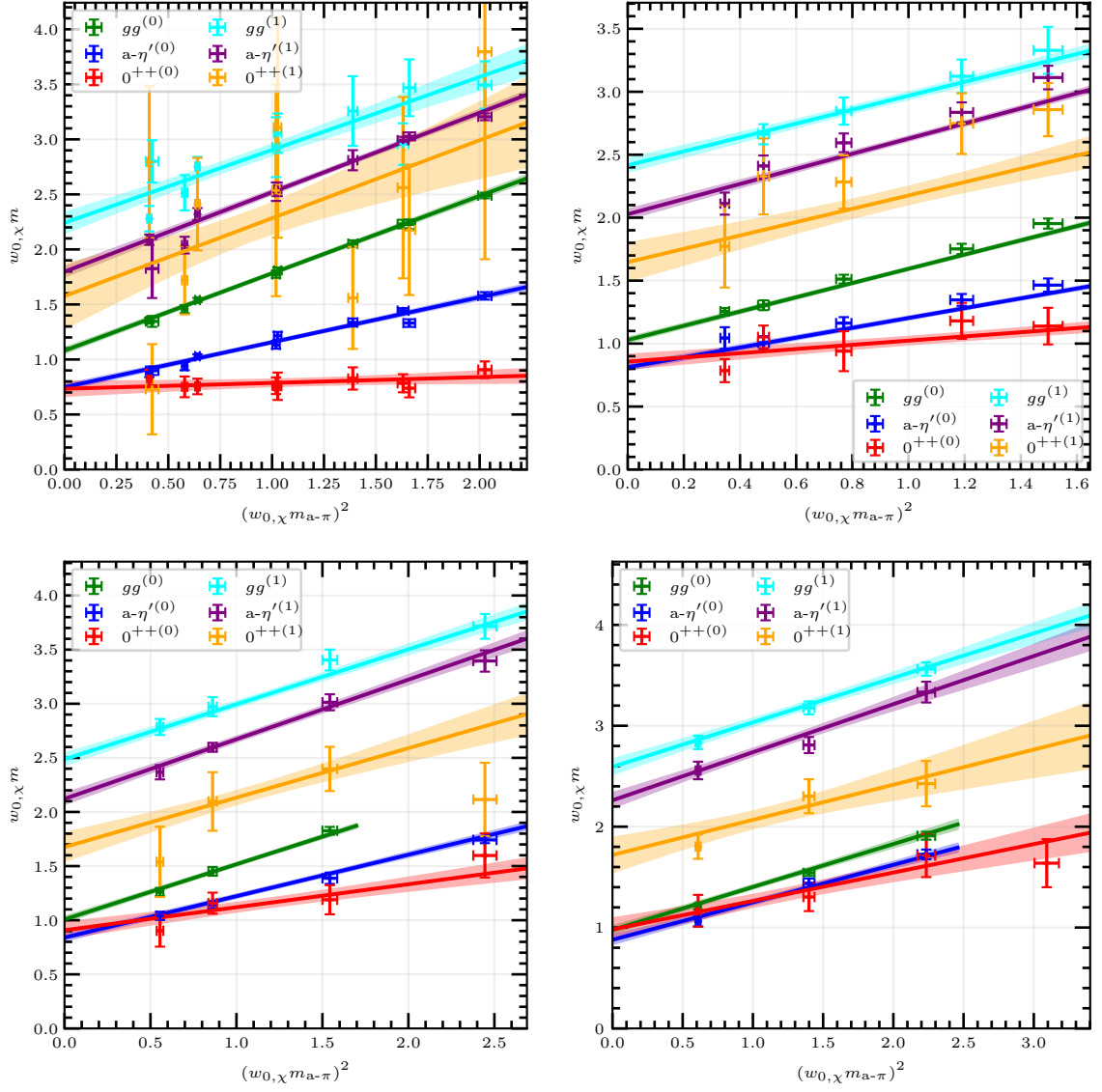


Figure A.3.: Measured mass spectrum of SU(3)-SYM and combined linear extrapolations, projected to the continuum plane ($a/w_{0,\chi}=0$) for the different simulated values of β . Top-left: $\beta = 5.4$, top-right: $\beta = 5.45$, bottom-left: $\beta = 5.5$, bottom-right: $\beta = 5.6$.

A. Appendix

A.7.2. Mixing coefficients

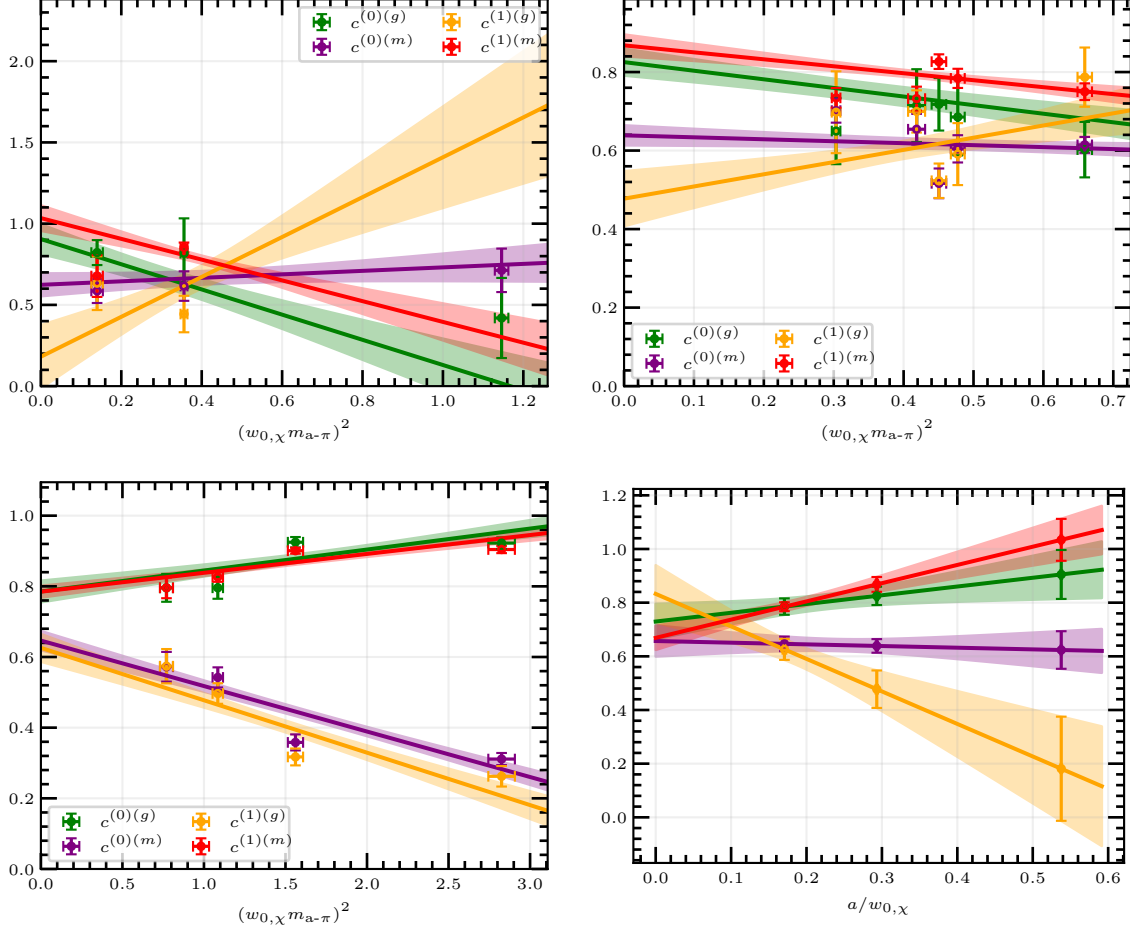


Figure A.4.: Combined linear extrapolations of the mixing coefficients $c_{0++}^{(g)}$ and $c_{0++}^{(m)}$ of the ground state (0) and first excited state (1) of the scalar channel for SU(2)-SYM. In the top row and in the bottom-left, the projections to the continuum plane ($a/w_{0\chi} = 0$) of the measured data points and the fits are shown for fixed values of β . Top-left: $\beta = 1.6$. Top-right: $\beta = 1.75$. Bottom-left: $\beta = 1.9$. In the bottom-right, the projection to the chiral plane ($w_{0\chi}, m_{a-\pi}^2 = 0$) is shown and the data point mark chirally extrapolated values at the simulated lattice spacings. Since the chiral and continuum extrapolation is done simultaneously, they align completely with the fit curves.

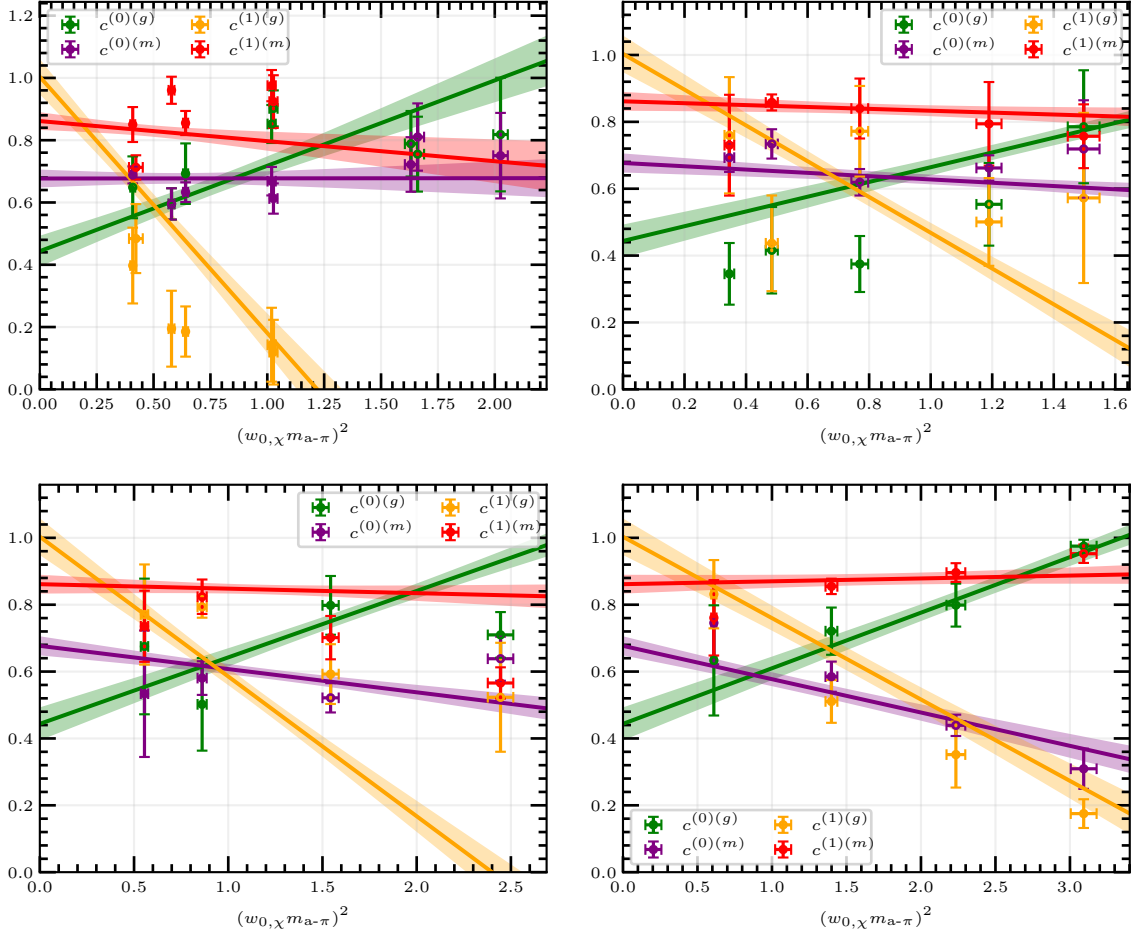


Figure A.5.: Combined extrapolation of the mixing coefficient $c_{0++}^{(g)}$ and $c_{0++}^{(m)}$ of the ground state (0) and first excited state (1) of the scalar channel for SU(3)-SYM, projected to the continuum plane ($a/w_{0,\chi}=0$) for the different simulated values of β . Top-left: $\beta = 5.4$. Top-right: $\beta = 5.45$. Bottom-left: $\beta = 5.5$. Bottom-right: $\beta = 5.6$. Note that the fit function is constant in the chiral limit, i.e. $c_2 = 0$.

Bibliography

- [1] A. Einstein. *Näherungsweise Integration der Feldgleichungen der Gravitation*. Sitzungsberichte der Königlich Preußischen Akademie der Wissenschaften (Berlin) (1916), pp. 688–696.
- [2] B. P. Abbott et al. *Observation of gravitational waves from a binary black hole merger*. Phys. Rev. Lett. **116**.6 (2016), p. 061102. arXiv: 1602.03837 [gr-qc].
- [3] T. Aoyama, M. Hayakawa, T. Kinoshita and M. Nio. *Tenth-order electron anomalous magnetic moment: Contribution of diagrams without closed lepton loops*. Phys. Rev. D **91**.3 (2015), pp. 1–54. arXiv: 1412.8284 [hep-ph].
- [4] K. G. Wilson. *Renormalization Group and Strong Interactions*. Phys. Rev. D **3**.8 (1971), pp. 1818–1846.
- [5] L. Susskind. *Dynamics of spontaneous symmetry breaking in the Weinberg-Salam theory*. Phys. Rev. D **20**.10 (1979), pp. 2619–2625.
- [6] M. Tanabashi et al. *Review of Particle Physics*. Phys. Rev. D **98**.3 (2018), p. 30001.
- [7] V. C. Rubin, N. Thonnard and J. Ford, W. K. *Rotational properties of 21 SC galaxies with a large range of luminosities and radii, from NGC 4605 ($R = 4kpc$) to UGC 2885 ($R = 122 kpc$)*. The Astrophys. J. **238** (1980), p. 471.
- [8] D. Clowe, A. Gonzalez and M. Markevitch. *Weak-Lensing Mass Reconstruction of the Interacting Cluster 1E 0657–558: Direct Evidence for the Existence of Dark Matter*. The Astrophys. J. **604**.2 (2004), pp. 596–603. arXiv: astro-ph/0312273.
- [9] L. Gao et al. *Simulations of the formation, evolution and clustering of galaxies and quasars*. Nature **435**.7042 (2005), pp. 629–636.
- [10] G. L. Kane. *Perspectives on Supersymmetry*. Vol. 18. Advanced Series on Directions in High Energy Physics. World Scientific, 1998.
- [11] T. Mannel. *Theory and Phenomenology of CP Violation*. Nucl. Phys. B - Proc. Sup. **167** (2007), pp. 170–174.
- [12] J. E. Kim and G. Carosi. *Axions and the strong CP problem*. Rev. Mod. Phys. **82**.1 (2010), pp. 557–601. arXiv: 0807.3125 [hep-ph].
- [13] G. Basini, A. Morselli and M. Ricci. *Matter and antimatter in the same universe?* La Rivista del Nuovo Cimento **12**.4 (1989), pp. 1–51. arXiv: 1204.4186 [hep-ph].

- [14] F. Couchot, S. Henrot-Versillé, O. Perdereau, S. Plaszczynski, B. Rouillé d'Orfeuil, M. Spinelli and M. Tristram. *Cosmological constraints on the neutrino mass including systematic uncertainties*. Astron. Astrophys. **606** (2017), A104. arXiv: [astro-ph.C0/1703.10829](#).
- [15] Katrin Collaboration. *KATRIN design report 2004*. FZKA Scientific report **7090** (2005).
- [16] P. J. E. Peebles and B. Ratra. *The cosmological constant and dark energy*. Rev. Mod. Phys. **75.2** (2003), pp. 559–606. arXiv: [astro-ph/0207347](#).
- [17] R. Kuchimanchi. *Solution to the strong cp problem: Supersymmetry with parity*. Phys. Rev. Lett. **76.19** (1996), pp. 3486–3489. arXiv: [hep-ph/9511376v2](#).
- [18] J. Maldacena. *The large N limit of superconformal field theories and supergravity*. Adv. Theor. Math. Phys. **2.2** (1998), pp. 231–252. arXiv: [arXiv:hep-th/9711200](#).
- [19] J. Wess and B. Zumino. *Supergauge transformations in four dimensions*. Nucl. Phys. B **70.1** (1974), pp. 39–50.
- [20] S. Dimopoulos and H. Georgi. *Softly broken supersymmetry and $SU(5)$* . Nucl. Phys. B **193.1** (1981), pp. 150–162.
- [21] S. Dürr et al. *Ab Initio Determination of Light Hadron Masses*. Science **322.5905** (2008), pp. 1224–1227.
- [22] P. Petreczky. *Lattice QCD at finite temperature*. Nucl. Phys. A **785.1-2** (2007), pp. 10–17. arXiv: [1203.5320 \[hep-lat\]](#).
- [23] G. Veneziano and S. Yankielowicz. *An effective lagrangian for the pure $N = 1$ supersymmetric Yang-Mills theory*. Phys. Lett. B **113.3** (1982), pp. 231–236.
- [24] G. Curci and G. Veneziano. *Supersymmetry and the lattice: A reconciliation?* Nucl. Phys. B **292** (1987), pp. 555–572.
- [25] K. Demmouche, F. Farchioni, A. Ferling, I. Montvay, G. Münster, E. E. Scholz and J. Wuilloud. *Simulation of $4d N = 1$ supersymmetric Yang-Mills theory with Symanzik improved gauge action and stout smearing*. Eur. Phys. J. C **69.1** (2010), pp. 147–157. arXiv: [1003.2073 \[hep-lat\]](#).
- [26] G. Bergner, I. Montvay, G. Münster, U. D. Özugurel and D. Sandbrink. *Towards the spectrum of low-lying particles in supersymmetric Yang-Mills theory*. J. High Energy Phys. **2013.11** (2013), pp. 1–10. arXiv: [1304.2168 \[hep-lat\]](#).

Bibliography

- [27] G. Münster and H. Stüwe. *The mass of the adjoint pion in $N = 1$ supersymmetric Yang-Mills theory*. J. High Energy Phys. **2014.5** (2014), pp. 1–6. arXiv: 1402.6616 [hep-th].
- [28] G. Bergner, P. Giudice, G. Münster, I. Montvay and S. Piemonte. *The light bound states of supersymmetric $SU(2)$ Yang-Mills theory*. J. High Energy Phys. **2016.3** (2016), pp. 1–19. arXiv: 1512.07014 [hep-lat].
- [29] S. Ali, G. Bergner, H. Gerber, I. Montvay, G. Münster, S. Piemonte and P. Scior. *Analysis of Ward identities in supersymmetric Yang-Mills theory*. The Eur. Phys. J. C **78.5** (2018), p. 404. arXiv: 1802.07067 [hep-lat].
- [30] S. Ali, G. Bergner, H. Gerber, S. Kuberski, I. Montvay, G. Münster, S. Piemonte and P. Scior. *Variational analysis of low-lying states in supersymmetric Yang-Mills theory*. J. High Energy Phys. **2019.4** (2019), p. 150. arXiv: 1901.02416 [hep-lat].
- [31] F. Farchioni, C. Gebert, R. Kirchner, I. Montvay, A. Feo, G. Münster, T. Galla and A. Vladikas. *The supersymmetric Ward identities on the lattice*. Eur. Phys. J. C **23.4** (2002), pp. 719–734. arXiv: hep-lat/0111008.
- [32] T. Galla, F. Farchioni, C. Gebert, R. Kirchner, R. Peetz, I. Montvay, A. Vladikas, A. Feo and G. Münster. *SUSY Ward identities in 1-loop perturbation theory*. Nucl. Phys. B - Proc. Sup. **106-107** (2002), pp. 941–943. arXiv: hep-lat/0110113.
- [33] I. Montvay, T. Galla, F. Farchioni, A. Feo, C. Gebert, A. Vladikas, R. Kirchner and G. Münster. *Lattice supersymmetric ward identities*. Nucl. Phys. B - Proc. Sup. **106-107.I** (2002), pp. 938–940.
- [34] G. Bergner and S. Piemonte. *Compactified $N=1$ supersymmetric Yang-Mills theory on the lattice: Continuity and the disappearance of the deconfinement transition*. J. High Energy Phys. **2014.12** (2014), p. 133. arXiv: 1410.3668 [hep-lat].
- [35] G. Bergner, P. Giudice, G. Münster, S. Piemonte and D. Sandbrink. *Phase structure of the $N=1$ supersymmetric Yang-Mills theory at finite temperature*. J. High Energy Phys. **2014.11** (2014), p. 49. arXiv: 1405.3180 [hep-lat].
- [36] S. Ali, G. Bergner, H. Gerber, P. Giudice, I. Montvay, G. Münster, S. Piemonte and P. Scior. *The light bound states of $N = 1$ supersymmetric $SU(3)$ Yang-Mills theory on the lattice*. J. High Energy Phys. **2018.3** (2018), p. 113. arXiv: 1512.07014 [hep-lat].

- [37] S. Ali, G. Bergner, H. Gerber, I. Montvay, G. Münster, S. Piemonte and P. Scior. *Numerical results for the lightest bound states in $N = 1$ supersymmetric $SU(3)$ Yang-Mills theory*. Phys. Rev. Lett., accepted (2019). arXiv: 1902.11127 [hep-lat].
- [38] G. Lüders. *On the Equivalence of Invariance under Time Reversal and under Particle-Antiparticle Conjugation for Relativistic Field Theories*. Det Kongelige Danske Videnskabernes Selskab Matematisk-fysiske Meddelelser **28.5** (1954), pp. 1–17.
- [39] K. Spanderen. *Monte-Carlo-Simulationen einer $SU(2)$ Yang-Mills-Theorie mit dynamischen Gluinos*. PhD thesis. WWU Münster, Germany, 1998.
- [40] S. Luckmann. *Supersymmetrische Feldtheorien auf dem Gitter*. PhD thesis. WWU Münster, Germany, 2001.
- [41] J. Wuilloud. *The Wilson-Dirac Operator Eigenspectrum for the Theories of QCD and Super Yang-Mills with One Flavour*. PhD thesis. WWU Münster, Germany, 2010.
- [42] D. Sandbrink. *Numerische Bestimmung von Quarkpotential, Glueball-Massen und Phasenstruktur in der $N=1$ supersymmetrischen Yang-Mills-Theorie*. PhD thesis. WWU Münster, 2014.
- [43] S. Piemonte. *$N = 1$ supersymmetric Yang-Mills theory on the lattice*. PhD thesis. WWU Münster, Germany, 2015.
- [44] A. Jaffe. *The millennium grand challenge in mathematics*. Notices of the AMS **53.6** (2006), p. 652.
- [45] S. Coleman and J. Mandula. *All Possible Symmetries of the S Matrix*. Phys. Rev. **159.5** (1967), pp. 1251–1256.
- [46] R. Haag, J. T. Łopuszański and M. Sohnius. *All possible generators of supersymmetries of the S -matrix*. Nucl. Phys. B **88.2** (1975), pp. 257–274.
- [47] I. Montvay. *Supersymmetric Yang-Mills theory on the lattice*. Int. J. Mod. Phys. A **17.18** (2002), pp. 2377–2412. arXiv: hep-lat/0112007.
- [48] E. Witten. *An $SU(2)$ anomaly*. Phys. Lett. B **117.5** (1982), pp. 324–328.
- [49] G. R. Farrar, G. Gabadadze and M. Schwetz. *Effective action of $N=1$ supersymmetric Yang-Mills theory*. Phys. Rev. D **58.1** (1998), p. 015009. arXiv: hep-th/9711166.
- [50] G. R. Farrar, G. Gabadadze and M. Schwetz. *Spectrum of softly broken $N=1$ supersymmetric Yang-Mills theory*. Phys. Rev. D **60.3** (1999), p. 035002. arXiv: hep-th/9806204.

Bibliography

- [51] S. Ali, G. Bergner, H. Gerber, C. Lopez, I. Montvay, G. Münster, S. Piemonte and P. Scior. *Baryonic states in supersymmetric Yang-Mills theory*. PoS (Lattice 2018). Proceedings of the 36th International Symposium on Lattice Field Theory, 2018, East Lansing, Michigan, USA. arXiv: 1811.02297 [hep-lat].
- [52] C. Gattringer and C. B. Lang. *Quantum Chromodynamics on the Lattice*. Lecture Notes in Physics. Berlin, Heidelberg: Springer Berlin Heidelberg, 2010.
- [53] I. Montvay and G. Münster. *Quantum Fields on a Lattice*. Cambridge, UK: Cambridge University Press, 1994.
- [54] K. Symanzik. *Schrödinger representation and Casimir effect in renormalizable quantum field theory*. Nucl. Phys. B **190**.1 (1981), pp. 1–44.
- [55] M. Lüscher and P. Weisz. *On-shell Improved Lattice Gauge Theories*. Communications in Mathematical Physics **77**.1985 (2011), pp. 59–77.
- [56] J. Kogut and L. Susskind. *Hamiltonian formulation of Wilson’s lattice gauge theories*. Phys. Rev. D **11**.2 (1975), pp. 395–408.
- [57] D. B. Kaplan. *A method for simulating chiral fermions on the lattice*. Phys. Lett. B **288**.3-4 (1992), pp. 342–347. arXiv: hep-lat/9206013.
- [58] H. Neuberger. *Exactly massless quarks on the lattice*. Phys. Lett. B **417**.1-2 (1998), pp. 141–144.
- [59] V. Novikov, M. Shifman, A. Vainshtein and V. Zakharov. *Exact Gell-Mann-Low function of supersymmetric Yang-Mills theories from instanton calculus*. Nucl. Phys. B **229**.2 (1983), pp. 381–393.
- [60] H. Nielsen and M. Ninomiya. *A no-go theorem for regularizing chiral fermions*. Phys. Lett. B **105**.2-3 (1981), pp. 219–223.
- [61] G. Bergner. *Complete supersymmetry on the lattice and a no-go theorem*. J. High Energy Phys. **2010**.1 (2010). arXiv: 0909.4791 [hep-lat].
- [62] P. H. Ginsparg and K. G. Wilson. *A remnant of chiral symmetry on the lattice*. Phys. Rev. D **25**.10 (1982), pp. 2649–2657.
- [63] K. Symanzik. *Continuum limit and improved action in lattice theories (I)*. Nucl. Phys. B **226**.1 (1983), pp. 187–204.
- [64] K. Symanzik. *Continuum limit and improved action in lattice theories (II)*. Nucl. Phys. B **226** (1983), pp. 205–227.
- [65] B. Sheikholeslami and R. Wohlert. *Improved continuum limit lattice action for QCD with wilson fermions*. Nucl. Phys. B **259**.4 (1985), pp. 572–596.

- [66] M. Lüscher, S. Sint, R. Sommer, P. Weisz and U. Wolff. *Non-perturbative $O(a)$ improvement of lattice QCD*. Nucl. Phys. B **491**.1-2 (1997), pp. 323–343. arXiv: [hep-lat/9609035](#).
- [67] K. Jansen and R. Sommer. *$O(a)$ improvement of lattice QCD with two flavors of Wilson quarks*. Nucl. Phys. B **530**.1-2 (1998), pp. 185–203.
- [68] K. Jansen and R. Sommer. *Erratum to: “ $O(a)$ improvement of lattice QCD with two flavors of Wilson quarks”*. Nucl. Phys. B **643**.1-3 (2002), pp. 517–518. arXiv: [hep-lat/9803017](#).
- [69] R. G. Edwards, U. M. Heller and T. R. Klassen. *Effectiveness of nonperturbative $O(a)$ improvement in lattice QCD*. Phys. Rev. Lett. **80**.16 (1998), pp. 3448–3451. arXiv: [hep-lat/9711052](#).
- [70] A.-M. Mykkanen, J. Rantaharju, K. Rummukainen, T. Karavirta and K. Tuominen. *Non-perturbative improvement of $SU(2)$ gauge theory with fundamental or adjoint representation fermions*. PoS (Lattice 2010) **105**, p. 064. Proceedings of the 28th International Symposium on Lattice Field Theory, 2010, Villasimius, Italy. arXiv: [1011.1781 \[hep-lat\]](#).
- [71] S. Musberg, G. Münster and S. Piemonte. *Perturbative calculation of the clover term for Wilson fermions in any representation of the gauge group $SU(N)$* . J. High Energy Phys. **2013**.5 (2013), pp. 1–6. arXiv: [1304.5741 \[hep-lat\]](#).
- [72] C. Morningstar and M. Peardon. *Analytic smearing of $SU(3)$ link variables in lattice QCD*. Phys. Rev. D **69**.5 (2004), p. 054501. arXiv: [hep-lat/0311018](#).
- [73] P. Weisz and R. Wohlert. *Continuum limit improved lattice action for pure Yang-Mills theory (II)*. Nucl. Phys. B **236**.2 (1984), pp. 397–422.
- [74] P. Weisz and R. Wohlert. *Erratum: Continuum limit improved lattice action for pure Yang-Mills theory (II)*. Nucl. Phys. B **347** (1984), pp. 544–545.
- [75] R. Sommer. *A new way to set the energy scale in lattice gauge theories and its application to the static force and α_s in $SU(2)$ Yang-Mills theory*. Nucl. Phys. B **411**.2-3 (1994), pp. 839–854. arXiv: [hep-lat/9310022](#).
- [76] M. Lüscher. *Properties and uses of the Wilson flow in lattice QCD*. J. High Energy Phys. **2010**.8 (2010), pp. 1–21. arXiv: [1006.4518 \[hep-lat\]](#).
- [77] S. Borsányi et al. *High-precision Scale setting in lattice QCD*. J. High Energy Phys. **2012**.9 (2012). arXiv: [1203.4469 \[hep-lat\]](#).
- [78] G. Bergner, I. Montvay, P. Giudice, G. Münster and S. Piemonte. *Influence of topology on the scale setting*. Eur. Phys. J. Plus **130**.11 (2015), p. 229. arXiv: [1411.6995 \[hep-lat\]](#).

Bibliography

- [79] M. Lüscher. “Computational strategies in lattice QCD”. *Modern Perspectives in Lattice QCD: Quantum Field Theory and High Performance Computing*. Oxford University Press, 2011, pp. 331–399. arXiv: 1002.4232.
- [80] I. Montvay. *An algorithm for gluinos on the lattice*. Nucl. Phys. B **466**.1-2 (1996), pp. 259–281. arXiv: hep-lat/9510042v3.
- [81] K. Demmouche. *$N = 1$ $SU(2)$ Supersymmetric Yang-Mills theory on the lattice with light dynamical Wilson gluinos*. PhD thesis. WWU Münster, Germany, 2009.
- [82] J. Sexton and D. Weingarten. *Hamiltonian evolution for the hybrid Monte Carlo algorithm*. Nucl. Phys. B - Proc. Sup. **26**.C (1992), pp. 613–616.
- [83] M. Lüscher and S. Schaefer. *Lattice QCD without topology barriers*. J. High Energy Phys. **2011**.7 (2011), pp. 1–26. arXiv: 1105.4749 [hep-lat].
- [84] G. Bergner and J. Wuilloud. *Acceleration of the Arnoldi method and real eigenvalues of the non-Hermitian Wilson-Dirac operator*. Comput. Phys. Comm. **183**.2 (2012), pp. 299–304. arXiv: 1104.1363 [hep-lat].
- [85] M. Lüscher. *Volume dependence of the energy spectrum in massive quantum field theories - II. Scattering states*. Comm. Math. Phys. **105**.2 (1986), pp. 153–188.
- [86] C. Michael. *Fitting correlated data*. Phys. Rev. D **49**.5 (1994), pp. 2616–2619. arXiv: hep-lat/9310026.
- [87] K. G. Wilson. *Talk at the Abingdon Meeting on Lattice Gauge Theories*. 1981.
- [88] B. Blossier, M. D. Morte, G. V. Hippel, T. Mendes and R. Sommer. *On the generalized eigenvalue method for energies and matrix elements in lattice field theory*. J. High Energy Phys. **2009**.4 (2009). arXiv: 0902.1265 [hep-lat].
- [89] C. Michael. *Adjoint sources in lattice gauge theory*. Nucl. Phys. B **259**.1 (1985), pp. 58–76.
- [90] M. Lüscher and U. Wolff. *How to calculate the elastic scattering matrix in two-dimensional quantum field theories by numerical simulation*. Nucl. Phys. B **339**.1 (1990), pp. 222–252.
- [91] U. Wolff. *Monte Carlo errors with less errors*. Comput. Phys. Comm. **156**.2 (2004), pp. 143–153. arXiv: hep-lat/0306017.
- [92] A. Donini, M. Guagnelli, P. Hernandez and A. Vladikas. *Towards $N = 1$ super-Yang-Mills on the lattice*. Nucl. Phys. B **523**.3 (1998), pp. 529–552. arXiv: arXiv:hep-lat/9710065.

- [93] M. Albanese et al. *Glueball masses and string tension in lattice QCD*. Phys. Lett. B **192**.1-2 (1987), pp. 163–169.
- [94] S. Güsken. *A study of smearing techniques for hadron correlation functions*. Nucl. Phys. B - Proc. Sup. **17** (1990), pp. 361–364.
- [95] C. R. Allton et al. *Gauge-invariant smearing and matrix correlators using Wilson fermions at beta=6.2*. Phys. Rev. D **47**.11 (1993), pp. 5128–5137. arXiv: [hep-lat/9303009v1](#).
- [96] G. S. Bali, H. Neff, T. Düssel, T. Lippert and K. Schilling. *Observation of string breaking in QCD*. Phys. Rev. D **71**.11 (2005), p. 114513. arXiv: [hep-lat/0505012](#).
- [97] E. Ziegel, W. Press, B. Flannery, S. Teukolsky and W. Vetterling. *Numerical Recipes: The Art of Scientific Computing*. Technometrics **29**.4 (1987), p. 501.
- [98] S. Kuberski. *Bestimmung von Massen in der supersymmetrischen Yang-Mills-Theorie mit der Variationsmethode*. Master Thesis. WWU Münster, 2017.
- [99] C. Bernard and T. DeGrand. *Perturbation theory for fat-link fermion actions*. Nucl. Phys. B - Proc. Sup. **83-84**.3 (2000), pp. 845–847. arXiv: [hep-lat/9909083](#).
- [100] B. de Wit and D. Z. Freedman. *Combined supersymmetric and gauge-invariant field theories*. Phys. Rev. D **12**.8 (1975), pp. 2286–2297.
- [101] G. Bergner, C. López and S. Piemonte. *A study of center and chiral symmetry realization in thermal N=1 super Yang-Mills theory using the gradient flow* (2019), pp. 1–19. arXiv: [1902.08469](#).
- [102] B. Joó, M. Smelyanskiy, D. D. Kalamkar and K. Vaidyanathan. “Wilson Dslash Kernel From Lattice QCD Optimization”. *High Performance Parallelism Pearls*. Vol. 2. Elsevier, 2015, pp. 139–170.
- [103] F. Knechtli, M. Günther and M. Peardon. *Lattice Quantum Chromodynamics*. SpringerBriefs in Physics. Dordrecht: Springer Netherlands, 2017.
- [104] S. Ali, G. Bergner, H. Gerber, P. Giudice, I. Montvay, G. Münster and S. Piemonte. *Simulations of N=1 supersymmetric Yang-Mills theory with three colours*. PoS (Lattice 2016) **201**, p. 222. Proceedings of 34th International Symposium on Lattice Field Theory, 2016, Southampton, UK. arXiv: [1610.10097 \[hep-lat\]](#).

Bibliography

- [105] S. Ali, G. Bergner, H. Gerber, P. Giudice, S. Kuberski, G. Münster, I. Montvay, S. Piemonte and P. Scior. *Improved results for the mass spectrum of $N = 1$ supersymmetric $SU(3)$ Yang-Mills theory*. EPJ Web of Conferences **175**, p. 08001. Proceedings of 35th International Symposium on Lattice Field Theory, 2017, Granada, Spain. arXiv: 1710.07105 [hep-lat].
- [106] S. Ali, G. Bergner, H. Gerber, P. Giudice, S. Kuberski, I. Montvay, G. Münster, S. Piemonte and P. Scior. *Supermultiplets in $N = 1$ SUSY $SU(2)$ Yang-Mills Theory*. EPJ Web of Conferences **175**, p. 08016. Proceedings of 35th International Symposium on Lattice Field Theory, 2017, Granada, Spain. arXiv: 1710.07464 [hep-lat].
- [107] S. Ali, G. Bergner, H. Gerber, P. Giudice, I. Montvay, G. Münster, S. Piemonte and P. Scior. *Ward identities in $N = 1$ supersymmetric $SU(3)$ Yang-Mills theory on the lattice*. EPJ Web of Conferences **175**, p. 08003. Proceedings of 35th International Symposium on Lattice Field Theory, 2017, Granada, Spain. arXiv: 1711.05504 [hep-lat].
- [108] S. Ali, G. Bergner, H. Gerber, P. Giudice, I. Montvay, G. Münster, S. Piemonte and P. Scior. *Investigation of Theories beyond the Standard Model*. NIC Series **49**, p. 195. Proceedings of the NIC Symposium, 2018, Jülich, Germany.

Hiermit versichere ich, dass die vorliegende Arbeit mit dem Titel *Non-perturbative investigations of light bound states of $\mathcal{N} = 1$ supersymmetric Yang-Mills theory* selbstständig verfasst worden ist, dass keine anderen Quellen und Hilfsmittel als die angegebenen benutzt worden sind und dass die Stellen der Arbeit, die anderen Werken - auch elektronischen Medien - dem Wortlaut oder Sinn nach entnommen wurden, auf jeden Fall unter Angabe der Quelle als Entlehnung kenntlich gemacht worden sind.

19th May 2020

(Henning Gerber)

Acknowledgments

I would like to thank my supervisor Gernot Münster for his continuous support and patience throughout my PhD studies. Furthermore, I thank my collaborators for valuable discussions and their help during my time in Münster. In particular, I would like to thank Georg Bergner, Simon Kuberski, Philipp Scior and Stefano Piemonte for proofreading this thesis.

Moreover, I want to thank the organizers and members of the RTG 2149: "Strong and Weak Interactions - from Hadrons to Dark Matter" for all their effort to provide an excellent learning environment for us doctoral students.

Finally, a huge thanks goes to my wife Sarah who has always supported me during my physics career, especially when I was writing this thesis.

Curriculum Vitae

Personal Information

Name	Henning Gerber
Adresse	Dürerstraße 43, 33615 Bielefeld
Date of Birth	October 08, 1989
Place of Birth	Bielefeld, Germany
Nationality	German

PhD Studies

10/2015 Beginning of PhD Studies at the Institute of Theoretical Physics, University of Münster, supervised by Prof. Dr. Gernot Münster. Member of the Research Training Group 2149 "Strong and Weak Interactions - from Hadrons to Dark Matter"

Higher Education

2013-2015	M.Sc. Physik Universität Bielefeld, GPA 1.0 Title of thesis: <i>Gravity-inspired extension of dissipative relativistic fluid dynamics for the description of heavy-ion collisions</i>
2010-2013	B.Sc. Physik Universität Bielefeld, GPA 1.1 Title of thesis: <i>Untersuchung eines zweidimensionalen topologischen Isolators in einem Zeeman-Feld</i>

Education

2000-2009	Allgemeine Hochschulreife Friedrich-v.-Bodelschwingh-Gymnasium Bethel, Bielefeld, GPA 1.3
1996-2000	Primary School: Dornberg, Bielefeld

Publications and Proceedings

The following list contains the publications and proceedings that have been published in the scope of my PhD thesis.

S. Ali, G. Bergner, H. Gerber, P. Giudice, I. Montvay, G. Münster and S. Piemonte. *Simulations of $N=1$ supersymmetric Yang-Mills theory with three colours*. PoS (Lattice 2016) **201**, p. 222. Proceedings of 34th International Symposium on Lattice Field Theory, 2016, Southampton, UK. arXiv: 1610.10097 [hep-lat]

S. Ali, G. Bergner, H. Gerber, P. Giudice, S. Kuberski, G. Münster, I. Montvay, S. Piemonte and P. Scior. *Improved results for the mass spectrum of $N = 1$ supersymmetric $SU(3)$ Yang-Mills theory*. EPJ Web of Conferences **175**, p. 08001. Proceedings of 35th International Symposium on Lattice Field Theory, 2017, Granada, Spain. arXiv: 1710.07105 [hep-lat]

S. Ali, G. Bergner, H. Gerber, P. Giudice, S. Kuberski, I. Montvay, G. Münster, S. Piemonte and P. Scior. *Supermultiplets in $N = 1$ SUSY $SU(2)$ Yang-Mills Theory*. EPJ Web of Conferences **175**, p. 08016. Proceedings of 35th International Symposium on Lattice Field Theory, 2017, Granada, Spain. arXiv: 1710.07464 [hep-lat]

S. Ali, G. Bergner, H. Gerber, P. Giudice, I. Montvay, G. Münster, S. Piemonte and P. Scior. *Ward identities in $N = 1$ supersymmetric $SU(3)$ Yang-Mills theory on the lattice*. EPJ Web of Conferences **175**, p. 08003. Proceedings of 35th International Symposium on Lattice Field Theory, 2017, Granada, Spain. arXiv: 1711.05504 [hep-lat]

S. Ali, G. Bergner, H. Gerber, P. Giudice, I. Montvay, G. Münster, S. Piemonte and P. Scior. *The light bound states of $N = 1$ supersymmetric $SU(3)$ Yang-Mills theory on the lattice*. J. High Energy Phys. **2018.3** (2018), p. 113. arXiv: 1512.07014 [hep-lat]

S. Ali, G. Bergner, H. Gerber, I. Montvay, G. Münster, S. Piemonte and P. Scior. *Analysis of Ward identities in supersymmetric Yang-Mills theory*. The Eur. Phys. J. C **78.5** (2018), p. 404. arXiv: 1802.07067 [hep-lat]

S. Ali, G. Bergner, H. Gerber, C. Lopez, I. Montvay, G. Münster, S. Piemonte and P. Scior. *Baryonic states in supersymmetric Yang-Mills theory*. PoS (Lattice 2018). Proceedings of the 36th International Symposium on Lattice Field Theory, 2018, East Lansing, Michigan, USA. arXiv: 1811.02297 [hep-lat]

S. Ali, G. Bergner, H. Gerber, P. Giudice, I. Montvay, G. Münster, S. Piemonte and P. Scior. *Investigation of Theories beyond the Standard Model*. NIC Series **49**, p. 195. Proceedings of the NIC Symposium, 2018, Jülich, Germany

S. Ali, G. Bergner, H. Gerber, S. Kuberski, I. Montvay, G. Münster, S. Piemonte and P. Scior. *Variational analysis of low-lying states in supersymmetric Yang-Mills theory*. J. High Energy Phys. **2019.4** (2019), p. 150. arXiv: 1901.02416 [hep-lat]

S. Ali, G. Bergner, H. Gerber, I. Montvay, G. Münster, S. Piemonte and P. Scior. *Numerical results for the lightest bound states in $N = 1$ supersymmetric $SU(3)$ Yang-Mills theory*. Phys. Rev. Lett., accepted (2019). arXiv: 1902.11127 [hep-lat]